A Thesis Submitted for the Degree of PhD at the University of Warwick

Integrating Cell Screening and Mechanism of Action data for Organometallic Anticancer Agents

A thesis submitted for the degree of

Doctor of Philosophy

Jessica M. Hearn, MChem. MSc.

Warwick Systems Biology Centre & Department of Chemistry

University of Warwick, UK

September 2014

Contents

Acknowledgements

Firstly, I would like to thank my supervisors, Peter and David, for creating an exciting area of research for me. Peter, thank you for your faith in me and giving me independence to make my own decisions throughout this project - hopefully you think they were wise! I thank you both for your continued support and encouragement and for the challenging experiences outside of my project - the opportunity to work with you both has been incredible.

Isolda, what can I say, you have been so supportive, right from the start. I have learnt so much from you and your incredibly efficient style of work - I have no doubt that you have a great career ahead of you. Although you were only here for a short while Bushra, I am thankful for your help and patience in getting me started, and for all the laughs along the way. Big thank you to Ana for working so hard with me in the beginning to get this project off the ground. And of course, thanks to the whole PJS group, particularly my homies in C411. I'll cherish the memories of all your blank faces whenever I presented work during group meetings.

Thanks to my PhD committee: Mike Khan, Claudia Blindauer and Rich Savage. You were all so supportive, I am a textbook self-doubter so your positive feedback went a very long way.

For the Edinburgh collaboration I thank Neil Carragher and Alison Munrow for all your hard work. At the School of Life Sciencies, thanks to Ian Portman for help with the imaging and accepting the new challenges that came your way. Thanks also to Paul Goode and Surinder Bhamra for help and support in the cell culture lab.

Thank you to my friends, both here at Warwick and back home. Namely Samuel, Markus, Jay and Thomas. You were all fantastic sources of advice and, more importantly, sources of relaxation and distraction.

Finally, the biggest thank you to my family. I will be forever grateful to you all. Getting here has been tough, and your financial and emotional support allowed me to both turn my life around when I thought I'd thrown it away and to keep me going when I felt close to quitting. I would never be here if it wasn't for you all.

Statement of candidate contribution

The experimental screening presented in Chapter 3 was performed by the National Cancer Institute (USA) and The Sanger Institute (Cambridge, UK). The statistical analysis of the National Cancer Institute screening data was performed by the author and for the Sanger data was performed by both the author and the Sanger Institute. Primary cell screening was performed by Dr Belen Rubio-Ruiz at the Edinburgh Cancer Research Centre, under the supervision of Dr Neil Carragher.

The sequencing experiments were designed by the author, and the RNA samples prepared and QC checked by the author. Samples were bioanalyzed by Lesley Ward at The University of Warwick, and sequenced at the Oxford Genomics Centre, part of The Wellcome Trust Centre for Human Genetics, under the project management of Dr Sarah Lamble (Oxford, UK). Sequence reads were mapped by the Oxford Genomics Centres bioinformatics team, and all downstream analysis was performed by the author.

Protein microarray experiments were designed, monitored and analysed by the author. All experimental work was performed at the Edinburgh Cancer Research Centre (Edinburgh, UK) by Dr Alison Munrow, supervised by Dr Neil Carragher.

MDI software was developed by Dr Paul Kirk, Dr Rich Savage and Mr Sam Mason. All were based at Warwick Systems Biology Centre.

Samples for high-content imaging were prepared and run by Dr Neil Carragher, at the Edinburgh Cancer Research Centre. Quantification of results were performed by the author. Transmission electron microscopy samples were prepared by the author, embedded by Dr Ian Portman, and imaged by the author and Dr Ian Portman. Captured images were analysed by the author.

Declaration

I hereby declare that except where specific reference is made to other sources, the work contained in this thesis is the original work of the author. It has been composed by myself and has not been submitted, in whole or in part, for any other degree, diploma or qualification.

Jessica M. Hearn
September 2014

Abstract

Both acquired and intrinsic drug resistance are established clinical problems in many areas of medicine. This is particularly evident with the growing resistance to platinum chemotherapy agents in cancer treatment programmes. New, alternative treatments for platinum-resistance patients are needed, with comparable potency, no platinum cross-resistance, better safety profiles and which target non-repairable areas of the cell, reducing acquired resistance.

This thesis focuses on osmium- and iridium-based organometallic anticancer agents to fill this clinical need. Previous work has validated their potency, safety and activity in platinum-resistant cancers, however, their mechanism of action (MOA) was yet to be identified. Knowing the MOA of new compounds is essential for personalising and stratifying cancer treatment, allowing for better patient selection and prediction of treatment outcomes. Often identifying the biological target of a new therapeutic is not essential. Instead, quantifying the cellular response to that treatment, and identifying cell types which hold beneficial biological properties to optimise compound effects, is more effective.

This thesis has applied the principles of systems biology to study the whole cell effect of osmium and iridium compounds in epithelial ovarian cancer. Cells were studied at the transcriptional, translational and structural level to investigate compound response, integrating a selection of these findings using novel statistical modelling.

Results propose that these compounds induce oxidative stress in cancer cells, and subsequently damage DNA to exert antiproliferative effects at submicromolar concentrations. This is the first example of studying organometallic compounds using this combination of techniques, and is a promising work flow for future efforts in this area.

Abbreviations

Os-1	$[Os(\eta^6\text{-bip})(NMe_2\text{-azpy})I]PF_6$
Os-2	$[Os(\eta^6\text{-}p\text{-cym})(NMe_2\text{-imino})I]PF_6$
Os-3	$[Os(\eta^6\text{-}p\text{-cym})(NMe_2\text{-azpy})I]PF_6$
Os-4	$[Os(\eta^6\text{-bip})(F\text{-azpy})I]PF_6$
Os-5	$[Os(\eta^6\text{-bip})(OH\text{-azpy})I]PF_6$
Ir-6	$[Ir(\eta^5\text{-}Cp^{xbiph})(phen)Cl]Cl$
Ir-7	$[Ir(\eta^5\text{-}Cp^{xph})(phen)Cl]Cl$
Ir-8	$[Ir(\eta^5\text{-}Cp^{xbiph})(bpy)Cl]PF_6$
Ir-9	$[Ir(\eta^5\text{-}Cp^{xbiph})(ppy)Cl]$
Ir-10	$[Ir(\eta^5\text{-}Cp^{xph})(NMe_2\text{-azpy})Cl]PF_6$
Ir-11	$[Ir(\eta^5\text{-}Cp^{xbiph})(dpq)Cl]Cl$

ATP	Adenosine triphosphate
Azpy	Azopyridine
Bpy	Bipyridine
CI	Electron transport chain complex I
CII	Electron transport chain complex II
CIII	Electron transport chain complex III
CIV	Electron transport chain complex IV
CV	Electron transport chain complex V
CDDP	Cisplatin
CNV	Copy number variation
DDI	Double deionised water
DE	Differential expression
DEG	Differentially expressed gene
DGE	Differential gene expression
DMSO	Dimethyl sulfoxide
Dpq	Dipyridoquinoxaline
DTP	Drug therapeutics program
ECACC	European Collection of Cell Cultures
EOC	Epithelial ovarian cancer
ETC	Electron transport chain
FDR	False discovery rate
GI	Gastrointestinal tract
GI_{50}	Concentration of drug-compound to inhibit 50% cell growth
GSH	Glutathione

HCS	High content screening
IAP	Inhibitor of apoptosis protein
IPA	Ingenuity pathway analysis
L-BSO	L-Buthionine sulfoximine
LC_{50}	Concentration of drug-compound to cause 50% cell death
LogFC	Log_2(fold change)
MCMC	Markov Chain Monte Carlo
MDI	Multiple dataset integration
MOA	Mechanisms of Action
MOMP	Mitochondrial outer membrane permeabilisation
MTT	3-(4,5-dimethylthiazol-2-yl)-2,5-diphenyltetrazolium bromide) assay
NCI	National Cancer Institute
NCI-60	National Cancer Institute 60 cell line screen
OXA	Oxaliplatin
OXPHOS	Oxidative phosphorylation
PCA	Principal component analysis
PI	Propidium iodide
Phen	Phenanthroline
Ppy	2-phenylpyridinato
Py	Pyridine
RFI	Relative fluorescence intensity
RIN	RNA integrity number
RNAseq	RNA sequencing
ROS	Reactive oxygen species
RPMI-1640	Roswell Park memorial institute medium 1640
RPPA	Reverse phase protein microarray
SIMS	Secondary ion mass spectrometry
SRB	Sulforhodamine B assay
TEM	Transmission electron microscopy
OXA	Oxaliplatin
p53	Tumour supressor protein 53
PBS	Phosphate buffered saline
PSM	Posterior similarity matrix
SIMS	Secondary ion mass spectrometry
TEM	Transmission electron microscopy
TGI	Concentration of drug-compound to cause 100% growth inhibition

I dedicate this thesis to Teams Hearn, Williams and Robertson.

Chapter 1. Introduction

As the cases of resistance continue to rise in the treatment of cancer, there is a drive to develop new anticancer agents. Additionally, there is desperate need to develop new therapeutics with better safety profiles and larger therapeutic indices. New treatments must have comparable potency, higher cancer cell selectivity and alternative mechanisms of action to those drugs currently used in the clinic. This thesis focuses heavily on developing new metal-based anticancer agents to tackle the current limitations of platinum-based drugs like cisplatin. These new drug compounds are osmium- and iridium-based, and in previous work have demonstrated desirable activity, equipotency in platinum-resistant cancers and promising selectivity profiles. However, their mechanism of action (MOA) still remains undetermined.

Therefore this thesis aims to gain insights into the biological activity of these compounds using a systems biology workflow. In the first instance, cancer cell screens are used to filter out lead compounds, and to obtain preliminary mechanistic information. Using RNA sequencing, protein microarrays and imaging techniques, the cellular effects of lead compounds are investigated in epithelial ovarian cancer (EOC) cells. Collectively this information could drive future studies to probe the direct targeting sites for these osmium and iridium compounds, and push them through preclinical development towards clinical studies.

1.1 Ovarian cancer

In 2009 there were 320,467 people diagnosed with cancer in the UK, a number projected to increase to over 400,000 by 2030.[1] As of April 2013, there are over 200 types of cancer, with breast, lung, bowel and prostate cancers accounting for over half of all new cases each year.[2] There are many risk factors linked to the development of cancer; age, lifestyle and epigenetics are main examples.

Ovarian cancer affects more than 6,500 women in the UK each year, and is the 5th most common cancer after breast, bowel, lung and uterine.[3] Ovarian cancer is a diverse disease with cell types falling into three main categories: epithelial, germ cell and stromal. Epithelial ovarian cancers (EOC) are the most common, effecting the surface layers of the ovary.[4–6] The treatment of ovarian cancers depends on the stage and grade with treatment covering surgery, radiotherapy or chemotherapy, or often all three. Ovarian cancers diagnosed below stage 2, which have not spread to other parts of the abdomen are generally treatable via one or more of these methods. However, diagnosis is often complicated as many women are asymptomatic and miss-diagnosed with irritable bowel syndrome, which delays detection and treatment considerably.[7] As the most common form of ovarian cancer, 70% of EOC are not diagnosed until late stage, after spreading to the abdomen. In general, the earlier the detection of ovarian cancer, the higher the 5-year survival rate, stressing the importance of regular screening in women.

1.2 Cancer chemotherapy

Chemotherapy plays an important role in both early and advance stage ovarian cancer treatment, reducing symptoms and pain through tumour shrinkage. However, cancers are highly heterogenous, therefore cells within the tumour may be susceptible to certain chemotherapeutics and others may be resistant.[8, 9] A study by Wang *et al* showed that from fourty-seven surgically assessed stage I EOC they could detect grade III tumour, grade I and II endometrioid, and clear-cell tumour cells, demonstrating significant heterogeneity.[10]

Patients are therefore often given a cocktail of drugs, with hopes of targeting all types of cancer cells within the tumour. However, in many cases patients experience relapse and subsequent resistance to first line therapies as a result of either insufficient surgical removal of all tumour cells, or an inability to appropriately target all tumour cell types with chemotherapy. Often, chemosensitive cells are successfully targetted with a chemotherapy agent, but cells with inherent resistance are unaffected and divide to become the dominant cell type in the tumour. For example, cancer stem cells (CSC), a cell type often found in tumours, can maintain a quiesent (G0) state which allows them to be chemoresistant, as chemotherapy agents are generally most effective against fast dividing cells.[11] It is also possible for chemosensitive cells to develop resistance mechanisms during treatment, for example by altering the drug target with mutations or expression changes, or decreasing cellular drug accumulation.[12] In cases of resistance, second line chemotherapy agents are administered, ideally with no cross-resistant to first line treatments. Unfortunately, relapse can continue to occur, until a patient no longer responds to any clinically available drugs. This problem highlights the need for research and development of new chemotherapeutics, ideally with little or no cross-resistance to current clinically used drugs.

1.2.1 Metallo-drugs

The administration of metal-based drugs into the body exposes them to reactions with a plethora of biological substances, although the main targets are assumed to be proteins and DNA.[13, 14] Most metal complexes have easily displaced ligands which allow modification when in contact with elements inside the cell. This can provide flexible mechanisms of action (MOA), but also increase the complexity of work conducted during research and development phases of drug design.

The serendipitous discovery of cisplatin, a platinum(II) based drug, together with its subsequent derivatives, oxaliplatin and carboplatin have shown incredible success in the clinic against testicular, ovarian and colorectal cancers (Figure 1.1).[15] Generally, the first line treatment for ovarian cancer patients is platinum based, where the length and dose of treatment is dependent on the patient and the stage and grade of the tumour.

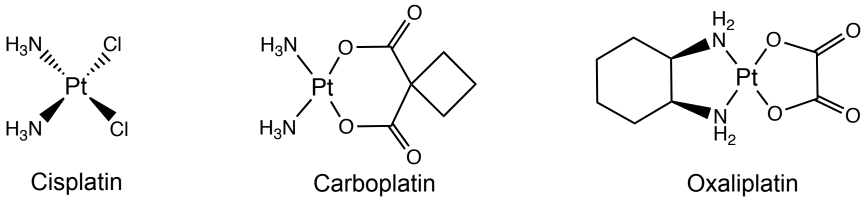

Figure 1.1: Clinically used platinum(II) metallodrugs cisplatin, carboplatin and oxaliplatin. Cisplatin and Carboplatin are commonly used to treat ovarian cancer, with oxaliplatin used to treat colorectal.[15]

Although platinum (Pt) drugs have marked a major breakthrough in cancer research, they are non-specific cytotoxic agents, which means they cannot distinguish between fast dividing host cells and fast dividing cancer cells.[16] This lack of specificity results in severe side effects, for example disrupting patient immune systems by killing lymphocytes required to fight off infection during the treatment duration. In addition, the cases of inherent and acquired resistance are a common occurrence.

Pt drugs are commonly associated with DNA binding mechanisms, and an ability to cross link DNA strands, causing irreparable damage and activating apoptotic cell death.[16] If patient resistance is acquired during treatment it occurs through three common mechanisms: increased drug efflux, increased DNA repair mechanisms and decreased drug influx.[17] In ovarian patients who have relapsed after first line platinum treatment, physicians will determine whether the patient has become platinum resistant based on the relapse interval.[18] A patient who suffers relapse $>$12 months after the first platinum treatment are still considered platinum sensitive, when relapse occurs sooner, they are considered resistant or partially sensitive. If a patient is deemed platinum resistant, it follows that any chemotherapy agent used as a second or third line treatment should have no cross resistance with platinum i.e. it should act through alternative MOA. Drugs able to fill this category are in high demand, and extensive research focuses on developing newer metal-based agents.[14, 19]

1.2.1.1 Ruthenium

Some metal-based compounds move away from DNA-targetting, like NAMI-A (New Anti-tumour Metastasis Inhibitor-A) a Ruthenium (Ru) compound in phase II clinical trials as a drug able to inhibit the process of metastasis (Figure 1.2).[13] This kind of drug has potential benefits when used prior to surgery, and during phase I clinical trials showed exceptionally low patient toxicity. NAMI-A is thought to have a low affinity for DNA binding, and instead binds to exposed imidazole sites (histidine residues) on human and bovine serum albumin and apo-transferrin.

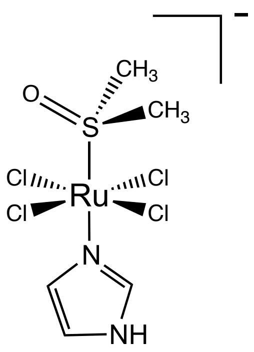

Figure 1.2: Ruthenium anticancer drug NAMI-A currently in phase II clinical trials to treat metastatic cancers.[13]

1.2.2 Organometallic drugs

1.2.2 Osmium and iridium

The success of Pt and Ru based drugs has sparked interest in neighbouring transition metals, like osmium (Os) and iridium (Ir).[20–23] Os and Ir organometallic compounds developed in the Sadler group at The University of Warwick are half-sandwich piano-stool compounds chelating a variety of coordinated ligands (Figure 1.3).[20, 24–27]

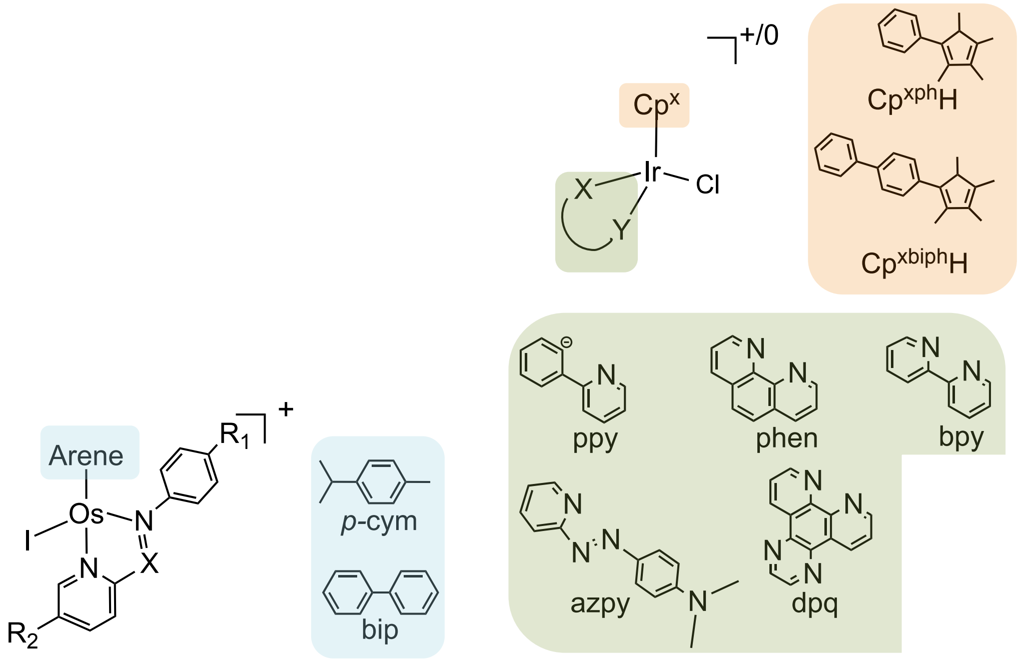

Complex	Arene	R_1	R_2	X
Os-1	bip	NMe$_2$	H	N
Os-2	*p*-cym	NMe$_2$	H	C
Os-3	*p*-cym	NMe$_2$	H	N
Os-4	bip	H	F	N
Os-5	bip	OH	H	N

Complex	Cp^xH	XY
Ir-6	Cp^{xbiph}	phen
Ir-7	Cp^{xph}	phen
Ir-8	Cp^{xbiph}	bpy
Ir-9	Cp^{xbiph}	ppy
Ir-10	Cp^{xph}	azpy
Ir-11	Cp^{xbiph}	dpq

Figure 1.3: Lead Osmium (Os) and Iridium (Ir) compounds synthesised in the Sadler group by Dr Fu Ying and Dr Zhe Liu, respectively. Highlight in blue are the various arena ligands chelated to Os compounds **Os-1** - **Os-5**. All Os compounds are chelated to N-N azopyridine (X=N) or iminopyridine (X=C) ligands, with varying R groups (R_1 and R_2) described in the left-hand table. All Os compounds have a +1 charge. Highlighted in orange are the various arena ligands chelated to Ir compounds **Ir-6** - **Ir-11**. Highlighted in green are the varying N-N and C-N chelating ligands (XY) for each Ir compound, as described in the right-hand table. All Ir compounds have a +1 charge, except for **Ir-9** which is neutral.[20, 24–27]

These compounds show remarkable activity in the high-grade serous EOC cell line A2780, and were designed to overcome the major hurdles currently in place with long-term use of drugs like cisplatin: namely Pt resistance and severe side-effects. The ligands are diverse, and allow each compound to exhibit a variety of properties. For example a neutral Ir compound is obtained by using the phenylpyridinato (ppy) chelating ligand, compared to the cationic complexes obtained when using neutral chelating ligands. These alterations in functionality have potential to alter the MOA of these compounds and provide a unique ability to tailor drug design to target a particular pathway or biological component inside cancer cells.

These compounds were initially designed to have the same mechanism as the Pt(II) drugs, where the labile halide ligand undergoes a substitution reaction to form an activated aqua compound, able to bind to the N7 group on guanine and adenine nucleobases. Although this mechanism is possible for some of the Ir-Cl containing compounds, in some cases the hydrolysis can be blocked, producing highly active compounds *in vitro*.[25, 28] This is also true for the Os compounds where the Os-I bond is generally non-hyrolysable.

The hydrolysis status shown for each of the compounds in Table 1.1 is measured by incubating each compound in deuterated methanol/water (5% MeOD/95% D_2O (v/v), and measuring the formation of new aqua species by the appearance of new peaks by proton NMR, over a 48 h time series.

Table 1.1: Table of the 11 compounds **Os-1** - **Os-5** and **Ir-6** - **Ir-11** describing their full structure, activity in A2780 ovarian cancer cells as the concentration to inhibit 50% of cancer cell growth, and the hydrolysis status for their metal-halide bond.[20, 24–26]

Complex	**[Structure] Counter ion**	**A2780 GI_{50} (μM)**	**Hydrolysis status***
Os-1	$[Os(\eta^6\text{-bip})(NMe_2\text{-azpy})I]PF_6$	0.14 ± 0.01	N
Os-2	$[Os(\eta^6\text{-}p\text{-cym})(NMe_2\text{-imino})I]PF_6$	0.80 ± 0.05	N
Os-3	$[Os(\eta^6\text{-}p\text{-cym})(NMe_2\text{-azpy})I]PF_6$	0.15 ± 0.01	Y
Os-4	$[Os(\eta^6\text{-bip})(F\text{-azpy})I]PF_6$	0.63 ± 0.10	N
Os-5	$[Os(\eta^6\text{-bip})(OH\text{-azpy})I]PF_6$	0.14 ± 0.01	N
Ir-6	$[Ir(\eta^5\text{-}Cp^{xbiph})(phen)Cl]Cl$	0.72 ± 0.01	Y
Ir-7	$[Ir(\eta^5\text{- }Cp^{xph})(phen)Cl]Cl$	6.70 ± 0.62	Y
Ir-8	$[Ir(\eta^5\text{-}Cp^{xbiph})(bpy)Cl]PF_6$	0.57 ± 0.09	Y
Ir-9	$[Ir(\eta^5\text{-}Cp^{xbiph})(ppy)Cl]$	0.70 ± 0.04	Y
Ir-10	$[Ir(\eta^5\text{-}Cp^{xph})(NMe_2\text{-azpy})Cl]PF_6$	0.40 ± 0.00	N
Ir-11	$[Ir(\eta^5\text{-}Cp^{xbiph})(dpq)Cl]Cl$	0.88 ± 0.09	Y

* Y = hydrolysis occurs in under 48 h and N = hydrolysis does not occur in 48 h

1.2.2.2 Benefits osmium compounds over platinum treatments

Circumventing platinum resistance. Figure 1.4 highlights the promising activity of the Os and Ir compounds in Pt resistant ovarian and colorectal cell lines, suggesting that these drug-compounds could fill an unmet clinical need.[29]

Activity in p53(-/-). Tumour protein 53 (p53) has a vital role in controlling cell cycle regulation and tumour suppression.[30] This protein can perform 3 main anti-cancer roles: activate DNA repair mechanisms, arrest cell growth in G1/S phase, whilst DNA is repaired, and finally activate apoptosis if DNA damage cannot be repaired. p53 mutations are highly important biomarkers in high grade serous ovarian cancer and are the thought to occur in approximately 50% of all cancers.

Figure 1.4 shows that the Os and Ir compounds not only demonstrate high activity in p53(-/-) cell lines, but that the absence of this mutation can actually increases this activity. For example compound **Os-4** is x4 more active in p53 mutated HCT116 colorectal cells compared to the wild-type.[29] These promising results highlight another clinical benefit, increasing the treatment window to cover p53 mutated cancers. Mechanistic insights can also be gained from these results, when compared to cisplatin and oxaliplatin, where the GI_{50} value for cisplatin increases by 4 times in the p53 mutated cell line, the same value for oxaliplatin is $>$ 25 times.[29] The results for the platinum drugs suggest that p53 is essential for there MOA, which is predictable given their activity focusses on DNA damage. As p53 is also required for **Os-3** to keep its high level of activity one might suspect that DNA damage is part of the MOA, however, **Os-3** was shown not to bind to DNA models, although it is the only Os compound to hydrolyse. The remaining compounds do not require p53 for activity.

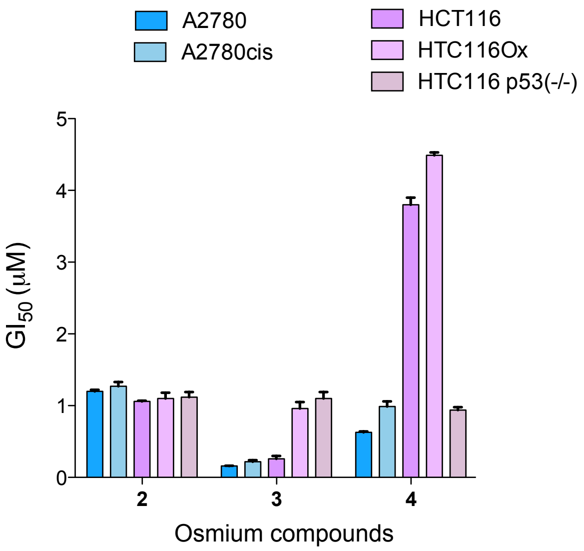

Figure 1.4: Graph showing GI_{50} values (± standard deviation) for compounds **Os-2**, **Os-3** and **Os-4** in different cell lines. Activity values were calculated from triplicate measurements in colorectal cell lines (purple) and ovarian cell lines (blue) and show that **Os-2** and **Os-3** hold their activity in cisplatin-resistant A2780 cells (A2780cis), but only **Os-2** maintains activity in oxaliplatin-resistant HCT116 (HCT116Ox). **Os-4** is more active in cisplatin-resistant A2780 and approximatively equipotent in oxaliplatin-resistant HCT116. Interestingly, **Os-4** is highly active in p53(-/-) HCT116 cells compared to wild-type HCT116.[29, 31]

Cancer cell selectivity. To investigate the activity of the Os and Ir compounds in normal, fast dividing cells versus activity in cancerous cells, the GI_{50} of **Os-2** and **Os-3** in ovarian cancer cells (A2780) and normal lung fibroblast cells (MRC-5) was determined.[29] Results show that the two Os complexes are $\approx$ 30 times more active in A2780 (Table 1.2). As a reference, the resistance factor for cisplatin is $\approx$ 10, highlighting the promising selectivity of the Os compounds.

Combination treatment with L-BSO. L-Buthionine sulfoximine (L-BSO) depletes the levels of glutathione (GSH) inside the cells, where GSH is an antioxidant, required to protect the cell from reactive oxygen species (ROS). L-BSO is currently in clinical trails as a cytostatic agent used in combination with Melphalan, an alkylating agent.[32] Table 1.3 shows that when cells are co-incubated with 5 μM L-BSO, the activity of the Os and Ir compounds increases by up to 50-fold.[31]

Table 1.2: Activity data for **Os-2** and **Os-3** compounds in A2780 ovarian cancer cells versus MRC-5 normal lung fibroblast cells.[29] GI_{50} values were calculated from triplicate measurements, shown as ±SD. The resistance factor compares the activity in each cell line, where a higher resistance factor shows a lower sensitivity of normal cell lines to each compound. The higher the resistance factor the safer the compound is predicted to be regarding off-target side-effects in patients, with both **Os-2** and **Os-3** showing promising levels of selectivity.

Compounds	**A2780 GI_{50} μM**	**MRC-5 GI_{50} μM**	**Resistance* factor**
Os-2	1.20 ± 0.003	31.8 ± 0.02	25.8
Os-3	0.16 ± 0.02	4.5 ± 0.09	28.1

* Resistance factor is calculated as the ratio of activity between MRC-5/A2780

Table 1.3: Synergistic behaviour between The activity of compounds **Os-2**, **Os-3**, **Ir-9** and **Ir-10** in A2780 cells with and without co-incubation with reactive oxygen species (ROS) scavenger L-buthionine sulfoximine (L-BSO). Activity values were calculated from triplicate measurements, shown as ±SD. The activity ratio describes the effect that co-incubation has on the anticancer activity, where a high value suggests that L-BSO increases the susceptibility of cancer cells to each compound. The data shows that L-BSO enhances the activity of all compounds, particularly **Ir-10**.[29, 31]

Compounds	**0 μM L-BSO GI_{50} μM**	**5 μM L-BSO GI_{50} μM**	**Activity* ratio**
Os-2	1.20 ± 0.003	0.080 ± 0.002	15.0
Os-3	0.16 ± 0.020	0.069 ± 0.002	2.3
Ir-9	0.68 ± 0.040	0.110 ± 0.040	6.2
Ir-10	0.40 ± 0.080	0.008 ± 0.002	50.0

* Activity ratio is the GI_{50} ratio between cells co-incubated with 0 μM/5 μM L-BSO.

Table 1.3 highlights their potential, when used in combination with L-BSO, to drop the administered dose into a safer range for patients. Developing drugs as combination treatments, whether synergist or additive, is an attractive prospect to reduce off target effects and to target tumour cell heterogeneity.

The work carried out to date on the Os and Ir compounds highlights them as promising therapeutics, particularly against EOC.

1.3 Exploring mechanisms of action

A personalised approach to clinical treatment aims to examine each patient individually, on a genetic level, and identify biomarkers responsible for disease development and for treatment prognosis.[33, 34] From this information, a physician would prescribe a specific drug able to increase the effectiveness of treatments in patients. This approach is already in use for some cancer biomarkers, however, the development of treatment systems like this heavily relies on patient populations and access for clinical trials.

This stratified approach puts large emphasise on identifying the MOA for any emerging anticancer compounds. If we could develop highly active chemotherapy drugs with the ability to target such biomarkers, differentiating between fast dividing cancer cells and fast dividing host cells, we may see a new treatment which is more effective and less harmful to patients.

Developing a new agent, is a long and commonly unsuccessful process. The most frequently used pipeline for drug development starts with identification of new carcinogenic targets, either RNA, DNA or proteins. Developing the agent involves activity/affinity screening against compound libraries.[35, 36] From here, qualitative and quantitative read outs of inhibition or binding to the target identify "hits". Systems using drop-based microfluidics can allow the testing of 100,000,000 reactions in 10 hours, reducing running costs significantly with smaller reactant volumes.[37] Identified hits are then validated with their target and the hit-to-lead optimisation stage begins.[38] The discovery of tyrosine kinase inhibitors by this method is an excellent example of its success.

Although this drug development pipeline has shown strong merit in drug discovery, library screening for inhibition of activity or for affinity binding is inherently complex. Like any high throughput technique, there are incidence of both false negative and false positive results, which makes hit selection criteria risky.[39] Instead, a reverse approach to early stage drug development is often preferable.[40]

Compounds are now synthesised based on prior knowledge and chemical and biological principles. Simple *in vitro* screening can establish structure-activity-relationships, and even allow compound optimisation at the earliest stage. Once activity has been proven, the hit is taken forward for target identification. There are many resources and methods available to investigate the targets and MOA of hit compounds, many of which can be complementary techniques. Identifying the MOA of a novel hit compound is often a daunting and expensive task, and relies heavily on scientific expertise across multiple disciplines.

1.3.1 Screening facilities

There are several institutions which offer help to early stage drug developers, screening new compounds to allow researchers to infer MOA, or to at least move projects in the right direction. This dramatically reduces cost in the long run.

1.3.1.1 National Cancer Institute

One of the most useful resources available is provided by the Developmental Therapeutics Program (DTP), together with the National Cancer Institute (NCI) and the Nation Institute of Health (NIH). Here, the NCI performs drug screening in their so-called NCI-60 assays.[41–43] The NCI-60 project was developed between 1985 and 1990, and became fully implemented by April 1990, now testing approximately 3,000 compounds per year. This NCI-60 screen tests the activity of submitted compounds in 60 of the most common cancer cell lines, including leukemias, non-small cell lung, central nervous system, colon, melanoma, renal, prostate, breast and ovarian. This service is free of charge for compounds deemed promising by the NCI, with a quick turn around of results.

This provides useful data in itself, but can also be used together with information in open access databases hosted by the DTP and NCI/NIH. Using these databases we can compare their NCI-60 results to other compounds using the so-called "COMPARE" algorithm.[41–44] This algorithm is maintained by the NCI and calculates a Pearson's correlation coefficient (r) between activity values for one variable (NCI-60 activity results for compound 1) and another variable (NCI-60 activity results for compound 2).

If correlated compounds have known MOA, it is possible to infer a MOA for their given seed, by similarity. Previous work has successfully used this method to predict MOA for anticancer compounds.[31, 45–48]

1.3.1.2 The Sanger Institute

The Wellcome Trust Sanger Institute is a non-profit organisation, run by Genome Research Limited (GRL). The Cancer Genome Project (CGP) within the Sanger Institute has a similar approach in drug development as the NCI, however, here compounds are tested in ca. 1000 cell lines. The Sanger Institute performs a 9-dose response for each compound on each cell lines, providing a GI_{50} value for each.

Like NCI data, Sanger screening provides an idea of the most suitable cancer cell models, and together with COSMIC, a database of somatic cancer mutations, can also provide biomarker information.[49–53] The COSMIC database houses sequence data for ca. 400 genes, describing both somatic mutations and copy number variations. These genes are predicted or known to be important in cancer development and prognosis. The GI_{50} values are then studied with respect to the cancer cell line and the respective genetic events involved in that cell line. A study by Cowin *et al* used this method to show that the high incidence of chemoresistance in patients with high-grade serous ovarian cancer may be due in part to the depletion of a lipid transporter protein, LRP1B.[54]

1.3.2 Systems biology

Systems biology has become a fashionable area of cancer research. Although its concepts are broadly interpreted, ‘assessing a system as the sum of its individual components’ is a common definition. This concept can be useful in assessing MOA of emerging drugs, gradually building up a complete picture of how a drug exerts its activity by seeing how it acts on individual aspects of a system. In a cell this could be achieved by combining information about how the genes, proteins and cellular structures are affected by a given compound. However, assessing an entire system as a sum of its components often creates large complex datasets, therefore a large chunk of cancer-based systems biology is bioinformatics focussed, developing tools to handle and manipulate these datasets to provide relevant clinical outcomes.

An emerging area of bioinformatics and systems biology produces tools to allow integration of heterogenous datasets. In 2012, The Cancer Genome Atlas Network used patient data in a breast cancer study designed to integrate genomics, DNA methylation, exome sequencing, transcriptomics, proteomics and breast cancer subtype.[55] The study used data from 825 patients showed a relation between basal-like breast tumours and high-grade serous ovarian tumours, highlighting the potential for similar therapeutic treatments. They also observed that plasticity and heterogeneity occurred within, and not across, the major breast cancer subtypes. This example nicely demonstrates the merit of a systems biology approach, combining as many different aspects of the breast cancer system to find a richer result.

Using time series data in this context introduces further complexity into heterogenous dataset integration, as the data are not strictly independent. Work conducted at the Warwick Systems Biology Centre, with Professor David Wild, uses multiple dataset integration (MDI) software to combine heterogenous datasets in a way to capture all dependences and complementary aspects in the data.[56–58] In a study by Kirk *et al*, transcriptomic, chIP and protein-protein interaction (PPI) data were integrated using publicly available databases for *S. cerevisiae* and produced a list of clustered genes which were “fused” across all three datasets.[56] A fused gene, is one which behaves similarly across all datasets, irrespective of the measurement type. MDI is an unsupervised Bayesian method, which allows the software to exploit the natural clustering of ‘omics data reducing data constraints and the potential loss of useful information. This is a promising concept, particularly as MDI is amenable to gaussian, time series, categorical and discreet datasets.

The work described above was performed in a simpler eukaryotic system, however, the use of MDI could also be extended to study more complex systems. For example, combining time series transcriptomic and proteomic data from cells exposed to a given compound, or to complement the Sanger screening data, capturing dependencies of drug sensitivity with tissue type and genetic events.

The former could provide information on where gene and protein behaviour overlay, and where there are discrepancies, both of which provide mechanistic insights. A study by Rogers *et al* demonstrated the potential of using such models to combine such data types. This study was performed with human mammary epithelial (HMEC) time series gene and protein data, where cells had been stimulated with epidermal growth factor (EGF).[58] The number of genes and proteins modelled was relatively small (ca. 500), however provided interesting results which demonstrated a poor correlation between mRNA and protein expression in some biological components. These same principles could be applied to study cancer systems, integrating gene and protein regulation from cells exposed to anticancer agents.

1.3.3 Transcriptomics

The central dogma of molecular biology describes the flow of genetic information; Marshall Nirenberg simply described it as "DNA makes RNA makes protein".[59] The transcriptome refers to the set of transcripts (mRNA sequences) in a cell, which reflect the gene expression profile as a result of the first step of the central dogma.[60] This gene expression can capture how a cell responds during a given process or after a given treatment. Transcriptomics, principally, allows us to determine the abundance of these transcripts in the cell.

The past decade saw the development of next generation sequencing (NGS), where RNA sequencing (RNAseq) is used to study transcriptomics, providing insights about the transcriptome of any species.[60] RNAseq provides superior sensitivity and resolution compared to DNA microarrays, allowing users to analyse a fuller dataset with increased accuracy for both lowly- and highly-expressed genes.[61–63]

The use of RNAseq in anticancer drug development has shown notable success, particularly to investigate resistance mechanisms, however, there are still few reported studies. For example, Houghtaling *et al* published a method to identify targets of known anticancer drugs BI 2536 and bortezomib by studying resistance mechanisms in drug-resistant clones.[64] The authors suggest that such an approach would only work with singly targetted drugs, as those with multiple targets would add too much complexity to their models. This highlights the potential issues with using a technique like RNAseq to investigate drug MOA, particularly if used for complex molecules likely to target many cellular profiles.

1.3.4 Proteomics

Although cancer is generally governed by genetics and epigenetics, the response to anticancer treatments are registered at a protein level.[40] Therefore the study of proteins in response to drug exposure can provide great insights into MOA and into patient selectivity. Proteomics is the concept of measuring the properties, whether it be abundance or modification, of proteins in a given sample. In theory, the level of protein X in a system should be positively correlated to the expression of gene X, however, this is not always the case.[58] For this reason it is often interesting to study both transcriptional and translational systems, particularly if investigating drug MOA.

A bottom-up proteomic approach, known as shotgun proteomics, would trypsinise native proteins and run the associated fragments through a mass spectrometer, using LC/MS/MS.[65, 66] These methods have provided positive results in the area of cancer research, for example, an extensive review by Flatley *et al* discussed studies using MALDI-MS to study prostate cancer biomarkers.[67] Ichibangase *et al* used a novel MS approach, with FD-LC-MS/MS to study both protein expression and cellular events in metastatic and non-metastatic breast cancer using fluorometry to select proteins of interest in the first step.[68]

Although MS proteomic studies have high resolving power, highly abundant protein signals often swamp smaller protein signals.[69] Protein binding assays are an alternative approach to proteomics developed from the same principles as enzyme-linked immunosorbent assays (ELISA), which were first introduced in 1971.[70] The concept of this approach is for a primary antibody to bind specifically to an antigen of interest, and then for a secondary antibody, with an enzyme conjugate to bind to the primary antibody. Substrate would then be added and subsequently processed by the conjugated enzyme to elicit a readable, and typically amplified, response.

A modern adaptation of this approach is to use fluorescently-labelled analyte-specific reagents, often an antibody, to quantify a response by fluorescence. Evolution of this technique has produced the protein microarray, allowing high throughput analysis of protein samples.[71] Protein microarrays have broad applications, requiring only a small amount of sample and a small amount of reagent. There are two types of protein arrays: capture microarrays and reverse-phase microarrays (RPPA).[72] The former are principally similar to the DNA microarray, where analyte-specific reagents (ASR) are spotted onto an array and a labelled experimental sample is exposed to the array.[73, 74] Labelled proteins of interest will bind to their ASR, allowing fluorescence detection. The latter, RPPA, is more applicable if users do not wish to chemically modify their samples.[71] Here, the sample is spotted onto the array, and labelled ASRs are flushed over the sample, binding to their proteins of interest.

This second method for studying proteomics is simpler, and less data intensive, however studying the whole proteome by this method would be extremely expensive. Using this method in combination with transcriptomics is a good way to gain global cellular insights whilst keeping the cost manageable.

1.3.5 Imaging

Clinical imaging is commonly used for diagnosis and to follow tumour progression in cancer patients. Techniques like computerised tomography (CT) and more recently, magnetic resonance imaging (MRI), allow direct 3D tumour evaluations to be made. Positron emission tomography (PET) imaging is also used for detection and monitoring of tumours by following radioactive tracer molecules, administered to patients. Glucose is the most commonly used tracer, given cancer cells use glucose differently to normal cells. PET is often used in combination with either CT or MRI imaging, with an ovarian cancer study concluding that PET/MRI generally provides fewer false positives.[75]

For investigating *in vitro* drug effects, a broad range of imaging techniques can be used, whether measuring fluorescent biomarkers or visualising entire cellular structures. For example, high-content screening (HCS) allows the study of multiple features simultaneously, in single cells, and has strong applications in mechanistic studies. Work by Carragher *et al* used HCS to identify structural alterations in cancer cells exposed to classified anticancer agents, by simultaneously measuring the cell membrane, cell nuclei and cytoplasm using different fluorescent dyes.[76] Applying principal component analysis (PCA) to measurable phenotypic parameters allowed the group to separate phenotypic behaviour into subpopulations. Each phenotypic subgroup corresponded to a particular class of anticancer agents, thus highlighting this method as a good predictive tool for new anticancer agents.

Other whole cell imaging techniques include electron microscopy, particularly transmission electron microscopy (TEM) which has been reported in MOA studies for Os-based picolinate compounds.[77] Here ovarian cancer cells were exposed to the drug, and the whole cell structures were studied. Given the heavy nature of Os atoms, if a high enough concentration is added to cells, it should be possible to follow directly the distribution of Os metal, due to extensive interactions with the electron beam.

Secondary ion mass spectrometry (nanoSIMS) is an imaging mass spectrometry (IMS) technique and has been used successfully to follow the distribution of both platinum and gold compounds in cancer cells.[78, 79] Here, drug-exposed cell sections are exposed to a primary caesium beam which sputters the cell surface and releases secondary ions. The detection of multiple, pre-determined masses, allows identification of the distribution of drug, and to investigate co-localisation with other elements in the cell e.g. phosphorus (^{31}P), to represent DNA.

Collectively, imaging has a prominent place in cancer research, both in clinical and preclinical applications.

1.4 Thesis structure

As the progression towards personalised and stratified medicine continues, the identification of drug compound MOA and target patient populations becomes increasingly important. The promising organometallic compounds introduced here will struggle to reach clinical trials unless we can gain further insights into their modes of activity.

1.4.1 Aims

The work included here, aims to use high-throughput screening techniques to filter out lead compounds from a batch of promising osmium and iridium candidates. Large scale experiments provide further understanding of lead compounds MOAs, combining cellular responses at the transcriptomic, translational and structural levels. RNA sequencing is used to study differential gene expression, reverse phase protein microarrays are used to study translational responses, and electron microscopy and high-content screening is used to study morphological changes in cancer cells responding to treatment with lead compounds.

This approach could pave the way for future studies to identify whether these cellular responses result from a directed MOA, and if so to determine the biological target.

Chapter 3: Cell Screening. This chapter discusses cell screening after the organometallic compounds were submitted to the National Cancer Institute (NCI), the Sanger institute and the Edinburgh Cancer Research Centre. From each screen the activity of each compound is discussed, as is the cell line selectivity. Using this information, together with basic statistical methods, the activity fingerprints of the organometallic compounds are quantitatively compared to other drug-compounds populating publicly available databases.

Chapter 4: Transcriptomics. Using RNA sequencing, the levels of gene expression are studied after ovarian cancer cells are exposed to **Os-3** and **Ir-10** at their respective GI_{50} concentrations (Table 1.1). Time course measurements are taken, over a 48 h period, and using pathway analysis the biological implications of compound-exposure are discussed.

Chapter 5: Proteomics. Reverse phase protein microarrays (RPPA) are used to quantify the levels of selected proteins after ovarian cancer cells are exposed to **Os-3** and **Ir-10** at a low and high concentration, across a 72 h time course. Flow cytometry experiments highlight key differences in cellular response between compounds.

Chapter 6: Multiple Dataset Integration. Using a Bayesian clustering algorithm, developed at the Warwick Systems Biology Centre, transcriptomic and proteomic datasets are combinatorially analysed. This method of clustering allows relationships between the heterogeneous data types to be extracted, and further conclusions about compound MOAs to be drawn.

Chapter 7: Imaging. High-content screening, using fluorescence microscopy investigates apoptosis in ovarian cancer cell lines exposed to **Os-1**, **Os-3**, **Os-4**, **Ir-9**, **Ir-10** and cisplatin at a range of concentrations. In addition, whole-cell transmission electron microscopy (TEM) is performed to explore compound-effects on ovarian cancer cells after exposure to **Ir-6** for 24 h.

References

[1] Cancer Research UK (2012) CancerStats: Cancer Statistics for the UK. *Online Source. www.cancerresearchuk.org/cancer-info/cancerstats/.*

[2] Cancer Research UK (2013) CanceStats: key facts. *Online Source. www.publications.cancerresearchuk.org/downloads/Product/CS_KF_ALLCANCERS.pdf.*

[3] NHS (2012) Ovarian cancer. *Online Source. www.nhs.uk/Conditions/Cancer-of-the-ovary/Pages/Introduction.aspx.*

[4] US Cancer Statistics Working Group (2013) United Cancer Statistics: 1999-2010 Incidence and Mortality Web-based Report.

[5] Kurman RJ, Shih IM (2010) The origin and pathogenesis of epithelial ovarian cancer: a proposed unifying theory. *The American Journal of Surgical Pathology* 34:433–443.

[6] Kurman RJ, Shih L (2011) Molecular pathogenesis and extraovarian origin of epithelial ovarian cancer-shifting the paradigm. *Human pathology* 42:918–931.

[7] Cancer Net (2013) Ovarian Cancer. *Online Source. www.cancer.net/cancer-types/ovarian-cancer/diagnosis.*

[8] Heppner GH (1984) Tumor heterogeneity. *Cancer Research* 44:2259–2265.

[9] Marusyk A, Polyak K (2010) Tumor heterogeneity: causes and consequences. *Biochimica et Biophysica Acta* 1805:105–17.

[10] Wang V, et al. (2005) Ovarian cancer is a heterogeneous disease. *Cancer Genetics and Cytogenetics* 161:170–173.

[11] Zhan Q, Wang C, Ngai S (2013) Ovarian cancer stem cells: a new target for cancer therapy. *BioMed Research International* 2013:916819.

[12] Michor F, Nowak MA, Iwasa Y (2006) Evolution of resistance to cancer therapy. *Current Pharmaceutical Design* 12:261–271.

[13] Dabrowiak JC (2009) Metallo-Drugs and Their Action. *Metals in Medicine* pp 49–71.

[14] Garbutcheon-Singh KB, et al. (2011) Transition metal based anticancer drugs. *Current Topics in Medicinal Chemistry* 11:521–542.

[15] Monneret C (2011) Platinum anticancer drugs. From serendipity to rational design. *Annales Pharmaceutiques Françaises* 69:286–295.

[16] Florea AM, Busselberg D (2011) Cisplatin as an anti-tumor drug: cellular mechanisms of activity, drug resistance and induced side effects. *Cancers* 3:1351–1371.

[17] Kelland L (2007) The resurgence of platinum-based cancer chemotherapy. *Nature Reviews Cancer* 7:573–584.

[18] Colombo N, Gore M (2007) Treatment of recurrent ovarian cancer relapsing 6-12 months post platinum-based chemotherapy. *Critical reviews in Oncology/Hematology* 64:129–138.

[19] Hannon MJ (2007) Metal-based anticancer drugs: From a past anchored in platinum chemistry to a post-genomic future of diverse chemistry and biology. *Pure and Applied Chemistry* 79:2243.

[20] Fu Y, et al. (2011) Structure-activity relationships for organometallic osmium arene phenylazopyridine complexes with potent anticancer activity. *Dalton Transactions* 40:10553–10562.

[21] Castonguay A, Doucet C, Juhas M, Maysinger D (2012) New ruthenium(II)-letrozole complexes as anticancer therapeutics. *Journal of Medicinal Chemistry* 55:8799–8806.

[22] Hartinger CG, Phillips AD, Nazarov AA (2011) Polynuclear ruthenium, osmium and gold complexes. The quest for innovative anticancer chemotherapeutics. *Current Topics in Medicinal Chemistry* 11:2688–702.

[23] Liu Z, Habtemariam A, Pizarro AM, Clarkson GJ, Sadler PJ (2011) Organometallic Iridium(III) Cyclopentadienyl Anticancer Complexes Containing C,N-Chelating Ligands. *Organometallics* 30:4702–4710.

[24] Liu Z, et al. (2011) Contrasting reactivity and cancer cell cytotoxicity of isoelectronic organometallic iridium(III) complexes. *Inorganic Chemistry* 50:5777–5783.

[25] Liu Z, et al. (2011) Organometallic half-sandwich iridium anticancer complexes. *Journal of Medicinal Chemistry* 54:3011–3026.

[26] Fu Y, et al. (2010) Organometallic osmium arene complexes with potent cancer cell cytotoxicity. *Journal of Medicinal Chemistry* 53:8192–8196.

[27] Shnyder S, et al. (2011) Anti-colorectal cancer activity of an organometallic osmium arene azopyridine complex. *Medical Chemistry Communications* 2:666–668.

[28] Liu Z, et al. (2014) The Potent Oxidant Anticancer Activity of Organoiridium Catalysts. *Angewandte Chemie (International ed. in English)* 53:3941–3946.

[29] Romero-Canelón I, Salassa L, Sadler PJ (2013) The contrasting activity of iodido versus chlorido ruthenium and osmium arene azo- and imino-pyridine anticancer complexes: control of cell selectivity, cross-resistance, p53 dependence, and apoptosis pathway. *Journal of Medicinal Chemistry* 56:1291–300.

[30] Vogelstein B, Lane D, Levine AJ (2000) Surfing the p53 network. *Nature* 408:307–310.

[31] Hearn JM, et al. (2013) Organometallic Iridium(III) Anticancer Complexes with New Mechanisms of Action: NCI-60 Screening, Mitochondrial Targeting, and Apoptosis. *ACS Chemical Biology* 8:1335–1343.

[32] Bailey HH, et al. (1994) Phase I clinical trial of intravenous L-buthionine sulfoximine and melphalan: an attempt at modulation of glutathione. *Journal of Clinical Oncology* 12:194–205.

[33] Schilsky RL (2010) Personalised Medicine in Oncology: The future is now. *Nature Reviews Drug Discovery* 9:363–366.

[34] Biankin A (2011) Genotype guided personalised cancer care using next generation sequencing. *AsiaPacific Journal of Clinical Oncology* 7:78–79.

[35] Makara GM, Athanasopoulos J (2005) Improving success rates for lead generation using affinity binding technologies. *Current Opinion in Biotechnology* 16:666–673.

[36] Comess KM, Schurdak ME (2004) Affinity-based screening techniques for enhancing lead discovery. *Current Opinion in Drug Discovery Development* 7:411–416.

[37] Agresti JJ, et al. (2010) Ultrahigh-throughput screening in drop-based microfluidics for directed evolution. *Proceedings of the National Academy of Sciences of the United States of America* 107:4004–4009.

[38] Keseru GM, Makara GM (2006) Hit discovery and hit-to-lead approaches. *Drug Discovery Today* 11:741–748.

[39] Popa-Burke IG, et al. (2004) Streamlined system for purifying and quantifying a diverse library of compounds and the effect of compound concentration

measurements on the accurate interpretation of biological assay results. *Analytical Chemistry* 76:7278–7287.

[40] Carragher NO, Brunton VG, Frame MC (2012) Combining imaging and pathway profiling: An alternative approach to cancer drug discovery. *Drug Discovery Today* 17:203–214.

[41] Paull K, et al. (1989) Display and analysis of patterns of differential activity of drugs against human tumor cell lines: development of mean graph and COMPARE algorithm. *Journal of The National Cancer Institute* 81:1088–1092.

[42] Shoemaker RH (2006) The NCI60 human tumour cell line anticancer drug screen. *Nature Reviews Cancer* 6:813–23.

[43] Holbeck S, Collins JM, Doroshow JH (2010) Analysis of Food and Drug Administration-Approved Anti-cancer Agents in the NCI60 Panel of Human Tumor Cell Lines. *Molecular Cancer Therapeutics* 9:1451–1460.

[44] Zaharevitz DW, Holbeck SL, Bowerman C, Svetlik PA (2002) COMPARE: a web accessible tool for investigating mechanisms of cell growth inhibition. *Journal of Molecular Graphics Modelling* 20:297–303.

[45] Fagan V, et al. (2012) COMPARE analysis of the toxicity of an iminoquinone derivative of the imidazo[5,4-f]benzimidazoles with NAD(P)H:quinone oxidoreductase 1 (NQO1) activity and computational docking of quinones as NQO1 substrates. *Bioorganic and Medicinal Chemistry* 20:3223–3232.

[46] Frédérick R, et al. (2012) Novel trisubstituted harmine derivatives with original in vitro anticancer activity. *Journal of Medicinal Chemistry* 55:6489–501.

[47] Zhou J, Et Al. (2005) COMPARE analysis of the NCI-60 cancer cell lines reveals a pharmacological interplay between farnesyltransferase and tubulin deacetylase. *Proceedings of the American Association of Cancer Research* 46:0.

[48] Fojo T, et al. (2005) Identification of non-cross-resistant platinum compounds with novel cytotoxicity profiles using the NCI anticancer drug screen and clustered image map visualizations. *Critical reviews in Oncology Hematology* 53:25–34.

[49] Forbes SA, et al. (2008) The Catalogue of Somatic Mutations in Cancer (COSMIC). *Current Protocols in Human Genetics* Chapter 10:Unit 10.11.

[50] Forbes SA, et al. (2010) COSMIC (the Catalogue of Somatic Mutations in Cancer): a resource to investigate acquired mutations in human cancer. *Nucleic Acids Research* 38:D652–D657.

[51] Forbes SA, et al. (2011) COSMIC: mining complete cancer genomes in the Catalogue of Somatic Mutations in Cancer. *Nucleic Acids Research* 39:D945–D950.

[52] Hart S, et al. (2013) VS-5584, a Novel and Highly Selective PI3K/mTOR Kinase Inhibitor for the Treatment of Cancer. *Molecular Cancer Therapeutics* 12:151–61.

[53] de la Rosa J, et al. (2013) Prelamin A causes progeria through cell-extrinsic mechanisms and prevents cancer invasion. *Nature Communications* 4:2268.

[54] Cowin PA, et al. (2012) LRP1B Deletion in High-Grade Serous Ovarian Cancers Is Associated with Acquired Chemotherapy Resistance to Liposomal Doxorubicin. *Cancer Research* 72:4060–4073.

[55] Cancer Genome Atlas Network (2012) Comprehensive molecular portraits of human breast tumours. *Nature* 490:61–70.

[56] Kirk P, Griffin JE, Savage RS, Ghahramani Z, Wild DL (2012) Bayesian correlated clustering to integrate multiple datasets. *Bioinformatics* 28:3290–3297.

[57] Savage R, Ghahramani Z, Griffin JE, de la Cruz BJ, Wild DL (2010) Discovering transcriptional modules by Bayesian data integration. *Bioinformatics* 26:158–167.

[58] Rogers S, et al. (2008) Investigating the correspondence between transcriptomic and proteomic expression profiles using coupled cluster models. *Bioinformatics* 24:2894–2900.

[59] Leavitt S (2010) Deciphering the genetic code: Marshall Nirenberg. *Online Source - http://history.nih.gov/exhibits/nirenberg/*.

[60] Wang Z, Gerstein M, Snyder M (2009) RNA-Seq: a revolutionary tool for transcriptomics. *Nature Reviews Genetics* 10:57–63.

[61] Ledford H (2008) The death of microarrays? *Nature* 455:847.

[62] Fathallah-Shaykh HM (2005) Microarrays: applications and pitfalls. *Archives of Neurology* 62:1669–1672.

[63] Venkatasubbarao S (2004) Microarrays status and prospects. *Trends in Biotechnology* 22:630–637.

[64] Houghtaling BR, Wacker SA, Elemento O, Kapoor TM (2012) Using transcriptome sequencing to identify mechanisms of drug action and resistance. *Nature Chemical Biology* 8:235–237.

[65] Karpievitch YV, Polpitiya AD, Anderson Ga, Smith RD, Dabney AR (2010) Liquid Chromatography Mass Spectrometry-Based Proteomics: Biological and Technological Aspects. *The Annals of Applied Statistics* 4:1797–1823.

[66] Chen G, Pramanik BN (2009) Application of LC/MS to proteomics studies: current status and future prospects. *Drug Discovery Today* 14:465–471.

[67] Flatley B, Malone P, Cramer R (2013) MALDI mass spectrometry in prostate cancer biomarker discovery. *Biochimica et Biophysica Acta* 1844:940–949.

[68] Ichibangase T, Imai K (2012) FD-LC-MS/MS Method for Determining Protein Expression and Elucidating Biochemical Events in Tissues and Cells. *Biological and Pharmaceutical Bulletin* 35:1393–1400.

[69] Pawlak M, et al. (2002) Zeptosens' protein microarrays: a novel high performance microarray platform for low abundance protein analysis. *Proteomics* 2:383–393.

[70] Engvall E, Jonsson K, Perlmann P (1971) Enzyme-linked immunosorbent assay. II. Quantitative assay of protein antigen, immunoglobulin G, by means of enzyme-labelled antigen and antibody-coated tubes. *Biochimica et Biophysica Acta* 251:427–434.

[71] LaBaer J, Ramachandran N (2005) Protein microarrays as tools for functional proteomics. *Current Opinion in Chemical Biology* 9:14–19.

[72] Wilson B, Liotta LA, Petricoin E (2010) Monitoring proteins and protein networks using reverse phase protein arrays. *Disease markers* 28:225–232.

[73] Predki PF (2004) Functional protein microarrays: ripe for discovery. *Current Opinion in Chemical Biology* 8:8–13.

[74] Jona G, Snyder M (2003) Recent developments in analytical and functional protein microarrays. *Current Opinion in Molecular Therapeutics* 5:271–277.

[75] Iyer VR, Lee SI (2010) MRI, CT, and PET/CT for ovarian cancer detection and adnexal lesion characterization. *American Journal of Roentgenology* 194:311–321.

[76] Caie PD, et al. (2010) High-content phenotypic profiling of drug response signatures across distinct cancer cells. *Molecular Cancer Therapeutics* 9:1913–1926.

[77] van Rijt SH, Mukherjee A, Pizarro AM, Sadler PJ (2010) Cytotoxicity, hydrophobicity, uptake, and distribution of osmium(II) anticancer complexes in ovarian cancer cells. *Journal of Medicinal Chemistry* 53:840–849.

[78] Wedlock LE, et al. (2013) NanoSIMS multi-element imaging reveals internalisation and nucleolar targeting for a highly-charged polynuclear platinum compound. *Chemical Communications* 49:6944–6946.

[79] Wedlock LE, et al. (2011) Visualising gold inside tumour cells following treatment with an antitumour gold(i) complex. *Metallomics* 3:917–925.

Chapter 2. Materials and Methods

2.1 Materials

For the biological experiments, Roswell Park Memorial Institute (RPMI-1640) medium, as well as foetal bovine serum, L-glutamine, penicillin/streptomycin mixture, trypsin, trypsin/EDTA, phosphate buffered saline (PBS) were purchased from PAA Laboratories GmbH. HPLC grade ethanol, β-mercaptoethanol, PI ($>$94%), Annexin V-FITC Apoptosis Detection Kit and RNAse A were obtained from Sigma Aldrich. The Abcam JC-10 Mitochondrial Membrane Potential Assay kit was obtained from Enzo. For RNA sequencing, cell shredders and mini-prep kits were purchased from Qiagen. For TEM, glutaraldehyde (2%), cacodylate buffer at pH 7.6, 2% uranyl acetate in maleate buffer, 100% propylene oxide and Embed 812 resin were all purchased from Agar Scientific and Poly/Bed 812 was purchased from Polysciences. For ICP-MS, osmium Specpure standard was obtained from Inorganic Ventures.

2.2 Methods

2.2.1 Compound synthesis and characterisation

All compounds were synthesised and characterised by Dr Fu Ying and Dr Zhe Liu in previous works.[1–5]

2.2.2 Cell maintenance

A2780, human ovarian carcinoma were obtained from the European Collection of Cell Cultures (ECACC). Cells were grown in Roswell Park Memorial Institute (RPMI-1640) medium supplemented with 10% foetal calf serum, 1% (v/v) 2 mM glutamine and 1% (v/v) penicillin (10 k units/mL)/streptomycin (10 mg/mL). All cells were maintained in 75 cm^3 culture flasks at 37^oC with 5% CO_2 humidified atmosphere. Cells were grown as adherent monolayers and split when 80-90% confluent, using 0.25% trypsin.

2.2.3 GI_{50} determinations

All GI_{50} values were determined in previous work by Dr Isolda Romero and Dr Ana Pizarro.[1–5] Briefly, A2780 cells were seeded in 96 well plates with ca. 5000 cells per well. The plates were incubated at 37^{o}C for 48 h. A 2 mM stock solution of each compound was prepared in 5% DMSO, 95% saline, from which final dilutions ranging from 0.1 to 100 μM were made with RPMI-1640. Drug exposure time was 24 h at 37^{o}C, after which supernatants were removed cells were allowed to recover for 72 h in drug-free medium at 37^{o}C. The sulforhodamine B (SRB) assay was used to determine cell viability.

2.2.4 Cell screening

2.2.4.1 NCI-60 screening with the National Cancer Institute

Compounds were submitted to the National Cancer Institute (USA) as solid samples. Submissions for all compounds used in this work were made between 2010 and 2011.

The full protocols used by the NCI have been described previously.[6–8] Briefly, cells were seeded into 96 well plates at a density of $5,000-40,000$ cells/well (depending on cell line doubling time). Plates were incubated at 37^{o}C, 5% CO_2, 95% air and 100% relative humidity for 24 h. After 24 h, two plates of each cell line were fixed *in situ* with TCA to represent a measurement of cell population (C) for each cell type at the time of drug addition (T_0). Stock solutions of each drug were made in DMSO and diluted. From this, 5 drug concentrations were made down to a 10-fold decreases from the maximum test concentration. Drug solutions were added to appropriate cell populations and the plates left to incubate for 48 h. Using the sulforhodamine B (SRB) assay the cell growth and survival (T_i) were measured on a plate reader and dose response curves plotted to calculate three parameters:

$\mathbf{GI_{50}}$ $[T_i/(C-T_0)] \times 100 = 50$

TGI $T_i = T_0$

$\mathbf{LC_{50}}$ $[T_i - T_0)/T_0] = -50$

Dose response curves, and activity values were returned to The University of Warwick for downstream analysis. All figures presented in this thesis were reconstructed using R which is a free programming language and software environment for statistical computing and graphics.

2.2.4.2 Screening with the Sanger Institute

Compounds **Os-1**, **Os-3**, **Os-4**, **Ir-9** and **Ir-10** were submitted in January 2012 for testing in the 'Genomics of Drug Sensitivity in Cancer' project at the Sanger Institute (Cambridge, UK).[9]

Briefly, cells were seeded in 96 well plates at ca.15% confluency and left to incubate for 24 h at 37^{o}C, 5% CO_2, 95% air and 100% relative humidity. For adherent cell lines, cells were treated with nine concentrations of each compound (2-fold dilution series over 256-fold concentration range) and returned to the incubator for 72 h. Cells were then fixed with 4% formaldehyde for 30 minutes and stained with 1 μM Syto60 for 1 h. Quantitation of fluorescent signal intensity was performed using a plate reader at excitation/emission wavelengths of 630/695 nm.

For suspension cell lines, cells were treated with compound immediately following plating, and returned to the incubator for 72 h. Cells were stained with 55 μg/mL Resazurin, prepared in gutathione-free media, for 4 h. Quantitation of fluorescent signal intensity was performed using a plate reader at excitation/emission wavelengths of 535/595 nm.

Dose response curves were constructed from the fluorescence data, and analysed as discussed in Chapter 3. GI_{50} values were returned to The University of Warwick for downstream analysis. MANOVA analysis was performed by the Sanger bioinformatics institute, and the results returned to The University of Warwick for interpretation. All figures presented in this thesis were reconstructed using the R statistical programme.

2.2.4.3 Primary cell screening with The Edinburgh Cancer Research Centre

Compounds **Os-1**, **Os-3**, **Os-4**, **Ir-9** and **Ir-10** were submitted in January 2012 and were tested for antiproliferative activity.

Primary patient cell lines were seeded in 96 well plates with ca. 5000 cells per well in RPMI-1640 with 1% (v/v) 2 mM glutamine. The plates were incubated at 37^oC for 48 h. Stock solutions of each compound were prepared and cells exposed across a dose range for a further 48 h. Cells were extracted and the MTT (3-(4,5-dimethylthiazol-2-yl)-2,5-diphenyltetrazolium bromide) assay (Life Technologies) was used to determine cell viability.

2.2.5 RNA sequencing

2.2.5.1 Experimental lab work

Experimental work performed at The University of Warwick. A2780 cells were seeded in P100 petri dishes at 3 x 10^6 cells per 100 mm petri dish. Plates were incubated for 24 h at 37^oC, 5% CO_2, 95% air and 100% relative humidity. Stock solutions of each compound and of the vehicle control solutions were prepared in 5% DMSO, 10% saline, and 85% RPMI-1640 medium. Cells were exposed to **Os-3** at a final concentration of 150 nM and to **Ir-10** at a final concentration of 400 nM, their respective GI_{50} values. A final DMSO concentration for all cell samples did not exceed 0.05%. After compound addition, cells were incubated for a further 4, 12, 24 and 48 h.

Media was aspirated from cells and cells were washed twice with PBS before trypsinising and collection. To each sample, 600 μL RTL lysis buffer (Qiagen) was added and the samples vortexed. Lysate was pipetted directly into QIAshredder spin columns (Qiagen) and centrifuged. Lysate was transfered to gDNA eliminator spin columns (RNeasy plus mini kit, Qiagen) and centrifuged. Columns were discarded and 600 uL of 70% ethanol was added to each sample flow-through. Samples were transfered into RNeasy spin columns (RNeasy plus mini kit, Qiagen) and centrifuged. Column-bound RNA samples were washed with RW1 and RPE buffer (RNeasy plus mini kit, Qiagen) before RNA collection in 70 μL RNAse-free water. Samples were stored at -80 C for no more than 2 months.

Samples were diluted 1:10 fold in RNAse free water and run on a NanoDrop 1000 spectrophotometer machine and the absorbance at 230, 260 and 280 nm recorded to calculate the 260/230 and 260/280 ratios. Samples with A260/230 $\geq$2.0 and A260/280 $\geq$1.9 were passed. The concentration of RNA in each solution was also estimated using the NanoDrop and was verified using a 2100 Agilent Bioanalyzer and an RNA 6000 Nano Kit (Agilent), and the Qubit assay (Life Technologies). All samples had a RNA integrity number (RIN) $\geq$ 9. A minimum of 1 μg RNA for each sample was transferred to Oxford Genomics Centre (Wellcome Trust Centre for Human Gentics) in a total of 30 μL RNAse free water in skirted 96 well plates.

Experimental work performed by the Oxford Genomics Centre. TruSeq kits (Illumina) were used to prepare samples for sequencing as per the manufacturers guidelines. From total RNA, mRNA samples were purified, fragmented and reverse transcribed to cDNA. Sequencing libraries were produced, with incorporated barcodes to allow multiplexing. Samples were sequenced on an Illumina Hiseq2000 instrument across 5 lanes (6 samples per lane). 50 base pair, paired-end reads were recorded producing ca. 60 million reads in total, per sample (Appendix 9.2).

2.2.5.2 Data analysis

Data analysis performed at Oxford Genomic Centre. Preliminary filtering was performed on the data to remove all samples with quality scores (Q) $<$ 20. FASTQ files for the forward and reverse reads were integrated and aligned to the hg19 (GRCh37) human genome using TopHat2.[10] Files were returned to The University of Warwick in BAM format.

Data analysis performed at Warwick. Integrative genome viewer (IGV, version 2.3.13) was used to visualise BAM file mapping, and to identify somatic mutations in mapped reads.[11] Samtools (version 0.1.19-44428cd) was used to explore the raw BAM files, extracting chromosomal reads and summary statistics.[12] BAM files were sorted by read name and then converted to SAM format.

HTSeq (version 0.5.4p5) was used to map the read locations to genomic regions using the hg19 genome construct with the intersection-nonempty program option.[13] Resulting mapped files, were then analysed for differential gene expression using the edgeR package (version 3.1.10) in the R statistical programme (version 3.0.2).[14] A workflow of the edgeR method is described in Chapter 4.

A list of differentially expressed genes was obtained for each time point (4, 12, 24 and 48 h) and used together with Ingenuity Pathway Analysis software to assign significantly expressed genes to biological pathways. A detailed description of how this pathway analysis is performed is discussed in Chapter 4.

2.2.6 Reverse phase protein microarrays (RRPA)

Compounds were submitted to The Edinburgh Cancer Research Centre (Edinburgh, UK) as solid samples. Compounds **Os-3** and **Ir-10** were tested by RPPA in March 2014.

4 x 10^5 A2780 cells were seeded per well in 6-well plates, with samples in duplicate. Cells were pre-incubated in drug-free media for 48 h at 37^{o}C in a 5% CO2 humidified

atmosphere. After this, cells were treated with each compound at 150 nM and 450 nM (apart from **Ir-9** which was only tested at 450 nM) for 4, 24, 48 and 72 h. Control samples were treated with media containing 0.1% DMSO. Following exposure, drug-containing medium was removed, and cells were washed twice with PBS and lysed with CLB1 buffer (Zepotsens, Bayer) according to manufacturers instructions.

Cell lysates were normalised to a uniform protein concentration of 2 mg/mL with spotting buffer CSBL1 (Zeptosens-Bayer) prior to preparing a final 4-fold concentration series of; 0.2; 0.15; 0.1 and 0.75 mg/mL. The diluted concentration series of each sample was printed onto hydrophobic Zeptosens protein microarray chips (ZeptoChipTM, Zeptosens-Bayer) under environmentally controlled conditions (constant 50% humidity and 14^o C temperature) using a non-contact printer (Nanoplotter 2.1e, GeSiM). A single 400 pL droplet of each lysate concentration was deposited onto the Zeptosens chip. A reference grid of AlexaFluor647 conjugate BSA was spotted onto each sub-array, each sample concentration series was spotted in between reference columns. After array printing, the arrays were blocked with an aerosol of BSA solution using a custom designed nebuliser device (ZeptoFOGTM, Zeptosen-Bayer) for 1 h to prevent non-specific antibody binding. The protein array chips were subsequently washed in double-deionised water (DDW) and dried prior to performing a dual antibody immunoassay comprising of a 24 h incubation of primary antibodies (Appendix 9.3) followed by 2.5 h incubation with secondary Alexa-Fluor A647 conjugated antibody detection reagent (anti-rabbit or anti-mouse A647 Fab, Invitrogen).

Following secondary antibody incubation and a final wash step in BSA solution, the immunostained arrays were imaged using the ZeptoREADER instrument (Zeptosens-Bayer). For each-sub-array, five separate images were acquired using different exposure times ranging from 0.5-10 s. Microarray images representing the longest exposure without saturation of fluorescent signal detection were automatically selected for analysis using the ZeptoViewTM 3.1 software.

A weighted linear fit through the 4-fold concentration series was used to calculate the relative fluorescence intensity (RFI) value for each sample replicate. Local normalisation of sample signal to the reference BSA grid was used to compensate for any intra- or inter-array/chip variation. RFI values were further normalised to a house keeping protein and to the negative control, to provide the final RFI to represent the relative abundance of total, phosphorylated and cleaved proteins in compound-treated samples relative to the DMSO control for each time point.

2.2.7 Flow cytometry

2.2.7.1 Live/dead cell assay

A2780 cells were seeded at 2.5 x 10^6 cells per well in 6-well plates. Cells were pre-incubated in drug-free media at 37^{o}C for 24 h in a 5% CO_2 humidified atmosphere. Drug-compound solutions were added and the cells left to incubate for a further 24, 48 or 72 h. Following exposure, the drug-containing medium was removed, and cells were washed, harvested and stained with Annexin V FITC and propidium iodide (Biovision, Annexin V-FITC Apoptosis Kit) according to the manufacturers instructions. Control samples stained with just propidium iodide or Annexin V FITC were also included for compensation purposes. The samples were analysed using Beckton Dickinson FACScan with fluorescence detection running Cell Quest software (20000 events were collected from each sample). Data were processed using Flowjo software (version 7.2.5).

2.2.7.2 Cell cycle

A2780 cells were seeded at a density of 2.5 x 10^6 cells per well in a 6-well plate and pre-incubated in drug-free media at 37^{o}C for 24 h in a 5% CO_2 humidified atmosphere. Drug solutions were added and the cells left to incubate for a further 24 h. Cells were collected and washed twice with PBS. Cells were fixed with 70% ethanol and stored at

-20^{o}C for 24 h. For analysis, cells were transferred into PBS, incubated with RNase (0.2 mg/mL) and propidium iodide (0.05 mg/mL) for 40 min at 37^{o}C and then analysed by flow cytometry using a Beckton Dickinson FACScan with fluorescence detection. The resulting DNA histograms were quantified using the FlowJo software (version 7.2.5).

2.2.7.3 Mitochondrial membrane polarisation

A2780 cells were seeded at 2.5 x 10^6 cells per well in 6-well plates and pre-incubated in drug-free media at 37^{o}C for 24 h in a 5% CO_2 humidified atmosphere. **Ir-6** was added and the cells left to incubate for a further 4 or 24 h. Cells were washed twice with PBS and transferred to 12 x 75 mm flow cytometry test tubes in 500 μL solution of JC-10 dye and the tubes protected from light for an incubation period of 0.5 h, at ambient temperature. CCCP was used as positive control, with a drug exposure time of 0.5 h. Samples were immediately run on a Beckton Dickinson FACScan with fluorescence detection and data were processed using Flowjo software (version 7.2.5).

2.2.8 Imaging

2.2.8.1 High content screening (HCS) with Edinburgh Cancer Research Centre

Compounds were submitted to The Edinburgh Cancer Research Centre (Edinburgh, UK) as solid samples. Compounds **Os-1**, **Os-3**, **Os-4**, **Ir-9** and **Ir-10** were imaged by HCS in June 2012.

A2780 cells were seeded in a 96-well plate at 5000 cells/well and incubated for 48 h before treatment with each compound for a further 48 h. Prior to image acquisition, cells were incubated with 4 μg/mL DAPI (Sigma D8417), and 1 μM NucViewTM (Biotium) reagent for 0.5 h. Microscopic images of DAPI and NucViewTM stained cells were acquired with a 10x objective and appropriate optical filters using the Olympus ScanR high-content imaging microscope. Merged images of DAPI and NucviewTM cells were created using the Olympus ScanR imaging software Cell-IRTM.

2.2.8.2 Transmission electron microscopy

A2780 cells were seeded at a density of 5 x 10^6 cells/100mm petri dish and pre-incubated in drug-free media at 37^{o}C for 24 h in a 5% CO_2 humidified atmosphere. **Ir-6** was added to a final concentration of either 1 or 5 μM and cells left to incubate for a further 24 h. Medium was removed and the cells were washed twice with PBS, fixed with 2% glutaraldehyde (Agar Scientific) in cadodylate buffer at pH 7.6 (Agar Scientific) and left for 1 h agitating on a shaker. Plates were rinsed with cadodylate buffer and the cells were transferred to falcon tubes, and centrifuged. Cells were dehydrated with graded levels of ethanol (20-100% ethanol). Samples were then infiltrated with 100% propylene oxide for 1 h followed by 1:1 mixture of propylene oxide and embed 812 resin for 6 h. This was then replaced with several changes of 100% resin over an 18 h period before curing for 24 h at 72^{o}C. Blocks were trimmed and sectioned on a Leica Ultracut E ultramicrotome (Leica Microsystems). Sections of 70-80 nm thick were collected on 400-mech Cu grids and stained with 2% uranyl acetate. Sections were imaged on a JOEL 1200EXII TEM with a Gatan 1 k x 1 k CCD camera.

References

[1] Liu Z, et al. (2011) Contrasting reactivity and cancer cell cytotoxicity of isoelectronic organometallic iridium(III) complexes. *Inorganic Chemistry* 50:5777–5783.

[2] Liu Z, et al. (2011) Organometallic half-sandwich iridium anticancer complexes. *Journal of Medicinal Chemistry* 54:3011–3026.

[3] Fu Y, et al. (2011) Structure-activity relationships for organometallic osmium arene phenylazopyridine complexes with potent anticancer activity. *Dalton Transactions* 40:10553–10562.

[4] Fu Y, et al. (2010) Organometallic osmium arene complexes with potent cancer cell cytotoxicity. *Journal of Medicinal Chemistry* 53:8192–8196.

[5] Shnyder S, et al. (2011) Anti-colorectal cancer activity of an organometallic osmium arene azopyridine complex. *Medical Chemistry Communications* 2:666–668.

[6] Holbeck SL, Collins JM, Doroshow JH (2010) Analysis of Food and Drug Administration-approved anticancer agents in the NCI60 panel of human tumor cell lines. *Molecular Cancer Therapeutics* 9:1451–1460.

[7] Shoemaker RH (2006) The NCI60 human tumour cell line anticancer drug screen. *Nature Reviews Cancer* 6:813–23.

[8] Shoemaker RH, et al. (1988) Development of human tumor cell line panels for use in disease-oriented drug screening. *Progress in Clinical and Biological Research* 276:265–286.

[9] Yang W, et al. (2013) Genomics of Drug Sensitivity in Cancer (GDSC): A resource for therapeutic biomarker discovery in cancer cells. *Nucleic Acids Research* 41:D955–961.

[10] Kim D, et al. (2013) TopHat2: accurate alignment of transcriptomes in the presence of insertions, deletions and gene fusions. *Genome biology* 14:R36.

[11] Thorvaldsdóttir H, Robinson JT, Mesirov JP (2013) Integrative Genomics Viewer (IGV): High-performance genomics data visualization and exploration. *Briefings in Bioinformatics* 14:178–192.

[12] Li H, et al. (2009) The Sequence Alignment/Map format and SAMtools. *Bioinformatics* 25:2078–2079.

[13] Anders S, Pyl PT, Huber W (2014) HTSeq A Python framework to work with high-throughput sequencing data. *Bioinformatics* p pii:btu638.

[14] Robinson MD, McCarthy DJ, Smyth GK (2010) edgeR: a Bioconductor package for differential expression analysis of digital gene expression data. *Bioinformatics* 26:139–140.

Chapter 3. Cell Screening

3.1 Introduction

This chapter analyses cell screening data obtained from two cancer institutes, for Os compounds **Os-1** (Os(η^6-bip)(NMe$_2$-azpy)I]PF$_6$), **Os-2** ([Os(η^6-*p*-cym)(NMe$_2$-imino)I]PF$_6$), **Os-3** ([Os(η^6-*p*-cym)(NMe$_2$-azpy)I]PF$_6$), **Os-4** ([Os(η^6-bip)(F-azpy)I]PF$_6$), **Os-5** ([Os(η^6-bip)(OH-azpy)I]PF$_6$) and Ir compounds **Ir-6** ([Ir(η^5-Cp^{xbiph})(phen)Cl]Cl), **Ir-7** ([Ir(η^5-Cp^{xph})(phen)Cl]Cl), **Ir-8** ([Ir(η^5-Cp^{xbiph})(bpy)Cl]PF$_6$), **Ir-9** (Ir(η^5-Cp^{xbiph})(ppy)Cl]), **Ir-10** (Ir(η^5-Cp^{xph})(NMe$_2$-azpy)Cl]PF$_6$) and **Ir-11** ([Ir(η^5-Cp^{xbiph})(dpq)Cl]Cl). Using these data, cell line selectivity is discussed and possible mechanisms of action (MOA) are proposed.

3.1.1 Cell screening by the National Cancer Institute

The National Cancer Institute 60 cell line screen (NCI-60) is a useful, free tool to explore cancer selectivity and mechanisms of action (MOA) of new drug candidates. For each of the cell lines in the screen the GI$_{50}$ (concentration of compound required to inhibit the growth of cells by 50%), TGI (concentration of compound required to inhibit 100% of cell growth) and LC$_{50}$ (concentration of drug required to kill 50% of cells) is calculated for each compound.[1–3] These measurements are made after a 48 h exposure period of each cell line to a selected compound, by determining cell viability using standardised methods (Methods section 2.2). The GI$_{50}$ and TGI values provide insight into the cytostatic potential of each compound, with the LC$_{50}$ providing insight into their cytotoxicity.

The fingerprints of activity for each compound in the NCI-60 screen can then be used together with an algorithm developed by Paull *et al* in 1989, which linearly compares fingerprints between compounds.[4] The so-called 'COMPARE algorithm' allows users to predict the MOA for new compounds based on fingerprint similarity with established compounds.[5–8] A seed compound can be compared to thousands of anti-cancer compounds populating various open access databases managed by the NCI, where the algorithm produces a quantifiable measure of similarity with a Pearson's correlation coefficient (r), where $-1 \geq r \leq 1$. For $r = -1$, two compounds are said to have a negative correlation i.e. the pattern of activity in the NCI-60 panel is completely opposite. When $r = 1$, there is positive correlation and when $r = 0$ there is no correlation.

There are also databases dedicated to gene expression, obtained through microarray analysis and supplied to the NCI by external companies like Novartis. Using these datasets it is possible to correlate activity with gene expression fingerprints in the panel of cell lines, and thus identify any pharmacogenomic relationships between compounds and oncogenes of interest.[3]

Collectively this screening process provides a wealth of information which can be used to both explore the MOA and to make predictions about patient selection criteria. Compounds **1 - 11** were all submitted to the National Cancer Institute (NCI) for analysis in the NCI-60 screen.

3.1.2 Cell screening with the Sanger Institute

The Cancer Genome Project (CGP), run by the Sanger Institute, aims to advance the development of new therapeutics in a similar manner to the NCI by investigating cell line selectivity, but focusing more on pharmacogenomics.[9] The CGP is on a larger scale, analysing data in ca. 1000 cell lines for a larger set of cancer subtypes, working on the same principle as the NCI-60; comparing activity fingerprints between a seed compound and between ca. 400 compounds in the Sanger database.

The pharmacogenomic comparisons take a different approach to that of the NCI, replacing gene expression with genetic mutation i.e. copy number variations (CNV) and point mutations, for 464 oncogenes of interest. A gene is said to be altered if it has a coding sequence variation, small insertion/deletion, gene-fusion or CNV of 0 or ≥ 7. These data were obtained from exome sequencing coupled with in-depth bioinformatics analysis, where all genes identified as oncogenic are stored in COSMIC, a publicly accessible database.[10–15]

Cell viability is measured using fluorescence techniques, extracting and dyeing viable cells before measuring fluorescence with a plate reader (Methods 2.2). Unlike NCI-60 screening, cell lines in the Sanger screen are exposed to a selected compound for 72 h, and the calculation of cell viability (GI_{50}) is more complex, to allow a more accurate prediction of GI_{50} values outside of the testable range (Figure 3.1).

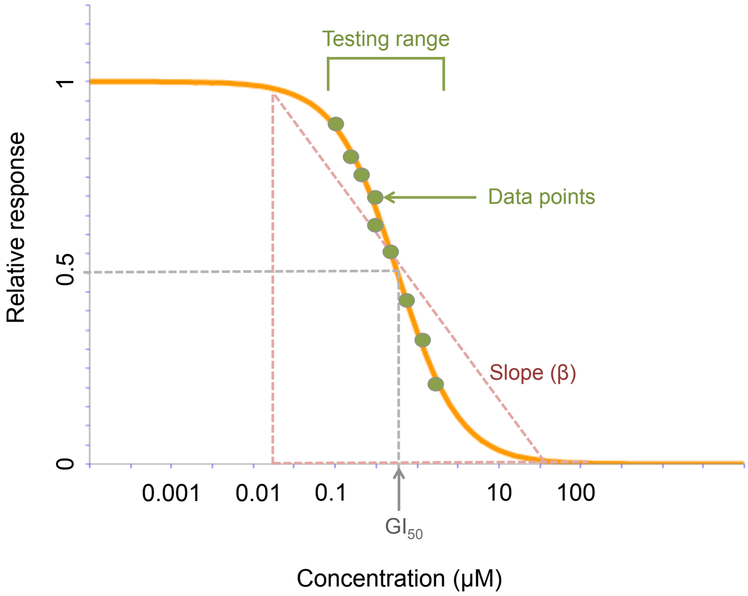

Figure 3.1: **Dose response curve.** Green data points represent the effect of the drug at varying concentrations. A sigmoid curve is fitted to these measurements and predicts drug-responses outside of the tested range. The slope parameter (β) measures the steepness of the drug-response, where a higher gradient represents a drug with a smaller therapeutic window, representing the concentration of a drug required to elicit a desired response against the concentration of drug required to elicit an adverse response. A larger therapeutic window (small β) is more clinically beneficial in reducing side-effects.

Fluorescence readings are fitted to a bespoke Bayesian sigmoid model, capturing the uncertainties in the data and allowing reasonable interpretation of predicted response values outside of the tested range (Figure 3.1 and Method 2.2). Resulting GI_{50} values cover ± 1000x the testing range, with 95% probability mass coverage. In addition to the GI_{50} values, a slope parameter (β), which is simply the dose-response gradient, is also provided. This gradient can give insights into the therapeutic index for an agent.

The main aim of Sanger screening is to extract significant correlations between compound activity and oncogenic behaviour. To do this, an analysis of variance (ANOVA) test is used, in place of the NCI-60's Pearson's correlation method. The dependent variable is presented as an $n\ X$ 2 matrix for each compound, containing GI_{50} and β values, therefore a multivariate ANOVA (MANOVA) is used for the analysis. For each gene, a linear model explains these activity observables with 'mutation status' as the predictive variable. Only genes found mutated in ≥ 2 cell lines were included in the analysis, and a Benjamin-Hochberg multiple testing correction was used to identify significant results (FDR < 0.20).

This quantitative assessment of pharmacogenomics uses an effect size parameter, calculated between wild type and mutant populations. If the effect size ≥ 1, the difference in mean value between the mutated and wild-type populations is greater than the variance in at least one population, and the effect is therefore *large*. If the effect size ≥ 2, the difference in mean value between the mutated and wild-type populations is greater than the variance of both populations, and the effect is therefore *very large*.

Compounds **Os-1** $[Os(\eta^6\text{-bip})(NMe_2\text{-azpy})I]PF_6$, **Os-3** $[Os(\eta^6\text{-}p\text{-cym})(NMe_2\text{-azpy})I]PF_6$, **Os-4** $[Os(\eta^6\text{-bip})(F\text{-azpy})I]PF_6$, **Ir-9** $[Ir(\eta^5\text{-}Cp^{xbiph})(ppy)Cl]$ and **Ir-10** $[Ir(\eta^5\text{-}Cp^{xph})(NMe_2\text{-azpy})Cl]PF_6$ were all submitted to the Sanger Institute for screening, this compound selection was made based on a combination of NCI-60 screening data, and prior *in vitro* and *in vivo* assays.[16–18]

3.1.3 Primary cell screening with the Edinburgh Cancer Research Centre

Primary cells are those which are derived directly from living tumour samples, and when cultured *in vitro* are generally more representative of *in vivo* environments, mostly as they have undergone fewer population doublings. Compounds **Os-1**, **Os-3**, **Os-4**, **Ir-9** and **Ir-10** were screened in three ovarian adenocarcinoma primary cell lines at the Edinburgh

Cancer Research Centre, where these cell lines were developed at the Edinburgh Medical Oncology Unit.[19]

PE01 - ovarian cancer cells prior to treatment
PE04 - ovarian cancer cells after taxane/cisplatin treatment
PE01-CDDP - ovarian cancer cells prior to treatment, which have been *ex vivo* cultured in low doses of cisplatin (CDDP) to create a CDDP resistant line

Compounds **Os-1**, **Os-3**, **Os-4**, **Ir-9** and **Ir-10** were all tested and the GI_{50} values determined after 48 h exposure.

3.2 Results

3.2.1 60 cell line screening with the National Cancer Institute

Table 3.1 shows the activity results for Os compounds **Os-1** - **Os-5** and Ir compounds **Ir-6** - **Ir-11** (for structures see Table 1.1 and Figure 1.3 in section 1.2), as well as cisplatin (CDDP) and oxaliplatin (OXA) in the NCI-60, as the average GI_{50} and LC_{50} value across all cell lines in the screen.

Table 3.1: Table of mean GI_{50} and LC_{50} values from the NCI-60 screen for compounds **1** - **11**, cisplatin (CDDP) and oxaliplatin (OXA) Mean values are calculated as the average value across all 60 cancer cell lines, with the ratio of cytostaticity (GI_{50}) against cytotoxicity (LC_{50}) exploring whether a compound inhibits cancer cell growth or kills cancer cells.

Compound	**Mean GI_{50} (μM)**	**Mean LC_{50} (μM)**	**Ratio LC_{50}/GI_{50}**
Os-1	0.07	2.50	35.71
Os-2	3.72	48.60	13.06
Os-3	0.31	7.76	25.03
Os-4	4.68	37.20	7.95
Os-5	0.17	3.52	20.71
Ir-6	2.34	31.60	13.50
Ir-7	10.7	93.30	8.72
Ir-8	4.17	67.60	16.21
Ir-9	0.71	8.13	11.45
Ir-10	0.59	6.61	11.20
Ir-11	0.83	19.50	23.49
CDDP*	1.49	44.00	29.53
OXA*	2.85	95.30	33.44

* Data for CDDP and OXA data were taken from the most recent round of NCI testing in March 2012, found in the DTP/NCI database

In most cases, the organometallic compounds are more active than the platinum metallodrugs, and all compounds apart from **Os-1** ($[Os(\eta^6\text{-bip})(NMe_2\text{-azpy})I]^+$) have a lower LC_{50}/GI_{50} ratio. This ratio is a good predictor of the cytostatic versus cytotoxic properties of compounds, where a lower value may indicate dual activity at low concentrations. As the mean GI_{50} values are much lower than the LC_{50} it can be said that these compounds are first and foremost cytostatic agents, with cytotoxicity occurring at higher concentrations. However, the LC_{50} values for **Os-1**, **Os-3** ($[Os(\eta^6\text{-}p\text{-cym})(NMe_2\text{-azpy})I]^+$), **Os-5** ($[Os(\eta^6\text{-bip})(OH\text{-azpy})I]^+$), **Ir-9** ($[Ir(\eta^5\text{-}Cp^{xbiph})(ppy)Cl]$) and **Ir-10** ($[Ir(\eta^5\text{-}Cp^{xph})(NMe_2\text{-azpy})Cl]^+$) were still below $<10\ \mu M$ suggesting that both cytotoxic and cytostatic activity are attainable with low exposure. Such multi-targetting activity has many benefits over singly targeted agents, particularly with regards to resistance, where cells would struggle to develop adequate resistance mechanisms if several areas of the cell are targeted simultaneously.

Figure 3.2 shows the GI_{50} values for each compound. The boxes of the box-and-whisker plots are constructed from the first and third quartiles and the median $\log_{10}GI_{50}$. The whiskers represent the lowest value (and highest value) still within 1.5 X interquartile range (IQR) of the lower (and upper) quartile. The IQR is a measure of the dispersion, and is calculated as the difference between the upper and low quartiles. $\log_{10}GI_{50}$ values outside of this range are labelled as outliers with empty circles.

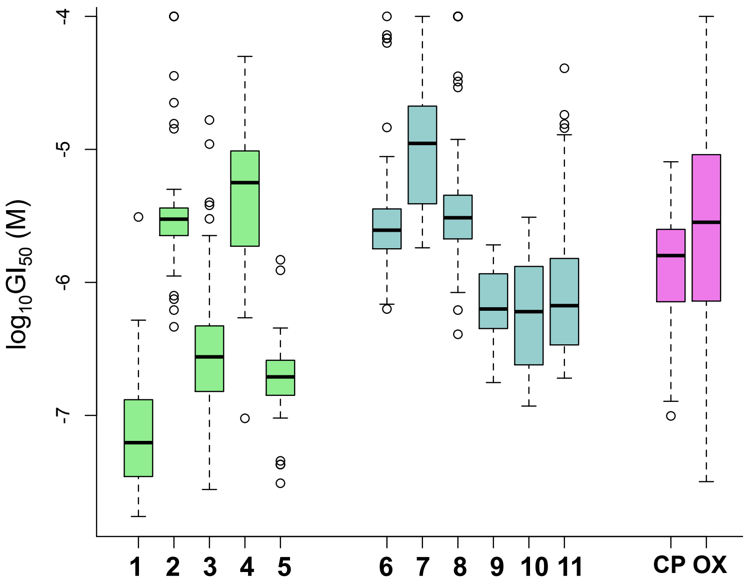

Figure 3.2: **Tukey box-and-whisker plots showing the distribution of GI_{50} values for Os compounds Os-1 - Os-5 and Ir compounds Ir-6 - Ir-11, cisplatin (CD) and oxaliplatin (OX) in the NCI-60 screen**. Boxes show the median and the first and third quarters. The whiskers represent the highest/lowest values within 1.5 times the interquartile range (IQR), calculated as the differences between the upper/lower quartiles. Open circles represent outliers in the data, which fall outside 1.5x IQR. The large number of outliers for **Os-2** result from a majority of the data points lying within a small range, and a smaller selection of cell lines showing significantly higher/lower sensitivity.

In Figure 3.2 the median activity values for compounds **Os-1**, **Os-3**, **Os-5**, **Ir-9**, **Ir-10**, **Ir-11** are all lower than that of CDDP and OXA, in the NCI-60 screen. Compound **Os-2** ($[Os(\eta^6\text{-}p\text{-cym})(NMe_2\text{-imino})I]^+$) has a broad distribution of outliers, suggesting strong selectivity in small selection of cell lines i.e. most activity values fall within a small range. OXA, in comparison has a generally broad range of selectivity in the screen, with no outliers.

Drug compounds with large ranges in cancer cell screens suggest a non-targeting nature, i.e. they show no specificity in their potency. Although this has it's benefits, it means that these compounds can be equally active against normal cells, resulting in significant side-effects. Oxaliplatin has the broadest selectivity in Figure 3.2, with the Os and Ir compounds, particularly the Ir compounds, show more targeted behaviour.

Figure 3.2 also shows that Ir compounds **Ir-6** ([Ir(η^5-Cp^{xbiph})(phen)Cl]$^+$), **Ir-7** ([Ir(η^5-Cp^{xph})(phen)Cl]$^+$) and **Ir-8** ([Ir(η^5-Cp^{xbiph})(bpy)Cl]$^+$) are all much less active than **Ir-9** ([Ir(η^5-Cp^{xbiph})(ppy)Cl]), **Ir-10** ([Ir(η^5-Cp^{xph})(NMe$_2$-azpy)Cl]$^+$) and **Ir-11** ([Ir(η^5-Cp^{xbiph})(dpq)Cl]$^+$). This suggests that phenanthroline and bipyridine chelated ligands produce lower activity compounds, compared to 2-phenylpyridinato, azopyridine and dipyridoquinoxaline.

This also highlights the importance of exploring the activity of compounds in more than one cell line, as Table 1.1 shows that activity in A2780 is similar for all compounds. The heat map in Figure 3.3 explores the cell line selectivity in the NCI-60 screen for each of the eleven compounds, together with CDDP and OXA.

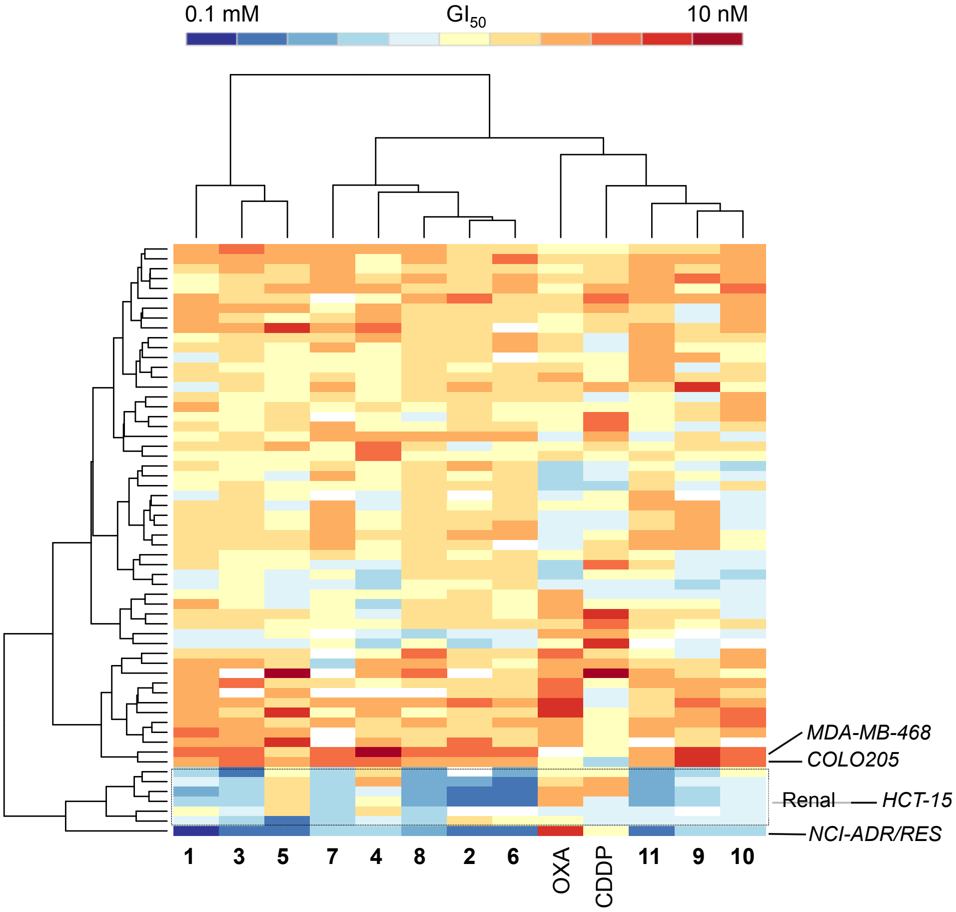

Figure 3.3: **Heat map of NCI-60 data for Os compounds Os-1 - Os-5 and Ir compounds Ir-6 - Ir-11, cisplatin (CDDP) and oxaliplatin (OXA).** Dendrograms show clustering of data by compound (top) and cell lines (side). CDDP and OXA data were taken from the most recent round of NCI testing in March 2012, found in the DTP/NCI database. Figure 3.4 highlights the trends shown in this heat map, with separation of compounds into a subsets of similarity $\{$**Os-1**, **Os-3**, **Os-2**, **Ir-6** - **Ir-8** and **Ir-11**$\}$. In addition, renal cell lines show significantly poor sensitivity to all compounds, and MDA-MB-468 (breast) and COLO205 (colon) cell lines showed significantly high sensitivity.

Figure 3.3 presents trends in selectivity across each of the compounds, including those compounds with similar patterns of selectivity and cell lines which similar sensitivities. The dendrograms along the rows shows clustering of individual cell lines by similarity in sensitivity to each compound, with the dendrogram along the columns clustering the compounds by similarity across all 60 cell lines. Figure 3.4 should be used as reference for Figure 3.3, highlighting these trends further.

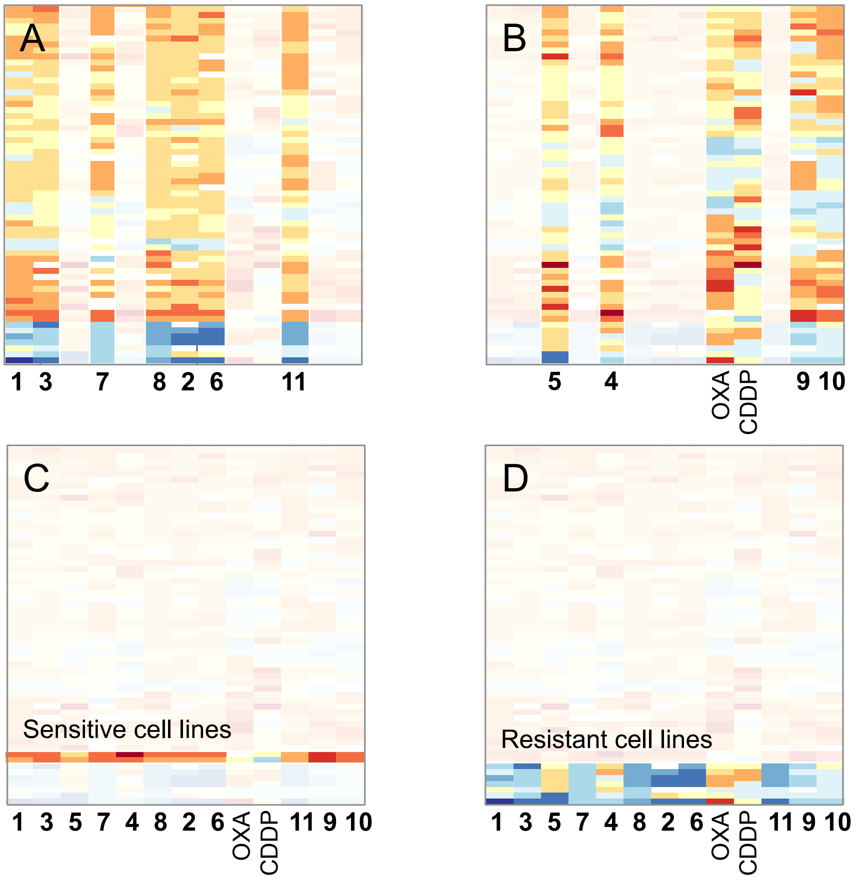

Figure 3.4: **Heat maps highlighting trends in NCI-60 data shown in Figure 3.3 for Os compounds Os-1 - Os-5 and Ir compounds Ir-6 - Ir-11, cisplatin (CDDP) and oxaliplatin (OXA).** (A) Compounds with similar patterns of selectivity, (B) Compounds with novel selectivity patterns, (C) Cell lines with higher sensitivity (MDA-MB-468 and COLO205) and (D) Cell lines with low sensitivity (renal cell lines).

Performing 2D principal component analysis (PCA) on the GI_{50} data for **Os-1 - Ir-11** separates the compounds and cell lines per the selectivity trends identified in Figure 3.3 (Figure 3.5). This PCA plot is called a bi-plots, showing the similarity of cell lines (black text) represented by euclidean distance i.e. the closer the cell lines in space, the more similar the sensitivity of each cell line to all compound. The similarity in compound selectivity is shown in red, where the angle between the vectors is proportional to the similarity i.e. the smaller the angle the more similar the compounds are.

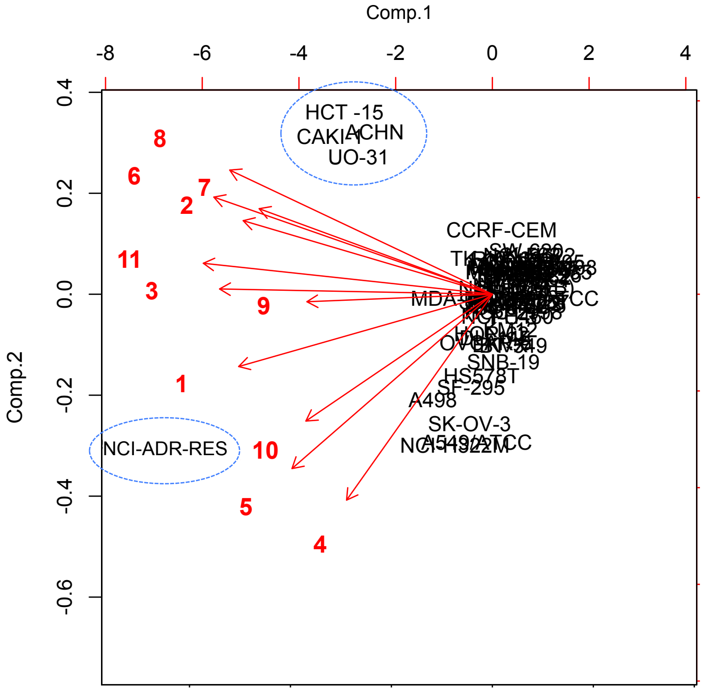

Figure 3.5: **Bi-plot of GI_{50} values for Os compounds 1 - 5 and Ir compounds 6 - 11.** Data were plotted using principle component analysis (PCA), which separates variables by euclidean distance, based on similarity. Cell lines were plotted in black, with those closer together having similar sensitivities to compounds. The resistant cell lines in the NCI-60 screen are circled in blue, with the renal cell lines in one cluster and ovarian cell line NCI-ADR-RES in the other. The remaining more sensitive cell lines are clustered together. The compounds were plotted in red, with their similarity in NCI-60 selectivity proportional to the vector angles between pairs of compounds.

The heat map (Figure 3.3) and the PCA plot (Figure 3.5) shows a high level of similarity in compound sensitivity across most of the cell lines, however there are several outliers. For example NCI-ADR-RES is isolated in the plot, suggesting the activity values in this cell line are significantly different to the other cell lines. The subset {HCT-15, CAKI, SCHN, UO-31} is also isolated in a cluster, where these cell lines showed poor sensitivity in Figure 3.3. The two subsets of compounds {**Ir-10**, **Os-5**, **Os-4**} and {**Os-2**, **Ir-6**, **Ir-7**, **Ir-8**} are plotted a wide distance apart, with **Os-1** appearing to plot alone from the others. **Os-1** was significantly more active than the other compounds.

The similarity matrix in Figure 3.6 displays a Pearson's correlation coefficients quantifying compound-to-compound similarity in GI_{50} values from the NCI-60 screen.

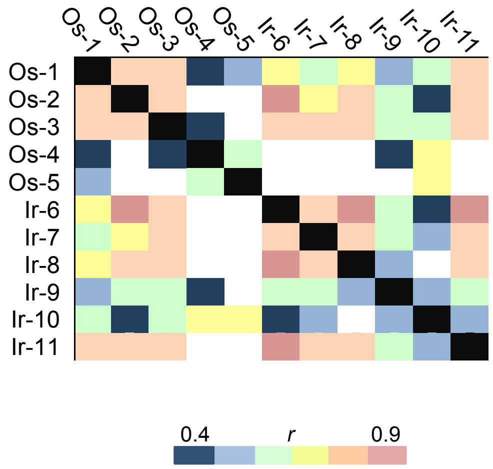

Figure 3.6: **Similarity matrix showing the Pearson's correlation coefficients (*r*) between the compounds.** Correlation coefficients were calculated from the NCI-60 data, ranging from 0.4 to 0.9. The higher *r* values between **Os-1**, **Os-2**, **Os-3**, **Ir-6**, **Ir-7**, **Ir-8** and **Ir-11** represent the subset of compounds identified in Figures 3.3 and 3.4. The lower *r* values for **Os-4**, **Os-5**, **Ir-9** and **Ir-10** highlight their more novel patterns of selectivity.

Figure 3.6 highlights again the subsets of compounds, in particular Os compounds **Os-4** and **Os-5** show very different selectivities to the rest of the compounds, with **Ir-9** and **Ir-10** showing lower levels of similarity.

3.2.1.1 COMPARE analysis

COMPARE analysis was performed for each compound, using the GI_{50} datasets. Activity fingerprints were compared to drugs populating both the standard agents database, which contains ca.175 agents selected as highly promising by the NCI, and the synthetic agents database containing $>$ 40,000 synthetic compounds and natural products of known structure. Only those results with $r > 0.5$, between Os compounds **Os-1** - **Os-5** and Ir compounds **Ir-6** - **Ir-11** and drugs with known MOA were included (Figure 3.7).

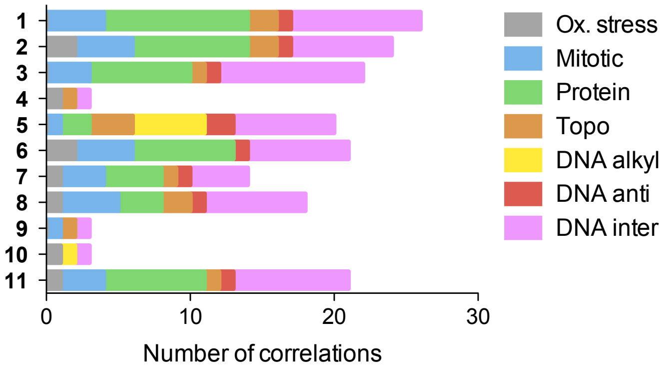

Figure 3.7: **COMPARE results for Os compounds Os-1 - Os-5 and Ir compounds Ir-6 - Ir-11** showing NCI-60 patterns of similarity against other compounds in the NCI/DTP compound database. Coloured bars shows a summary of the top 100 positive correlations to each compound, including only those with known mechanisms of action (MOA) and $r > 0.5$. Correlations were split into seven classes: oxidative stress inducers, mitosis inhibitors, protein synthesis inhibitors, topoisomerase inhibitors. DNA alkylating agents, DNA antimetabolites, DNA interacting agents. Compounds **Os-1**, **Os-2**, **Os-3**, **Ir-6**, **Ir-7**, **Ir-8** and **Ir-11** all correlated to the same classes of compound, primarily DNA interacting agents and protein synthesis inhibitors. **Os-5** correlates to different classes of compounds, namely DNA alkylating agents and **Os-4**, **Ir-9** and **Ir-10** correlated to few compounds, highlighting their novelty.

Results show positive correlations to DNA interactors, DNA antimetabolites, topoisomerase inhibitors, protein synthesis inhibitors, mitosis inhibitors and redox mediators, suggesting a multi-targetted MOA. The subset {**Os-1**, **Os-2**, **Os-3**, **Ir-6**, **Ir-7**, **Ir-8**, **Ir-11**} showed high similarity in the correlations returned, with drugs in a broad range of MOA subclasses. **Os-5** showed an increased correlation to DNA alkylating agents, as did **Ir-10**, with overall fewer returned correlations for **Os-4**, **Os-5**, **Ir-9** and **Ir-10**. This suggests that these compounds are not only different within this set of organometallics, but are also novel in MOA with respect to drugs populating the NCI databases.

COMPARE can also be used to assess pharmacogenomic relationships to determine whether compound activity is dependent on cell line genetics. Figure 3.8 shows the correlation coefficients when the activity of Os compounds **Os-1** - **Os-5** and Ir compounds

Ir-6 - **Ir-11** were compared to gene expression in the NCI-60 cell lines.

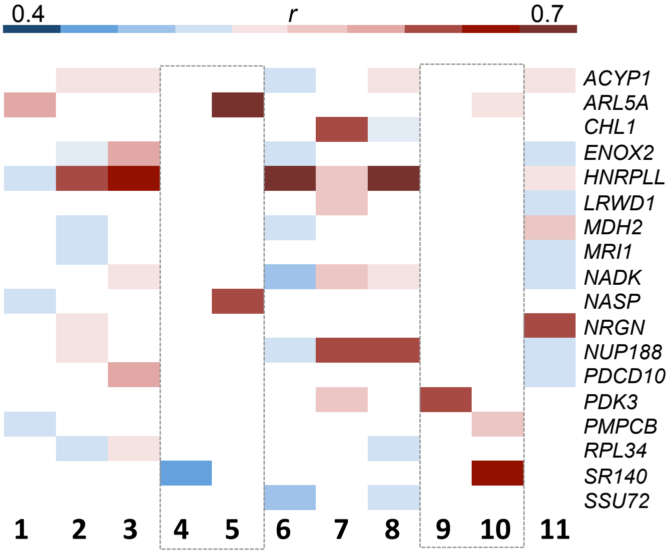

(a)

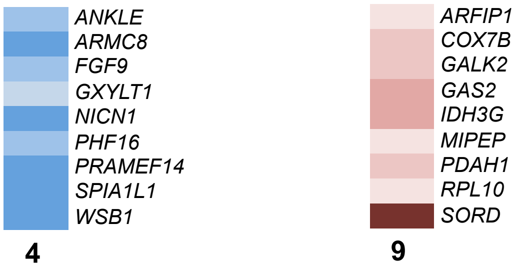

(b)

Figure 3.8: **Heat maps representing Pearson's correlation coefficients (*r*) for comparisons of similarity between the GI$_{50}$ values for compounds Os-1 - Ir-11 and the expression of genes, in the NCI-60 cell lines** (a) Heat map showing genes which correlated to $n > 2$ compounds and (b) Individual analysis showing the lack of correlation in the top 10 genes returned for **Os-4** and a higher level of correlation between GI$_{50}$ and expression of the top 10 genes returned for **Ir-9**. Microarray data were taken from the DTP/NCI database.

Figure 3.8 shows the top 10 correlations returned after compounds **Os-1** - **Ir-11** were run through the COMPARE algorithm together with all microarray datasets in the NCI database. These microarrays have measured the expression of important cancer genes in NCI-60 cell lines, and are often donated from pharmaceutical companies.

Figure 3.8(a) shows common correlations between compounds, reflecting the selectivity shown in previous figures. Figure 3.8(b) shows the top 10 correlations to the most novel compounds **Os-4** and **Ir-9**, with no commonality between compounds and much higher r values for **Ir-9**. This suggests that the activity fingerprint of **Os-4** has little dependence on the genetics of the cancer cells. The selectivity pattern of this compounds could therefore be related to uptake mechanisms instead of intracellular targetting.

The overlapping genes which correlated primarily to **Os-1** - **Os-3**, **Ir-6** - **Ir-8** and **Ir-11** encode a broad spectrum of proteins. Selecting out a few examples, like *HNRPLL* (heterogenous nuclear ribonucleoprotein L-like), *NUP188* (nucleoporin), *MDH2* (malate dehydrogenase 2) can provide insights into the MOA of the seven similar compounds. Heterogenous ribonucleoproteins bind to and control RNA processing, mediating the formation of mature mRNAs from pre mRNAs.[20] Nucleoporin is part of a nuclear pore complex (NPC) in the nuclear membrane, which controls the transport of molecules between the nucleus and cytoplasm.[21] Malate dehydrogenase is a mitochondrial-based protein which catalyses the oxidation of malate and utilises NAD^+ in the citric acid cycle.[22]

Figure 3.9 shows that all three genes are found in high levels in cell lines which show high sensitivity to osmium compound **3**, and conversely are found in low levels in renal cell lines like UO-31 and TK-10, which were particularly resistant to most of the compounds. Here gene expression is shown as log (mRNA level in a cell line/mRNA level in pool of NCI-60 cell lines).

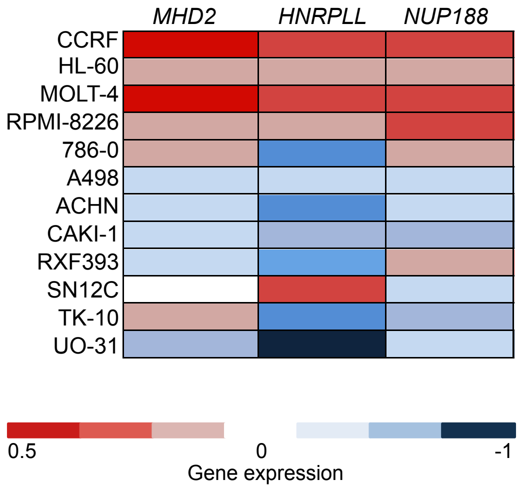

Figure 3.9: **Heat map showing the expression levels of genes *MDH2*, *HNRPLL* and *NUP188* in a selection of cell lines in the NCI-60 screen.** Gene expression values for each cell line were calculated by subtracting the mean expression across the NCI-60 screen from the individual cell line expression values. Positive values indicate high expression in a given cell line with respect to the mean, negative values indicate low expression compared to the mean expression in the screen. The cell lines will high expression levels were cell lines with high sensitivity to the organometallic compounds, cell lines with low expression levels were those which showed poor sensitivity to the organometallic compounds. This suggests a possible pharmacogenomic relationship for the mechanisms of action.

This suggests that the compounds are most active when cells are efficiently producing mature mRNA, transporting molecules and undergoing respiration, suggesting that cell division could play an important role in the MOA of **3**.

Collectively this section has utilised NCI-60 activity data for **Os-1** - **Os-5**, **Ir-6** - **Ir-11**, cisplatin and oxaliplatin to explore similarities and differences between the compounds with regards to cell line selectivity. There appeared to be no discrimination between the different metals, Os and Ir compounds commonly clustered together and gave similar selectivity profiles. Correlating the fingerprints of activity with other anticancer compounds suggested that the compounds possess multiple MOA, with **Os-4**, **Os-5**, **Ir-9** and **Ir-10** emerging as particularly novel compounds. In addition, the possible molecular targets were explored and showed that when genes associated with cell growth were amplified in a given cell line, this cell line showed higher sensitivity to the compounds.

From these eleven compounds, five were taken forward for screening by the Sanger Institute. The compound selection was based on both the level of activity in the NCI-60 screen and on the novelty of the selectivity patterns.

3.2.2 Cell screening with the Sanger Institute

Compounds **Os-1**, **Os-3**, **Os-4**, **Ir-9** and **Ir-10** were selected for Sanger Institute screening based on their selectivity patterns in the NCI-60 panel, where **Os-1** and **Os-3** had highly similar activities and were highly active, **Os-4**, **Ir-9** and **Ir-10** showed more novel patterns of selectivity, with **Ir-10** showing the highest potency.

Screening was performed in 974 cancer cell lines. Table 3.2 shows the mean GI_{50} values for each of the compounds and Figure 3.10 shows the median and the distribution of the $\log_{10}GI_{50}$ values.

Table 3.2: Table of the mean GI_{50} from the Sanger Institute screen for **Os-1**, **Os-3**, **Os-4**, **Ir-9**, **Ir-10** and cisplatin (CDDP). Mean values were calculated as an average across 974 cancer cell lines

Compound	**Mean GI_{50} (μM)**
Os-1	2.10
Os-3	40.36
Os-4	420.44
Ir-9	251.44
Ir-10	38.54

The levels of activity for the compounds fits the same trend as that shown in the NCI-60 screen, where compounds **Os-1**, **Os-3** and **Ir-10** are the most active, and **Os-4** and **Ir-9** are the least. **Os-1** and **Os-3** show a large number of outliers, as the majority of activity occurs within a small range, shown with the small boxes in the Tukey plots. **Ir-10** also presents a large number of outliers, primarily with low sensitivity.

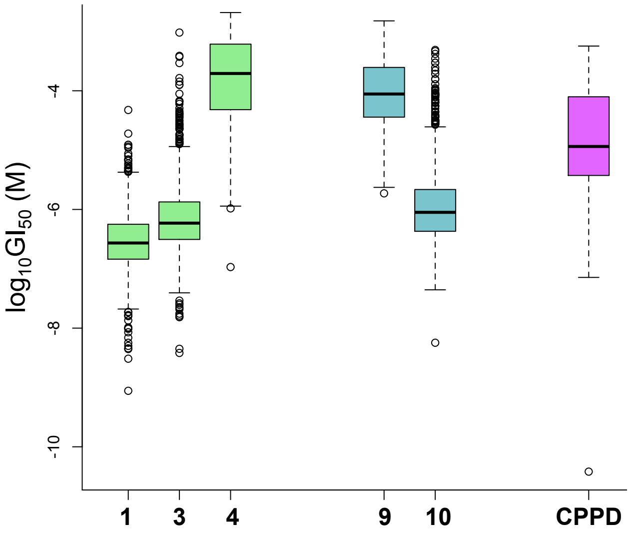

Figure 3.10: **Tukey box-and-whisker plots showing the distribution of GI$_{50}$ values of each compound in the Sanger screen, together with cisplatin (CDDP).** Boxes show the median and the first and third quarters. The whiskers represent the highest/lowest values within 1.5x the interquartile range (IQR), calculated as the differences between the upper/lower quartiles. Open circles represent outliers in the data, which fall outside 1.5x IQR. The large number of outliers for **Os-1** and **Os-3** result from a majority of the data points lying within a small range, and a smaller selection of cell lines showing significantly higher/lower sensitivity. The weighted outliers for **Ir-10** suggest a small selection of cell lines show significantly higher sensitivity.

The heat map in Figure 3.11 clusters compounds by GI$_{50}$ value and shows the similarities in selectivity between **Os-1** and **Os-3**. The increased number of blue values for **Os-4** and **Ir-9** highlights their poor activity.

Figure 3.11 shows minimal segregation of activity into cancer subtypes, however, there are a few boxed areas highlighting low sensitivity. Particularly in the gastrointestinal (G.I) cell lines, where the majority show poor sensitivity towards compound **Ir-10**. There are also a selection of leukemia/lymphoma cell lines, and central nervous system (CNS) lines which show poor sensitivity towards to **Os-1** and **Os-3**.

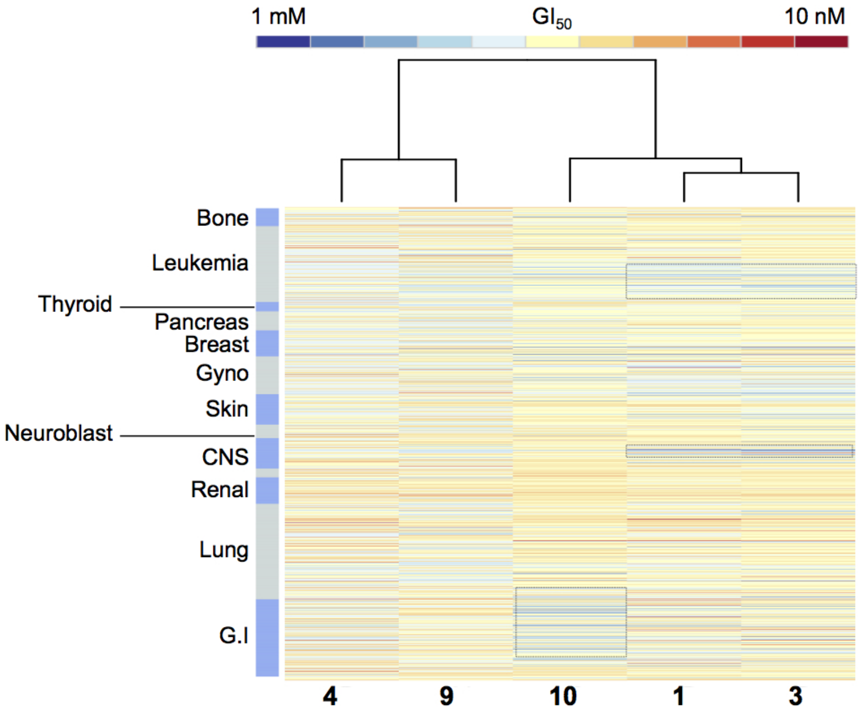

Figure 3.11: **Heat map of GI_{50} values for compounds Os compounds Os-1 and Os-3 and Ir compounds Ir-9 and Ir-10 in 974 cell lines of the Sanger screen.** Visible clustering of low sensitivity are highlighted with grey boxes showing resistance of gastrointestinal (GI) cancers to **Ir-10** and leukaemia and central nervous system (CNS) cancers to **Os-1** and **Os-3**. The dendrogram clusters the compounds by similarity and shows that **Os-1** and **Os-3** share high similarity in the screen and that **Os-4** and **Ir-9** share similarity to each other, but significant differences to **Os-1**, **Os-3** and **Ir-10**.

Further analysis focussed only on **Os-3** and **Ir-10**. **Os-3** was selected as the Sadler group had previously published *in vivo* and in-depth *in vitro* data for this potent compound. In addition, **Os-3** was part of a large subset of compound which behaved similarly in the NCI-60 screen. **Ir-10** was chosen for it's potency and it's novelty in NCI-60 selectivity. correlating more similarly to DNA-targeting agents than the other Os and Ir compounds. Given Os and Ir centers chelated to para-substituted azopyridine ligands, this would also provide a good comparison of ligand dependencies on mechanisms of action.

The mean and median activities of **Os-3** and **Ir-10** are similar in Table 3.2 and Figure 3.10, however the outlying data points for **Ir-10** are skewed towards more resistant cell lines. Figure 3.12 breaks down the activity into stricter cancer subtypes for **Os-3** and

Ir-10 to investigate where these differences arise.

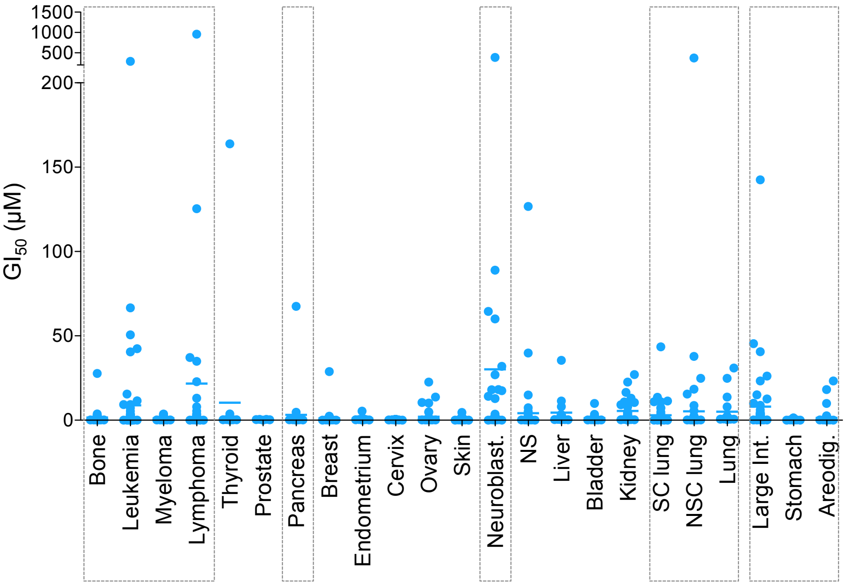

(a)

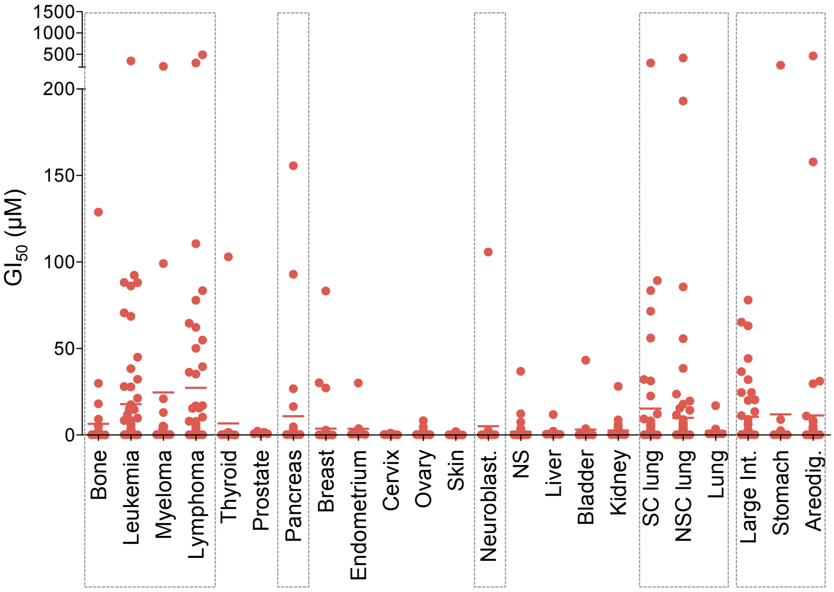

(b)

Figure 3.12: **GI_{50} values in cancer subtype for compounds Os-3 (a) and Ir-10 (b) in the Sanger Institute screen.** The mean values for each population are shown with coloured lines, boxed sections highlight the key differences in activity between the two compounds. These differences are highlighted in the blood cancers, pancreatic, neuroblastoma, lung and gastrointestinal. For example, neuroblastoma cell lines are significantly more susceptible to **Ir-10** than to **Os-3** and blood cancers like leukemia and lymphomas are more susceptible to **Os-3**.

Figure 3.12 highlights the significant difference in GI_{50} values for compound **Os-3** and **Ir-10** in leukaemia, myeloma and lymphoma cell lines, with poor sensitivity for **Ir-10**. The female cancers retain similar sensitivity between **Os-3** and **Ir-10**, however, shown in the second grey box is a significant drop in activity in neuroblastoma cell lines exposed to **Os-3**. The third and fourth grey boxes highlight poor activity of both **Os-3** and **Ir-10** towards lung and GI cancers, particularly so for **Ir-10**. This behaviour was shown in the heat map of Figure 3.11.

3.2.2.1 Pharmacogenomic studies

Gaining insights into the most sensitive and least sensitive cancer cell lines in screens like the NCI-60 and the CGP can help select patient populations, and in some cases provide insight into drug MOA. To build on this, it is useful to investigate the genetics upon which each cancer line is defined and to link these carcinogenic properties with compound activity.

A MANOVA analysis was performed to correlate compound activity with the genetic status of 379 cancer genes in the screen. Table 3.3 shows the genetic mutations that had an effect size ≥ 0.5 (and FDR ≤ 0.20) on the GI_{50} of the five compounds. These include point mutations in genes *PGR, HGF, ERBB3, FOXP1, CASP8* and *KIT*, and amplifications of regions *R184*, and *R198*. Regions of gene amplification or deletion may contain multiple genes. For example *R184* covers twenty-one genes and *R198* covers four (Appendix Table 9.1).

Table 3.3: Table showing the most significantly correlated genes to the activity of Os compounds **Os-1** and **Os-3** and Ir compounds **Ir-9** and **Ir-10**. The effect size measures the significance of this correlation between genomic expression and cell susceptibility, the higher the effect size the higher the correlation. The most significant correlation was for **Os-1** with *PGR* mutation (m), where cell lines carrying this mutation were more sensitive (s) to this compound. Conversely cell lines carrying mutations in *HGF* were more resistant (r) to **Os-3**.

Compound	**Gene**	**No. cell lines**	**Effect size**	**FDR**	
Os-1	*R184* [a]	9	0.95	0.07	r
	PGR [m]	3	2.00	0.01	s
	R198 [a]	17	0.87	0.02	r
Os-3	*R184* [a]	9	0.93	0.02	r
	HGF [m]	5	1.70	0.01	r
Os-4	*ERBB3* [m]	3	1.10	0.01	s
	FOXP1 [m]	9	0.63	0.01	s
Ir-9	*CASP8* [m]	17	0.57	0.02	s
Ir-10	*KIT* [m]	4	0.83	0.08	s

[a] = amplification; [m] = mutation; r = amplification/mutation infers resistance; s = amplification/mutation infers sensitivity

Figure 3.13 graphically highlights the effect of *R184*, *HGF* and *KIT* alterations on the GI_{50} values for compounds **Os-3** and **Ir-10**.

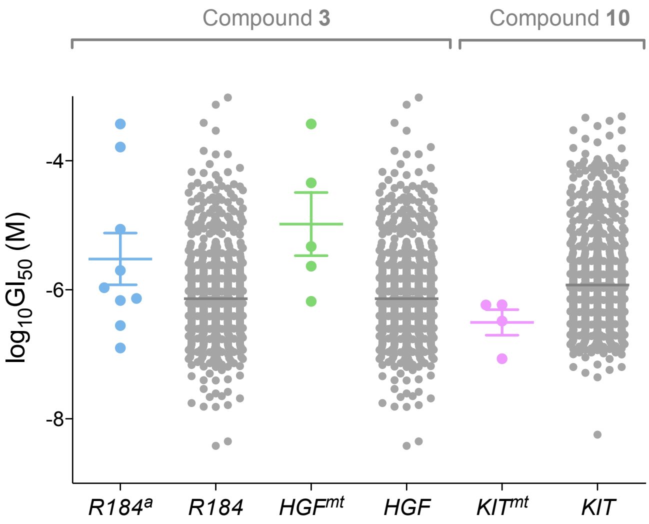

Figure 3.13: **Plot showing the effect of genetic mutation on compound activity for Os-3 and Ir-10.** All grey dots represent wild-type cancer cells lines not carrying mutations/amplifications of *R184*, *HGF* and *KIT*. Blue dots represent cell lines carrying amplified *R184* (a), green dots are *HGF* mutated (mt) cell lines and pink dots are *KIT* mutated cell lines. Blocked central lines are the mean values, with the upper and lower bars showing the standard deviation. The plot shows that *R184* amplifications (effect size 0.93) and *HGF* mutations (effect size 1.70) both cause cell lines to show resistance to **Os-3**, where as *KIT* mutated cell lines (effect size 0.83) are more sensitive to **Ir-10**.

Taking a closer look at cell lines with mutations in *KIT*, *HGF* and amplifications in *R184* could provide reasons for the cell line selectivity for **Os-3** and **Ir-10** shown in Figure 3.12.

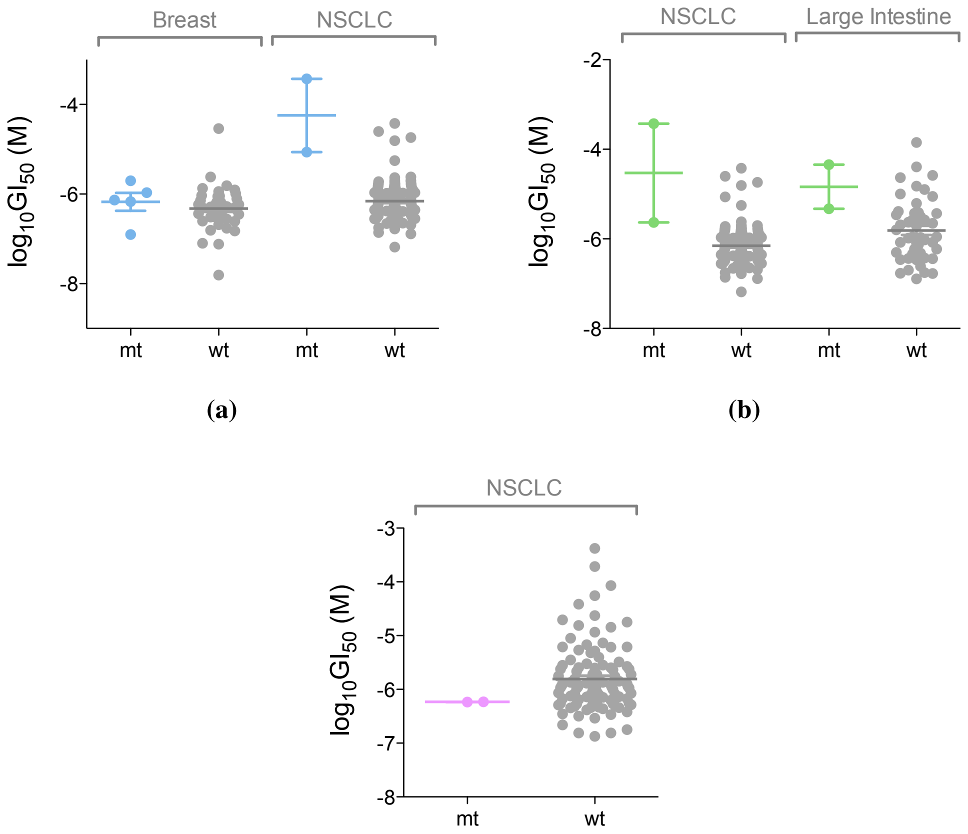

(a)

(b)

(c)

Figure 3.14: **Plot showing the breakdown of pharmacogenomic responses into cancer cell subtypes for *R184* (a), *HGF* (b) and *KIT* (c).** (a) show the cell line sensitivities to **Os-3**, with the wild-type cell lines in grey and the *R184* amplified breast and lung cancer cell lines in blue, showing that in both cancer subtypes this amplifed region increases resistance to **Os-3**. (b) shows the sensitivity of *HGF* mutated lung and large intestine cancers (green) and wild-type cancers (grey) to **Os-3**, again showing that mutated cell lines showed lower susceptibility to **Os-3**. (c) shows the sensitivity of *KIT* mutated lung cancers (pink) and wild-type cancers (grey) to **Ir-10**, this time showing that mutated cell lines are ore sensitive to the drug compound.

Amplifications in *R184* only occur in either breast or non-small cell lung cancer (NSCLC) in the screen. Figure 3.14(a) shows that alterations in *R184* causes **Os-3** to lose activity. *HGF* is only mutated in NSCLC and large intestine cancers in the screen, again, when genes related to this region are altered, the cell is less sensitive to the action of **Os-3**. In contrast, *KIT* mutations are only found in NSCLC, and when present, cell lines become more sensitive to **Ir-10**.

Looking at the function of proteins encoded by *HGF* and *KIT* can provide insight into the MOA of these compounds. *HGF* codes for the hepatocyte growth factor, which regulates cell growth and motility through tyrosine kinase activity. HGF is a multifunctional cytokine, and is commonly associated with increased tumor motility and migration.[23] Alterations in HGF expression, particularly of increased expression have been linked to intrinsic and acquired drug resistance, and may be the cause for reduced sensitivity to **Os-3**.[24]

KIT encodes the human homolog of the proto-oncogene C-KIT and is a type III transmembrane receptor for the stem cell growth factor.[25] Once bound to growth factor, this protein activates signal transduction through the cell, affecting cell survival and differentiation. Disrupting this gene might render cancer cells less viable, resulting in higher susceptibility to **Ir-10**.

Given the broad activity of these proteins it is more useful to use an approach similar to that of the COMPARE analysis, and to explore the MOA by assessing which other anticancer drugs share the pharmacogenomic properties shown for compounds **Os-3** and **Ir-10**. Table 3.4 lists the other drug compounds in the Sanger database whose activity correlated with genetic mutations in *R184*, *HGF* and *KIT*. In all cases, *HGF* mutations and *R184* amplifications were associated with low drug sensitivity. *KIT* mutations were not shown to be associated with any other drug compound.

Table 3.4: Table showing all drug compounds in the COSMIC database that are also associated with mutations/amplifications in *R184*, *HGF* and *KIT*. *R184* amplifications caused cells to show resistance to both **Os-1** and **Os-3**, and also to bleomycin and SN-38, where the latter is a known topoisomerase inhibitor. Conversely, **Ir-10** was the only compound in the COSMIC database which showed an increased potency towards *KIT* mutated cell lines, highlighting it's novelty.

Gene	Function	Drug associations	Drug target
R184		**Os-1** and **Os-3**	-
		SN-38	TOPO1
		Bleomycin	
HGF		**Os-3**	-
		CEP701	FLT3, JAK2, NTRK1, RET
		AZD7762	CHK1/2
		Obatoclax mesylate	BCL-2, BCL-x, MCL-1
		CI-1040	MEK1/2
KIT		**Ir-10**	-

The MOA of bleomycin is thought to result in DNA and RNA damage via production of reactive oxygen species.[26] In contrast, SN-38 is the active metabolite of irinotecan, a topoisomerase I inhibitor.[27] All three of these MOAs were predicted for compounds **Os-1** and **Os-3** by the COMPARE algorithm.

CEP-701 (lestaurtinib) is a tyrosine kinase inhibitor, targetting FLT3, JAK2, NTRK1 and RET and is currently in phase II clinical trials.[28, 29] AZD7762 is often used to potentiate the activity of standard chemotherapy agents, as it targets CHK1/2 proteins which ordinarily detect DNA damage during the S/G2 phase of the cell cycle.[30] Obatoclax, also in phase II trials, activates apoptosis by inhibiting the family of BCL proteins.[31] Finally, CI-1040, is a highly specific MEK (MAPKK) inhibitor, however, due to poor solubility and tolerability by patients, analogues of this drug are in development.[32]

The Sanger screen allowed an assessment of more tumor subtypes, and highlighted GI cancers and NSCLC as potentially insensitive cell lines, particularly for **Os-3** and

Ir-10. Much like the results from the NCI, the Sanger screen results in similar MOAs between the organometallic compounds and a broad range of other drug compounds, thus reinforcing a proposed multitargeted mechanism.

3.2.3 Primary cell screening with the Edinburgh Cancer Research Centre

Os compounds **Os-1**, **Os-3** and **Os-4** and Ir compounds **Ir-9** and **Ir-10** were tested in ovarian patient-derived lines PE01 (patient prior to treatment), PE04 (patient after taxane/platinum treatment) and PE01-CDDP (PE01 cells exposed to low levels of CDDP, to create Pt resistance). Table 3.5 summarises the activity of each compound.

Table 3.5: Compound activity in primary ovarian cell lines: PE01 patient prior to treatment, PE04 patient after taxane/platinum treatment and PE01-CDDP cells from PE01 exposed to low levels of CDDP *in vitro* to create Pt resistance. Table shows that **Os-1**, **Os-3** and **Ir-10** all maintain activity in platinum/taxol-treated and platinum-resistant ovarian cancer, highlight a clear clinical benefit. However, **Os-4** and **Ir-9** lost activity in platinum-treated and platinum-resistant cancers, respectively.

Cell line	**Compound**	**GI_{50} (μM)**
PE01	**Os-1**	0.26
	Os-3	0.85
	Os-4	2.24
	Ir-9	22.4
	Ir-10	1.21
PE04	**Os-1**	0.58
	Os-3	2.15
	Os-4	20.8
	Ir-9	64.3
	Ir-10	1.65
PE01-CDDP	**Os-1**	0.17
	Os-3	0.68
	Os-4	2.01
	Ir-9	110.3
	Ir-10	1.56

Os-1, **Os-3** and **Ir-10** maintain reasonable activity in all four cell lines. Conversely, **Os-4** loses activity in patient cells treated with taxane/cisplatin, although retains activity in PE01-CDDP cells, suggesting that taxane cross-resistance becomes a problem for **Os-4** and not CDDP resistance. Given taxane is a mitotic inhibitor, the data could suggest that **Os-4** has significant involvement in disrupting mitosis. Unfortunately, compound **Ir-9** showed low activity in all of the primary cell lines suggesting that neutral complexes may not exert as potent an activity over cationic complexes, in patient-derived lines.

3.3 Discussion

3.3.1 Cytotoxicity versus cytostaticity

Os compounds **Os-1** - **Os-5** and Ir compounds **Ir-6** - **Ir-11** were all tested in the NCI-60 screen, and their activity finger prints compared to established anticancer agents. Table 3.1 and Figures 3.2 and 3.3 display the GI_{50} values for each organometallic compound, together with those for the platinum metallodrugs CDDP and OXA. Compounds **Os-1** - **Ir-11** show comparable activity values to CDDP and OXA, with **Os-1**, **Os-3**, **Os-5** and **Ir-9** - **Ir-11** showing an improved activity compared to the platinums.

Assessing the cytostatic versus cytotoxic nature of the compounds highlights further differences between the organometallic compounds and the platinum metallodrugs. The ratio of cytotoxicity:cytostaticity is generally higher for the platinums, with LC_{50} values outside of the acceptable *in vitro* range ($\leq 100\ \mu M$). In comparison, Os compounds **Os-1**, **Os-3** and **Os-5** and Ir compounds **Ir-9** and **Ir-10** all achieve cytotoxic activity at $<10\ \mu M$.

Such dual cytostatic/cytotoxic activity has been demonstrated for organometallic ruthenium anticancer compounds.[33] This dual activity is often first obtained through cell cycle arrest and subsequent activation of pro-apoptotic signals.[34, 35] For example, the treatment of prostate cancer cells with dihydroartemisinin (DHA), results in cell cycle arrest, induced by disrupting the interaction of specificity protein 1 (Sp1) and the CDK4 promoter. This dissociation of the Sp1-CDK4 complex goes on to promote caspase activation and subsequent cell death.[36] By exhibiting both cytostatic and cytotoxic activity in this sequential manner, it is possible for a single agent to both control tumour size and allow tumour shrinkage, perhaps reducing the need for combination therapy.

3.3.2 Structure activity relationships

It is possible to propose optimum chemical structures within this selection of organometallic compounds by using the activity values presented in Table 3.1 and the selectivity patterns in both the NCI-60 and the Sanger cell screens. For example the structures of Os compounds **Os-1** ($[Os(\eta^6\text{-bip})(NMe_2\text{-azpy})I]^+$) and **Os-3** ($[Os(\eta^6\text{-}p\text{-cym})(NMe_2\text{-azpy})I]^+$) are identical except for the additional phenyl substituent on the arene ligand for **Os-1**. Given their similarity in patterns of selectivity in both screens, this suggests that the additional phenyl group does not play a key role in the MOA, it more likely increases uptake for **Os-1**, resulting in a more potent compound. Indeed, this was also shown for Ir where **Ir-6** ($[Ir(\eta^5\text{-Cp}^{xbiph})(phen)Cl]^+$) > **Ir-7** ($[Ir(\eta^5\text{- Cp}^{xph})(phen)Cl]^+$), and has been previously linked to cellular uptake.[18, 37]

Table 3.1 and Figure 3.2 show that when the NMe_2 group on the azopyridine ligand is exchanged for an OH, the activity is retained, shown between **Os-1** and **Os-5** ($[Os(\eta^6\text{-bip})(OH\text{-azpy})I]^+$). However, if the NMe_2 group is exchanged for a F, now at the para position (Figure 1.3) activity is lost, as shown between **Os-1** and **Os-4** ($[Os(\eta^6\text{-bip})(F\text{-azpy})I]^+$)). Figure 3.3 and 3.6 also shows a significance difference in the pattern of selectivity between **Os-1**, **Os-4** and **Os-5**, as a result of exchanging the NMe_2. This change in selectivity is most significant in renal cell lines, which show low sensitivity to all compounds, including CDDP and OXA, apart from **Os-4** and **Os-5**. This loss in activity and change in cancer cell selectivity is either due to the exchange of the electron donating amine for the strongly electron withdrawing halide, or to the change in position on the azopyridine ligand.

Changing either the charge or the electron density around a compound can have a significant effect on cellular targeting. For example, a positively charged compound could feasibly target the mitochondria, as a negatively charged organelle. Negatively charged DNA could also be a more favourable target to positively charged compounds. A recent study reported the difference in activity between neutral compound **Ir-9** ($[Ir(\eta^5\text{-}$

Cp^{xbiph})(ppy)Cl]) and a charged analogue, $[Ir(\eta^5\text{-}Cp^{xbiph})(ppy)py]^+$, which substitutes the Cl ligand for a pyridine.[38] The charged complex proved to have higher potency compared to **Ir-9**, linked to the slow hydrolysis of the Ir-py bond, compared to the rapid hydrolysis of the Ir-Cl bond for **Ir-9**, which affected downstream mechanisms of action.

Collectively, these data show that the activity and selectivity of these compounds can be tailored.

3.3.3 Cancer cell selectivity

The clustering of cell lines and compounds in the NCI-60 cell line screen (Figure 3.3) provides specific information regarding the cancer cell selectivity. The least sensitive cancer subtype was renal, including cell lines CAK-I, ACHN and UO-31. This panel showed low sensitivity to all compounds, apart from **Os-4** and **Os-5**.

Renal cell chemoresistance is a common occurrence; these lines often have a high abundance of multi-drug resistant (MDR1) protein expression, related to the levels of P-glycoprotein (Pgp).[39, 40] This increased expression means that drug efflux is a major problem in the treatment of these cancers.[41] As **Os-4** and **Os-5** have increased activity in these cell lines it could be proposed that the F and OH substituents on the azopyridine ligand are better able to circumvent Pgp efflux. However, NCI-ADR-RES, which is an adriamycin-resistant ovarian cell line, also has a large abundance of Pgp and MDR1 expression and Figure 3.3 shows that this cell line is insensitive to all compounds, including **Os-4** and **Os-5**. Therefore the increased activity of these two compounds in renal cell lines may be mechanistically based, and not due to uptake mechanisms.

Common to all of the organometallic compounds in the NCI-60 were the high sensitivities of breast cell line MDA-MB-468 and colorectal cell line COLO205 (Figure 3.3). COLO205 colorectal cells have reduced levels of glutathione-S-transferase P1 (GSTP1), an enzyme which detoxifies drugs by conjugating them to glutathione (GSH) often limiting the efficacy of anticancer agents.[42] Without this enzyme, there may be less conjugation and inactivation by GSH, which could make cells more sensitive to anticancer compounds. Interestingly, HCT-15 which is also a colorectal cell line, showed poor sensitivity to all of the Os and Ir compounds, thus highlighting a good level of selectivity for these compounds, even within cancer subtypes.

The breast cell line, MDA-MB-468 showed a consistently high sensitivity in the NCI-60 (between 17 nM and 1.8 μM). This cell line has a glucose 6-phosphate dehydrogenase (G6PD) A phenotype, meaning it lacks the proper functioning of this enzyme in the pentose phosphate pathway.[43] G6PD is the rate-limiting enzyme in this pathway; its deficiency blocks the conversion of glucose-6-phosphate to 6-phosphoglucono-δ-lactone and in the process prevents the conversion of NADPH from NADP$^+$, a required step in GSH synthesis.[44] This suggests that a GSH deficiency may play an important role in potentiating the activity, something previously demonstrated when A2780 cells were co-incubated with low levels of the GSH inhibitor, L-buthionine sulfoxamine (Table 1.3). Multiple studies have shown that this deficiency prevents the cells from mediating oxidative stress, and often results in apoptosis and necrosis of cells in patients.[45]

3.3.4 Correlations to drug fingerprints

Each of the compounds was run through the COMPARE algorithm, and the top 100 "hits" were studied for correlations to known drug compounds in the NCI databases, using the GI_{50} fingerprints. In addition, using the Sanger database, compounds with similar pharmacogenomic profiles were studied.

The COMPARE analysis showed that these compounds do not correlate to one singular class of anti-cancer agents, instead correlating to a number of classes. A group was classified if $n > 2$ compounds correlated within it. Compounds appear to correlate primarily to DNA and protein-targetting drugs in the database, although it is not possible to deduce that this is therefore their primary MOA. This could be because the databases used for this analysis do not have an equal number of compounds from each MOA class i.e. there may be more DNA interacting agents in the database than there are redox mediators, which would skew the results. Instead, only qualitative conclusions can be drawn.

Compounds **Os-4**, **Ir-9** and **Ir-10** each correlated to only 3 known drugs, suggesting they are novel with respect to the NCI database.[46] **Os-1** - **Os-3** and **Ir-6** - **Ir-8** and **Ir-11** not only correlated to the same class of anti-cancer agents, but to the same drugs within each class. Although **Os-5** showed novel selectivity in Figure 3.3 with respect to the other organometallic compounds, it is not novel with respect to the NCI database, correlating to twenty known anti-cancer agents. However, the correlation classes for **Os-5** were distinct from the others, with a notable increase in alkylating agents.

3.3.4.1 Protein synthesis inhibitors

The loss in control of protein synthesis can often promote tumour growth, with common upregulation of translation initiation factors like eIF4A to allow increased cell division.[47, 48] There is often thought to be good selectivity with this sort of MOA, as elongation factors can often control specific protein translation.[49] For example eIF4F controls translation of pro-survival components like MCL-1. In addition, cancer cells often have inherent deficiencies in the protein synthesis machinery; for example ovarian, thyroid, pancreatic and colorectal cancer cell lines all have mutations in 12S and 16S rRNA, both of which are required for protein synthesis.[50, 51] It is evident that blocking protein synthesis would have global downstream effects and has gained significant interest in the area of cancer research, where blood cancers seem to be the most susceptible to inhibitors of protein synthesis.[47]

Correlations to a large number of protein synthesis inhibitors included phyllanthoside, aurantimycin B, undulatone and bouvardin, which inhibit translation by a variety of different mechanisms.[52, 53] The defective ribosomes found in ovarian cancer cell lines, could correlate to the high sensitivity of A2780 cells to these compounds, as shown in Table 1.1.[54] Mechanisms for translational inhibition could involve direct protein targeting, or occur through DNA interactions. Protein synthesis inhibition is closely linked to interactions with DNA, particularly as DNA targeting can only occur when unwound from nucleosomes, which occurs during replication and protein synthesis. Indeed, the binding of platinum-based drugs to the DNA has been shown to hinder both transcription and translation.[55]

3.3.4.2 DNA targetting

The most well known DNA-targetting chemotherapeutics are the platinum metallodrugs, cisplatin, carboplatin and oxaliplatin. The development of resistance to these standard agents has brought to light new anticancer agents, with higher specificity for DNA targeting. For example, targetting telomeric DNA is a new approach, specifically designed to cause genomic instability inside cancer cells.[56] Ruthenium compounds have also shown selectivity in DNA attack, specifically targetting the DNA of chromatin.[57] However, this direct-targetting of DNA has its limitations, irrespective of how selective they are, most agents cause significant adverse side effects and increasing the metastatic properties of tumours in clinical studies.[58]

This is where Os compounds **Os-1** - **Os-5** show promise, as they do not hydrolyse, and do not directly bind to DNA, yet according to the COMPARE results they are still able to damage DNA.[59] In contrast, chlorido Ir(III) cyclopentadienyl compounds can interact with DNA, binding both directly via Ir coordination to DNA bases (N7 in guanine) and via intercalation of extended (phenylated) cyclopentadienyl ligands.[18] Compound **Ir-6** was shown to bind to nucleobases in pSP73KB plasmid DNA, blocking RNA/DNA synthesis.[18]

However, given that both Os and Ir compounds correlated to the same DNA interacting agents, it could be proposed that DNA-binding by the Ir compounds is not the primary MOA. Correlated DNA-interacting agents include drugs like daunorubucin, olivomycin and chromomycin, all DNA binding antibiotics.[60, 61] Interestingly, anthracylines like daunorubicin have been shown to induce oxidative stress, and to damage DNA through generation of reactive oxygen species (ROS) generation.[62] As a result, cell lines with redox deficiencies, like MDA-MB-468 show particular sensitivity to this drug, as do compounds **Os-1** - **Ir-11**, but not the platinums.[63]

Os-1, **Os-3** and **Ir-10** compounds also showed similar pharmacogenomic profiles to DNA damaging agents and to topoisomerase inhibitors. The activity of compounds **Os-1** and **Os-3** were both affected when genes within *R184* regions were amplified in breast and NSCLC cell lines. Drug compounds SN-38 and bleomycin were also affected by this amplification with effect sizes of 1.1 and 0.91, respectively (Table 3.4).

Bleomycin is used as an anticancer antibiotic in the treatment of a variety of cancers, namely testicular, cervical, lymphoma and cancers of the head and neck.[64, 65] Bleomycin causes both single- and double-DNA strand breaks in cancer cells, although the exact mechanism continues to be studied.[66, 67] Reports have shown that it can directly bind to DNA and cause breaks and that it can chelate with metals and molecular oxygen to create reactive oxygen species (ROS) and damage DNA.[68]

Topoisomerase enzymes are required for the unwinding of supercoiled DNA and the cutting and religation of DNA during replication and protein synthesis.[69] As the active metabolite of irinotecan, SN-38 is a topoisomerase I (TOP1) inhibitor.[27] TOP1 relaxes supercoiled DNA during replication and transcription, and generates and ligates cleaved single strands. Inhibitors of TOP1 prevent the ligation of cleaved strands, maintaining DNA breaks and activating cell death mechanisms in cancer cells.

COMPARE analysis also reported correlations of **Os-1** and **Os-3** to topoisomerase inhibitors, although not specifically to SN-38. Instead they included drugs like doxorubicin and etoposide, topoisomerase II (TOP2) poisons.[53] TOP2 poisons specifically target the TOPO-DNA complex, preventing re-ligation of double strand DNA and resulting in lethal breaks.

Through *HGF*, **Os-3** also had a similar pharmacogenomic profile to AZD7762 (effect size 2.1), which targets the CHK1/2 proteins in the DNA damage response pathway.[30] This correlation was made through the *HGF* gene, which infers resistance in NSCLC and large intestine cancers for both compounds. Inhibiting check point proteins like CHK1 and 2, mean that cancer cells cannot repair DNA damage and maintain genomic stability.

Inhibitors like AZD7762 are generally used in combination with DNA-damaging agents, like gemcitabine, to potentiate their activity.[70]

Interestingly, in both the NCI and the Sanger database, **Ir-10** was highlighted as novel with respect to other drug compounds. In the Sanger screen, it was the only drug to have a sensitivity association with mutations in the *KIT* gene, primarily found in NSCLC. *KIT*, encodes C-KIT, an important cytokine receptor commonly associated with blood and bone cancers. Once the receptor is activated it controls signalling for cell survival, proliferate and differentiation. *KIT* mutations have been associated with an increased sensitivity to imatinib and has been proposed as an important biomarker in imatinib treatment.[71] The sensitivity of cell lines to **Ir-10** also increased in response to *KIT* mutations. Functional C-KIT often infers chemoresistance by augmenting the expression of DNA repair genes. Its mutated form may therefore render cells more sensitive to DNA damage.[72] It is possible therefore to propose that **Ir-10** has some involvement in DNA damage.

3.3.4.3 Mitosis inhibitors

The most well known anticancer agent which inhibits mitosis is taxol, disrupting microtubule polymerisation.[73, 74] Unfortunately anti-mitotic agents are often associated with poor patient response, and are often used in combination with DNA-targetting agents, hitting multiple areas of the cell cycle in dividing cancer cells.[75] Interestingly, recent research has taken a different approach to inhibiting mitosis, by targeting kinase enzymes like CDK1 to prevent cells from entering into mitosis, resulting in cell death. However, these compounds still have poor clinical efficacy.[76]

From the COMPARE algorithm, compounds correlated to anti-mitotic agents include taxol, vinblastine sulfate and vincristine sulfate.[77, 78] Recent experimental work in the Sadler group has measured disruption of microtubule polymerisation by several of the Os compounds used in this work (Fu, Y., Sanchez, C., unpublished work). As is evident in Table 3.5, **Os-4** retains activity in primary ovarian cancer cell lines with and without

CDDP resistance, however, in cell lines pretreated with both CDDP and taxol, the activity of **Os-4** dropped drastically. This could suggest that cells have developed resistance mechanisms to taxol, and that **Os-4** may have involvement in the inhibition of mitosis.

3.3.4.4 Apoptosis activators

One of the cancer hallmarks is the ability for cells to evade apoptotic signals, this is sometimes achieved due to high levels of BCL-2 protein which prevent pro-apoptotic proteins from diffusing through pores in the mitochondria.[79] In efforts to disrupt the over expression of pro-survival elements like BCL-2, BCL-X and MCL-1 and to sensitise cells to apoptosis, small molecules like ABT-263, were developed to mimic proteins able to bind to BCL-2, allowing the release of pro-apoptotic proteins.[79, 80]

Obatoclax, is an example of a BCL-targeting agent, able to bind with high affinity to BCL-2, BCL-X and MCL-1.[81] Obatoclax shows a dependence of activity related to *HGF* mutations (effect size 1.5), and like **Os-3**, is less active in cell lines with this mutation. This could suggest that **Os-3** has some direct pro-apoptotic effects.

3.3.4.5 Redox mediation

Cancer cells are naturally oxidatively stressed, this is often coupled to the function of mitochondria which are the biggest source of reactive oxygen species (ROS) inside cells.[82] Anticancer agents may therefore indirectly produce ROS by targeting the mitochondria.[82] Given that cancer cells are already oxidatively-stressed, and have deficiencies in their detoxification systems, drugs able to increase ROS may show a strong selectivity towards cancer cells over normal cells.

COMPARE analysis returned correlations to redox mediators like asiaticoside, which induces an oxidative stress response in cancer cells as a result of collagen formation and angiogenesis.[83] In addition, previous reports have shown that the activity of **Os-1**, **Os-3**, **Os-5**, **Ir-8**, **Ir-9** and **Ir-10** increased dramatically when cells were co-incubated with agents targeting the detoxification/antioxidant response in A2780 cells.[7, 59, 84] For example, when cells were co-incubated with L-BSO, an inhibitor of GSH production, the activity off **Ir-8** - **Ir-10** increased by 6.3-, 6.4- and 5.0-fold, respectively.[7]

The production of ROS has a global effect on the cells, with mitochondrial ROS having a cyclic effect on the dysfunction of the mitochondria.[82] DNA and proteins are notable targets of ROS, it is therefore possible that the DNA damage proposed by COMPARE and the Sanger screen is a result of ROS production, as measured experimentally for these organometallic compounds.[85, 86]

3.4 Summary and Conclusions

Cancer screens like those used in this chapter can provide a wealth of information, not just on activity/selectivity towards cancer cells, but also to explore MOA and molecular targets. Collectively both the NCI-60 and the Sanger Institute screens suggest multiple MOAs for Os compounds **Os-1** - **Os-5** and Ir compounds **Ir-6** - **Ir-11**. It is possible that these targets are either hit simultaneously, or more likely that there are primary, secondary and tertiary phases to the compounds MOA. Cell lines with redox deficiencies seem to be more sensitive to these compounds, therefore it is highly possible for redox mediation, resulting in reactive oxygen species (ROS) production to be the cause of the proposed DNA and protein disruption.

In general, cancer cells are more oxidatively-stressed compared to normal cells, and redox mediation by metal-based compounds is a well-documented mechanism.[87] Any targeting of DNA by this indirect method may provide a much more selective treatment, given non-cancerous cells have functional mitochondrial and adequate detoxification systems, which could recover the cell from drug-induced ROS production.

This chapter has shown the wealth of information that can be extracted from screening results, particularly when correlating those findings with other sources. However, *in vitro* cultured cells often undergo adaptive mutations, which can effect compound activity. Therefore these screens provide more of a preliminary set of results, highlighting areas of focus for researchers. In addition, the pharmacogenomics conclusions drawn from the Sanger Institute screening hold little significance due to the low *n* values for cell lines with cancer gene mutations. Therefore these findings need to be supported with further *in vitro* investigations.

The results obtained in this chapter, have allowed the identification of two lead compounds **Os-3** and **Ir-10**, and has suggested multiple areas in which their MOAs may lie. Given the broadness of these MOA predictions, Chapter 4 assess how cells response to both lead compounds on a whole transcriptome level.

References

[1] NCI (2013) Developmental Therapeutics Program (DTP). *Online Source. www.dtp.nci.nih.gov/index.html*.

[2] Holbeck S, Collins JM, Doroshow JH (2010) Analysis of Food and Drug Administration-Approved Anti-cancer Agents in the NCI60 Panel of Human Tumor Cell Lines. *Molecular Cancer Therapeutics* 9:1451–1460.

[3] Shoemaker RH (2006) The NCI60 human tumour cell line anticancer drug screen. *Nature Reviews Cancer* 6:813–23.

[4] Paull KD, et al. (1989) Display and analysis of patterns of differential activity of drugs against human tumor cell lines: development of mean graph and COMPARE algorithm. *Journal of The National Cancer Institute* 81:1088–1092.

[5] Zaharevitz DW, Holbeck SL, Bowerman C, Svetlik PA (2002) COMPARE: a web accessible tool for investigating mechanisms of cell growth inhibition. *Journal of Molecular Graphics Modelling* 20:297–303.

[6] Chan J, Khan SN, Harvey I, Merrick W, Pelletier J (2004) Eukaryotic protein synthesis inhibitors identified by comparison of cytotoxicity profiles. *RNA* 10:528–543.

[7] Hearn JM, et al. (2013) Organometallic Iridium(III) Anticancer Complexes with New Mechanisms of Action: NCI-60 Screening, Mitochondrial Targeting, and Apoptosis. *ACS Chemical Biology* 8:1335–1343.

[8] Das SG, et al. (2011) Structure-activity relationship and molecular mechanisms of ethyl 2-amino-6-(3,5-dimethoxyphenyl)-4-(2-ethoxy-2-oxoethyl)-4H-chromene-3-carboxylate (CXL017) and its analogues. *Journal of Medicinal Chemistry* 54:5937–5948.

[9] Yang W, et al. (2013) Genomics of Drug Sensitivity in Cancer (GDSC): A resource for therapeutic biomarker discovery in cancer cells. *Nucleic Acids Research* 41:D955–961.

[10] Forbes SA, et al. (2011) COSMIC: mining complete cancer genomes in the Catalogue of Somatic Mutations in Cancer. *Nucleic Acids Research* 39:D945–D950.

[11] Forbes SA, et al. (2010) COSMIC (the Catalogue of Somatic Mutations in Cancer): a resource to investigate acquired mutations in human cancer. *Nucleic Acids Research* 38:D652–D657.

[12] Sensen CW, Soh J (2009) in *Advanced Imaging in Biology and Medicine: Technology, Software Environments, Applications* pp 289–300.

[13] Ye K, Schulz MH, Long Q, Apweiler R, Ning Z (2009) Pindel: A pattern growth approach to detect break points of large deletions and medium sized insertions from paired-end short reads. *Bioinformatics* 25:2865–2871.

[14] Lawrence MS, et al. (2013) Mutational heterogeneity in cancer and the search for new cancer-associated genes. *Nature* 499:214–8.

[15] Tamborero D, Gonzalez-Perez A, Lopez-Bigas N (2013) OncodriveCLUST: Exploiting the positional clustering of somatic mutations to identify cancer genes. *Bioinformatics* 29:2238–2244.

[16] Fu Y, et al. (2011) Structure-activity relationships for organometallic osmium arene phenylazopyridine complexes with potent anticancer activity. *Dalton Transactions* 40:10553–10562.

[17] Shnyder SD, et al. (2011) Anti-colorectal cancer activity of an organometallic osmium arene azopyridine complex. *Medical Chemistry Communications* 2:666–668.

[18] Liu Z, et al. (2011) Organometallic half-sandwich iridium anticancer complexes. *Journal of Medicinal Chemistry* 54:3011–3026.

[19] Langdon SP, et al. (1988) Characterization and properties of nine human ovarian adenocarcinoma cell lines. *Cancer research* 48:6166–6172.

[20] Shur I, Ben-Avraham D, Benayahu D (2004) Alternatively spliced isoforms of a novel stromal RNA regulating factor. *Gene* 334:113–121.

[21] Doye V, Hurt E (1997) From nucleoporins to nuclear pore complexes. *Current Opinion in Cell Biology* 9:401–411.

[22] Minárik P, Tomásková N, Kollárová M, Antalík M (2002) Malate dehydrogenases–structure and function. *General Physiology and Biophysics* 21:257–265.

[23] Maulik G, et al. (2002) Role of the hepatocyte growth factor receptor, c-Met, in oncogenesis and potential for therapeutic inhibition. *Cytokine and Growth Factor Reviews* 13:41–59.

[24] Yano S, et al. (2011) Hepatocyte Growth Factor Expression in EGFR Mutant Lung Cancer with Intrinsic and Acquired Resistance to Tyrosine Kinase Inhibitors in a Japanese Cohort. *Journal of Thoracic Oncology* 6:2011–2017.

[25] Yarden Y, et al. (1987) Human proto-oncogene c-kit: a new cell surface receptor tyrosine kinase for an unidentified ligand. *The EMBO Journal* 6:3341–3351.

[26] Hecht SM (2000) Bleomycin: New perspectives on the mechanism of action. *Journal of Natural Products* 63:158–168.

[27] Mullangi R, Ahlawat P, Srinivas NR (2010) Irinotecan and its active metabolite, SN-38: Review of bioanalytical methods and recent update from clinical pharmacology perspectives. *Biomedical Chromatography* 24:104–123.

[28] Knapper S, et al. (2006) A phase 2 trial of the FLT3 inhibitor lestaurtinib (CEP701) as first-line treatment for older patients with acute myeloid leukemia not considered fit for intensive chemotherapy. *Blood* 108:3262–3270.

[29] Hexner EO, et al. (2008) Lestaurtinib (CEP701) is a JAK2 inhibitor that suppresses JAK2/STAT5 signaling and the proliferation of primary erythroid cells from patients with myeloproliferative disorders. *Blood* 111:5663–5671.

[30] Zabludoff SD, et al. (2008) AZD7762, a novel checkpoint kinase inhibitor, drives checkpoint abrogation and potentiates DNA-targeted therapies. *Molecular Cancer Therapeutics* 7:2955–2966.

[31] Konopleva M, et al. (2008) Mechanisms of antileukemic activity of the novel Bcl-2 homology domain-3 mimetic GX15-070 (obatoclax). *Cancer Research* 68:3413–3420.

[32] Barrett SD, et al. (2008) The discovery of the benzhydroxamate MEK inhibitors CI-1040 and PD 0325901. *Bioorganic and Medicinal Chemistry Letters* 18:6501–6504.

[33] Gaiddon C, et al. (2005) Ruthenium (II)-derived organometallic compounds induce cytostatic and cytotoxic effects on mammalian cancer cell lines through p53-dependent and p53-independent mechanisms. *The Journal of Pharmacology and Experimental Therapeutics* 315:1403–1411.

[34] Chen H, Sun B, Pan S, Jiang H, Sun X (2009) Dihydroartemisinin inhibits growth of pancreatic cancer cells in vitro and in vivo. *Anti-Cancer Drugs* 20:131–140.

[35] Wang SJ, et al. (2010) Dihydroartemisinin inactivates NF-kappaB and potentiates the anti-tumor effect of gemcitabine on pancreatic cancer both in vitro and in vivo. *Cancer letters* 293:99–108.

[36] Willoughby JA, et al. (2009) Artemisinin blocks prostate cancer growth and cell cycle progression by disrupting Sp1 interactions with the cyclin-dependent kinase-4 (CDK4) promoter and inhibiting CDK4 gene expression. *The Journal Of Biological Chemistry* 284:2203–2213.

[37] Mendoza-Ferri MG, et al. (2008) Influence of the spacer length on the in vitro anticancer activity of dinuclear ruthenium arene compounds. *Organometallics* 27:2405–2407.

[38] Liu Z, et al. (2014) The Potent Oxidant Anticancer Activity of Organoiridium Catalysts. *Angewandte Chemie (International ed. in English)* 53:3941–3946.

[39] Türk D, et al. (2009) Identification of compounds selectively killing multidrug-resistant cancer cells. *Cancer Research* 69:8293–8301.

[40] Bellamy WT (1996) P-glycoproteins and multidrug resistance. *Annual Review of Pharmacology and Toxicology* 36:161–183.

[41] Huo H, Magro PG, Pietsch EC, Patel BB, Scotto KW (2010) Histone methyltransferase MLL1 regulates MDR1 transcription and chemoresistance. *Cancer Research* 70:8726–8735.

[42] Mueller J, et al. (2012) Thiazolide-induced apoptosis in colorectal cancer cells is mediated via the Jun kinaseBim axis and reveals glutathione-S-transferase P1 as Achilles heel. *Oncogene* 31:4095–4106.

[43] Wang YP, et al. (2014) Regulation of G6PD acetylation by SIRT2 and KAT9 modulates NADPH homeostasis and cell survival during oxidative stress. *The EMBO Journal* 33:1304–1320.

[44] Frank JE (2005) Diagnosis and management of G6PD deficiency. *Am.Fam.Physician* 72:1277–1282.

[45] Efferth T, Fabry U, Glatte P, Osieka R (1995) Increased induction of apoptosis in mononuclear cells of a glucose-6-phosphate dehydrogenase deficient patient. *Journal of Molecular Medicine* 73:47–49.

[46] Lu J, et al. (2012) Antiproliferative mechanisms of action of the flavin dehydrogenase inhibitors diphenylene iodonium and di-2-thienyliodonium based on molecular profiling of the NCI-60 human tumor cell panel. *Biochemical Pharmacology* 83:1195–1207.

[47] Lindqvist LM, et al. (2012) Translation inhibitors induce cell death by multiple mechanisms and Mcl-1 reduction is only a minor contributor. *Cell Death and Disease* 3:e409.

[48] Thornton S, Anand N, Purcell D, Lee J (2003) Not just for housekeeping: Protein initiation and elongation factors in cell growth and tumorigenesis. *Journal of Molecular Medicine* 81:536–548.

[49] Koromilas AE, Lazaris-Karatzas A, Sonenberg N (1992) mRNAs containing extensive secondary structure in their 5' non-coding region translate efficiently in cells overexpressing initiation factor eIF-4E. *The EMBO journal* 11:4153–4158.

[50] Finnil S, Hassinen IE, Majamaa K (2001) Phylogenetic analysis of mitochondrial DNA in patients with an occipital stroke: Evaluation of mutations by using sequence data on the entire coding region. *Mutation Research Genomics* 458:31–39.

[51] van den Bogert C, van Kernebeek G, de Leij L, Kroon AM (1986) Inhibition of mitochondrial protein synthesis leads to proliferation arrest in the G1-phase of the cell cycle. *Cancer letters* 32:41–51.

[52] Chan J, Khan S, Harvey I, Merrick W, Pelletier J (2004) Eukaryotic protein synthesis inhibitors identified by comparison of cytotoxicity profiles. *RNA* 10:528–543.

[53] Zalacaín M, Zaera E, Vázquez D, Jiménez A (1982) The mode of action of the antitumor drug bouvardin, an inhibitor of protein synthesis in eukaryotic cells. *FEBS letters* 148:95–97.

[54] Carew JS, Huang P (2002) Mitochondrial defects in cancer. *Molecular cancer* 1:9.

[55] Ahmad S (2010) Platinum-DNA interactions and subsequent cellular processes controlling sensitivity to anticancer platinum complexes. *Chemistry and Biodiversity* 7:543–566.

[56] Maji B, Bhattacharya S (2014) Advances in the molecular design of potential anticancer agents via targeting of human telomeric DNA. *Chemical communications* 50:6422–6438.

[57] Adhireksan Z, et al. (2014) Ligand substitutions between ruthenium-cymene compounds can control protein versus DNA targeting and anticancer activity. *Nature Communications* 5:3462.

[58] Gurova K (2009) New hopes from old drugs: revisiting DNA-binding small molecules as anticancer agents. *Future oncology* 5:1685–1704.

[59] Fu Y, et al. (2010) Organometallic osmium arene complexes with potent cancer cell cytotoxicity. *Journal of Medicinal Chemistry* 53:8192–8196.

[60] Van Dyke MW, Dervan PB (1983) Chromomycin, Mithramycin, and Olivomycin Binding-Sites on Heterogeneous Deoxyribonucleic-Acid - Footprinting with (Methidiumpropyl-Edta)Iron(Ii). *Biochemistry* 22:2373–2377.

[61] Purewal M, Liehr JG (1993) Covalent modification of DNA by daunorubicin. *Cancer Chemotherapy and Pharmacology* 33:239–244.

[62] Müller I, Niethammer D, Bruchelt G (1998) Anthracycline-derived chemotherapeutics in apoptosis and free radical cytotoxicity (Review). *International Journal of Molecular Medicine* 1:491–494.

[63] Fico A, et al. (2004) Glucose-6-phosphate dehydrogenase plays a crucial role in protection from redox-stress-induced apoptosis. *Cell Death and Differentiation* 11:823–831.

[64] Amrein PC, Colecchi CH, Finkelstein DM, Fabian RL (1997) Adjuvant Chemotherapy in Advanced Head and Neck Cancer. *The Oncologist* 2:135–141.

[65] Friedman MA (1978) A review of the bleomycin experience in the United States. *Recent Results in Cancer Research* 63:152–168.

[66] Takeshita M, Grollman AP, Ohtsubo E, Ohtsubo H (1978) Interaction of bleomycin with DNA. *Proceedings of the National Academy of Sciences of the United States of America* 75:5983–5987.

[67] Chen J, Ghorai MK, Kenney G, Stubbe J (2008) Mechanistic studies on bleomycin-mediated DNA damage: Multiple binding modes can result in double-stranded DNA cleavage. *Nucleic Acids Research* 36:3781–3790.

[68] Burger RM, Projan SJ, Horwitz SB, Peisach J (1986) The DNA cleavage mechanism of iron-bleomycin. Kinetic resolution of strand scission from base propenal release. *The Journal of Biological Chemistry* 261:15955–15959.

[69] Wang JC (2002) Cellular roles of DNA topoisomerases: a molecular perspective. *Nature Reviews Molecular cell biology* 3:430–440.

[70] Sausville E, et al. (2014) Phase I dose-escalation study of AZD7762, a checkpoint kinase inhibitor, in combination with gemcitabine in US patients with advanced solid tumors. *Cancer Chemotherapy and Pharmacology* 73:539–49.

[71] Hodi FS, et al. (2013) Imatinib for melanomas harboring mutationally activated or amplified KIT arising on mucosal, acral, and chronically sun-damaged skin. *Journal of Clinical Oncology* 31:3182–90.

[72] Wichmann C, et al. (2014) Activating c-KIT mutations confer oncogenic cooperativity and rescue RUNX1/ETO-induced DNA damage and apoptosis in human primary CD34+ hematopoietic progenitors. *Leukemia* In print.

[73] Schiff PB, Fant J, Horwitz SB (1979) Promotion of microtubule assembly in vitro by taxol. *Nature* 277:665–667.

[74] Jordan MA, Toso RJ, Thrower D, Wilson L (1993) Mechanism of mitotic block and inhibition of cell proliferation by taxol at low concentrations. *Proceedings of the National Academy of Sciences of the United States of America* 90:9552–9556.

[75] Chan KS, Koh CG, Li HY (2012) Mitosis-targeted anti-cancer therapies: where they stand. *Cell Death and Disease* 3:e411.

[76] Shapiro GI (2006) Cyclin-dependent kinase pathways as targets for cancer treatment. *Journal of Clinical Oncology* 24:1770–1783.

[77] Rai SS, Wolff J (1996) Localization of the vinblastine-binding site on beta-tubulin. *The Journal of Biological Chemistry* 271:14707–14711.

[78] Tsutsui T, Suzuki N, Maizumi H, Barrett JC (1986) Vincristine sulfate-induced cell transformation, mitotic inhibition and aneuploidy in cultured Syrian hamster embryo cells. *Carcinogenesis* 7:131–135.

[79] Bodur C, Basaga H (2012) Bcl-2 Inhibitors: Emerging Drugs in Cancer Therapy. *Current Medicinal Chemistry* 19:1804–1820.

[80] Vogler M, Dinsdale D, Dyer MJS, Cohen GM (2009) Bcl-2 inhibitors: small molecules with a big impact on cancer therapy. *Cell Death and Differentiation* 16:360–367.

[81] Rahmani M, et al. (2012) Inhibition of Bcl-2 antiapoptotic members by obatoclax potently enhances sorafenib-induced apoptosis in human myeloid leukemia cells through a Bim-dependent process. *Blood* 119:6089–6098.

[82] Henchcliffe C, Beal MF (2008) Mitochondrial biology and oxidative stress in Parkinson disease pathogenesis. *Nature Clinical Practice. Neurology* 4:600–609.

[83] Pittella F, Dutra RC, Junior DD, Lopes MTP, Barbosa NR (2009) Antioxidant and cytotoxic activities of Centella asiatica (L) Urb. *International Journal of Molecular Sciences* 10:3713–3721.

[84] Romero-Canelón I, Salassa L, Sadler PJ (2013) The contrasting activity of iodido versus chlorido ruthenium and osmium arene azo- and imino-pyridine anticancer complexes: control of cell selectivity, cross-resistance, p53 dependence, and apoptosis pathway. *Journal of Medicinal Chemistry* 56:1291–300.

[85] Barzilai A, Yamamoto KI (2004) DNA damage responses to oxidative stress. *DNA Repair* 3:1109–1115.

[86] Klaunig JE, Kamendulis LM, Hocevar BA (2010) Oxidative stress and oxidative damage in carcinogenesis. *Toxicologic Pathology* 38:96–109.

[87] Jungwirth U, et al. (2011) Anticancer activity of metal complexes: involvement of redox processes. *Antioxidants and Redox Signaling* 15:1085–1127.

Chapter 4. Transcriptomics

4.1 Introduction

This chapter investigates the transcriptome profiles in A2780 human ovarian cancer cells exposed to compound **Os-3** ([Os(η^6-p-cym)(NMe$_2$-azpy)I]PF$_6$) and **Ir-10** ([Ir(η^5-Cp^{xph})(NMe$_2$-azpy)Cl]PF$_6$) at their GI$_{50}$ concentration (Table 1.1) over 48 h time series using RNA sequencing (RNAseq). These two compounds were selected based on the results presented in Chapter 3, where both were highlight active, both had azopyridine chelated ligands, yet both had different screening patterns. The A2780 ovarian cancer cell line was chosen as a highly invasive form of serous ovarian cancer, and one which is commonly used for *in vitro* cell work.

The transcriptome refers to the set of transcripts (mRNA sequences) in a cell, which reflect the gene expression profiles. This gene expression will capture how A2780 cells responds during exposure to **Os-3** and **Ir-10** treatment. Transcriptomics, principally, allows us to determine the abundance of these transcripts in the cell.

The past decade saw the development of next generation sequencing (NGS), where RNA sequencing (RNAseq) is used to study transcriptomics.[1] RNAseq provides superior sensitivity and resolution compared to DNA microarrays.[2–4] Studying cancer cells using sequencing has it's difficulties, primarily contending with copy number variations (CNV) which can cause over expressed mRNA transcripts to swamp the reads of those less abundant. To tackle this problem, sequencing must be performed with high coverage, ideally between 25 - 30 million reads per sample. The experiments presented here measured 30 million, paired-end reads per sample in efforts to avoid missing important, lowly-expressed genes.

In depth pathway analysis aims to pull out specific response profiles in A2780 cells exposed to both compounds, and gain insights into compound MOAs.

4.1.1 Experimental overview

Shown in Figure 4.2 is the experimental work flow, where library preparation and sequencing were performed at The Wellcome Trust Centre for Human Genetics in the Oxford Genomics Centre.

4.1.1.1 RNA extraction

In two separate experiments, A2780 cells were seeded and incubated for 24 h, after this time they were either exposed to a vehicle control solution or to a solution of **Os-3** at 0.15 μM (Experiment I) and **Ir-10** at 0.40 μM (Experiment II). Cells were collected at 4, 12, 24 and 48 h after addition of either solution. In addition, six 0 h time points were collected during Experiment I. After exposure, collected cell pellets were lysed in RNase-denaturing buffer using detergents to solubilise proteins and salts like guanidine isothiocyanate to disrupt RNase enzymes. Whole cell RNA was collected and purified using Qiagen RNAeasy extraction kits, which allows for a series of spin column procedures to collect and wash the RNA. Lysed solutions were passed through a DNA-eliminating column, where DNA and RNA have different, pH dependent, binding to the column matrix. Column-bound RNA was then washed with ethanol and multiple buffer solutions designed to remove residual proteins and salts. RNA was collected in RNase-free water and stored at -80 C before QC checking.

4.1.1.2 Quality control checks

NanoDrop. The NanoDrop 1000 allows direct measurement of RNA sample solutions, using surface tension to hold the sample in place. A light was passed through the solution, between 220-750 nm, and a spectrum measured. The absorbance was recorded at 230, 260 and 280 nm to test for RNA purity, and to estimate RNA concentration using the Beer Lambert equation. A_{230} measures for protein peptide bonds and organic contaminants,

A_{280} measures amino acids and phenolic contaminants and A_{260} measures the RNA. Generally, researchers check the A_{260}/A_{230} and A_{260}/A_{280} ratios to determine purity, aiming for the first ratio to be > 1.8 and the second to be > 2.0. All samples from both Experiments I and II passed this QC check.

Bioanalyzer. The Agilent 21000 Bioanalyzer was a secondary means of measuring the RNA integrity by assessing the rRNA. It is more accurate than the NanoDrop, analysing RNA samples dispensed onto chips using capillary electrophoresis, based on the same principles as gel electrophoresis. Each chip holds sixteen wells for sample, gel and reference ladder, with micro-channels interconnecting the wells. During manufacturing, the micro-channels are filled with a sieving polymer and a fluorescent dye, which intercalates with RNA. 16-pin electrodes were inserted into each well and a charge applied. The charged biomolecules were separated by size, as smaller fragments migrate faster through the gels than larger fragments. The laser-induced fluorescent dye molecules intercalate with the RNA samples and with the RNA ladder, passing the detector at speeds relative to the size of the fragment. Data were produced as both gel-like bands and as peaks in an electropherogram. Figure 4.1 shows the gels for the six 0 h control samples extracted from A2780 cells (1 - 6).

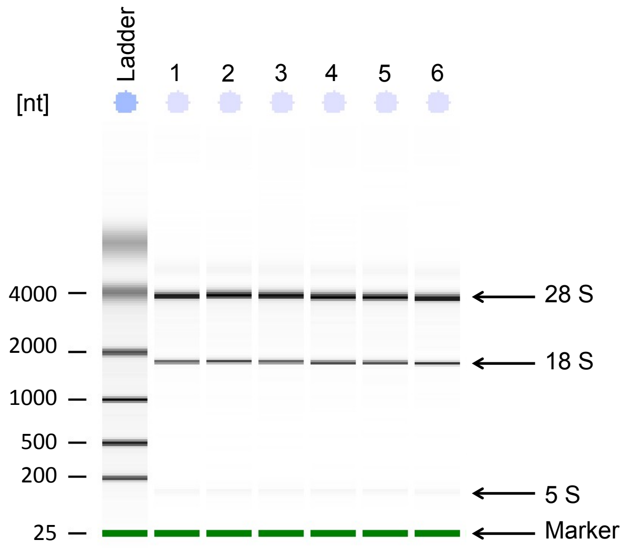

Figure 4.1: **Gel showing the RNA integrity for 0 h control samples 1 - 6.** The bands for each sample correspond to subunits of rRNA present in each sample, and is a measure of RNA degradation as a result of the extraction process. A high quality sample will have two main bands, one for 18S and one for the 28S subunit, and sometimes for the 5.8S subunit. The intensity of these peaks, and any other bands around these, are used to calculate the RNA integrity number (RIN). For the 6 samples in this Figure, all samples had RIN of 10/10.

The total eukaryotic RNA has two ribosomal bands/peaks, corresponding to the 18S and 28S subunits. A pure sample produces a flat baseline between the peaks in the corresponding electropherogram. Agilent have developed an algorithm which assess all features of the electrophoreogram and produces an RNA integrity number (RIN) between 1 and 10, where 1 is a highly degraded RNA sample and 10 is an intact sample. Generally a sample should have an RIN > 7 to be suitable for sequencing. All RNA samples from Experiment I and II had RIN ≥ 9.50.

Qubit assay. The Qubit 2.0 Fluorometer was used to quantify the concentration of RNA in each sample. Again, a fuorescent dye was used, emitting selected signals when bound to the RNA. This signal was referenced against a calibration curve, and the concentration of RNA in each sample determined. Samples were transferred to the Oxford Genomics Centre for sequence analysis.

The schematic in Figure 4.2 summarises the experimental work flow performed at Warwick, and introduces the work performed by the Oxford Genomics Centre.

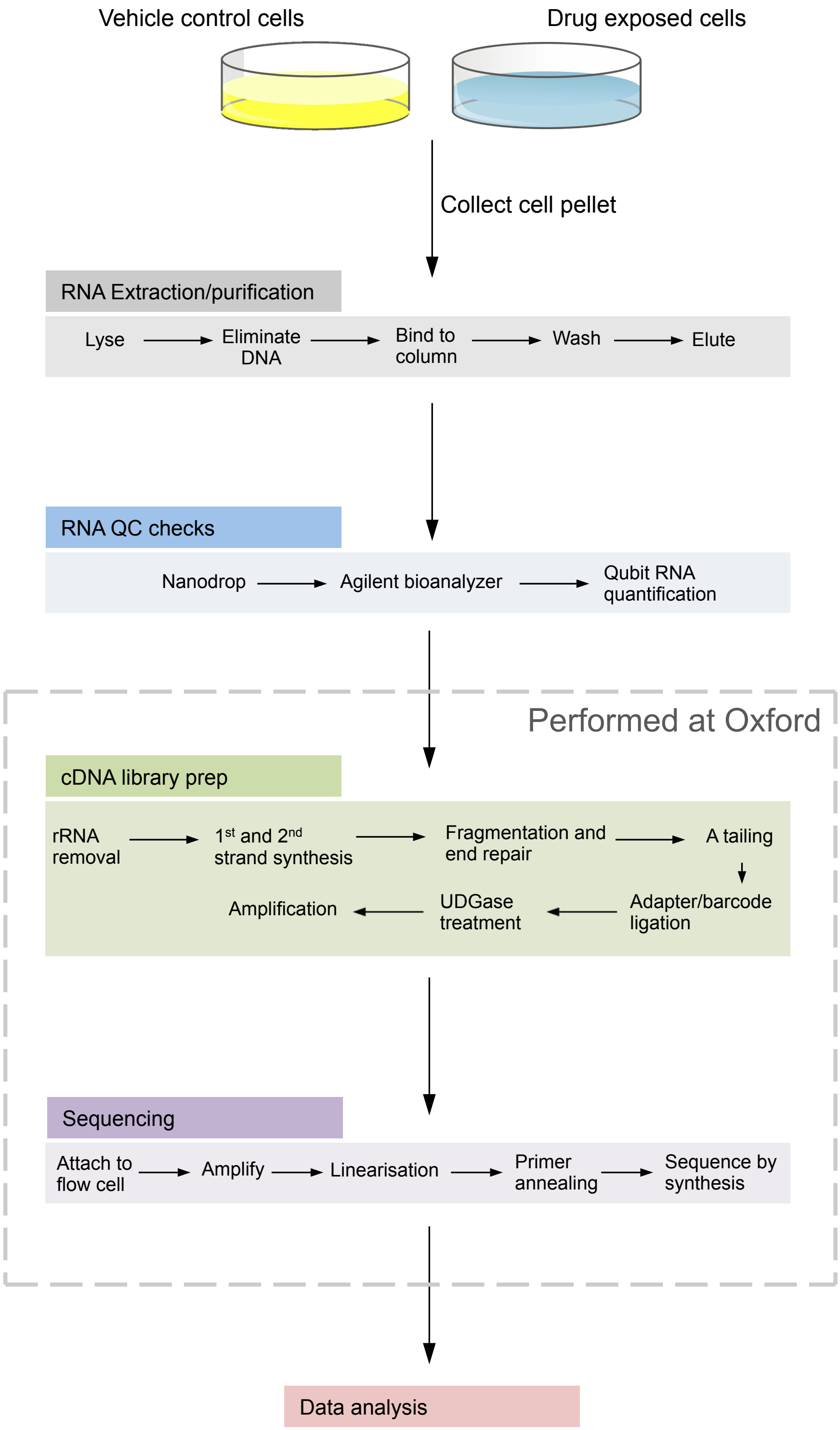

Figure 4.2: **RNAseq experimental workflow showing RNA extraction, purification, library preparation and sequencing.** Boxed area highlights the work performed by Oxford Genomics Centre, with everything outside of this box performed at the University of Warwick.

4.1.1.3 Library preparation[5]

It is cDNA, not RNA, which is used during the sequencing procedure as DNA is more stable than RNA, and samples are amplified by polymerase chain reaction (PCR) which requires DNA. RNA can be used but RNA-dependent RNA polymerase are known to incorporate errors. The complementary DNA strands were reverse transcribed from the mRNA provided in each sample. cDNA strands were fragmented to allow more accurate sequencing, and the end tails paired to allow adapter ligation. These adapters (in red in Figure 4.3) were required for paired-end sequencing to maintain forward and backward strand polarity (Figure 4.3).

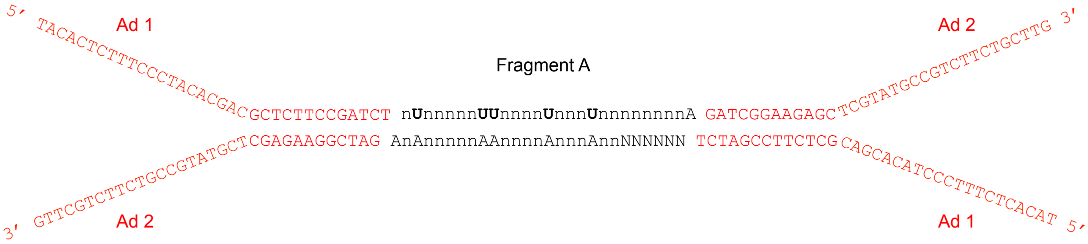

Figure 4.3: **cDNA fragment A, together with its complementary strand are ligated with Y-shaped adapter sequences 1 (Ad 1) and 2 (Ad 2) at the 3' and 5' ends.** Ad 1 and Ad 2 allow sequencing to be performed along the forward and reverse strands, which is the fundamental benefit of using paired-end sequencing, maintaining strand polarity. Figure 4.4 details the use of these adapters. *Image adapted from Parkhomchuk (2009) Nuc. Acid Res. 37(18):e123*[5]

Uridine bases were removed to prevent second strand amplification during PCR. Primers were attached to each adapter during PCR, as well as an index sequence to allow barcoding and multiplexing during sequencing. Multiplexing allowed multiple samples to be sequenced in a single lane on the sequencer, saving time and money.

4.1.1.4 Sequencing[6]

Once strands were bound and amplified into clusters on the sequencer flow cell the process of sequencing could begin. In these experiments each sample was subject to 30 million paired-end reads (60 million in total) across five sequencing lanes, using multiplexing. Figure 4.4 outlines the process of nucleotide reading for each strand.

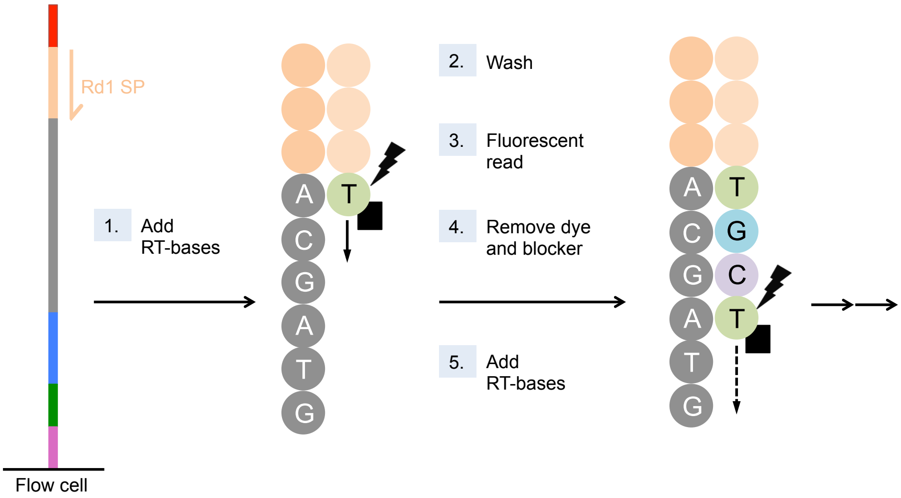

Figure 4.4: **Process of nucleotide reading during strand sequencing.** Shown in grey on the far left is a cDNA sequence (grey); attached either side are the forward and reverse primers (beige and blue), adapters 1 and 2 (pink and red) and sample-specific barcode (green). Figure 9.2.2.3 will detail sequencing of the reverse strand, utilising the barcode, reverse primer and adapter 2. The first step exposes the strand to a pool of labelled nucleotides, which complementarily bind using the read 1 sequence primer (Rd1SP), and are read using lasers to excite fluorescent tags attached to each nucleotide. Once the signal is read, and the nucleotide identified, the tags and blocker groups are removed, and the process repeated until 50 base pairs have been read. *Image adapted from an Illumina multiplexing worksheet*[6]

In step 1, fluorescently labelled nucleotides with blocker groups, bind complementarily to the strand clusters, starting from the read 1 sequence primer (Rd1 SP). The blocker groups prevent more than one nucleotide from binding before the fluorescence can be read. Each nucleotide was read as a different colour, excited by two lasers (step 2 and 3).

After reading, the blocker group was chemically removed and the process repeated with a second nucleotide pool (step 4 and 5). For the work conducted in this chapter, 50 nucleotides were to be read at each end of each strand. The process of paired-end sequencing is shown in Figure 4.5.

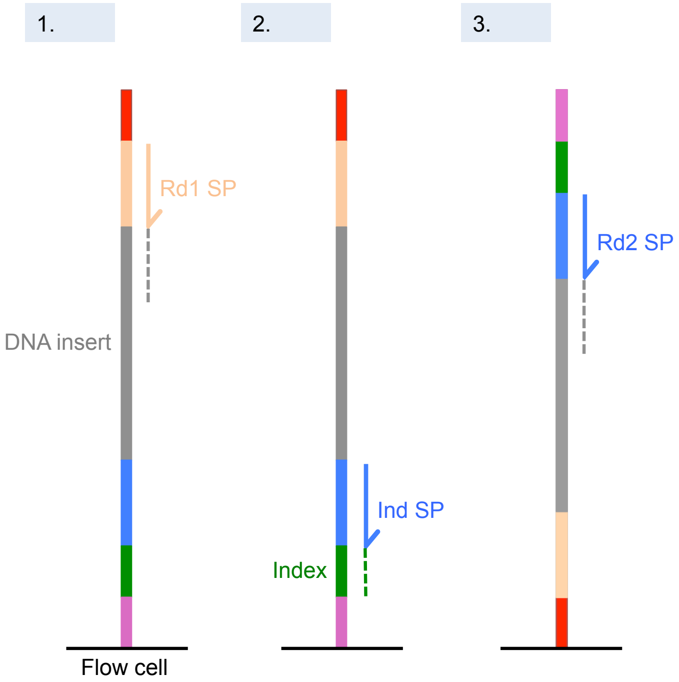

Figure 4.5: **Process of paired-end sequencing.** Step 1 shows the forward strand being sequenced, as shown in Figure 4.4, with step 2 showing the sequencing of the barcode index (green) required for multiplexed samples. This barcode is read using the index primer (IndSP), and assigns a particularly set of sequencing reads to a specific sample. Between steps 2 and 3, a complementary reverse strand is constructed so that in step 3 the reverse strand is sequenced, now using the reverse strand read 2 primer (Rd2 SP). Once 50 nucleotides have been read from both the forward and reverse strands, the information is combined using sequencing analysis software. *Image adapted from an Illumina multiplexing worksheet*[6]

In step 1, nucleotides were read down the forward strand starting from the Rd1 SP. In step 2, the barcode index (Ind SP) was read. To read nucleotides for the reverse strand, a complementary strand was synthesised for the entire strand, including adapters, primers and barcodes. From this complementary strand, the reverse nucleotide sequence was determined starting from the read 2 sequence primer (Rd2 SP).

The associated quality score, assigned per nucleotide read is a measure of the accuracy of that read. Although four different colours were used for the detection of each of the four nucleotides, only two lasers were used to excite the fluorescent probes. For example A and C were both read by red lasers and both G and T read by green lasers.

The quality score for each base call was calculated using a phred-like algorithm, which is a four-phase procedure assessing the observed versus the predicted peak locations.[7, 8] The value produced for each base call represents the probability p that that base call is incorrect, usually presented as $-10\log_{10}$p. Therefore, a quality score of 30 for a nucleotide read, means that the probability that the base call is incorrect is 1 in 1000 (accuracy of 99.9%), therefore the higher the quality score the more accurate the read. Generally a quality score > 20 (i.e. 1 in 100) is accepted as an accurate read, therefore this is the cut off value during data analysis.

4.1.2 Data analysis overview

The data analysis is generally the most time consuming and complex stage of any next generation sequencing project. As discussed in Chapter 1, there are numerous tools which can be used to analyse RNAseq data, each offering users different capabilities and statistical methods. The Tuxedo suite, including TopHat, Bowtie and Cufflinks is the most commonly used tool set for this analysis.[9–11] However, packages like DESeq and edgeR generally offer a more accurate data analysis for differential expression, making fewer statistical assumptions and allowing a better incorporation of time series data.[12–17] Figure 4.6 summarises the chosen work flow for the data analysis.

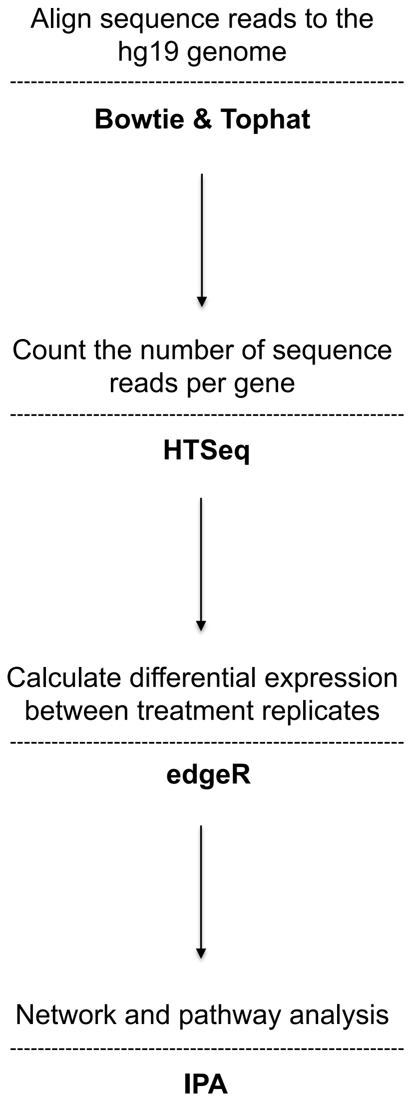

Figure 4.6: **Data analysis work flow chosen to analyse Experiments I and II.** Tophat and Bowtie were used for filtering out poor quality sequence reads and for aligning reads to the human genome. HTSeq was used to count the number of reads associated to each gene in the human genome. And edgeR was used to explore differential gene expression between drug-exposed and control samples.

4.1.2.1 Bowtie and Tophat

Bowtie and Tophat mappings were performed at the Oxford Genomics Centre. Bowtie is a program and was used to align the short DNA sequences, read from the RNA sequencing experiment, to the hg19 human genome.[10] Bowtie is integrated into TopHat, a splice junction mapping tool which uses the Bowtie program to align reads before identifying splice junctions.[11] Tophat analysis produces a so-called BAM file for each sequenced sample. These files describe the chromosomal positions to which each sequence read has mapped, and the number of times this mapping has occurred. These data are paired-end, which also identifies whether partner read mapping is conserved.

4.1.2.2 HTSeq

HTSeq is a Python program used to prepare datasets for downstream analysis in edgeR.[18] The purpose of this program is to construct a list of genes and an associated count for the number of reads mapped to that gene. HTSeq used a hg19 genome annotation file and the chromosomal read positions generated from Tophat to construct a list of genes expressed for each sample in Experiment I and II.

4.1.2.3 edgeR

Although the Tuxedo suite, specifically Cuffdiff, is the most comprehensive software to use for differential expression (DE) analysis, it does not support multifactorial experimental designs and is therefore not optimal for time series DE analysis. A recent review by Rapaport *et al* highlighted several other limitations with Cuffdiff when compared to other sources of DE analysis like edgeR or limmaVoom.[19]

The edgeR package was selected for DEG analysis, a summary of the steps involved is shown in Figure 4.7.[12, 20–23]

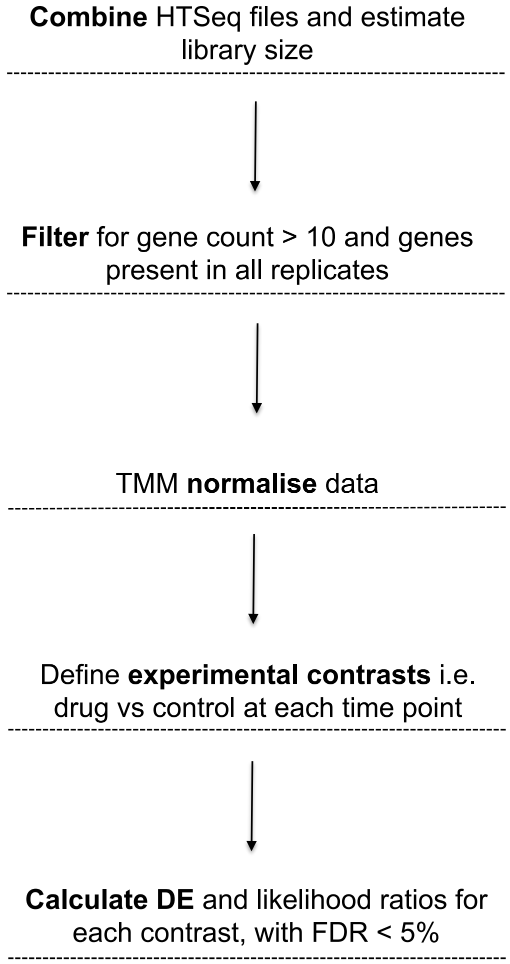

Figure 4.7: **edgeR data analysis work flow.** HTseq was used to count the number of reads per gene, with edgeR filtering out those genes with low counts or which did not provide ¿10 counts in all three triplicate samples. edgeR then normalised the data using trimmed mean of M-values (TMM) which scales each dataset so that genes with large read counts do not swamp those with low. Finally edgeR allows exploration of differential gene expression between treatment and control groups.

edgeR focusses on DE analysis and not on relative expression levels, minimising technical influences and focusing on relative changes between conditions. The normalisation process in edgeR was model-based, estimating scaling factors to account for RNA composition between each pair of samples. These scaling factors were estimated using a trimmed mean of M-values (TMM), and were used to adjust the sample library size.[22] This scaled 'effective library size', was implemented for library size normalisation of each sample.

When performing DE analysis, edgeR fits a negative binomial distribution to the count data and estimates dispersions using the Cox-Reid profile-adjusted likelihood method, which allows for multifactorial experiments by using general linear models (GLMs) together with a given design matrix.[24] This process accounts for all sources of variation in the experiment.

The GLM likelihood ratio test is used to compute a p value for significance testing between genes in each sample, based on a given null hypothesis.[23] The Benjamin-Hochberg method was used to account for multiple testing correction and false discovery rate (FDR) estimation.[25]

edgeR provided a list of differentially expressed genes (DEG) and associated logFC ratios (i.e. the fold change in expression between compound-exposed and control-exposed) and FDR values, for which pathway analysis was performed and biological significance investigated.

4.1.2.4 Ingenuity pathway analysis (IPA).

Functional analysis was performed with IPA (Ingenuity Pathway Analysis, Ingenuity® Systems) using the Information Knowledge Base (IKB).[26] All data contained within the IKB database are sourced from published literature and currently contains information on 16,900 human genes, 968,000 biological/chemical concepts from 2.44 million literature findings. IPA is used to produce functional networks and pathways of interest based on a dataset of DE values. Figure 4.8 summarises each stage used by the IPA network algorithm.

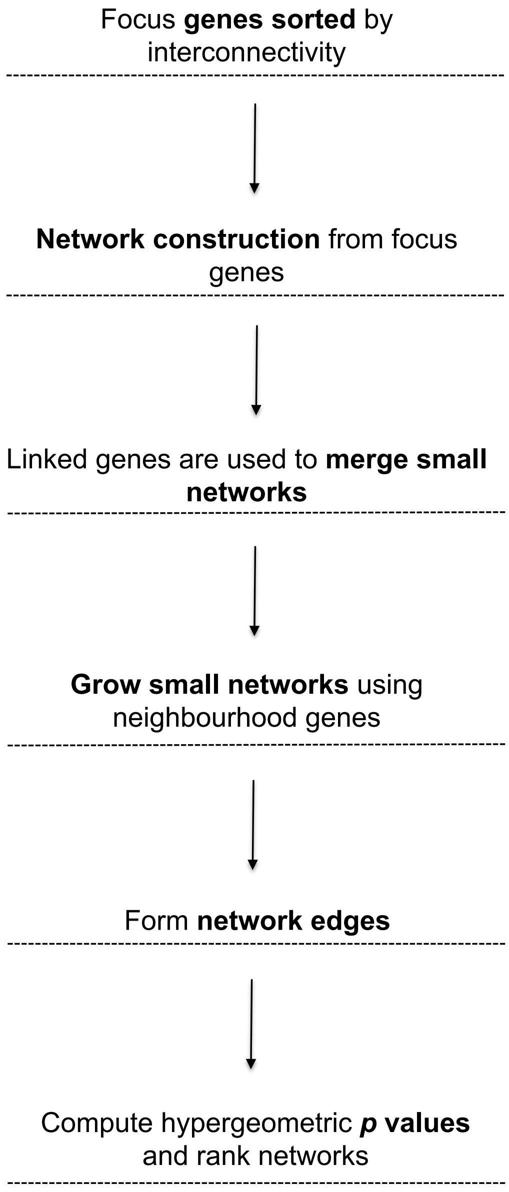

Figure 4.8: **Ingenuity Pathway Analysis (IPA) data analysis work flow.** IPA was used to allocate highly- and lowly-differentially expressed genes into biological pathways to allow interpretation of results. Networks of expression are gradually built up by IPA, by first forming nodes for key genes and then gradually growing networks outwards from these genes. Each pathway formed is associated with a hypergeometric probability for over-representation and identifies the significance of a particular pathways involvement in drug-response with respect to all other pathways in the dataset.

IPA provides ranked information on biological processes, cellular networks, functional networks, upstream regulators and disease profiles. Biological inferences for compound-effects can be made from collating this information.[27]

4.2 Results

This chapter investigates the differential gene expression for ovarian cancer cell line, A2780, when exposed to compound **Os-3** ($[\mathrm{Os}(\eta^6\text{-}p\text{-cym})(\mathrm{NMe_2\text{-}azpy})\mathrm{I}]^+$) for 4, 12, 24 and 48 h at its GI_{50} concentration of 0.15 μM (Experiment I) and to compound **Ir-10** ($[\mathrm{Ir}(\eta^5\text{-Cp}^{xph})(\mathrm{NMe_2\text{-}azpy})\mathrm{Cl}]^+$) for 4, 12, 24 and 48 h at its GI_{50} concentration of 0.40 μM (Experiment II). The experiments were performed independently, however, their results are presented side-by-side. **Os-3** and **Ir-10** were chosen based on screening results presented in Chapter 3, where **Os-3** was active and performed similarly to many of the other compounds, and **Ir-10** was both active and novel.

4.2.1 Sample quality checks

Nanodrop and bioanalyzer data for sample quality checks all passed with A260/230 $\geq$ 1.8, A260/280 $\geq$ 2.0 and RIN $>$ 9.50 (Appendix 9.2 and 9.4).

4.2.2 Sequencing sample statistics

Tables 4.1 and 4.2 summarise the RNAseq statistics for all samples in Experiment I (**Os-3**). Samples were multiplexed across 5 lanes (6 samples per lane), with lane clusters and yields shown in Table 4.1 and the total reads per sample, mapping and quality scores shown in Table 4.2. Samples were paired-end sequenced, which means that 50 base pairs were sequenced from each end of each transcript fragment, bringing the total number of reads per sample to ca. 60 million. The sample statistics for Experiment II are shown in Appendix 9.2.

Table 4.1: Summary statistics for each lane. Showing yields, mapping and quality scores. The % of mapped reads are those which have mapped successfully to the human genome, the few percent that did not map may be mutated reads or may be of poor quality. Only those nucleotide calls with a quality score (Q) ¿ 20 were included for analysis.

Lane*	**Yield (Mb Q20******)**	**% Mapped reads**	**Mean quality score**
1	20,999	98.1	34.4
2	18,291	97.9	35.6
3	19,081	98.5	35.3
4	16,367	98.3	36.5
5	16,860	98.3	36.4

*6 samples per lane. **A quality score of 20

4.2.3 Mapping to the human genome

The % mapped reads shown in Tables 4.1 and 4.2 for Experiment I refers to the number of nucleotide reads in each sequence which were mapped to the hg19 genome successfully. The ca. 2% which were not mapped could be due to several things. This could stem from Tophats inability to tolerate too many sequencing errors, or where a pairing has failed and thus not been mapped. It could also be that cancer progression has re-arranged the genome to the extent that some read pairs will not map. As the % of unmapped reads is so low, it does not affect the analysis. The same tables are shown for Experiment II, in Appendix 9.2.

Table 4.2: Summary statistics for each sample, showing total reads, mapping and quality scores. The total reads refers to the total number of reads measured, however, the total number of paired-end reads is exactly half of this. The % mapped shows the total number of reads which were able to map to the human genome, with the mean quality score signifying whether these mapped reads were of high quality. Any reads with quality scores ¡ 20 were filtered out before reads were mapped.

Sample number	**Sample name**	**Total reads**	**% Mapped reads**	**Mean quality score**
1	0 h control	58,453,334	98.53	36.5
2	0 h control	52,958,428	98.32	36.4
3	0 h control	52,411,032	98.11	36.5
4	0 h control	57,489,392	98.72	36.5
5	0 h control	53,112,138	97.75	36.5
6	0 h control	54,962,488	98.12	36.4
7	4 h control	82,071,522	98.19	34.4
8	4 h control	84,555,686	98.11	34.4
9	4 h control	73,333,434	97.93	34.4
10	4 h **3**	69,130,568	97.87	34.4
11	4 h **3**	59,742,704	97.99	34.5
12	4 h **3**	72,018,526	98.38	34.4
13	12 h control	50,690,134	97.87	36.4
14	12 h control	55,041,730	99.25	36.4
15	12 h control	60,723,390	97.88	36.4
16	12 h **3**	58,813,794	98.12	36.4
17	12 h **3**	57,945,078	98.82	36.4
18	12 h **3**	56,092,354	97.97	36.4
19	24 h control	60,331,926	98.14	35.6
20	24 h control	67,939,036	98.93	35.0
21	24 h control	59,240,982	98.09	35.6
22	24 h **3**	64,300,818	95.65	35.5
23	24 h **3**	61,522,272	98.48	35.6
24	24 h **3**	61,343,334	98.18	35.5
25	48 h control	69,027,526	98.61	35.4
26	48 h control	65,550,492	97.69	35.3
27	48 h control	55,141,160	98.55	35.3
28	48 h **3**	66,793,080	98.39	35.4
29	48 h **3**	66,227,334	99.20	35.3
30	48 h **3**	69,306,494	98.19	35.3

Figure 4.9 shows a heat map of the mean number of reads (from Table 4.2) mapped

to chromosomes 1-22, X and M, for each sample type: 0 h control (inner circle), 4 h control, 4 h **Os-3**-exposed, 12 h control, 12 h **Os-3**-exposed, 24 h control, 24 h **Os-3**-exposed, 48 h control and 48 h **Os-3**-exposed (outer circle). The mean read counts for each sample type are represented as $\log_{10}$FPKM, and thus normalised to chromosome length and sample library size (total reads). The $\log_{10}$FPKM values for mapping to the mitochondrial chromosome (ChrM) were significantly higher than that of the other chromosomes. This is a result of length bias, since ChrM is much shorter than the other chromosomes (ca. 16,600 base pairs). In addition to length bias, the copy number variations in the mitochondria of cancer cell lines may also weight read mapping.[28]

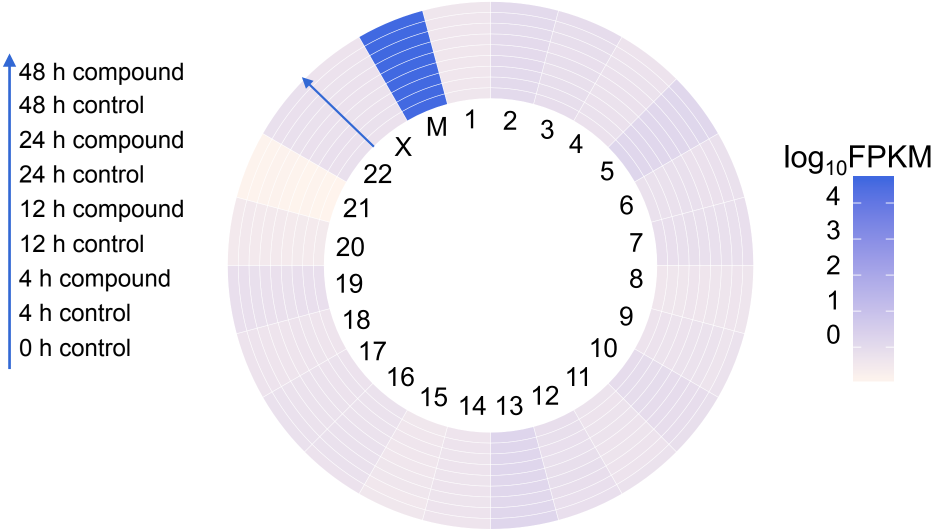

Figure 4.9: **Mapping of reads to individual chromosomes from Experiment I.** Heat map showing chromosomal mapping of sequence reads to the human genome after normalisation to chromosome length and sample library size (FPKM). Chromosomes are described in the centre of the heat map, from 1 - 22, X and M. The key on the left describes the sample order, starting from the inner most circle (0 h control) to the outer most circle (48 h compound-exposed), where each ring is a mean value from each triplicate sample. Darker boxes indicate a large number of reads per length of each chromosome. For all samples, control- and compound-exposed, the mitochondrial chromosome (M) has the largest $\log_{10}$FPKM values, suggesting a significant expression of mitochondrial genes both before and after compound-exposure.

In Figure 4.9, the ChrM $\log_{10}$FPKM values appear to be equal across the sample range, however, Figure 4.10 shows a significant differential mapping between control- (blue) and compound-exposed (green) samples after exposure to **Os-3** and **Ir-10**.

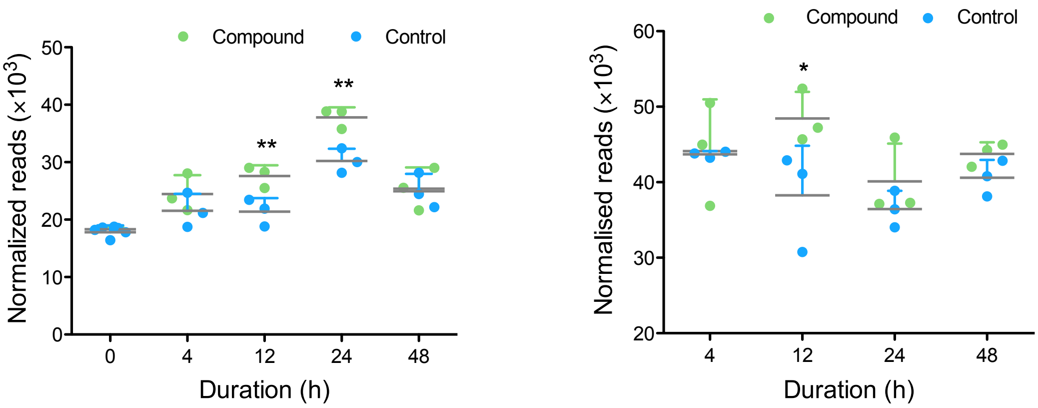

(a)

(b)

Figure 4.10: **Graph showing total number of reads mapped to the ChrM.** Graphs show normalised reads for control- and compound-exposed samples across each time series for **Os-3** (left) and **Ir-10** (right). The reads are normalised to sample library size, with the grey line as the mean across the triplicate values. * indicates $p < 0.10$ and ** indicates $p < 0.05$ after a Welch two sample t-test. In response to **Os-3** there is a significant increase in mitochondrial gene expression after 12 and 24 h. In contrast, the response to **Ir-10** is only significant after 12 h exposure.

The differential mapping after exposure to **Os-3** is particularly evident at 12 and 24 h, where there are significantly more reads mapped in the compound-exposed versus the control samples (p = 0.030 and 0.016, respectively, after a Welch two sample t-test), suggesting that **Os-3** induces a mitochondrial genomic response. Interestingly, **Ir-10** does not induce as significant a mitochondrial response, except at 12 h (p = 0.097).

4.2.4 Mitochondrial mutations

The ChrM encodes 13 polypeptides which constitute the hydrophobic cores of components in the electron transport chain (ETC) and oxidative phosphorylation pathway (OXPHOS). The remaining genes on ChrM code for RNA machinery required for mitochondrial translation.[29] Figure 4.11 is a simplified schematic of the ETC, showing the positions of protein complexes I-V (CI-CV) which orchestrate the transfer of electrons and protons, and the production of ATP.

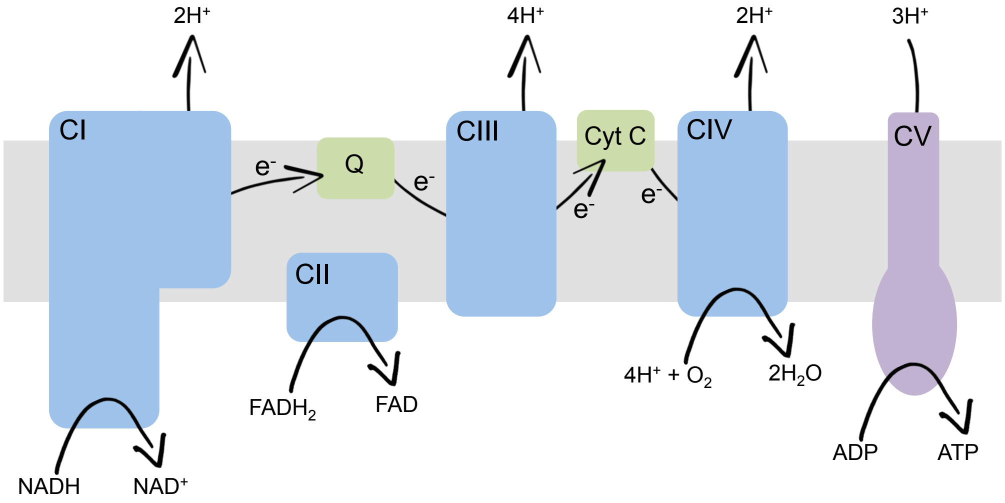

Figure 4.11: **Schematic of the components in the electron transport chain (ETC).** The grey coloured region is the inner mitochondrial membrane, with the blue and purple structures as enzyme complex I (NADH dehydrogenase), II (succinate dehydrogenase), III (coenzyme Q reductase), IV (cytochrome C reductase) and V (ATPase) of the ETC. During oxidative phosphorylation, the last step in aerobic respiration, electrons are transferred from complex I to complex IV utilising NADH, $FADH_2$, co-enzyme Q (Q) and cytochrome C (Cyt C) electron carriers. As these electrons are transferred, protons are pumped across the inner membrane to the outer membrane space by complexes I, III and IV. This creates a proton-motive gradient which is used by complex IV to catalyse the production of ATP from ADP and organic phosphate. A byproduct of this process is water, through reaction of protons with molecular oxygen.

Given the transcriptomic response associated with the mitochondria, and that mutations in mtDNA are well documented in cancer cells, the ChrM sequence reads from Experiment I were compared with those in the hg19 human genome, highlighting multiple nucleotide read discrepancies.[30, 31]

These mutations were found in all 30 samples of Experiment I, with $\geq 99\%$ homology in ca. 1200 2000 counts. Most base substitutions resulted in silent mutations, however, the *MT-ND5* gene, coding for the ND5 membrane-bound subunit of CI, had 3 missense mutations at positions m.13106, m.13677 and m.13887. These mutations translate to peptide substitutions at p.I257V (isoleucine > valine), p.N447S (asparagine> serine) and p.L517P (leucine > proline).

Multiple mutations were identified throughout the mtDNA, although most were silent mutations. However, 3 missense mutations resulting in amino acid substitutions p.I257V, p.N447S and p.L517P were identified in the coding sequence of the *MT-ND5* gene.

The p.I257V (dbSNP variant rs2853501) and p.N447S have been reported in previous work, the former is thought to have no functional effect, however, the p.447 asparagine substitution has been demonstrated in patients with CI deficiencies.[32–34] The p.L517P mutation has been reported in cases of optic neuropathy, however, this report provides an incorrect assignment for the associated *MT-ND5* nucleotide substitution.[35]

The *MT-ND* genes on the ChrM encode helical polypeptides which constitute the membrane bound subunits of NADH dehydrogenase complex I (CI), responsible for maintaining a proton gradient between the matrix and inter-membrane space.[36] *MT-ND5* codes for the 5th subunit in this complex.

Figure 4.12 shows the point mutations in the MT-ND5 amino acid sequence (red), where residues highlighted in blue are transmembrane helices in the subunit. In addition to multiple transmembrane domains, the ND5 subunit of CI has a transverse helix, which stretches across ND4 and ND2 before ending with a final transmembrane helix.[37]

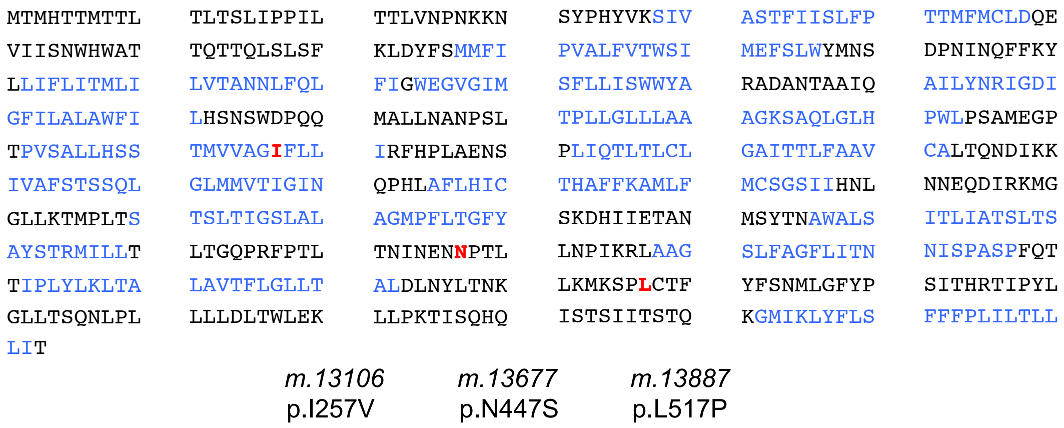

```
MTMHTTMTTL  TLTSLIPPIL  TTLVNPNKKN  SYPHYVKSIV  ASTFIISLFP  TTMFMCLDQE
VIISNWHWAT  TQTTQLSLSF  KLDYFSMMFI  PVALFVTWSI  MEFSLWYMNS  DPNINQFFKY
LLIFLITMLI  LVTANNLFQL  FIGWEGVGIM  SFLLISWWYA  RADANTAAIQ  AILYNRIGDI
GFILALAWFI  LHSNSWDPQQ  MALLNANPSL  TPLLGLLLAA  AGKSAQLGLH  PWLPSAMEGP
TPVSALLHSS  TMVVAGIFLL  IRFHPLAENS  PLIQTLTLCL  GAITTLFAAV  CALTQNDIKK
IVAFSTSSQL  GLMMVTIGIN  QPHLAFLHIC  THAFFKAMLF  MCSGSIIHNL  NNEQDIRKMG
GLLKTMPLTS  TSLTIGSLAL  AGMPFLTGFY  SKDHIIETAN  MSYTNAWALS  ITLIATSLTS
AYSTRMILLT  LTGQPRFPTL  TNINENNPTL  LNPIKRLAAG  SLFAGFLITN  NISPASPFQT
TIPLYLKLTA  LAVTFLGLLT  ALDLNYLTNK  LKMKSPLCTF  YFSNMLGFYP  SITHRTIPYL
GLLTSQNLPL  LLLDLTWLEK  LLPKTISQHQ  ISTSIITSTQ  KGMIKLYFLS  FFFPLILTLL
LIT
```

Figure 4.12: **Amino acid sequence of protein MT-ND5.** The MT-ND5 subunit sits in the inner mitochondrial membrane and is responsible for pumping protons across the membrane. Residues highlighted in blue are part of transmembrane helices, with those in black found outside of the membrane. The mutations identified in A2780 cells were highlighted in red: p.I257V (isoleucine to valine substitution at the 257th residue), p.N447S (asparagine to serine substitution) and p.L517P (leucine to proline substitution). The p.N447S and p.L517P substitutions would have the most significant structural implications.

Only the p.I257V substitution is found in a transmembrane domain, the p.N447S substitution known to cause CI deficiencies is outside of the membrane, and the new p.L517P substitution is found in the transverse helix. The ND5 subunit is responsible for proton pumping from the matrix to the intermembrane space of the mitochondria, therefore mutations in the CI machinery could impact on the metabolic efficiency.

4.2.5 Compound-induced differential expression

Using HTSeq and edgeR, differential gene expression analysis was performed for samples exposed to **Os-3** and **Ir-10**, relative to the negative controls in each experiment. Prior to differential expression (DE) analysis, the samples in each experiment were compared for similarity.

Using multidimensional scaling (MDS) plots, compound- and control-exposed samples across both time series were plotted. These plots are a means of visualising the level of similarity in sample sets, by placing each of them in N-dimensional space, where between-object distances are preserved. Coordinates were assigned to each of the samples in two dimensions, where those plotted closer together share higher similarity (Figures 4.13 and 4.14).

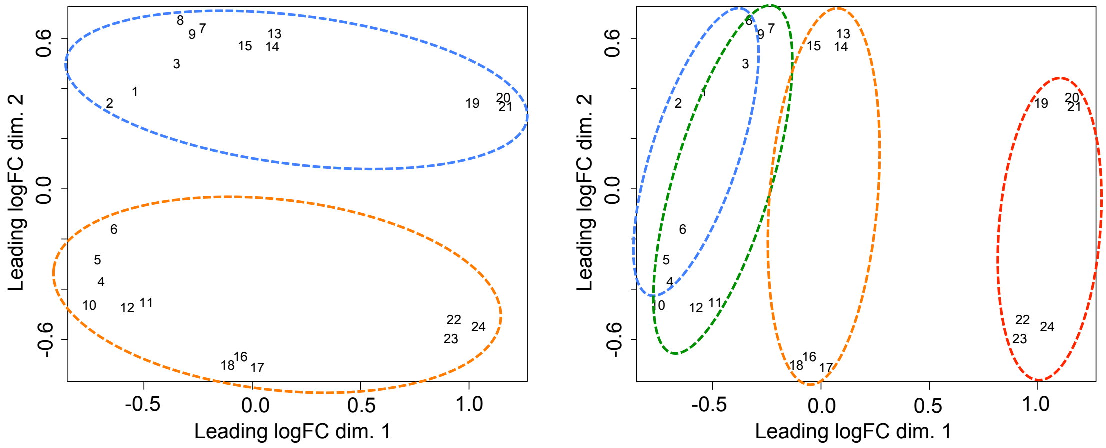

Figure 4.13: **Multidimensional scaling (MDS) plot for Experiment I.** MDS allows the similarity between variables to be assessed by plotting each dataset in space, by euclidean distance. In these plots, samples which are plotted close together share higher similarity. Both plots display the same data, grouping samples 1-24 by similarity where samples 1-3 are 4 h controls, 4-6 are 4 h **Os-3**-exposed, 7-9 12 h control, 10-12 12 h **Os-3**-exposed, 13-15 are 24 h controls, 16-18 are 24 h **Os-3**-exposed, 19-21 are 48 h controls and 22-24 are 48 h **Os-3**-exposed. The plot on the left highlights grouping of samples into control (blue) and **Os-3**-exposed (orange) demonstrating a drug-induced differential response at the gene level. The right-hand plot shows grouping of samples across the time series, with 4 h control and **Os-3**-exposed samples in blue, 12 h in green, 24 h in orange and 48 h in red. This second plot highlights how different the 48 h datasets are, compared to earlier time points.

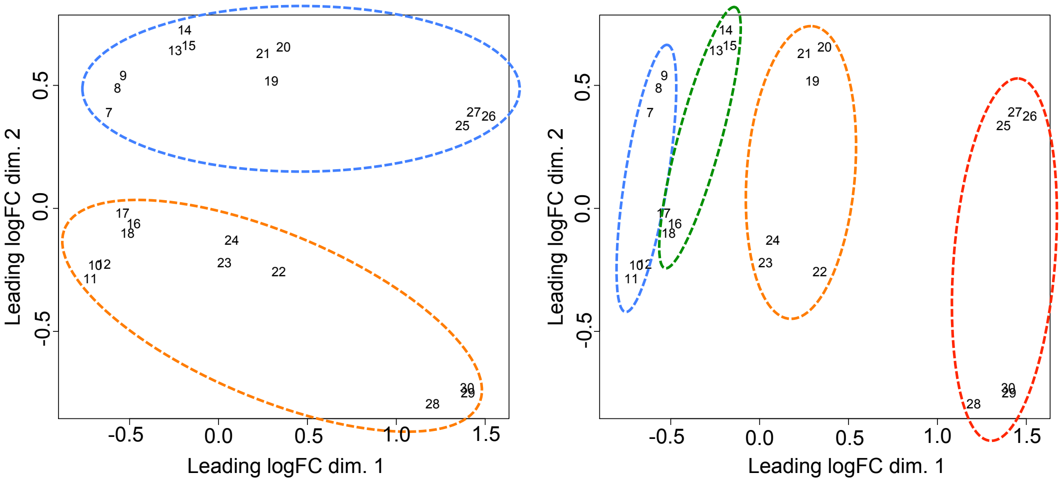

Figure 4.14: **Multidimensional scaling (MDS) plot for Experiment I.** MDS allows the similarity between variables to be assessed by plotting each dataset in space, by euclidean distance. In these plots, samples which are plotted close together share higher similarity. Both plots display the same data, grouping samples 7-30 by similarity where samples 7-9 are 4 h controls, 10-12 are 4 h **Ir-10**-exposed, 12-15 12 h control, 16-18 12 h **Ir-10**-exposed, 19-21 are 24 h controls, 22-24 are 24 h **Ir-10**-exposed, 25-27 are 48 h controls and 28-30 are 48 h **Ir-10**-exposed. The plot on the left highlights grouping of samples into control (blue) and **Ir-10**-exposed (orange) demonstrating a drug-induced differential response at the gene level. The right-hand plot shows grouping of samples across the time series, with 4 h control and **Ir-10**-exposed samples in blue, 12 h in green, 24 h in orange and 48 h in red. This second plot highlights how different the 48 h datasets are, compared to earlier time points.

Both Figures 4.13 and 4.14 show natural separation of the samples into clusters, and show good agreement between the triplicate measurements. The biggest source of variation is by time point, the second by exposure-status i.e. whether they are exposed to a control or to a compound. Therefore the first dimension, allows the separation of the samples across the time series, with 4 h in blue, 12 h in green, 24 h in orange, and 48 h in red. In the second dimension, samples separate into two clusters, one for control samples (blue) and the second for compound-exposed samples (orange). These plots provide clear evidence that the samples exposed for 48 h to both **Os-3** and **Ir-10** are significantly different from those exposed for shorter time periods, both in the control and in the compound-exposed samples.

Using edgeR, the number of differentially expressed genes (DEGs) at each time point was determine. The number of DEG at 4, 24 and 48 h post-exposure to **Os-3** and **Ir-10** are shown in Figure 4.15.

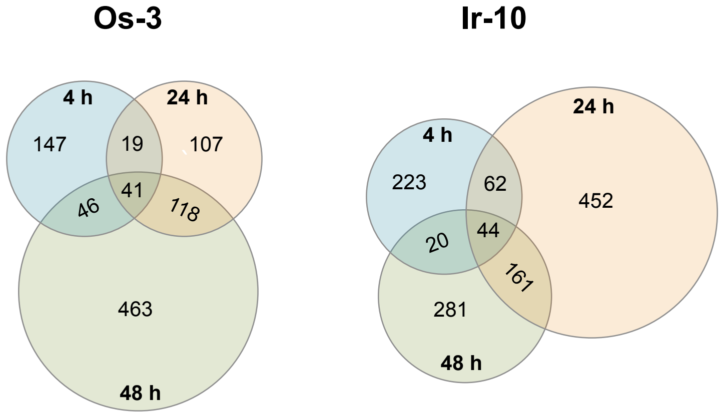

Figure 4.15: **Venn diagrams showing the number of differentially-expressed genes at 4, 24 and 48 h after exposure to Os-3 (left) and Ir-10 (right).** Only those genes with -1.0 < LogFC > 1.0 and FDR < 0.05 were included. The Venn diagrams show that cells exposed to **Os-3** have the largest gene response after 48 h, compared to those exposed to **Ir-10** where the largest response is after only 24 h. Overall there were 668 genes differentially-expressed at these time points in response to **Os-3** and 746 in response to **Ir-10**.

The maximum number of DEGs after exposure to **Os-3** was at the 48 h time point (668), in contrast to 12 h for **Ir-10** (746), highlighting a difference in response for each compound. Overall, there was a higher level of differential expression in cells exposed to **Ir-10**. Figure 4.16 looks at the number of genes which were DE by both **Os-3** and **Ir-10** compared to the number which were specific to each compound.

Figure 4.16 shows some overlap between the compound responses, however, the responses are predominantly specific. Figure 4.17 shows the number of DEG which are up- and down-regulated at each time point in cells exposed to **Os-3** (left) and **Ir-10** (right).

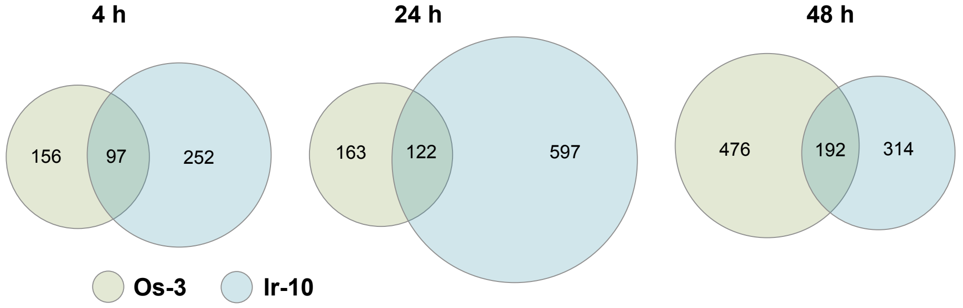

Figure 4.16: **Venn diagrams showing the overlap in differential-expression between Os-3 and Ir-10 at 4, 24 and 48 h.** Only those genes with -1.0 $<$ LogFC $>$ 1.0 and FDR $<$ 0.05 were included. After 4 and 24 h there were more genes differentially expressed in response to **Ir-10** (blue) compared to **Os-3** (green), with $\approx$ 100 genes differentially expressed to both, and the remainder showing compound-specific expression. At 48 h, there were more genes differentially expressed to **Os-3**, with almost 200 genes differentially expressed to both compounds, and the remainder compound-specific.

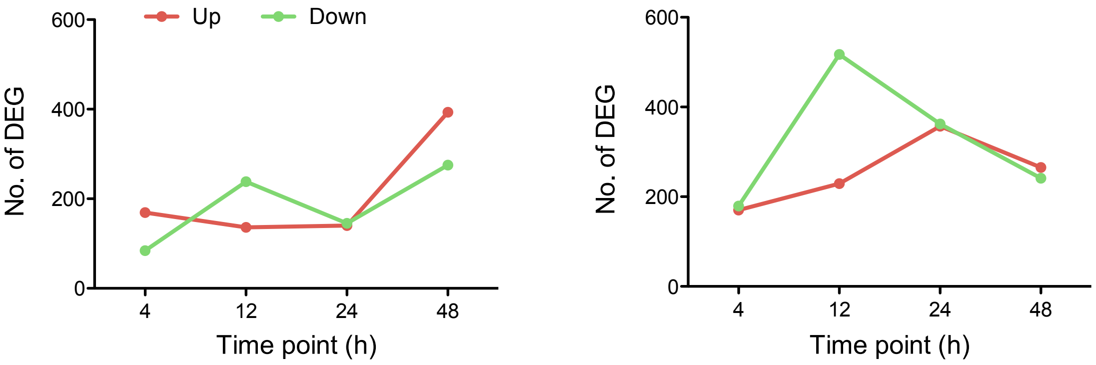

Figure 4.17: **Graphs showing the number of up- (red) and down-regulated (green) genes at each time point.** The results for **Os-3** are shown in the left graph, and for **Ir-10** on the right. Only those genes with -1.0 $<$ LogFC $>$ 1.0 and FDR $<$ 0.05 were included. The graph on the left shows that at 4 and 48 h there are more genes down-regulated (green) then up (red), in contrast to 12 h, where there are more genes up-regulated in response to **Os-3**. In response to **Ir-10** there are significantly more down-regulated genes after 12 h exposure, compared to 4, 24 and 48 h where the number of genes up- and down-regulated was almost equal.

Again, these plots show a different response in cells exposed to **Os-3** and **Ir-10**. The Venn diagrams showed that maximum DE was at 48 h after exposure to **Os-3**; Figure 4.17 shows that at this time point there are slightly more up- (393) than down-regulated (275) genes. Maximum DE to **Ir-10** was achieved after 12 h, where the graph shows significantly more down-regulation (229) than up- (517).

4.2.6 Pathway analysis for Os-3 and Ir-10

Using Ingenuity Pathway Analysis (IPA) software, the DEG with $1.0 < \text{LogFC} > 1.0$ and $\text{FDR} < 0.05$ were assigned to biological pathways. Tables 4.3 and 4.4 show the top five upstream regulators of these pathways, across the time series, for each compound. The tables show the p value as calculated by a hypergeometric test of over representation, and the z-score which describes the extent of activation/inhibition of each pathway.

Table 4.3: The upstream regulators from IPA analysis for the top five most mapped processes for DEGs with -1.0 $<$ LogFC $>$ 1.0 and FDR $<$ 0.05 after exposure to **Os-3**. IPA has identified the pathways with the most differential expression and has then performed a hypergeometric test for over-representation to provide a p-value to identify the most significant results. The z-score is a measure of how much a pathway is up- or down-regulated (activated or inhibited), where -2 $<$ z $>$ 2 is said to be a significant result. There are similar pathways affected by **Os-3** across the time course, including tumour necrosis factor (TNF), transforming growth factor (TGF), interleukin-β1 (IL-β1) and interferon γ (IFNγ), which are all activated.

Time point (h)	**Upstream regulator**	**p-value**	**Activation z-score**	**Predicted activity**
4	UO126	4.41×10^{-14}	-3.709	Inhibited
	TGFβ1	5.90×10^{-14}	2.169	Activated
	TNF	1.65×10^{-13}	3.794	Activated
	LY294002	6.76×10^{-12}	-2.313	Inhibited
	LPS	1.59×10^{-11}	3.867	Activated
12	SB203580	2.12×10^{-10}	-3.542	Inhibited
	IL1β	4.52×10^{-10}	3.742	Activated
	NFKβ	1.20×10^{-09}	3.170	Activated
	TGFβ1	2.05×10^{-09}	1.342	-
	LY294002	2.36×10^{-09}	-2.293	Inhibited
24	TGFβ1	3.56×10^{-11}	1.876	Activated
	TNF	7.97×10^{-10}	4.622	Activated
	Tretinoin	2.41×10^{-09}	1.323	-
	IL1β	6.86×10^{-09}	4.218	Activated
	IFNγ	1.46×10^{-08}	3.404	Activated
48	TNF	1.48×10^{-15}	3.752	Activated
	IL1β	1.12×10^{-14}	3.501	Activated
	LPS	3.79×10^{-14}	4.061	Activated
	TGFβ1	1.01×10^{-10}	1.714	-
	IFNγ	2.38×10^{-10}	2.347	Activated

From Table 4.3, UO126 is a selective MEK kinase inhibitor, found to inhibit AP-1 (activator protein) complex transcription. The AP-1 complex, regulates gene expression due to many different stimuli, including stress response.[38] After 4 h exposure, pathway analysis suggested that the associated downstream effects of the UO126 drug were inhibited (z score -3.709). This suggests that the AP-1 complex was not transcriptionally inhibited by **Os-3**; in fact AP-1 transcription was activated. This is discussed later with elements like *FOS* genes, which code for components of the AP-1 transcription factor complex, together with Jun, which was also up-regulated.

The other upstream regulators at 4 h were transforming growth factor (TGFβ1, z score 2.169), tumour necrosis factor (TNF, z score 3.794), LY294002 (z score -2.313) and lipopolysaccharide (LPS, z score 3.867), which also control up-regulation of genes involved in stress response. For example, LPS activation can initiate an immune response in cancer cells and LY294002 is a PI3K inhibitor, suggesting that **Os-3** does not inhibit PI3K.[39]

The same stress response pathways continued to be activated throughout the rest of the time series, and progress to include the activation of interleukin 1 (IL1β, z score 3.742) and interferon gamma (IFNγ, z score 3.404) pathways at 12 and 24 h, respectively. IL1β is a pro-inflammatory cytokine, essential for both innate and adaptive immune response.[40, 41] IFNγ is a cytokine commonly associated with adaptive chemotherapy response in cancer, and can be both anti- and pro-tumorigenic.[42]

Table 4.4: The upstream regulators for the top five most mapped processes for DEGs with -1.0 < LogFC > 1.0 and FDR < 0.05 after exposure to **Ir-10**. Similar to Table 4.3, IPA has identified pathways of interest, with associated significance *p*- and z-values. The biological pathways responding to **Ir-10** show more variability across the time series then they did for **Os-3**. Tumour necrosis factor (TNF) and transforming growth factor (TGF) were still consistently activated, however there was also involvement from platelet-derived growth factor (PDGF BB).

Time point (h)	Upstream regulator	p-value	Activation z-score	Predicted activity
4	TNF	3.25×10^{-15}	3.676	Activated
	LY294002	2.67×10^{-14}	-2.413	Inhibited
	PDGF BB	2.15×10^{-13}	4.766	Activated
	TGFβ1	2.62×10^{-13}	3.063	Activated
	ERK	1.31×10^{-12}	4.221	Activated
12	TNF	1.48×10^{-14}	3.238	Activated
	UO126	2.19×10^{-11}	-2.470	Inhibited
	LY294002	2.34×10^{-11}	-2.466	Inhibited
	beta-estradiol	3.29×10^{-11}	-0.400	-
	TREM1	6.67×10^{-11}	1.771	Activated
24	TGFβ1	1.30×10^{-24}	2.206	Activated
	TNF	3.94×10^{-22}	6.101	Activated
	LPS	7.13×10^{-22}	7.223	Activated
	PDGF BB	1.33×10^{-21}	5.287	Activated
	beta-estradiol	3.42×10^{-21}	2.230	Activated
48	TNF	4.93×10^{-12}	3.646	Activated
	IL1β	7.74×10^{-09}	3.343	Activated
	LPS	1.87×10^{-09}	2.211	Activated
	ESR1	3.17×10^{-09}	0.282	-
	TGFβ1	3.48×10^{-09}	1.717	Activated

Interestingly, similar pathways were activated in response to **Ir-10**, including TNF, TGFβ1, ILβ1 and LPS. However, platelet-derived growth factor (PDGF) and extracellular signal-related kinase (ERK) were not a pathway activated by **Os-3**, yet showed significant activation by **Ir-10**. Likewise, beta-estradiol and estrogen receptor 1 (ESR1) were pathways only activated/inhibited by **Ir-10**, although the z-scores were not significant.

ERK and PDGF were the most significant pathways involved in the response at 4h (z score 4.221 and 4.766), with PDGF also highly activated at 24 h (z score 5.287). ERKs are widely expressed in the cell, and control a plethora of biological processes, including cell division. PDGF is another widely expressed component, and has involvement in regulating cell division, and angiogenesis.[43, 44]

Assessing upstream regulators makes it difficult to pinpoint the MOA of either compound, although these results show that cells are activating stress response pathways even after short exposure. Probing further down the pathways can provide more insights.

4.2.6.1 Oxidative stress

Some of the most prominently activated pathways in cells exposed to both **Os-3** and **Ir-10** were in response to oxidative stress. For example, genes associated with a vitamin C antioxidant response (p = 1.58 x 10^{-3} at 24 h) and an NRF2 (nuclear factor erythroid-derived 2-like 2) oxidative stress response (p = 3.74 x 10^{-17} at 4 h) were activated in response to **Os-3**. With the **Ir -10** response also showing NRF2 activation after 4 h exposure (p = 8.72 x 10^{-3} at 4 h).[45]

The NRF2 transcription factor (encoded by the *NFE2L2* gene) is involved in an important antioxidant response pathway, binding to the hARE (human antioxidant response element) cis-element to transactive detoxifying/antioxidant genes. AP-1 complexes C-FOS/C-JUN and FRA-1/c-JUN, encoded by *FOS*, *FOSL1* and *JUN* genes, compete with NRF2 for binding to hARE to active antioxidant genes.[46]

Figure 4.18 shows some of the components of the NRF2/AP-1 oxidative response pathway, with transactivation of eight response genes. Upon detection of ROS, NRF2 dissociates from actin and KEAP1, translocates to the nucleus, and interacts with cofactor proteins (e.g MAF) to allow binding to hARE.

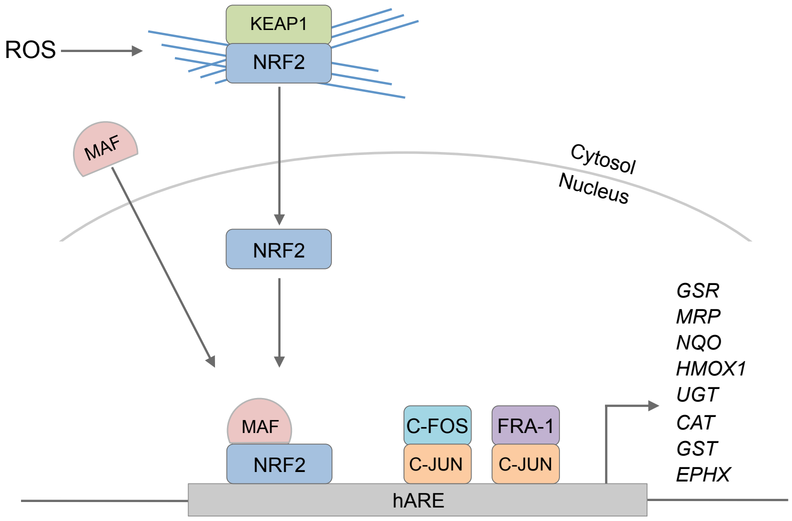

Figure 4.18: **Diagram showing the main components in the NRF-2 and AP-1 transcription factor pathways during oxidative stress response.** Upon detection of oxidative stress, NRF2 dissociates its KEAP1/actin complex and translocates from the cytosol to the nucleus. Using co-factors like MAF, NRF2 binds to the human antioxidant regulatory element (hARE) and transactivates the expression of various antioxidant genes. In addition to this, two AP-1 transcription factor complexes (C-FOS/C-JUN and FRA-1/C-JUN) also bind to the hARE cis-regulatory element and activate different antioxidant genes. All three transcription factors bind competitively to hARE depending on the type of antioxidant response activated.

Figure 4.23 shows that after exposure to **Os-3** NRF2 (*NFE2L2*) and one of its co-factors, MAF (*MAF*), are up-regulated at 4 h and remain so throughout the time series, showing a maximum level of DE at 48 h (LogFC 1.57, FDR 1.17 x 10^{-17} and LogFC 1.18, FDR 2.57 x 10^{-19}, respectively). Interestingly, even though *NFE2L2* is up-regulated throughout the time series in response to **Ir-10**, the MAF co-factor is significantly down-regulated throughout the time series.

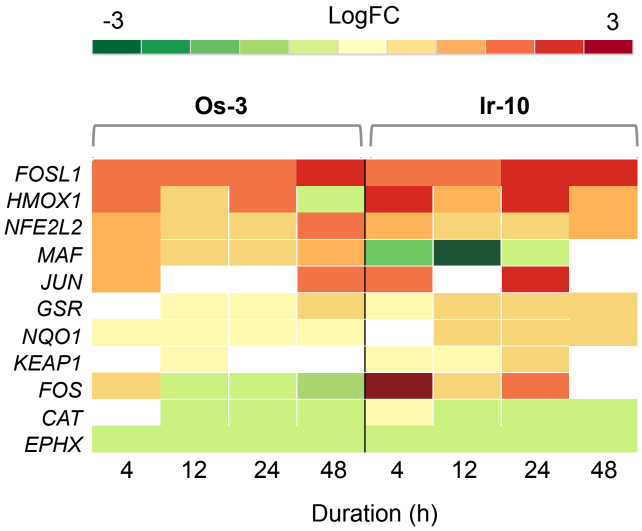

Figure 4.19: **Heat map of DEG in the oxidative stress response pathway across the time series after exposure to Os-3 (left) and Ir-10 (right).** Only DEG with FDR < 0.10 are included, blank values lie outside of this significance threshold. In response to **Os-3**, cells activate the NRF2 (*NFE2L2*) and FRA-1(*FOSL1*)/C-JUN (*JUN*) complexes, with up-regulation of these genes after just 4 hours, and maximum expression after 48 h. In contrast, in response to **Ir-10**, cells activate the FOS (*FOS*)/C-JUN (*JUN*) and FRA-1/C-JUN complex, with a particularly high up-regulation of *FOS* after just 4 h exposure. Although *NFE2L2* is up-regulated in response to **Ir-10**, it's co-factor *MAF* is significantly down-regulated, suggesting less involvement of NRF2 compared to the AP-1 transcription factor complexes.

Of the two AP-1 complexes, only FRA-1 (*FOSL1*) is the most up-regulated throughout the time series, showing significant DE after just 4 h to both **Os-3** and **Ir-10**. The second AP-1 complex, with C-FOS (*FOS*) is up-regulated for **Ir-10**, but down-regulated for **Os-3**. This suggests that this AP-1 complex does not play a role in **Os-3**-induced oxidative stress response, but may have involvement in **Ir-10** response. This could explain the increased DE of transactivation genes by **Ir-10**.

Only a selection of antioxidant genes downstream of the transcriptional activators are up-regulated. Antioxidant genes *CAT* (catalase) and *EPHX* (epoxide hydrolase), are both down-regulated in response to **Os-3** and **Ir-10**. This may suggest that the C-FOS/C-JUN AP-1 complex controls activation of these genes and not NRF2 nor FRA-1/C-JUN.

GSR (glutathione reductase) and *NQO* (NADP(H) quinone oxidoreductase) are both up-regulated by **Os-3** and **Ir-10**, although more so by **Ir-10**. This expression only becomes significant after 12 h exposure, highlighting the delay between transcription/translation of NRF2 and AP-1 and the activation of antioxidant genes. Although these genes are activated after 12 h, they remain expressed at low levels, even after 48 h.

4.2.6.2 Mitochondrial dysfunction

Pathway analysis for **Os-3** exposed samples, also suggested that mitochondrial dysfunction plays a role in compound response (p = 7.78 x 10^{-15} at 4 h). Figure 4.20 shows the DEG (FDR 0.10) of nuclear encoded mitochondrial genes.

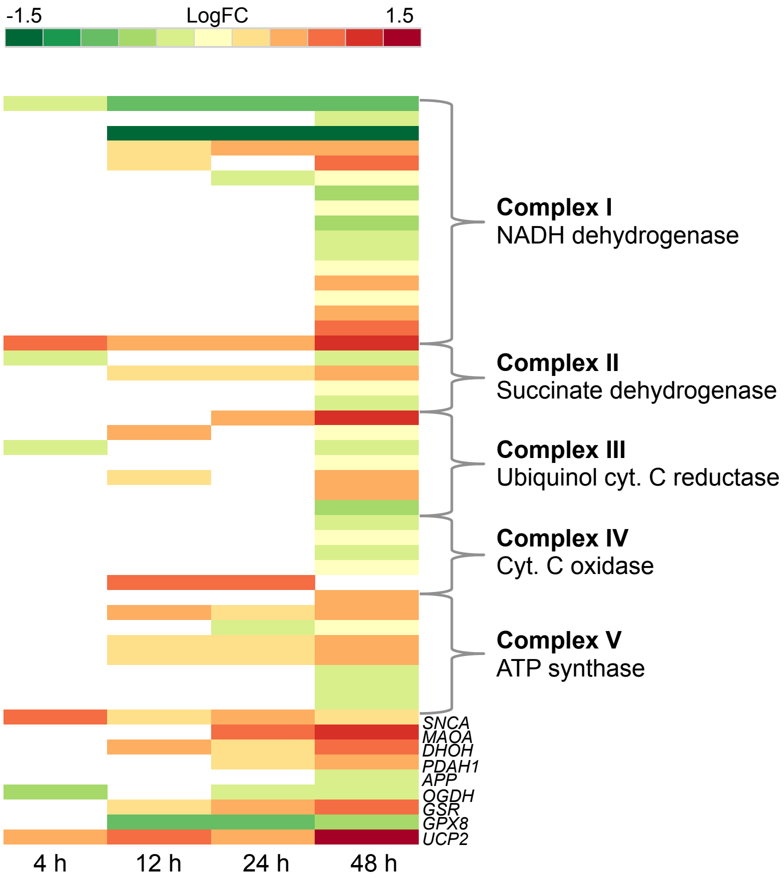

Figure 4.20: **Heat map showing the differential gene expression of elements involved in mitochondrial function after exposure to Os-3.** Only DEG with FDR < 0.10 are included, blank values lie outside of this significance threshold. In response to **Os-3** there is a significantly higher level of differential expression after 48 h, compared to earlier time points, so nuclear-genes encoding mitochondrial proteins. There is a mixture of up- and down-regulation, however, there is significant down-regulation of genes coding for Complex I components, suggesting an impact in the electron transport chain (ETC). Up-regulation of genes like *UCP2* and *MAOA* occur when reactive oxygen species (ROS) are detected at the mitochondrial inner membrane, suggesting mitochodrially-driven oxidative stress.

Figure 4.20 shows an increase in DE through the time series, with a large number of DEGs at 48 h only. This is compared to the mitochondrial-encoded genes, which were maximally, differentially expressed at 24 h (Figure 4.10). Interestingly, many of the nuclear-encoded mitochondrial genes were down-regulated. For example, eleven of eighteen genes encoding subunits of complex I (CI) were significantly down-regulated, with the NADH dehydrogenase alpha subcomplex 2 (NDUFA2) and NDUFA6 being the most significantly down-regulated of all the other components. This is in contradiction to the mitochondrial genes for CI, which were consistently up-regulated in the compound-exposed samples, throughout the time series. NDUFA2 and NDUFA6 are accessory subunits to CI and as such do not directly take part in CI activity, but are involved with complex I assembly.[47] Down-regulation of these genes could imply mitochondrial damage, which would no longer require CI assembly.

Up-regulation of *SNCA* (α-synucein), *MAOA* (monoamine oxidase) and *UCP2* (mitochondrial uncoupling protein 2) supports mitochondrial specific ROS production. SNCA is primarily located in the cytoplasm, but has been shown to localize in the mitochondria and have involvement in mitochondrial dysfunction and cell death.[48] MAOA is found in the outer mitochondrial membrane, and produces hydrogen peroxide from deamination of dietary amines.[49] It is generally implicated in Parkinson's disease; however, recent studies have shown an overlap in cancer.[50] Significant up-regulation of *MAOA*, particularly at 48 h, highlights a route to the production of hydrogen peroxide by the mitochondria.

UCP2 is found on the inner mitochondrial membrane, and is responsible for the detoxification of mitochondrial superoxide produced in the matrix by increasing the influx of protons into the matrix and reducing electron leakage.[51, 52] Up-regulation of *UCP2* has been shown during drug-induced oxidative stress, and when functional, can drastically reduce the levels of mitochondrial superoxide. The continual up-regulation of this gene could suggest that too much superoxide is being produced for this protein to control.

Figure 4.20 also shows down-regulation of nuclear-encoded mitochondrial genes, particularly *OGDH* (2-oxoglutarate dehydrogenase) and *GPX8* (glutathione peroxidase 8). OGDH is responsible for the conversion of 2-oxoglutarate to succinyl-CoA and is known to increase the superoxide and hydrogen peroxide levels inside mitochondria.[53] This step in the Krebs cycle produces NADH, protons and carbon dioxide, from NAD^+ and ketoglutarate. Its down-regulation in response to compound **Os-3** could suggest disruption of the Krebs cycle and OXPHOS, and therefore targeting of multiple pathways in mitochondrial metabolism. GPX8 is another antioxidant protein, which catalyzes the reaction of glutathione with hydrogen peroxide as a detoxification step. Both *CAT* (catalase) and *GPX8* are down-regulated after 12 h, suggesting that hydrogen peroxide detoxification is disrupted.

4.2.6.3 Immune response and cell migration

The activation of an immune response in cancer cells exposed to chemotherapy compounds indicates a stress response *in vitro*. *In vivo* there are many downstream events linked to the activation of an immune response, including up-regulating epithelial-mesenchymal transition and cell migration components. The purpose of these cellular responses is to recruit immune cells to the sight of stress and involves initial remodelling of the cell, and release of cytokines and interleukins which facilitate leukocyte recruitment.

Of the main upstream regulators, most were immune and inflammation related cytokines like interferon, TNFα and TGF-β after exposure to both **Os-3** and **Ir-10**. For example, after 4 h exposure to **Os-3**, cells up-regulated interferon signalling, with *IFIT3* (LogFC 1.25, FDR 7.65 x 10^{-28}) and *SOCS1* (LogFC -1.49, FDR 0.0017), where *IFIT3* codes for an interferon-induced protein, and *SOCS1* encodes a suppressor of cytokine immune signalling. After 12 h, both **Os-3** and **Ir-10** induced expression of components controlling the agranulocyte adhesion and diapedes pathway, which controls the migration of leukocytes from the vascular system during inflammation. *iCAM1* (intracellular adhesion molecule 1) is important in this signalling pathway, encoding a cell surface glycoprotein which facilitate leukocyte recruitment, and was up-regulated in response to **Os-3** (LogFC 1.06, FDR 1.5 x 10^{-4}) and **10** (LogFC 1.97, FDR 2.82 x 10^{-19}) after 12 h.

Other inflammatory pathways activated by **Os-3** and **Ir-10** include fibrosis and coagulation, controlled by genes like TGFα, PDGFβ and *SERPINE1*. *SERPINE1* was highly up-regulated by both **Os-3** (LogFC 2.36, FDR 8 x 10^{-26} at 48 h) and **Ir-10** (LogFC 2.84, FDR 3.19 x 10^{-34} at 24 h).

4.2.6.4 Cell death

There are three main methods of cell death: type I (apoptosis), type II (autophagy) and type III (necrosis). **Os-3** appears to have an affect on the mitochondria, which is a key regulator of apoptosis in the cell. Investigating the method of cell death can provide important insights into the MOA of a compound. Figure 4.21 summarises the two apoptotic mechanisms of cell death; extrinsic and intrinsic.

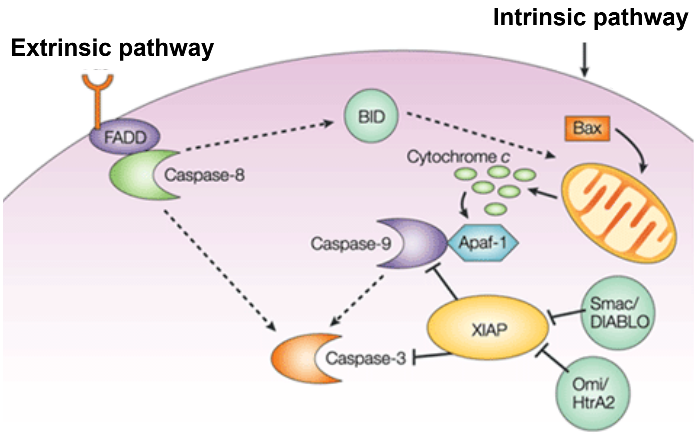

Figure 4.21: **Diagram showing the main components in the extrinsic and intrinsic apoptosis pathways.** Intrinsic pathway activation is normally associated with chemotherapy and UV damage, first triggering BAX and BID, before activating cytochrome C release from the mitochondrial and subsequent capsize activation. The extrinsic pathway is activated by death ligands, which trigger caspase-8 activity through FADD. Inhibitor of apoptosis (IAP) proteins can control the process of apoptosis at the capsize level, for example XIAP inhibiting the caspase-3 and -9 activity. *Image taken from Legewie S, et al (2006) PLoS Comput. 2(9): e120*

Figure 4.22 is a heat map for the DEGs related to apoptotic cell death in cells exposed to **Os-3**. Classical caspase markers include caspase (*CASP*)-3, -7 and -9 as downstream markers, or caspase-8 as an upstream marker of extrinsic apoptosis.

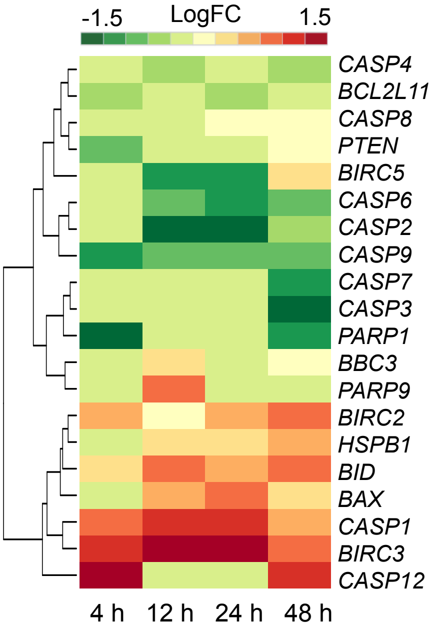

Figure 4.22: **Heat map of DEG in the apoptosis pathway across the time series after exposure to Os-3.** Only DEG with FDR < 0.10 are included, blank values lie outside of this significance threshold. Shown with high levels of differential expression are non-apoptotic capsizes like *CASP1* and *CASP12*, mostly associated with inflammatory responses. There is some up-regulation of intrinsic apoptotic genes *BID* and *BAX* after 12 h exposure to **Os-3**, suggesting some apoptotic invitation. However, down-regulation of apoptotic capsases like *CASP3* and *CASP9* suggest apoptosis may only be initiated and not put into effect. Cell survival gene *BIRC3* which codes for survivin, an inhibitor of apoptosis (IAP) protein shows significant up-regulation after just 4 h exposure, suggesting further that caspase activity is not activated within 48 h exposure.

Figure 4.22 shows significant down-regulation of *CASP-9* after 4 h, *CASP-6*, *-2* and *-9* after 12 h, and *CASP-3* and *-7* after 48 h. Genes for inhibitors of apoptosis (IAP) proteins, which inhibit the activation of caspase proteins, like *BIRC2* and *BIRC3*, are up-regulated after 4 h (LogFC 2.06, FDR 1.53 x 10^{-12}). *BIRC5*, which codes for survivin, another IAP, was down-regulated until 24 h (LogFC -0.43, FDR 1.03 x 10^{-5}), suggesting specific modulation of apoptotic signals through caspase inhibition.

Figure 4.22 also shows up-regulation of *BID* (LogFC 0.90 (48 h), FDR 1.77 x 10^{-14}) and *BAX* (LogFC 0.50 (24 h), FDR 3.46 x 10^{-6}) which both code for apoptotic initiators, BID from extrinsic activation and BAX from intrinsic apoptotic activation. This suggests that apoptotic signals are being initiated in response to **Os-3**, but that signals do not translate through to the effector caspases. The only caspase genes which were up-regulated, were *CASP-1* and *CASP-12* which are inflammatory caspases, activated by IL-1β, which was one of the most significant upstream regulators after 12 h (Table 4.3).

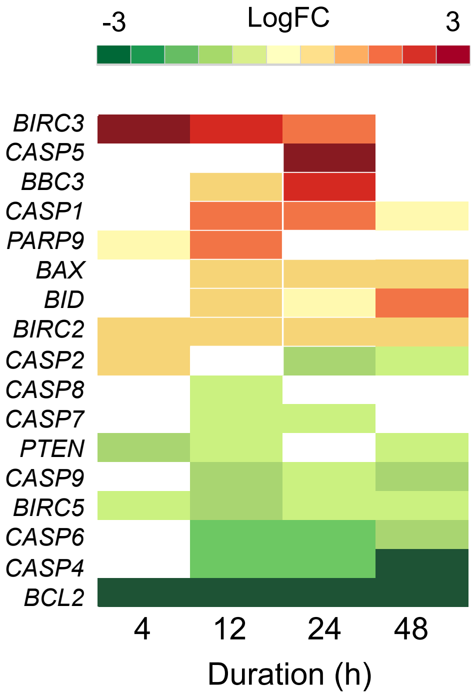

Figure 4.23: **Heat map of DEG in the apoptosis pathways across the time series after exposure to Ir-10.** Only DEG with FDR < 0.10 are included, blank values lie outside of this significance threshold. There are noticeably fewer genes with significant differential expression after cells were exposed to **Ir-10** compared to **Os-3**. However, there are similarities in the up-regulation of apoptotic inhibitor *BIRC3*, and inflammatory caspases like *CASP5* and *CASP1*. The expression of apoptotic initiator genes like *BAX* and *BID* were hardly affected by **Ir-10**, suggesting there may be less initiation of apoptosis compared to that shown after **Os-3**-exposure.

A similar expression pattern is shown in response to **Ir-10**, with down-regulation of *BCL2* and apopotic caspases, and up-regulation of IAPs like *BIRC3*. As with **Os-3**, *BAX* and *BID* apoptotic initiators showed some low level up-regulation after 12 h and inflammatory caspases, *CASP-5* and *-1* were significantly up-regulated after 12, and 24 h, respectively.

Overall, this suggests a similar apoptotic profile between **Os-3** and **Ir-10**, with expression of apoptotic initiators and inflammatory caspases and down-regulation of apoptotic effector caspases possibly due to IAP intervention. This shows strong control of the apoptotic pathway by stressed cells, and may suggest prolonged exposure or multiple dosing is required for cell death.

Autophagy was proposed as another potential mechanism of cell death, given its link to an immune response, as an effector. Both **Os-3** and **Ir-10** showed activated immune responses, particularly evident with up-regulation of inflammatory caspases. Figure 4.24 shows the expression profiles of autophagic genes.

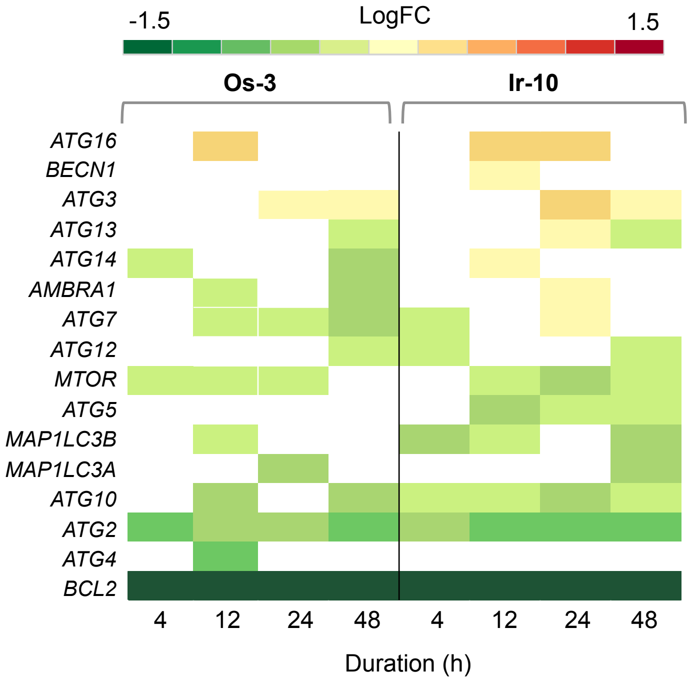

Figure 4.24: **Heat map of DEG in the autophagy pathways across the time series after exposure to Ir-10.** Only DEG with FDR < 0.10 are included, blank values lie outside of this significance threshold. Autophagy is an important mechanism of cell death, often linked to inflammation. The heat map shows minimal up-regulation of autophagy markers, the most common of which are *BECN1* (beclin) and *MAP1LC3B/A* (LC3), in response to both **Os-3** and **Ir-10** across the time series. This suggests that this mechanism of cell death does not play an important role in drug-response.

The classical markers for autophagy are *BECN1* which codes for beclin, and *MAP1LC3A/B* which codes for LC3-I/II. Beclin and BCL-2 proteins are involved in the initiation phase of autophagy, with LC-3 and the ATG proteins involved further downstream. Figure

4.24 shows down-regulation of most of these components throughout the time series, suggesting autophagy does not feature significantly in cellular response.

Necrosis is another form of programmed cell death and similar to autophagy, can activate an immune response. Necrosis results in the emptying of cell contents into the extracellular space, as a result of the loss of cell membrane integrity. Unlike apoptotic cell death, immune cells are not recruited to the degraded cellular debris, instead necrotic tissue can build up and often has to be removed surgically. Interestingly, necrosis also has strong links to reactive oxygen species (ROS) production, a response pathway which showed involvement to both **Os-3** and **Ir-10**.

RIP proteins are involved in the activation stage of necrosis,[54] for example, *RIPK1* which codes for the RIP1 protein. In response to **Os-3**, *RIPK1* was down-regulated throughout the time series, most significantly at 48 h (LogFC -0.55, FDR 5.79 x 10^{11}). A similar profile was shown in response to **Ir-10**, with maximum down-regulation at 12 h (LogFC -0.55, FDR 4.78 x 10^{14}), suggesting programmed necrosis is not activated in exposed-cells.

4.3 Discussion

4.3.1 Mitochondrial deficiencies in A2780 epithelial ovarian cancer cells

The mitochondrion is fast becoming an important target in cancer research.[55, 56] This organelle introduces an element of selectivity for therapeutic targeting, as the metabolic profile of cancer cells is often primarily glycolytic to increase the efficiency of cancer cell division and distinct from that of normal cells, which produce ATP primarily by oxidative phosphorylation (OXPHOS).[57–61] This phenomenon is known as the Warburg effect. Glycolysis is generally less efficient for ATP production, however, it is faster than OXPHOS, permits macromolecule biosynthesis and can function during hypoxic conditions.[62, 63] This is thought to reduce the production of reactive oxygen species (ROS), which are often byproducts of the OXPHOS pathway, and can be deadly to cellular function.

Copy number variations in the mitochondria of cancer cells can account for an abnormal number of reads mapping to the mitochondrial chromosome (ChrM) during RNA or DNA sequencing. In response to both **Os-3** and **Ir-10**, the cells showed increased reads mapped to ChrM, with a more significant result for **Os-3**.

The genes found on the ChrM code for important polypeptides present in components of the electron transport chain (ETC), controlling the process of oxidative phosphorylation (OXPHOS). The overall increase in reads mapped to the mtDNA after exposure to these compounds suggested that the mitochondrion is mobilising components required for a functional ETC, and thus shifting the metabolism from favourable glycolysis to unfavourable OXPHOS. **Os-3** and **Ir-10** may therefore be targeting glycolysis in some form, forcing the cells to use alternative OXPHOS energy production.

This effect has been shown in several reported studies, where glycolysis has been targeted by an inhibitor like 2-deoxyglucose, and the cell has responded with a shunt of metabolism into OXPHOS, increasing sensitivity to chemotherapy agents.[62, 64] OXPHOS is not an optimal process in cancer cell division; therefore if **Os-3** and **Ir-10** shift the metabolism in this way, the cell may be energetically strained.

Point mutations in the mtDNA of A2780 affect complex I components. Mutations in the mtDNA are a common occurrence in cancer cells, and are thought to be partly responsible for a favouring of glycolysis.[65, 66] There are two main types of mtDNA mutations, the first are major mutations, which directly affect OXPHOS machinery and ROS production. The second are minor mtDNA mutations, which allow cancer cells to adapt to new environments. The presence of mutations in mtDNA was therefore investigated, which could result in defective OXPHOS machinery in A2780 cells.

The *MT-ND* genes on the ChrM encode helical polypeptides which constitute the membrane bound subunits of NADH dehydrogenase complex I (CI), responsible for maintaining a proton gradient between the matrix and inter-membrane space.[36] The efficiency of maintaining this coupling gradient is directly proportional to the efficiency of ATP production by the last complex in the ETC, ATPase complex V (CV).[65] CI actually accounts for 40% of the proton gradient generated in NADH oxidation.[67]

Point mutations in CI machinery have been found in breast, colon, prostate, thyroid and EOC, however, most reported mutations in EOC focus on the D-loop of ChrM.[37, 66, 68–72] This is the first report of p.I257V, p.N447S and p.L517P MT-ND5 mutations in EOC.[69] Errors in the function of CI have been shown to potentiate electron transport errors and create an inherently, oxidatively-stressed environment inside cancer cells.[31]

4.3.2 Oxidative stress

Performing pathway analysis of differentially expression genes (DEGs) revealed the activation of oxidative stress response pathways by both **Os-3** and **Ir-10**, and mitochondrial dysfunction in response to **Os-3**.

The mitochondrion is the biggest source of superoxide production in the cell, particularly from CI. Superoxide species are normally broken down by superoxide dismutase (SOD) to hydrogen peroxide, which is then broken down by catalase (CAT) to water and oxygen.[73] Neither *CAT* nor *SOD* genes were up-regulated after exposure to compounds **Os-3** or **Ir-10**. In fact, *CAT* was expressed in higher levels in the control samples, highlighting the oxidatively-stressed nature of A2780 cells, and that no response to hydrogen peroxide was mobilised after compound exposure. Disruption of CAT and SOD function has been shown to have a knock-on effect on the function of other antioxidant enzymes, potentiating the damage caused by ROS.[74]

Generally, both the antioxidant and detoxifying systems work in synergy to remove damaging ROS inside cells.[75] The down-regulation of key response genes suggests that **Os-3** and **Ir-10** both induce ROS production and reduce the ability of A2780 cells to respond to excessive ROS.

The production of ROS from mitochondria has a cyclic effect on the function of mitochondria, potentiating the production of higher and higher levels of ROS.[76] These ROS can damage mtDNA and proteins within the mitochondria, in addition to disrupting the polarisation of the mitochondrial membrane.[28] Previous work on **Os-3** has shown polarisation of the mitochondrial membrane after just 4 h exposure towards A549 lung cancer cells.[77] Mutations in OXPHOS machinery causes ROS production, and that this ROS production is potentiated by compound 1 through metabolic targeting.

Mitocans, which target the bioenergetics of cancer cells and increase ROS, are becoming a focus of anticancer drug development.[78] ROS production can damage mitochondrial components, however, ATP depletion and imbalance in calcium homeostasis are also caused by mitochondrial targeting.[76] Calcium overload, in particular is common in tumors, so disrupting these levels further can have multiple downstream effects, including cell death.[79]

Of course, ROS may not be generated through the mitochondria, and instead **Os-3** and **Ir-10** may induce them by some other mechanism. ROS production during cell stress is well documented, and occurs indirectly in response to many drugs, including cisplatin.[80]

In previous studies, **Os-3** has been shown to induce ROS production in lung cancer cells.[77] The results here build on this, identifying an NRF2 cellular response. Given NRF2 is also up-regulated in response to **Ir-10**, it is likely that this compound also induces ROS. Future studies should determine whether these ROS originate from the mitochondria or from another source and **Os-3** and **Ir-10** would need to be validated as oxidative stress inducers, by comparing their activity to other agents in this class.

4.3.3 Immune response

An immune response seems to play a prominent role in the response of A2780 cells to **Os-3** and **Ir-10**, with both type I (interferon, TNFα) and type II (TGFβ) cytokine involvement. Chemotherapy agents have been shown to activate an immune response, and for this response to be beneficial. They do this through various methods, including promoting remodelling of targeted cancer cells, which make them visible to the immune system.[81]

Epithelial remodelling was highlighted as one of the pathways activated in response to both compounds, and if it occurs *in vivo* would help the recruitment of leukocytes to the cell. Chemotherapy agents have also shown to induce an immunogenic type of cell death, for example pyroptosis.[81] This mechanism of cell death is characterised by high levels of CASP-1 and ILβ1, which were both up-regulated in response to **Os-3** and **Ir-10**.

On the other hand, an inflammatory response via TNF can also be indicative of metastasis by kick-starting the invasion of tumour cells and increasing angiogenesis.[82] This is often also accompanied by growth factor release, like PDGF, which was a prominent upstream regulator activated in response to **Ir-10**, but not **Os-3**. The induction of tumour invasion by chemotherapy treatment is an established occurrence, activating a host response which is tumour-promoting.[83] Successful experiments have prevented tumourigenesis by co-incubating chemotherapeutic agents with growth factor suppressors.[84]

There are several methods in which **Os-3** and **Ir-10** may be activating an immune response, the production of ROS is often linked to the production of inflammatory cytokines. A study by Taulet *et al* showed that ROS can modulate networks which control protrusion in mammalian epithelial cells, which would facilitate leukocyte recruitment.[85] Interestingly, ovarian cancers are highly immunogenic, which means that inherently they are highly capable of activating immune response.

Future work, following on from results obtained here will need to assess the outcome of an immune response, performing metastatic *in vitro* assays and studying the immune response in *in vivo* models.

4.4 Summary and Conclusions

Studying the mechanism of action (MOA) of new anticancer agents using sequencing is a relatively unexplored strategy, and subject to various limitations. Due to the complex nature of drug-targetting, the exact mechanisms can be masked behind dominant processes. In this work, a lot of the mechanisms have been masked by an overall immune response in cells, which did not reveal the exact nature of the immune response, but did highlight some differences between the compounds. For example, **Ir-10** showed a growth factor response which **Os-3** did not; this could suggest that cells exposed to **Ir-10** could be activating a stronger invasive response. By assessing the cell line A2780, and identifying the mitochondrial deficiencies, it was possible to start unravelling how the immune response may have been activated, linking in oxidative stress.

Both **Os-3** and **Ir-10** appear to elicite an inflammatory response, related to caspase-1 and a response to oxidative stress, related to NFR2 and possibly to the mitochondria. Zhong *et al* highlighted a link between these two processes, starting with ROS generation by the mitochondria, followed by inflammasome activation through TRPM2 and NLRP3.[86] The inflammasome could subsequently activate caspase-1 which stimulates interleukin/cytokine maturation, and allows the cell to attempt the recruitment of leukocytes (early response) but may eventually activate cell death via pyroptosis/apoptosis (late response). The immune response may also be indicative of tumour invasion, and should be assessed in future studies outside of this thesis.

The mitochondrial mutations identified in the ND5 protein also need future in-depth investigation to determine whether there is a functional link between OXPHOS-generated ROS and deficiencies in this ETC machinery. Given cell lines can spontaneously develop mutations, A2780 cell lines from multiple sources would need to be sequenced to confirm whether this is an inherent mutation for this cell line, or an adaptive response during *in vitro* culturing at The University of Warwick.

In efforts to investigate downstream effects of oxidative stress, Chapter 5 explores differential protein levels in A2780 cells exposed to **Os-3** and **Ir-10**, using flow cytometry to validate these findings. In addition, Chapter 7 further explores the mechanisms of cell death using imaging techniques.

References

[1] Wang Z, Gerstein M, Snyder M (2009) RNA-Seq: a revolutionary tool for transcriptomics. *Nature Reviews Genetics* 10:57–63.

[2] Ledford H (2008) The death of microarrays? *Nature* 455:847.

[3] Fathallah-Shaykh HM (2005) Microarrays: applications and pitfalls. *Archives of Neurology* 62:1669–1672.

[4] Venkatasubbarao S (2004) Microarrays status and prospects. *Trends in Biotechnology* 22:630–637.

[5] Parkhomchuk D, et al. (2009) Transcriptome analysis by strand-specific sequencing of complementary DNA. *Nucleic Acids Research* 37:e123.

[6] Illumina (2014) Multiplexed sequencing with the illumina genome analyzer system. *Online. http://res.illumina.com.*

[7] Ewing B, Green P (1998) Base-calling of automated sequencer traces using phred. II. Error probabilities. *Genome Research* 8:186–194.

[8] Ewing B, Hillier L, Wendl M, Green P (1998) Base-calling of automated sequencer traces using Phred. I. Accuracy assessment. *Genome Research* pp 175–185.

[9] Kim D, et al. (2013) TopHat2: accurate alignment of transcriptomes in the presence of insertions, deletions and gene fusions. *Genome biology* 14:R36.

[10] Langmead B, Salzberg SL (2012) Fast gapped-read alignment with Bowtie 2. *Nature Methods* 9:357–359.

[11] Trapnell C, et al. (2010) Transcript assembly and quantification by RNA-Seq reveals unannotated transcripts and isoform switching during cell differentiation. *Nature Biotechnology* 28:511–515.

[12] Robinson MD, McCarthy DJ, Smyth GK (2010) edgeR: a Bioconductor package for differential expression analysis of digital gene expression data. *Bioinformatics* 26:139–140.

[13] Anders S, Huber W (2010) Differential expression analysis for sequence count data. *Genome Biology* 11:R106.

[14] Griffith M, et al. (2010) Alternative expression analysis by RNA sequencing. *Nature Methods* 7:843–847.

[15] Hardcastle TJ, Kelly KA (2010) baySeq: empirical Bayesian methods for identifying differential expression in sequence count data. *BMC bioinformatics* 11:422.

[16] Bi Y, Davuluri RV (2013) NPEBseq: nonparametric empirical bayesian-based procedure for differential expression analysis of RNA-seq data. *BMC bioinformatics* 14:262.

[17] Rapaport F, et al. (2013) Comprehensive evaluation of differential gene expression analysis methods for RNA-seq data. *Genome Biology* 14:R95.

[18] Anders S (2010) HTSeq: Analysing high-throughput sequencing data with Python. *Online. http://www-huber.embl.de/users/anders/HTSeq/.*

[19] Rapaport F, et al. (2013) Comprehensive evaluation of differential gene expression analysis methods for RNA-seq data. *Genome Biology* 14:R95.

[20] Robinson MD, Smyth GK (2008) Small-sample estimation of negative binomial dispersion, with applications to SAGE data. *Biostatistics* 9:321–332.

[21] Robinson MD, Smyth GK (2007) Moderated statistical tests for assessing differences in tag abundance. *Bioinformatics* 23:2881–2887.

[22] Robinson MD, Oshlack A (2010) A scaling normalization method for differential expression analysis of RNA-seq data. *Genome Biology* 11:R25.

[23] McCarthy DJ, Chen Y, Smyth GK (2012) Differential expression analysis of multifactor RNA-Seq experiments with respect to biological variation. *Nucleic Acids Research* 40:4288–97.

[24] Nelder AJA, Wedderburn RWM (1972) Generalized Linear Models. *Journal of the Royal Statistical Society. Series A (General)* 135:370–384.

[25] Benjamini Y, Hochberg Y (1995) Controlling the False Discovery Rate: A Practical and Powerful Approach to Multiple Testing. *Journal of the Royal Statistical Society. Series B (Methodological)* 57:289 – 300.

[26] Qiagen (2005) IPA network generation algorithm. *Online Source. URL: www.ingenuity.com/wp-content/themes/ingenuitytheme/pdf/ipa/IPA-netgen-algorithm-whitepaper.pdf.*

[27] Wu S, Li RW, Li W, Li Cj (2012) Transcriptome Characterization by RNA-seq Unravels the Mechanisms of Butyrate-Induced Epigenomic Regulation in Bovine Cells. *PLoS ONE* 7:e36940.

[28] Meng S, Han J (2013) Mitochondrial DNA copy number alteration in human cancers. *North American Journal of Medicine and Science* 6:22–25.

[29] Friedman JR, Nunnari J (2014) Mitochondrial form and function. *Nature* 505:335–343.

[30] Taylor RW, Turnbull DM (2005) Mitochondrial DNA mutations in human disease. *Nature Reviews Genetics* 6:389–402.

[31] Chatterjee A, Mambo E, Sidransky D (2006) Mitochondrial DNA mutations in human cancer. *Oncogene* 25:4663–4674.

[32] Horai S, Hayasaka K, Kondo R, Tsugane K, Takahata N (1995) Recent African origin of modern humans revealed by complete sequences of hominoid mitochondrial DNAs. *Proceedings of the National Academy of Sciences of the United States of America* 92:532–536.

[33] Maca-Meyer N, González AM, Larruga JM, Flores C, Cabrera VM (2001) Major genomic mitochondrial lineages delineate early human expansions. *BMC genetics* 2:13.

[34] Calvo SE, al E (2010) High-throughput, pooled sequencing identifies mutations in NUBPL and FOXRED1 in human complex I deficiency. *Nature Genetics* 42:851–858.

[35] Qu J, et al. (2009) Extremely Low Penetrance of Leber's Hereditary Optic Neuropathy in 8 Han Chinese Families Carrying the ND4 G11778A Mutation. *Ophthalmology* 116:558–564.

[36] Rich PR, Maréchal A (2010) The mitochondrial respiratory chain. *Essays in Biochemistry* 47:1–23.

[37] Hirst J (2013) Mitochondrial complex I. *Annual review of biochemistry* 82:551–75.

[38] Wisdom R (1999) AP-1: one switch for many signals. *Experimental Cell Research* 253:180–185.

[39] Huang B, et al. (2005) Toll-like receptors on tumor cells facilitate evasion of immune surveillance. *Cancer research* 65:5009–5014.

[40] Carmi Y, et al. (2013) The role of IL-1β in the early tumor cell-induced angiogenic response. *Journal of Immunology* 190:3500–3509.

[41] Netea MG, et al. (2010) IL-1β processing in host defense: beyond the inflammasomes. *PLoS Pathogens* 6:e1000661.

[42] Zaidi MR, Merlino G (2011) The Two Faces of Interferon-γ in Cancer. *Clinical Cancer Research* 17:6118–6124.

[43] Sato N, et al. (1993) Platelet-derived growth factor indirectly stimulates angiogenesis in vitro. *The American Journal of Pathology* 142:1119–1130.

[44] Xue Y, et al. (2011) PDGF-BB modulates hematopoiesis and tumor angiogenesis by inducing erythropoietin production in stromal cells. *Nature Medicine* 18:100–110.

[45] Hybertson BM, Gao B, Bose SK, McCord JM (2011) Oxidative stress in health and disease: the therapeutic potential of Nrf2 activation. *Molecular Aspects of Medicine* 32:234–46.

[46] Katoh Y, et al. (2001) Two domains of Nrf2 cooperatively bind CBP, a CREB binding protein, and synergistically activate transcription. *Genes to Cells* 6:857–868.

[47] Mckenzie M, Ryan MT (2010) Assembly factors of human mitochondrial complex I and their defects in disease. *IUBMB life* 62:497–502.

[48] Zhu M, Li W, Lu C (2012) Role of alpha-synuclein protein levels in mitochondrial morphology and cell survival in cell lines. *PLoS ONE* 7:e36377.

[49] Menazza S, et al. (2010) Oxidative stress by monoamine oxidases is causally involved in myofiber damage in muscular dystrophy. *Human Molecular Genetics* 19:4207–4215.

[50] Devine M, Plun-Favreau H, Wood N (2011) Parkinson's disease and cancer: two wars, one front. *Nature Reviews Cancer* 11:812–823.

[51] Dalla Pozza E, et al. (2012) Role of mitochondrial uncoupling protein 2 in cancer cell resistance to gemcitabine. *Biochimica et Biophysica Acta* 1823:1856–1863.

[52] Derdak Z, Garcia TA, Baffy G (2009) Detection of uncoupling protein-2 (UCP2) as a mitochondrial modulator of apoptosis. *Methods in Molecular Biology* 559:205–217.

[53] Quinlan CL, et al. (2014) The 2-oxoacid dehydrogenase complexes in mitochondria can produce superoxide/hydrogen peroxide at much higher rates than complex I. *The Journal of biological Chemistry* 289:8312–8325.

[54] Vandenabeele P, Declercq W, Van Herreweghe F, Vanden Berghe T (2010) The role of the kinases RIP1 and RIP3 in TNF-induced necrosis. *Science Signaling* 3:re4.

[55] Fulda S, Kroemer G (2011) Mitochondria as therapeutic targets for the treatment of malignant disease. *Antioxidants & Redox Signaling* 15:2937–2949.

[56] Ralph SJ, Low P, Dong L, Lawen A, Neuzil J (2006) Mitocans: mitochondrial targeted anti-cancer drugs as improved therapies and related patent documents. *Recent Patents on Anti-Cancer Drug Discovery* 1:327–346.

[57] Ward PS, Thompson CB (2012) Metabolic reprogramming: a cancer hallmark even warburg did not anticipate. *Cancer Cell* 21:297–308.

[58] Warburg O (1956) Injuring of Respiration the Origin of Cancer Cells. *Science* 123:309–314.

[59] Koppenol WH, Bounds PL, Dang CV (2011) Otto Warburg's contributions to current concepts of cancer metabolism. *Nature Reviews Cancer* 11:325–337.

[60] Hamanaka RB, Chandel NS (2011) Warburg effect and redox balance. *Science* 334:1219–1220.

[61] Gogvadze V, Zhivotovsky B, Orrenius S (2010) The Warburg effect and mitochondrial stability in cancer cells. *Molecular Aspects of Medicine* 31:60–74.

[62] Zheng J (2012) Energy metabolism of cancer: glycolysis versus oxidative phosphorylation (Review). *Oncology Letters* 4:1151–1157.

[63] Pfeiffer T, Schuster S, Bonhoeffer S (2001) Cooperation and competition in the evolution of ATP-producing pathways. *Science* 292:504–507.

[64] Palorini R, Simonetto T, Cirulli C, Chiaradonna F (2013) Mitochondrial complex I inhibitors and forced oxidative phosphorylation synergize in inducing cancer cell death. *International Journal of Cell Biology* 2013:243876.

[65] Brandon M, Baldi P, Wallace DC (2006) Mitochondrial mutations in cancer. *Oncogene* 25:4647–62.

[66] Parrella P, al E (2001) Detection of mitochondrial DNA mutations in primary breast cancer and fine-needle aspirates. *Cancer Research* 61:7623–7626.

[67] Hinchliffe P, Sazanov LA (2005) Organization of iron-sulfur clusters in respiratory complex I. *Science* 309:771–774.

[68] Larman TC, al E (2012) Spectrum of somatic mitochondrial mutations in five cancers. *Proceedings of the National Academy of Sciences of the United States of America* 109:14087–14091.

[69] Guerra F, et al. (2012) Mitochondrial DNA mutation in serous ovarian cancer: implications for mitochondria-coded genes in chemoresistance. *Journal of Clinical Oncology* 30:373–378.

[70] Aikhionbare FO, et al. (2008) mtDNA sequence variants in subtypes of epithelial ovarian cancer stages in relation to ethnic and age difference. *Diagnostic Pathology* 3:32–43.

[71] Liu VW, et al. (2001) High incidence of somatic mitochondrial DNA mutations in human ovarian carcinomas. *Cancer Research* 61:5998–6001.

[72] Van Trappen PO, et al. (2007) Somatic mitochondrial DNA mutations in primary and metastatic ovarian cancer. *Gynecologic Oncology* 104:129–133.

[73] Murphy MP (2009) How mitochondria produce reactive oxygen species. *The Biochemical journal* 417:1–13.

[74] Turkseven S, et al. (2005) Antioxidant mechanism of heme oxygenase-1 involves an increase in superoxide dismutase and catalase in experimental diabetes. *American Journal of Physiology. Heart and Circulatory Physiology* 289:701–707.

[75] Dong J, Sulik KK, Chen SY (2008) Nrf2-mediated transcriptional induction of antioxidant response in mouse embryos exposed to ethanol in vivo: implications for the prevention of fetal alcohol spectrum disorders. *Antioxidants & Redox Signaling* 10:2023–2033.

[76] Henchcliffe C, Beal MF (2008) Mitochondrial biology and oxidative stress in Parkinson disease pathogenesis. *Nature Clinical Practice. Neurology* 4:600–609.

[77] van Rijt SH, Romero-Canelón I, Fu Y, Shnyder SD, Sadler PJ (2014) Potent organometallic osmium compounds induce mitochondria-mediated apoptosis and S-phase cell cycle arrest in A549 non-small cell lung cancer cells. *Metallomics* 6:1014–1022.

[78] Neuzil J, Dong LF, Rohlena J, Truksa J, Ralph SJ (2013) Classification of mitocans, anti-cancer drugs acting on mitochondria. *Mitochondrion* 13:199–208.

[79] Wojtczak L, et al. (1999) Effect of glucose and deoxyglucose on the redistribution of calcium in ehrlich ascites tumour and Zajdela hepatoma cells and its consequences for mitochondrial energetics. Further arguments for the role of Ca(2+) in the mechanism of the crabtree effect. *European Journal of Biochemistry* 263:495–501.

[80] Chen Y, Jungsuwadee P, Vore M, Butterfield DA, St Clair DK (2007) Collateral damage in cancer chemotherapy: oxidative stress in nontargeted tissues. *Molecular Interventions* 7:147–156.

[81] Bracci L, Schiavoni G, Sistigu A, Belardelli F (2014) Immune-based mechanisms of cytotoxic chemotherapy: implications for the design of novel and rationale-based combined treatments against cancer. *Cell Death and Differentiation* 21:15–25.

[82] Grivennikov SI, Karin M (2011) Inflammatory cytokines in cancer: tumour necrosis factor and interleukin 6 take the stage. *Annals of The Rheumatic Diseases* 70 Suppl 1:i104–i108.

[83] Kerbel RS, Ebos JM (2010) Peering into the aftermath: The inhospitable host? *Nature Medicine* 16:1084–1085.

[84] Daenen LGM, et al. (2011) Chemotherapy Enhances Metastasis Formation via VEGFR-1-Expressing Endothelial Cells. *Cancer Research* 71:6976–6985.

[85] Taulet N, Delorme-Walker VD, DerMardirossian C (2012) Reactive Oxygen Species Regulate Protrusion Efficiency by Controlling Actin Dynamics. *PLoS ONE* 7:e41342.

[86] Zhong Z, et al. (2013) TRPM2 links oxidative stress to NLRP3 inflammasome activation. *Nature Communications* 4:1611.

Chapter 5. Proteomics

5.1 Introduction

This chapter focusses on the study of protein behaviour when ovarian cancer cells are exposed to compounds **Os-3** ($[\mathrm{Os}(\eta^6\text{-}p\text{-cym})(\mathrm{NMe_2\text{-}azpy})\mathrm{I}]\mathrm{PF_6}$) and **Ir-10** ($[\mathrm{Ir}(\eta^5\text{-}\mathrm{Cp}^{xph})(\mathrm{NMe_2\text{-}azpy})\mathrm{Cl}]\mathrm{PF_6}$), using reverse phase protein microarrays (RRPA) in collaboration with the Edinburgh Cancer Research Centre. In this chapter, the results for **Os-3** and **Ir-10** are discussed in relation to the sequencing results presented in Chapter 4.

RPPA is a technique which measures the levels of protein in a sample using epitope-specific fluorescently-tagged antibodies. The RPPA analysis was done using a Zepto-MARK platform, produced by Bayer.[1, 2] This is considered the gold standard in proteomic analysis, allowing measurements of protein concentrations in the zepto-molar range. The cost of reagents are also much lower compared to mass spec-based proteomics and the automated slide spotting is environmentally controlled, and is highly reproducible.

The Edinburgh Cancer Research Centre has applied this technique in a number of areas, with a number of collaborations.[3] For example, together with the Edinburgh Experimental Cancer Medicine Centre, RPPA has been used in breast cancer work to study protein kinase cascades in response to cancer treatment.[1, 3, 4] A similar approach is applied in this chapter, studying the effect of **Os-3** and **Ir-10** on protein pathways in ovarian cancer.

5.1.1 Experimental overview

A2780 cells were exposed to **Os-3** and **Ir-10** at two concentrations each, 0.15 and 0.45 μM, and protein samples collected at 4, 24, 48 and 72 h. This allowed the extension of the 48 h time course performed with RNA sequencing. This chapter also includes validation of findings by RNAseq and RPPA, using flow cytometry, and in Chapter 7, using imaging techniques. Shown in Figure 5.1 is the experimental work flow, all of which was carried out at the Edinburgh Cancer Research Centre. All samples, for each of the time points, were measured on the same chip, and therefore each compared to the same vehicle controls.

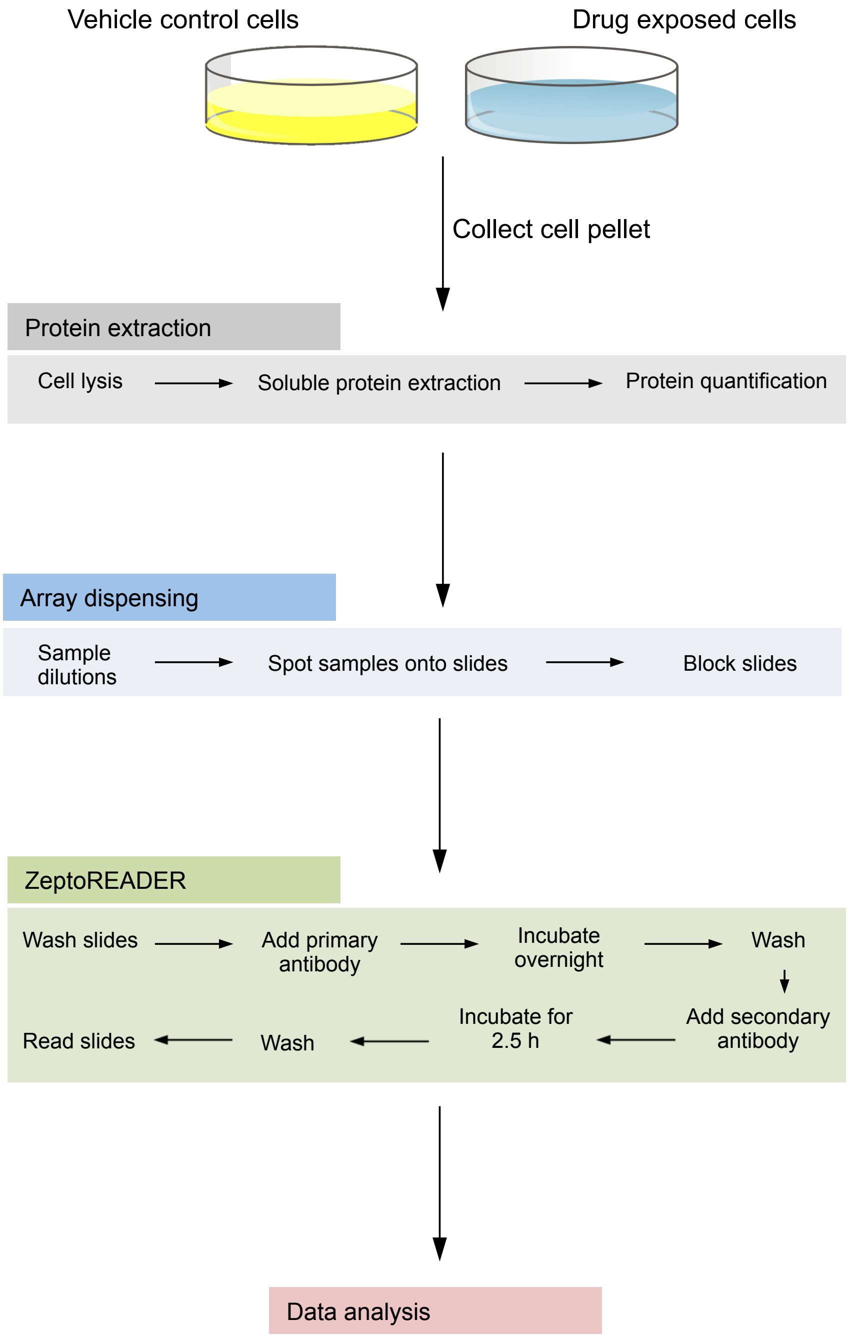

Figure 5.1: **Figure summarising the experimental workflow for reverse phase protein microarrays (RPPA).** Once seeded cells were exposed to either control- or drug-containing solutions across a 72 h time series. Cells were then collected, and the soluble protein extracted. Protein lysates were then immobilised onto microarray slides, and using antibody staining, the levels of individual proteins were determined. All experimental work was performed at the Edinburgh Cancer Research Centre, with the data analysis performed by the author at University of Warwick.

5.1.1.1 Cell lysate collection

Cells were exposed to each compound and to a DMSO control for 4, 24, 48 and 72 h. After this time, cells were lysed and soluble protein extracted. Protein concentrations were determined using the Bradford reaction and diluted down to a maximum of 2 mg/mL. Samples were then diluted to construct a dose curve for each sample on the chip with final protein concentrations of 0.2, 0.15, 0.1 and 0.05 mg/mL.

5.1.1.2 ZeptoCHIP dispensing

In a single run, the Zeptosens machine can analyse ten ZeptoCARRIERS, each holding six ZeptoCHIPS. Each ZeptoCHIP holds six arrays, with each array holding sixty-four spots for protein lysates, and eighty reference points used for background measurements. The diluted protein extracts were spotted using a GeSIM Nanoplotter and left to dry, before blocking and washing. A schematic of the slide design is shown in Figure 5.2.

Each array has its own microfluidics setup, allowing each array to be exposed to a single antibody, and therefore six antibodies to be tested simultaneously per ZeptoCHIP.

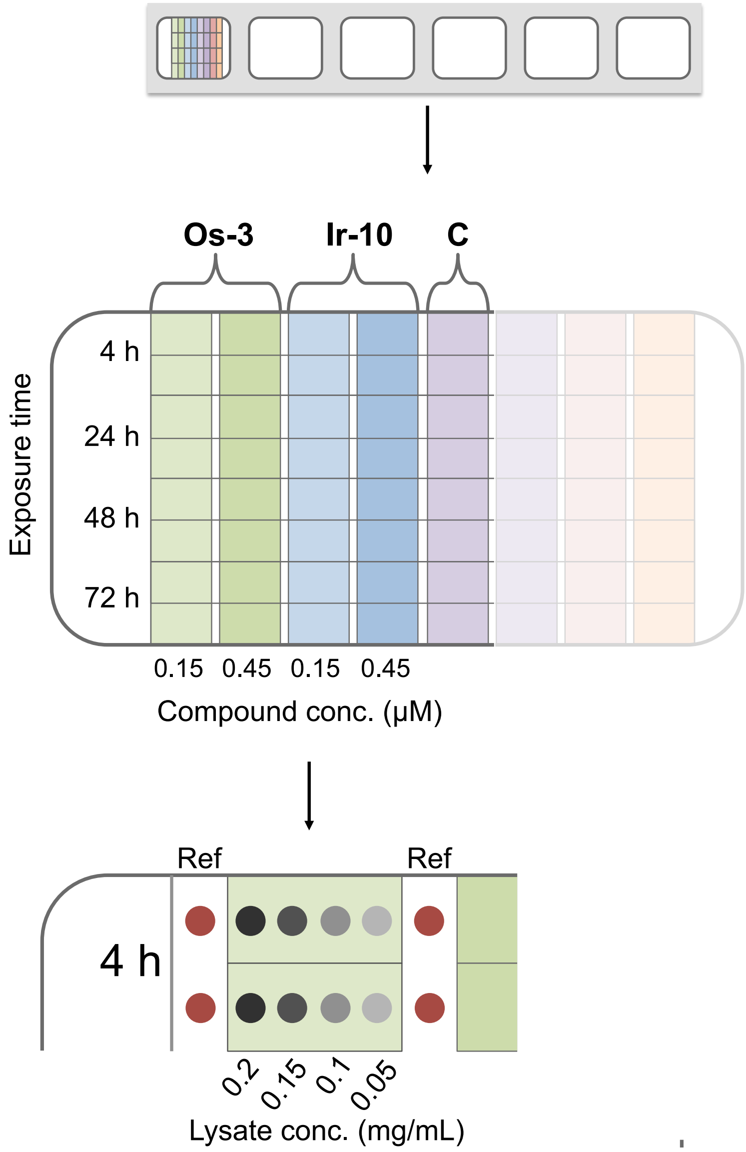

Figure 5.2: **Schematic of the layout of a ZeptoCHIP.** The top diagram shows 6 microarrays per ZeptoCHIP, with the experimental layout of each array (middle) described. The 2 columns for each compound (**Os-3** and **Ir-10**) represent duplicate measurements, with the respective time series points down the rows: 4, 24, 48 h and 72 h. The 0.1% DMSO control sample (C) is run on the same array as each sample. Each protein lysate extracted from each sample is serial diluted across 4 concentrations: 0.2, 0.15, 0.1 and 0.05 mg/mL. This allows a concentration gradient to be plotted for fluorescence measurements of each protein. Either side of these dilutions are reference controls, shown in red. These are used to correct for slide variation.

5.1.1.3 Immunoassay

Antibodies were selected based on pathways of interest highlighted after RNA sequencing, namely assessing apoptosis, cell cycle arrest and cytokine activation. All antibodies were validated by the Edinburgh Cancer Research Centre, and a complete list together with manufacturer is shown in Appendix 9.3. Primary antibodies were incubated with the spotted lysates, before secondary incubation with Alexa-Fluor647 conjugated antibody detection reagents.

5.1.1.4 ZeptoREADER

The fluorescence readings recorded by the ZeptoREADER were collected through waveguide technology. Here, gratings on each side of the ZeptoCHIPs direct light across the surface of the chip, preventing excitation of free fluorophore in the rest of the matrix (Figure 5.3).

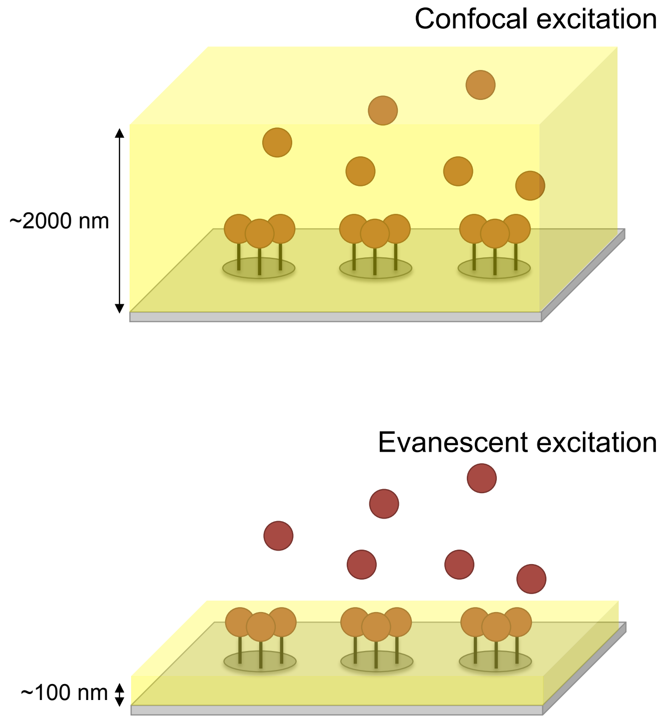

Figure 5.3: **Schematic showing the difference in excitation between standard confocal excitation compared to that for RPPA.** Each schematic shows bound antibodies to a surface, with unbound fluorescently-labelled antibodies floating above the surface. The top figure shows standard confocal excitation, with a 2μm distance exciting both the bound and unbound antibodies. The figure below shows the excitation achieved using an evanescent technique with RPPA, where the excitation distance from the surface is much smaller at $0.1\ \mu$m, thus exciting only bound antibodies. Fluorescence measurements using evanescent instead of confocal excitation reduce background noise and allow the high-sensitivity achieved using RPPA.

This so-called evanescent excitation increases the sensitivity of readings compared to conventional confocal excitation achieved with standard techniques, by reducing background noise. The increased sensitivity of Zeptosens technology negates the need for enzymatic signal amplification, even for low abundant protein detection.

Fluorescence readings were normalised for each sample, to a house keeping protein (Prohibitin). A ratio of fluorescence between the exposed sample and the negative control sample was then calculated to give relative fluorescence intensity (RFI) values.

5.2 Results

5.2.1 RPPA analysis of A2780 cells exposed to Os-3 and Ir-10

5.2.1.1 Cell cycle arrest and DNA damage

Chapter 4 explored the potential for reactive oxygen species (ROS) production in cells exposed to both **Os-3** and **Ir-10** at their GI_{50} doses, with activation of oxidative stress response pathways. Whether this induction of oxidative stress was due to disruption of respiration in A2780 cells, by exploiting the mutation in their machinery, or by another means, the downstream effects of ROS production can be studied at the protein level.

DNA is a well-known target for ROS, particularly at guanine bases.[5] The cell is equipped with mechanisms to repair such damage, however, ovarian cancers often lack the proper tools for DNA damage repair (DDR). Using Zeptosens reverse phase protein microarrays (RPPA), the abundance and activation state of proteins involved in DDR were studied.[2]

Figure 5.4 shows two DDR/cell cycle arrest pathways, the CDC25A rapid response pathway and the p53/p21 delayed response pathway.[6, 7]

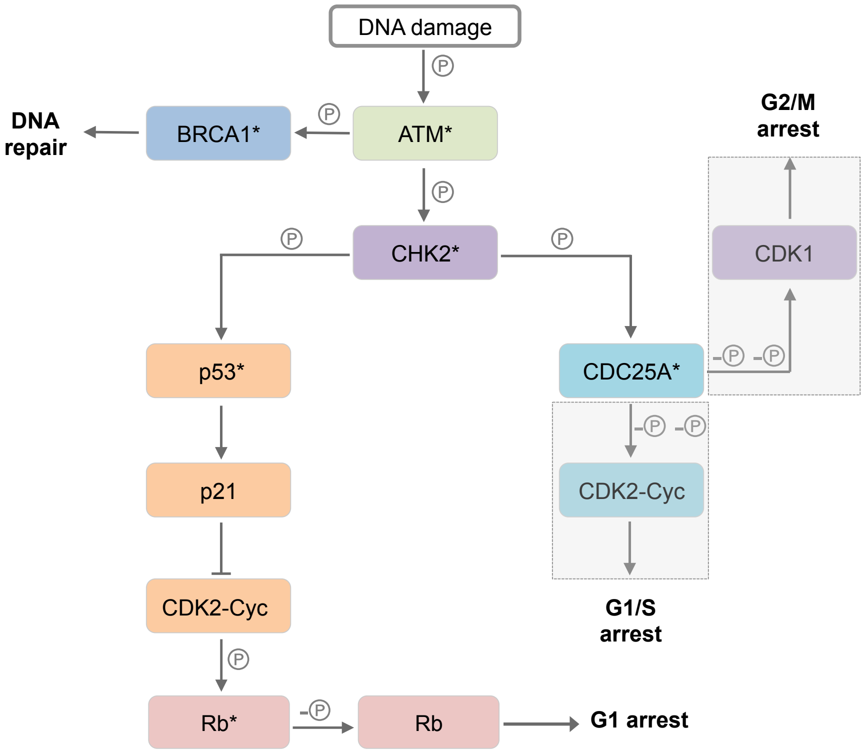

Figure 5.4: **Diagram showing some of the components in the DNA damage response (DDR) pathways.** Boxed components indicate areas where cell cycle arrest may occur. Circled-P symbols designate phosphorylation/dephosphorylation processes and * counterparts as the phosphorylated form of the protein. When DNA damage is detected, ATM is phosphorylated to ATM* which in turn phosphorylates CHK2 and BRCA1. There are two main branches of activation after this point, the right branch acting as a faster response and the left as a delayed response. Both branches primarily control the progression of cells from G1 into S phase, thus preventing damaged DNA being replicated during S phase.

The boxed areas highlight areas where successful progression from one component to the next would result in cell cycle progression, if the process within these boxes does not occur then cell division is halted at either G1, S or G2/M. Components with an asterisk (*) represent the phosphorylated form of the protein. For example, the Rb protein can be phosphorylated at two sites and is therefore labeled Rb, Rb* and Rb**. The circled-P symbol represents a phosphorylation step. For example phosphorylated CDC25A* must be dephosphorylated itself, before dephosphorylating CDK1, which then allows progression through the G2/M transition.

ATM, among other proteins, is mobilised in response to DNA double strand breaks.

ATM is auto-phosphorylated to ATM*, which in turn phosphorylates CHK2 to CHK2*. At this point, the response pathway branches, the first, a rapid response to DNA damage, permits phosphorylation of the CDC25A phosphatase to CDC25A* by CHK2*. CDC25A or CDC25C must be dephosphorylated, before dephosphorylating CDK1-CyclinA/B to allow G2/M cell cycle transition. Dephosphorylated CDC25A can also dephosphorylate CDK2-CyclinA to permit S progression or CDK2-CyclinE to allow cells to pass the G1/S transition.

The slow response pathway, involves the p53 activation, and expression of downstream targets like the p21 protein. p21 inhibits CDK2-CyclinE and CDK4/6-CyclinD, preventing the phosphorylation of Rb to Rb* and Rb** by these CDK-Cyc complexes. In the phosphorylated form, Rb dissociates from the E2F transcription factor complex, which activates transcription of DNA-synthesising enzymes and allows cells to pass into S phase. With CDK2/Cyc inhibited, Rb cannot be phosphorylated, and therefore remains bound to E2F preventing progression into S phase.

RPPA was used to study the cellular levels of twenty proteins involved in DDR and cell cycle arrest, in **Os-3**- and **Ir-10**-exposed cells across a 72 h time series. A2780 cells were exposed to **Os-3** at 0.15 (GI_{50}) and 0.45 μM (3 x GI_{50}) and to **Ir-10** at 0.15 ($\approx\frac{1}{3}$ x GI_{50}) and 0.45 ($\approx GI_{50}$), and the protein levels measured after 4, 24, 48 and 72 h.

Figure 5.5 shows the relative fluorescence intensity (RFI) values for the proteins shown in Figure 5.4, for RFI $<$ 1 the protein levels were lower in the compound-exposed versus the control, for RFI = 1, the levels did not change with compound addition, and for RFI $>$ 1, the protein levels increased in response to compound. The RFI values for p21* and ATM* at 72 h are not presented as they did not pass QC check.

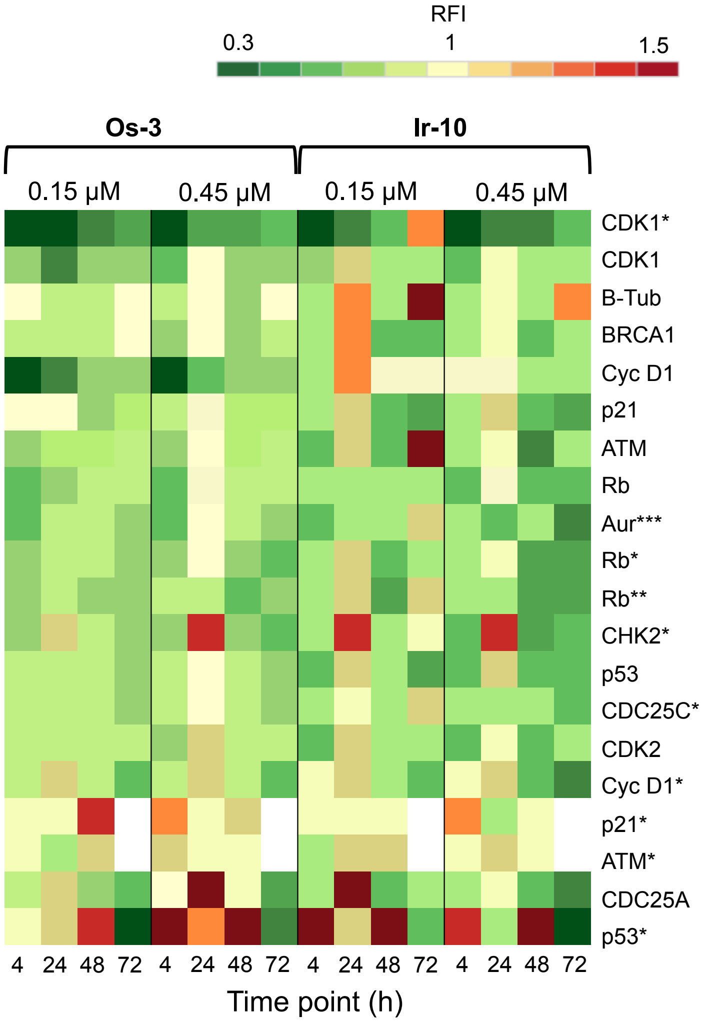

Figure 5.5: **Heat map showing the relative fluorescence intensity (RFI) values for a selection of DNA damage response (DDR) proteins in cells exposed to Os-3 and Ir-10 across a 72 h time series.** RFI values $<$ 1 indicate a drug-induced decrease in protein levels, RFI = 1 indicates no-drug effect and RFI $>$ 1 indicates drug-induced increases in protein levels. The responses to **Os-3** and **Ir-10** differ at the protein level. This is most clear with βtubulin (B-Tub) which is down-regulated in response to **Os-3**, but up-regulated in waves in response to **Ir-10**. This could suggest that **Os-3** holds cells in earlier phases of the cell cycle, therefore not needing mitotic proteins like B-Tub to be expressed.

The levels of BRCA1, ATM and CHK2 are good indicators of DNA damage detection in A2780 cells. BRCA1 does not show increased levels in response to **Os-3** at either concentration. Dephosphorylated ATM is found in low levels throughout the time series in response to **Os-3**, however, active (phosphorylated) ATM* is found in higher levels, particularly with higher doses of **Os-3**. Activated CHK2* can also activate p53 to p53* during DDR. p53* can activate the expression of multiple downstream genes, including p21. CHK2* is found in high levels in cells exposed to the higher dose of **Os-3**, less so at the lower concentration.

Moving further down the DDR branches, Figure 5.5 shows that CDC25A, required for G1/S transition is in high levels after 24 h exposure to **Os-3**, which could permit the progression of cells through to S phase. However, CDK2, also required for G1/S transition is down-regulated, which could prevent entry into S phase.

Active p21* is found in differentially higher levels after 48 h exposure to **Os-3** at the lower dose and maximum after just 4 h, during exposure to the higher dose. The collectively higher levels of activated ATM, CHK2, p53 and p21 highlights the activation of DDR after cells are exposed to **Os-3**. Low levels of Rb* and Rb**, due to p21 inhibition of CDK2 complexes, suggest that cells are not preparing for entry into S phase. With low levels of CDK1 and β-tubulin suggesting cells are also not at the G2 or M phase. This likely suggests that cells are being held in G1 phase by **Os-3**, throughout the time series.

Flow cytometry experiments were performed in cells exposed to **Os-3**, to detect which stage of the cell cycle was most populated. This experiment works by measuring the red fluorescence of propidium iodide (PI), which intercalates with the DNA inside cells. Given the DNA content is duplicated during S phase, following the fluorescence levels of PI can identify which phases of the cycle are most populated. In other words the PI fluorescence will gradually increase through S phase, before stabilising at double the original fluorescence reading, going into G2.

Figure 5.6 summarises the flow cytometry results for cells exposed to **Os-3** for 24 h, where control values are shown in blue and osmium-treated cells in orange.

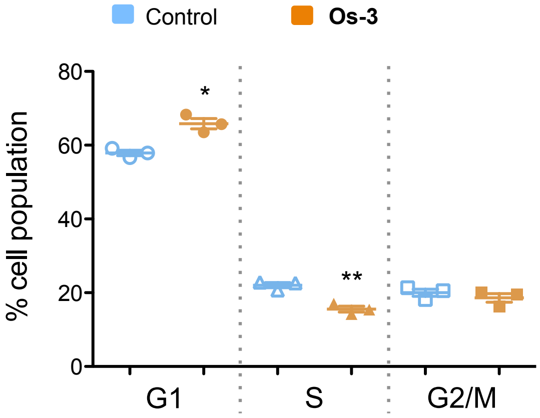

Figure 5.6: **Graph showing flow cytometry data for cells exposed to Os-3.** Each pair of values corresponds to a particular phase of the cell cycle, described on the x axis, with cell populations for control samples shown in blue, and those for **Os-3**-exposed samples in orange. * indicates $p < 0.10$ and ** indicates $p < 0.05$ after a Welch two sample t-test between control- and compound-exposed samples in each stage of the cell cycle. The most significant drug effects were shown in G1 and S phase of the cell cycle. Where **Os-3** increased the population of cells found in G1 phase and reduced the population of cells in S phase.

At any one time, in the control sample most cells are found in G1 phase, this is normal as G1 phase is the longest phase in the cell cycle. A significant increase in cells populating G1 phase in response to **Os-3**, with a subsequent reduction in both S and G2/M phase cells. This supports the RPPA data for **Os-3** which showed differentially lower levels of S, G2 and M phase markers.

In contrast to **Os-3**, **Ir-10** appears to mobilise a BRCA1 DNA damage response after 24 h, at both low and high concentrations. However, similarly to **Os-3**, there is activation of downstream DDR components, e.g. CHK2*, p53* and p21*. This suggests that DNA damage is also detected in response to **Ir-10**, but that this type of DNA damage caused may differ, resulting in BRCA1 involvement.

Assessment of cell cycle markers in response to **Ir-10**, tells a very different story to that shown for **Os-3**. After exposure to **Ir-10**, there are M-phase markers, particularly after exposure to the lower dose of **Ir-10**. For example, there is a high level of β-tubulin in response to 0.15 μM **Ir-10** at both 24 and 48 h, with an additional increase in the levels of CDK1. This suggests that cells have the proteins available to allow progression from G2 to M phase of the cell cycle. At the higher dose of **Ir-10**, both tubulin and CDK1 levels do not change from the control, suggesting a larger cell cycle affect is induced. The higher levels of Rb* protein suggest that cells have passed, or are at least able to pass, the G1/S transition point. This was not shown after exposure to **Os-3**. Therefore in response to **Ir-10**, cells may be in late S phase, or G2 phase of the cell cycle.

A second flow cytometry experiment was conducted to explore cell cycle populations in response to **Ir-10**, with the results shown in Figure 5.7.

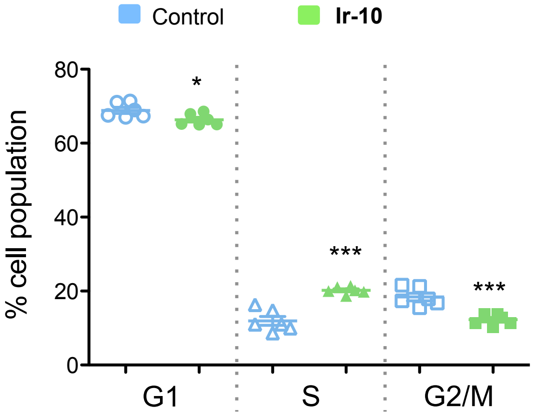

Figure 5.7: **Graph showing flow cytometry data for cells exposed to Ir-10.** Each pair of values corresponds to a particular phase of the cell cycle, described on the x axis, with cell populations for control samples shown in blue, and those for **Ir-10**-exposed samples in green. * indicates $p < 0.10$ and *** indicates $p < 0.01$ after a Welch two sample t-test between control- and compound-exposed samples in each stage of the cell cycle. In comparison to **Os-3**, **Ir-10** affects all three stages of the cell cycle, decreasing the population of cells in G1 phase and G2/M phase, and significantly increasing the number of cells in S phase.

Figure 5.7 shows a highly significant increase in cells populating S phase of the cell cycle, with a subsequent decrease in those in G1 and G2/M, compared to the control. This, together with the RPPA, confirms that DNA damage is detected in response to **Ir-10** and that cells are arrested in S phase of the cell cycle after 24 h exposure.

5.2.1.2 Cytokine response

The results from the RNA sequencing experiments in Chapter 4 suggested that cells activated an immune response to both **Os-3** and **Ir-10**. Figure 5.8 shows the involvement of components in the interferon pathway, activating STAT (signal transducer and activator of transcription) proteins.

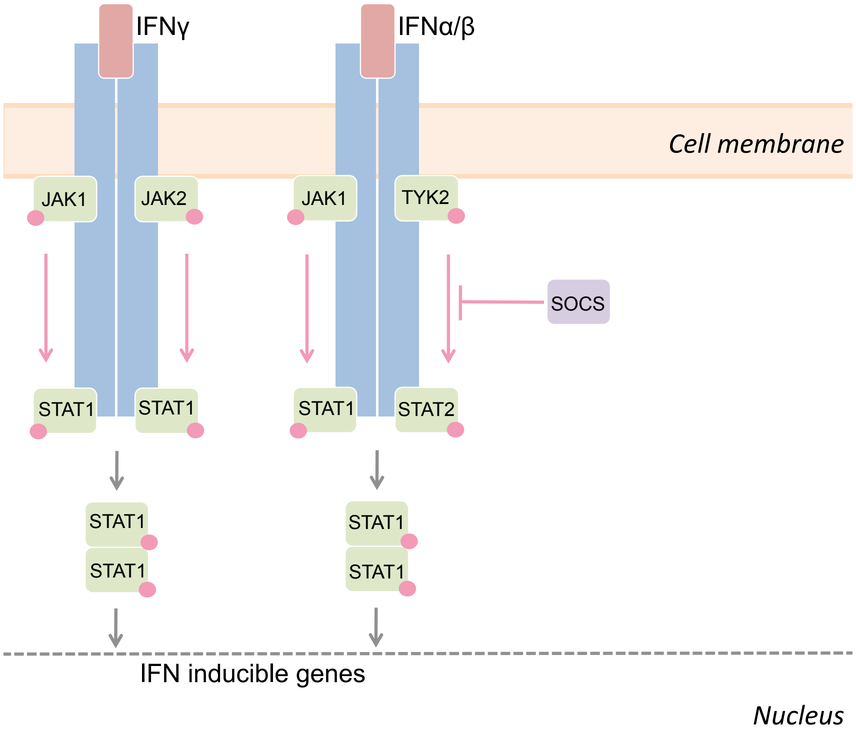

Figure 5.8: **Schematic showing components involved in interferon signalling.** Interferon γ, α and β (IFN) bind to interferon receptors activating phosphorylation events between JAK, STAT and TYK proteins, where pink spots highlight phosphorylated proteins. Downstream phosphorylated STAT complexes translocate to the nucleus and initiate the expression of interferon, interleukin and growth factor inducible genes.

Interleukin and growth factor receptors present similar activation to that of the interferon receptors shown in Figure 5.8, where STAT1 and 2 are used in interferon inducible gene expression and the other STAT proteins, 3,4,5,6, are used to activate interleukin/growth factor responses. In each case, cytokine molecules would either be produced by cancer cells responding to stress and diffuse from the cell to bind to the cell surface receptors. In an *in vivo* situation, cytokines are primarily produced by host immune cells, binding to cell surface receptors to initiate a cellular response to target the intracellular "infection".

STAT proteins are phosphorylated by JAK and TYK proteins, before forming STAT*/STAT* complexes and translocating to the nucleus to induce response genes. The interferon, interleukin and growth factor inducible genes are involved in controlling a variety of processes inside cells, with complex crosstalk mechanisms between pathways.

Using RPPA, 15 upstream components were studied, again at two concentrations (0.15 and 0.45 μM) of **Os-3** and **Ir-10** across a 72 h time course (Figure 5.9).

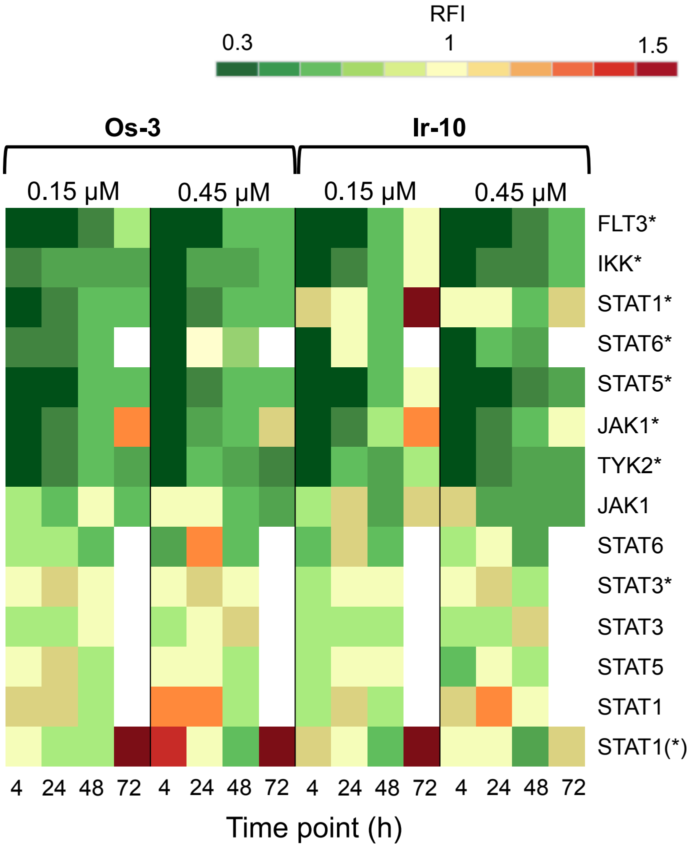

Figure 5.9: **Heat map showing the relative fluorescence intensity (RFI) values for a selection of cytokines in cells exposed to Os-3 and Ir-10 across a 72 h time series.** RFI values $<$ 1 indicate a drug-induced decrease in protein levels, RFI = 1 indicates no-drug effect and RFI $>$ 1 indicates drug-induced increases in protein levels. The heat map shows a differential response between the two compounds, most notably shown with increased levels of phosphorylated STAT1 (STAT1*, P Tyr701) in response to **Ir-10**, but not in response to **Os-3**. In response to both compounds, STAT1 and its second phosphorylated form STAT1(*) (P Ser727) were detected in high-levels, particularly STAT1(*) after 72 h exposure. This suggests that cells are activating the JAK-STAT pathway in response to both compounds.

Figure 5.9 shows that in response to both **Os-3** and **Ir-10**, most of the STAT proteins and their phosphorylated STAT* counterparts were down-regulated across the time series. Components that were particularly down-regulated included STAT5*, TYK2* (tyrosine kinase 2), FLT3 (fms-like tyrosine kinase 3) and IKK (IκB kinase). STAT3/3* and STAT5/5* are used in growth factor-activated pathways, with the remaining STAT proteins involved in various interleukin responses, together with IKK. FLT3 is regulated by different cytokine receptors, namely TNFα and TGFβ which inhibit this proteins activity.

Therefore the down-regulation of FLT3 agrees with the assignment of TNF and TGF as upstream regulators involved in cellular response to both **Os-3** and **Ir-10** in Chapter 4.

Assessing the proteins found in differentially higher levels provides more information about the immune response. There were only a few components shown in Figure 5.9 that were up-regulated in response to the compounds. For example, STAT1 and STAT1(*) (phosphorylated at Ser727) were up-regulated in response to **Os-3** and **Ir-10**, and STAT1* (phosphorylated at Tyr701) in response to just **Ir-10**.

This suggests specific modulation of the cytokine response pathways, and highlights differences between the osmium and iridium compounds. JAK1/1*, which phosphorylates STAT1, showed some up-regulation in response to both compounds, particularly after 72 h, where JAK1* was at a maximum in response to both compounds, together with phosphorylated STAT1. TKY2*, which phosphorylates STAT2, was consistently down-regulated throughout the time series which suggests that cytokine activation is primarily though IFNγ, and not IFNα/β.

5.2.1.3 Apoptosis

The RNAseq results in Chapter 4 showed that apoptoitc initators were up-regulated between 12 and 24 h, but that pro-apoptotic caspases were down-regulated throughout the 48 h time series. In addition, apoptotic inhibitor proteins (IAPs) were up-regulated. Figure 4.21 summarised the components involved in extrinsic and intrinsic apoptosis.

RPPA was used to study the differential levels of eighteen apoptotic proteins, five pro-survival proteins and thirteen pro-apoptotic proteins, in cells responding to **Os-3** and **Ir-10** across a 72 h time series. Figure 5.10 summarises the results as RFI values, where components above the black line are pro-survival, and below are pro-apoptotic.

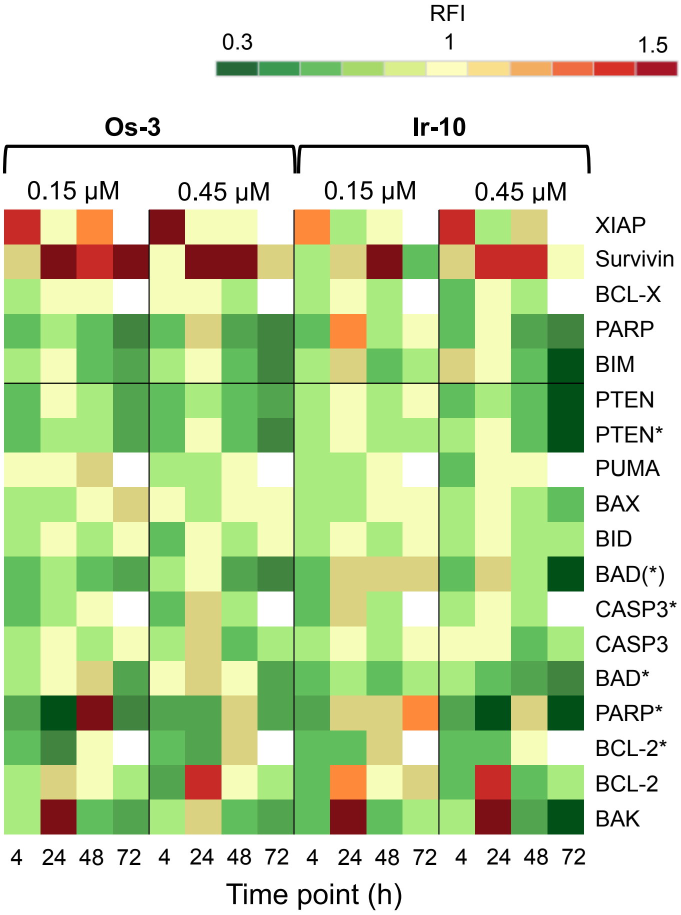

Figure 5.10: **Heat map showing the relative fluorescence intensity (RFI) values for a selection of apoptotic proteins in cells exposed to Os-3 and Ir-10 across a 72 h time series.** RFI values < 1 indicate a drug-induced decrease in protein levels, RFI = 1 indicates no-drug effect and RFI > 1 indicates drug-induced increases in protein levels. XIAP, Survivin, BCL-X, PARP and BIM represent pro-survival proteins, with the remaining, pro-apoptotic proteins. In response to both compounds, most pro-apoptotic proteins are down-regulated, with the exception of apoptotic-initiation proteins like BCL-2 and BAK, which were detected in significantly high levels after 24 h exposure. High levels of pro-survival proteins like XIAP and Survivin suggest that apoptosis is blocked at the caspase level, as these are inhibitor of apoptosis (IAP) proteins and target caspase-activation during the effector phase of apoptosis.

As a general observation, proteins were detected in equal levels for both compounds, at both concentrations. Compounds **Os-3** and for **Ir-10** induced high levels of IAP proteins, survivin and XIAP. The RFI values across the time series for these up-regulated pro-survival proteins were notably higher in **Os-3** exposed cells compared to **Ir-10**. BCL-X, which is a pro-survival protein located in the mitochondria, was down-regulated suggesting specific modulation of the apoptotic pathway.

Of the pro-apoptotic proteins, most were down-regulated, however, BCL-2 and BAK, which are initiator proteins, were up-regulated between 24 and 48 h. In addition, cleaved PARP (PARP*), which is cleaved by CASP-3, was present in higher levels during the middle of the time course. However, likely due to XIAP, the levels of CASP-3 remained low, suggesting PARP may have been cleaved by another cellular component (e.g. IFN). BAD(*), which is also an apoptotic initiator, was found at higher levels in cells exposed to **Ir-10**, but consistently lower levels in response to **Os-3**.

Collectively, RPPA provided a similar conclusion to that of the RNAseq results in Chapter 4, that apoptosis may occur within a 72 h time period, but that only a small apoptotic response is activated.

Flow cytometry studies were performed to measure the level of apoptotic cells after exposure to **Ir-10**. These experiments measure the fluorescence of annexin V and propidium iodide dyes, where the former identifies early apoptotic cells and the latter identifies late-apoptotic and/or necrotic cells. During early apoptosis membrane-bound phosphatidylserine proteins, which ordinarily face into the cytoplasm, translocate to the outside of the cell membrane and allow annexin V binding. A cell in early apoptosis, will still maintain its membrane integrity, therefore DNA intercalating dye, propidium iodide, cannot pass through. Once the cell has lost viability, its membrane becomes permeable to propidium iodide, which fluoresces upon binding to DNA.

It is noted that without further assays it is difficult to identify whether necrotic cells are those which have died via the process of necrosis, or whether the cells are in secondary necrosis and are therefore in the final stages of apoptotic, autophagic or oncotic cell death.

Figure 5.11 shows a flow cytometry trace measuring annexin (green) and propidium iodide (red) fluorescence split into four quadrants representing alive, early apoptotic, late apoptotic and necrotic cells.

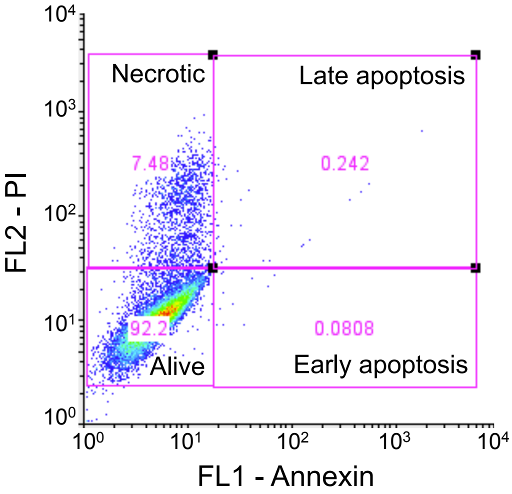

Figure 5.11: **Graph showing the segregation of an example flow cytometry trace into cell death quadrants.** Measuring the level propidium iodide (PI) and annexin fluorescence in single cells allows separation of cell populations into different stages of apoptosis. Cells with high annexin fluorescence are said to be in early apoptosis as annexin binds to phosphatidylserine proteins, which are extracellular markers of early apoptosis. High PI fluorescence indicates the loss of membrane integrity, allowing the dye to intercalate with DNA, and is a marker for necrosis which either signifies cells are in the final stages of apoptosis or that they have used necrosis as their primary mechanism for cell death. Here, the majority off cells are still alive (92 %), with 7 % necrotic and the remainder in apoptosis.

A series of experiments was performed to measure the level of apoptosis in A2780 cells exposed to **Os-3** and **Ir-10** under various different conditions. The first experiment assessed the level of apoptosis in cells exposed to **Os-3** for 24 and 72 h at $\frac{1}{3}\text{GI}_{50}$, compared to a negative control. Figure 5.12 summarises the results as a % of cells in each of the four quadrants, in each sample.

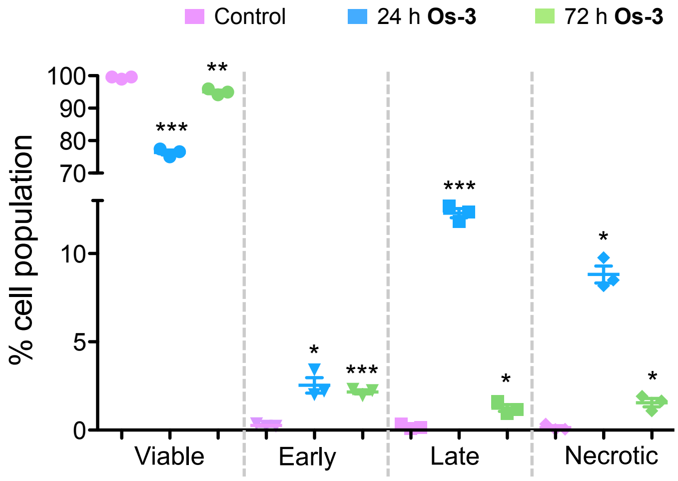

Figure 5.12: **Graph showing the % of cells populating each stage of apoptosis/cell death after exposure to Os-3 for 24 and 72 h.** Each triplicate set of values corresponds to a particular phase of cell death (described along the x axis), with cell populations for control samples shown in purple, those for 24 h **Os-3**-exposed in blue and those for 72 h **Os-3**-exposed samples in green. * indicates $p < 0.10$, ** indicates $p < 0.05$ and *** indicates $p < 0.01$ after a Welch two sample t-test between control- and compound-exposed samples in each stage. After 24 h exposure, there is a significant drop in viable cells, and a significant increase in late apoptotic and necrotic cells. However, after 72 h exposure the cells have started to recover, with an increase in viable cells and a decrease in apoptotic/necrotic cells.

The control cells appeared to remain viable throughout the time series with >99% of cells remaining in this quadrant. After 24 h, 76.5 % of cells were viable, 2.5% in early apoptosis, 12.3% in late apoptosis and 8.8% necrotic. After 72 h exposure, 95.0% were viable, 2.2% were early, 1.2% were late apoptotic and 1.6% were necrotic. This could suggest that **Os-3** kills off an initial percentage of cells within 24 h, but after this time, the remaining cells recover and maintain integrity.

The remaining experiments assess apoptosis in **Ir-10**-exposed cells under different conditions. The two graphs in Figure 5.13 show the levels of apoptosis after 24 and 48 h exposure to **Ir-10** at two doses, 0.13 μM and 0.40 μM.

After 24 h exposure, there was a slight decrease in cell viability, with a more significant decrease when exposed to a higher dose of **Ir-10** (95.1%) compared to the lower dose (94.2%). There was a higher population of cells in early apoptosis at the higher dose compared to the lower (2.0% and 1.3%, respectively), but a lower number of late apoptotic (1.1% and 1.5%) and necrotic cells (2.2% and 2.3%).

After 48 h there was a more significant drop in cell viability, now down to 58.0% at 0.13 μM and 56.4% at 0.40 μM. The population of cells in early apoptosis was actually lower in drug exposed cells than control cells. This is likely due to a lack of nutrients available in freely dividing control cells. There were on average, a larger population of cells in late apoptosis at the higher dose of iridium compared to the low, 41.2% and 30.2%. However, there were more necrotic cells present after exposure to the lower dose of **Ir-10**, 11.8% and 2.5%.

Finally, an experiment was performed to investigate the recovery of cells exposed to 0.13 μM **Ir-10**. Here, cells were exposed to **Ir-10** for 24 h, before drug-containing medium was removed and replaced with fresh medium. The cells where then left for a further 48 h to recover, and the level of apoptosis compared to that for cells which had been exposed to **Ir-10** for a full 72 h period (Figure 5.14).

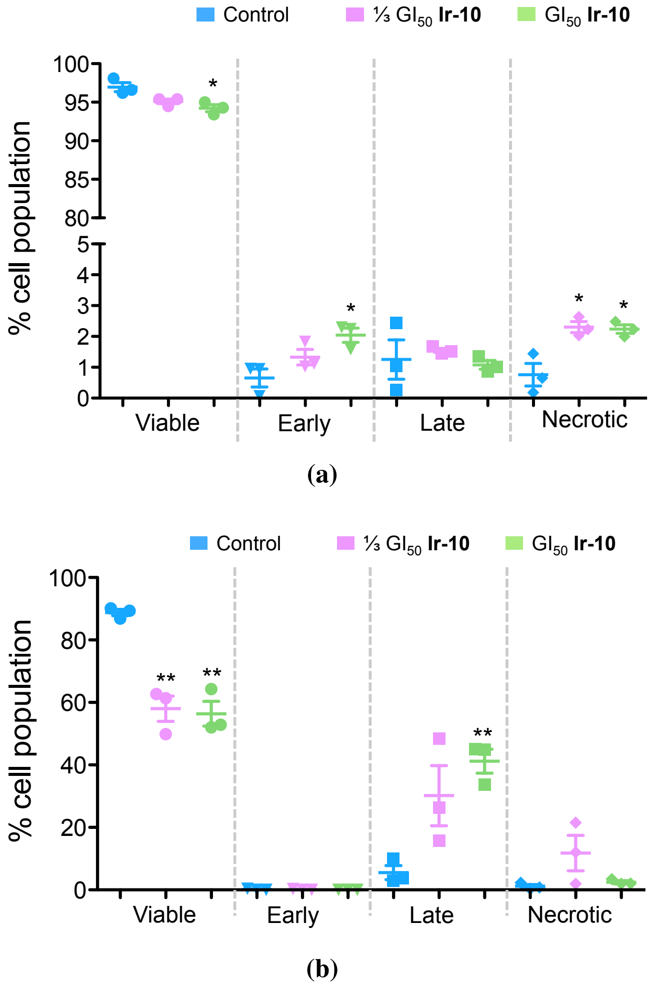

(a)

(b)

Figure 5.13: **Graph showing the % of cells populating each stage of apoptosis/cell death after exposure to Ir-10 for 24 h (top) and 48 h (bottom), at 0.13 μM ($\frac{1}{3}$GI$_{50}$) and 0.40 μM (GI$_{50}$).** Each triplicate set of values corresponds to a particular phase of cell death (described along the x axis), with cell populations for control samples shown in blue, those for 0.13 μM **Ir-10**-exposed in pink and those for 0.40 μM **Ir-10**-exposed samples in green. * indicates $p < 0.10$ and ** indicates $p < 0.05$ after a Welch two sample t-test between control- and compound-exposed samples in each stage. Significance testing was done between each treatment and the control (for each quadrant), using a Welch unpaired t test. In contrast to **Os-3**, **Ir-10** doesn't cause a significant reduction in viable cells after 24 h, instead the activation of cell death is more pronounced after longer exposure. Both the low and high concentrations of **Ir-10** cause a similar decrease in cell viability, however at the lower concentration there is more necrosis compared to the higher.

This figure shows a slight increase in cell viability with a 48 h recovery period, with a 95.9% population of live cells compared to 94.9% without a recovery period. However, the level of early apoptotic cells, and the level of necrotic cells showed little difference,

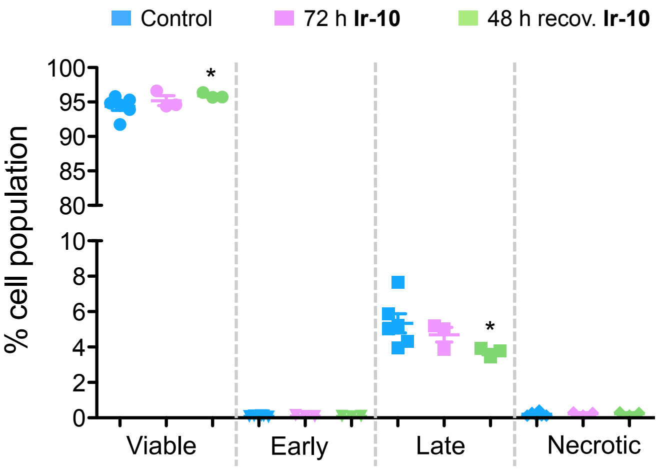

Figure 5.14: **Graph showing the % of cells populating each stage of apoptosis/cell death after exposure to $\frac{1}{3}GI_{50}$ Ir-10 for 72 h, with and without a 48 h recovery period.** Each triplicate set of values corresponds to a particular phase of cell death (described along the x axis), with cell populations for control samples shown in blue, those for 72 h **Ir-10**-exposed in pink and those for exposed to **Ir-10** for 24 h, and then left to recover for 48 h, in green. * indicates $p < 0.10$ after a Welch two sample t-test between control- and compound-exposed samples in each stage. There is a slight recovery in cell viability when cells are given 48 h recovery in drug-free media and a decrease in late-apoptotic cells.

in fact comparing Figure 5.13 with Figure 5.14 there is a further recovery in necrotic cells from 48 h to 72 h. With regards to late apoptosis, there were fewer cells in this stage with 48 h recovery, compared to 72 h exposure (4.7% and 3.7%). Again, this assay highlights the nutrient restraints for control cells left to grow for 72 h.

5.3 Discussion

This chapter aimed to explore cellular response at the translational level, and compare findings to those presented in Chapter 4. Chapter 4 proposed the production of reactive oxygen species (ROS) had involvement in the MOA of **Os-3** and **Ir-10**, possibly through mitochondrial targeting. Chapter 3 further supported this, showing all compounds to be most active in breast cell line MDA-MB-468 in the NCI-60 screen, which had inherent deficiencies in oxidative stress response machinery. Both the upstream mechanisms which produce ROS and the downstream effects of ROS production span a vast array of pathways inside cells. Specific pathways were selected for RPPA study, namely DNA damage response, cell cycle arrest, cytokine activation and apoptosis to tie in with those findings by RNA sequencing.

5.3.1 DNA damage response

DNA is an established target for metal-based anticancer agents, namely cisplatin and its derivatives.[8] Cells are equipped with mechanisms to repair such damage, however, ovarian cancers often lack the proper tools for DNA damage repair (DDR).[9, 10] Resistance to conventional platinum therapy often originates from the ability of cancer cells to repair DNA lesions caused by cisplatin, even in cell lines with DDR deficiencies.[11] DNA damage caused by cisplatin is often not selective for cancer cells, and can be just as damaging to normal cells if used in high doses.

In contrast, it is also possible to damage DNA through indirect mechanisms, and DNA is a well-known target for reactive oxygen species, particularly guanine bases.[5] DNA damage caused indirectly by anticancer compounds, through selective ROS generation, could provide a more targeted approach to achieving this MOA.

Assessing DNA damage caused by **Os-3** and **Ir-10** provided different insights into each compound. In previous studies, **Os-3**, has been shown to undergo hydrolysis, but not to bind to DNA nucleobases. The remaining osmium compounds studied in this thesis have also been shown not to bind to DNA. However, Chapter 3 showed a large correlation of the osmium compounds to DNA interacting agents, although largely not to alkylating agents like cisplatin.

The RPPA work for **Os-3** highlighted the detection of DNA damage response (DDR), particularly with the typical ATM-CHK2-p53-p21 pathway activation which acts to maintain arrest in G1 to allow DNA repair. Flow cytometry experiments suggested that DDR activation resulted in an increase in cells populating the G1 phase of the cell cycle. Interestingly, at higher concentrations, **Os-3** begins to induce S phase arrest in A549 lung cancer cells.[12] As shown in Chapter 1 (Figure 5.15) in colorectal cell line HCT116p53(-/-), **Os-3** is ca. x4 less potent compared to the wild-type cell line. This suggests that **Os-3** requires p53 for potent activity (G1/S arrest), however it is noted that in the HCT116p53(-/-) cell line the GI_{50} value was still in the submicromolar range.

In contrast to the osmium compounds, the iridium compounds have been shown to have direct DNA-binding tendencies. For example **Ir-6** has been shown to bind nucleobases in pSP73KB plasmid DNA, blocking RNA/DNA synthesis.[13] However, in this same study, only a small percentage of iridium accumulated inside cells as DNA-bound, suggesting interactions with other molecules to be a more primary MOA.[14] In Chapter 3, **Ir-10** established itself as a novel compound, sharing little similarity to any of the other organometallic compounds nor to drugs populating the NCI-60 database. However, it did share the highest level of similarity in selectivity to **Os-5**, where these were the only two compounds to correlate to alkylating agents. From the Sanger Institute screening, the activity of **Ir-10** was shown to be linked with *C-KIT* mutations, which is required for functioning of DNA repair mechanisms. Lung cancer cells with mutations in this gene were more sensitive to **Ir-10**, suggesting DNA-targetting may play a role in the MOA of **Ir-10**.

Much like **Os-3**, there was measurable activation of DDR through the ATM-CHK2-p53-

p21 pathway, however there was also activation of the BRCA1 protein, not shown for **Os-3**. RPPA suggested either S or G2/M phase arrest was possible in cells exposed to **Ir-10**, with measurements of S and G2/M phase markers at 24 and at 72 h. Interestingly, flow cytometry experiments showed S phase arrest after 24 h exposure. BRCA1 is an important protein in S phase of the cell cycle during DNA damage and is required for homologous recombination and DNA damage-induced S and G2/M phase arrest.[15] It could therefore follow that **Ir-10** does not require functional p53 for its MOA, as it does not require cells to be held in G1. This has been previously demonstrated in HCT116p53(-/-) where **Ir-10** did not lose activity, in fact it showed a 2-fold increase in potency (Figure 5.15).

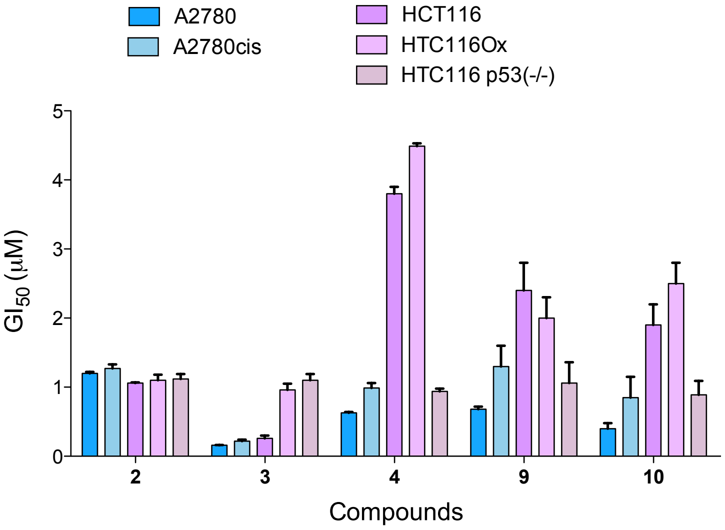

Figure 5.15: **Graph showing GI$_{50}$ values (± standard deviation) for compounds Os-2, Os-3, Os-4, Ir-9 and Ir-10 in different cell lines.** Ovarian cancer cell lines are shown in blue, and colorectal cell lines shown in purple. **Os-2** shows little dependence on cell type, showing equal activity in all 5 cell types. **Os-3** is significantly less active in oxaliplatin and p53(-/-) HCT116 cells, suggesting this compound may target DNA. In comparison **Os-4**, **Ir-9** and **Ir-10** show preferential activity in p53(-/-) cells. All compounds, except **Os-2** show increased potency in ovarian cancer cell lines compared to colorectal.[14, 16]

Collectively this could suggest that **Ir-10** has a more directed effect on DNA by exerting its activity either during DNA replication (S phase) or after the DNA content has been doubled (G2 phase). Unlike **Os-3** which appears to be most effective prior to DNA replication (G1 phase), and therefore may not have a DNA focussed MOA.

Unfortunately this means that **Ir-10** may have a more cisplatin-type MOA, and therefore may suffer from the same resistance mechanisms. Although, **Ir-10** did not correlate with cisplatin, or any of the platinum compounds through COMPARE. In contrast **Os-3** may be providing a newer approach to damaging DNA, through indirect mechanisms. **Os-3** is equipotent in platinum resistant cancer cell lines (Figure 5.15), suggesting that either the damage to DNA by ROS is not repairable by platinum-induced DDR enhancement, or that DNA damage is not a primary MOA.[17] Conversely, **Ir-10** loses activity in platinum-resistant A2780 cells suggesting that it is affected by cisplatin-induced resistance mechanisms.

5.3.2 Activating an immune response

One of the biggest issues with using high-content assays like RNAseq and MS-proteomics is that a drug's MOA can be swamped by larger cellular responses, like cell survival/death and stress signalling. Identifying these processes does not serve to help identify the underlying MOA of compounds, but can help to predict a response for *in vivo* and phase I studies.

Most of the upstream regulators identified during pathway analysis for the RNA sequencing were immune-related, identifying a general stress response to both compounds. Combining those findings with RPPA, highlighted some specific immune modulation, particularly regarding interferonγ (IFNγ), tumour necrosis factor (TNF), transforming growth factor (TGFβ) and interleukin signalling. Collectively these pathways control a plethora of cellular processes.

Studies have shown that interferonγ (IFNγ) administration *in vitro* and *in vivo* has antiprolfierative properties, even activating apoptosis in ovarian cancers via p53 and caspase-1.[18, 19] However, the release of INFs from cancer cells, and the interplay between IFNs and other cytokines with normal and with immune cells in the extracellular space can dictate tumour invasion. For example cancer cells which release anti-inflammatory cytokines like TGFβ are generally associated with resistance to immune attack by surrounding host cells.[19]

TNF and INFγ have also been linked to the direct production of reactive oxygen species (ROS) and nitric oxide (NO). It is therefore possible that the ROS generation measured for **Os-3** and proposed for **Ir-10** could be linked to this cytokine response, and not just to mitochondrial targeting.

We can only know the outcome of cytokine involvement in A2780 cells responding to **Os-3** and **Ir-10** in a physiologically relevant environment i.e. containing a variety of cell types. As proposed in Chapter 4, more assays will need to be conducted to determine the outcome of immune activation, and whether this response demonstrates an increase in tumour invasion in response to **Os-3** and **Ir-10**.

5.3.3 Cell death mechanisms

There are many different types of cell death and it is generally easiest to distinguish modes of cell death with whole cell imaging techniques.[20] However, there are often specific protein and gene markers which can also be studied. For example, apoptosis is normally characterised by caspase production, and by distinct budding of cell membrane structures into so-called apoptotic bodies. In contrast, oncosis involves swelling and not shrinking of the cell and is caused by accidental damage to the cell.[21] Necrosis is commonly identified as its own mode of cell death, but in fact necrosis is the last stage in any cell death pathway, i.e. both oncosis and apoptosis lead to necrosis and cell death.

Most anti-cancer agents aim to activate apoptosis in cancer cells, simply because this is the most controlled form of cell death, involving phagocytosis in the final stages. However, cancer cells often develop mechanisms to evade apoptotic cell death which starts to highlight the merits of alternative mechanisms, like pyroptosis, an immune-induced mechanism of cell death.[22]

Chapter 4 suggested poor transcriptional activation of apoptotic caspase markers, but some transcription of apoptotic initiators. RPPA has further supported this conclusion, with waves of apoptotic initiation towards the middle of the time course, followed by recovery towards the end. By flow cytometry, late apoptosis was measurable in **Os-3**-exposed cells at the 24 h time point, and in **Ir-10**-exposed cells at the 48 h time point. However, by 72 h, cells had recovered viability to both compounds.

This suggests that there is a wave of cell death occurring, perhaps as the top layer of cells in the petri dish are exposed to each compound and that the cells below this top layer remain intact and viable. To determine whether these remaining cells continue to divide or arrest cell division a more stringent time series experiment would need to be performed, either by flow cytometry or RPPA.

It is possible that cells either require a second bolus to activate cell death in a larger population or that a higher concentration of **Os-3** and **Ir-10** is needed. A previous study in A549 lung cancer cells showed that apoptosis could be increased when **Os-3** was administered at concentrations up to 5 μM (33 x GI_{50}).[12] This would be inline with conventional chemotherapy regimes which require repeat dosing. Chapter 7 studies apoptosis in A2780 cells exposed to higher doses of both compounds, measuring the outcome with imaging techniques.

5.4 Summary and Conclusions

The work in this chapter has helped to support the cell-wide findings presented in Chapter 4, and more accurately highlighted the subtle differences in the MOAs of **Os-3** and **Ir-10**. DNA damage response was activated in response to both compounds, accompanied with cell cycle arrest and a small level of apoptosis.

The purpose of the investigations into these organometallic compounds was to find a safer and more effective alternative to cisplatin. In this sense, only **Os-3** emerged as a good candidate, able to maintain it's activity in platinum resistant cancers. In contrast, **Ir-10** may activate DNA damage response inline with that of cisplatin as it is exhibits cisplatin cross-resistance. However, **Ir-10** does not require functional p53 to retain its potency, where as **Os-3** does. This is likely linked to the G1 arrest shown in cells responding to **Os-3**. This therefore highlights beneficial and detrimental properties for each compound.

The work in both Chapters 4 and 5 has helped to identify areas for future investigation, and has established methods for both RNA sequencing and protein microarrays to study cellular response at both the transcriptional and translational level. However, future experiments should use a larger number of time points between 4 and 48 h. This would help to better map the process of DNA damage repair, cell cycle progression and cytokine production. Measuring ROS over a tighter time course could also identify whether cytokines activate ROS production or whether the mitochondria are the main source. This would also reveal the exact point at which apoptotic initiators were up-regulated, and help identify whether dead cells passed though early/late apoptosis before becoming necrotic.

Chapter 6 integrates the RNAseq and RPPA for **Os-3** and **Ir-10**, directly comparing the transcriptomic and translational responses simultaneously.

References

[1] Weissenstein U, et al. (2006) Protein chip based miniaturized assay for the simultaneous quantitative monitoring of cancer biomarkers in tissue extracts. *Proteomics* 6:1427–1436.

[2] Pawlak M, et al. (2002) Zeptosens' protein microarrays: a novel high performance microarray platform for low abundance protein analysis. *Proteomics* 2:383–393.

[3] Akbani R, et al. (2014) Realizing the promise of reverse phase protein arrays for clinical, translational and basic research : a workshop report. *Molecular & Cellular Proteomics* pp 1625–1643.

[4] Boyd ZS, et al. (2008) Proteomic analysis of breast cancer molecular subtypes and biomarkers of response to targeted kinase inhibitors using reverse-phase protein microarrays. *Molecular Cancer Therapeutics* 7:3695–3706.

[5] Jena NR (2012) DNA damage by reactive species: Mechanisms, mutation and repair. *Journal of Biosciences* 37:503–507.

[6] Carroll J, Marangos P (2013) The DNA damage response in mammalian oocytes. *Frontiers in Genetics* 4:117.

[7] Ashwell S, Zabludoff S (2008) DNA damage detection and repair pathways-recent advances with inhibitors of checkpoint kinases in cancer therapy. *Clinical Cancer Research* 14:4032–4037.

[8] Siddik Z (2003) Cisplatin: mode of cytotoxic action and molecular basis of resistance. *Oncogene* 22:7265–7279.

[9] Assis J, Pereira D, Medeiros R (2013) Ovarian cancer and DNA repair: DNA ligase IV as a potential key. *World Journal of Clinical Oncology* 4:14–24.

[10] Curtin NJ (2012) DNA repair dysregulation from cancer driver to therapeutic target. *Nature Reviews Cancer* 12:801–17.

[11] Galluzzi L, et al. (2012) Molecular mechanisms of cisplatin resistance. *Oncogene* 31:1869–1883.

[12] van Rijt SH, Romero-Canelón I, Fu Y, Shnyder SD, Sadler PJ (2014) Potent organometallic osmium compounds induce mitochondria-mediated apoptosis and S-phase cell cycle arrest in A549 non-small cell lung cancer cells. *Metallomics* 6:1014–1022.

[13] Liu Z, et al. (2011) Organometallic half-sandwich iridium anticancer complexes. *Journal of Medicinal Chemistry* 54:3011–3026.

[14] Hearn JM, et al. (2013) Organometallic Iridium(III) Anticancer Complexes with New Mechanisms of Action: NCI-60 Screening, Mitochondrial Targeting, and Apoptosis. *ACS Chemical Biology* 8:1335–1343.

[15] Foray N, et al. (2003) A subset of ATM- and ATR-dependent phosphorylation events requires the BRCA1 protein. *The EMBO Journal* 22:2860–2871.

[16] Romero-Canelón I, Salassa L, Sadler PJ (2013) The contrasting activity of iodido versus chlorido ruthenium and osmium arene azo- and imino-pyridine anticancer complexes: control of cell selectivity, cross-resistance, p53 dependence, and apoptosis pathway. *Journal of Medicinal Chemistry* 56:1291–300.

[17] Fu Y, et al. (2010) Organometallic osmium arene complexes with potent cancer cell cytotoxicity. *Journal of Medicinal Chemistry* 53:8192–8196.

[18] Wall L, Burke F, Barton C, Smyth J, Balkwill F (2003) IFN-{gamma} Induces Apoptosis in Ovarian Cancer Cells in Vivo and in Vitro. *Clinical Cancer Research* 9:2487–2496.

[19] Brandacher G, Winkler C, Schroecksnadel K, Margreiter R, Fuchs D (2006) Antitumoral activity of interferon-gamma involved in impaired immune function in cancer patients. *Current Drug Metabolism* 7:599–612.

[20] Kroemer G, et al. (2009) Classification of cell death: recommendations of the Nomenclature Committee on Cell Death 2009. *Cell Death and Differentiation* 16:3–11.

[21] Majno G, Joris I (1995) Apoptosis, oncosis, and necrosis. An overview of cell death. *The American Journal of Pathology* 146:3–15.

[22] Bergsbaken T, Fink SL, Cookson BT (2009) Pyroptosis: host cell death and inflammation. *Nature Reviews Microbiology* 7:99–109.

Chapter 6. Dataset Integration

6.1 Introduction

This chapter analyses the transcriptomic (Chapter 4) and proteomic (Chapter 5) data in an integrative manner, using Bayesian modelling software, MDI (multiple dataset integration). This software was developed by Dr Paul Kirk and Sam Mason, extending the previous work of Dr Rich Savage, all based at Warwick Systems Biology Centre.[1, 2]

The analysis of complex biological data is often performed using clustering methodology, identifying co-expression or co-regulation of groups of genes and/or proteins.[3–5] Common clustering methods like k-means and hierarchical clustering treat each dataset independently, neglecting to consider the dependence between datasets.

MDI allows a unique ability to cluster genes/proteins within and between datasets, modelling each dataset using a Dirichlet-multinomial allocation (DMA) mixture model.[6] A mixture model is a probabilistic model used to identify subpopulations within an overall population i.e. used to identify groups of co-regulated genes/proteins. Bayesian inference is performed using a Markov chain Monte Carlo (MCMC) numerical method.

During modelling, each dataset is linked to capture the dependencies between datasets. MDI looks for items (genes or proteins) which are fused across datasets i.e. which group similarly across datasets. The main strength of MDI is the ability to cluster heterogenous datasets, which is particularly useful when studying genes and proteins, given the link between the two. The use of MDI has been demonstrated before, integrating three different data types: gene expression, ChIP data and protein-protein interactions (PPI).[1] This study demonstrated MDIs ability to separate fused components across all three datasets, into three main clusters with items in each cluster falling into functional categories. MDI has also been optimised for more clinical studies, identifying cancer subtypes based on genomic, transcriptomic and epigenetic data.[7]

MDI should identify where transcriptional and translational behaviour in cells is consistent, and whether this behaviour is observed under different treatment conditions. In addition to identifying groups of genes/proteins which cluster together in one or all datasets, MDI allows the similarity between this grouping in each pair of datasets, to be numerically quantified with an inferred posterior parameter (ϕ) (Figure 6.1).

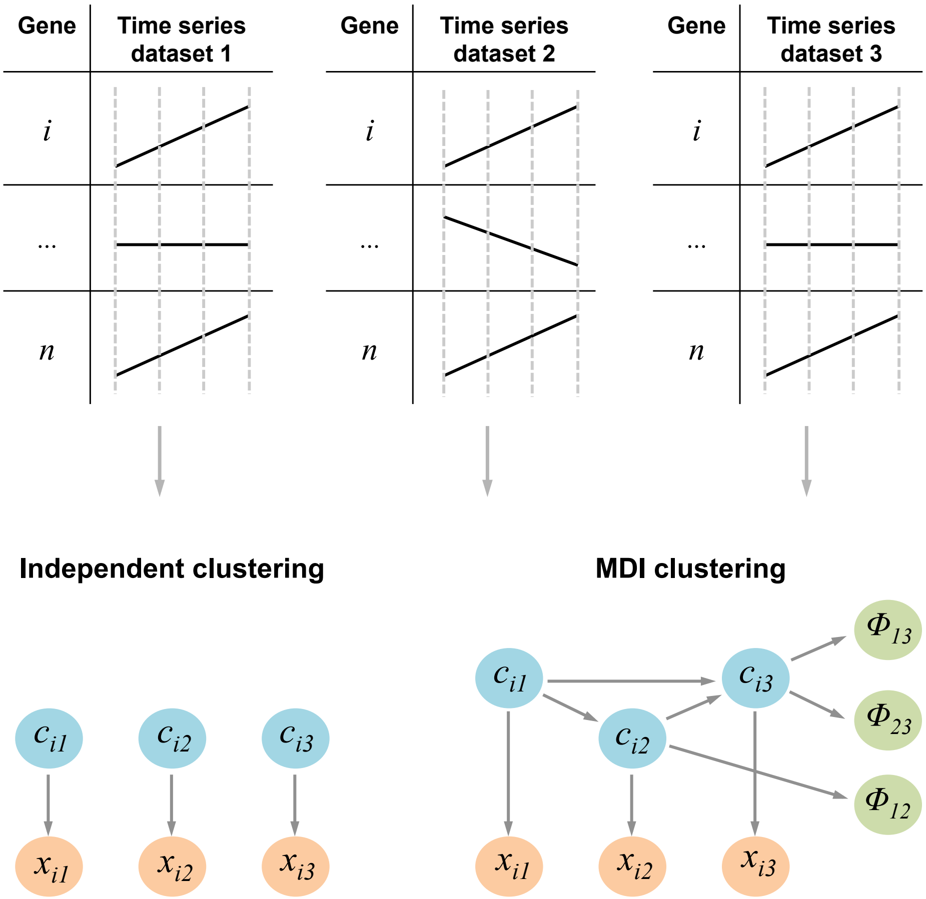

Figure 6.1: **Schematic showing the clustering of three time series datasets (*1, 2* and *3*), for genes *i* to *n*.** The top tables present hypothetical expression profiles across four time points, for each gene. These three datasets are then either clustered using independent methods (bottom left) or using MDI, which shares clustering allocations (bottom right). Here, c is the cluster allocation for each gene, where c_{i1} is the cluster allocation of gene i with time series expression observation x_{i1} in dataset *1*. MDI presents an additional parameter, ϕ, which measures the similarity in clustering across the datasets, where ϕ_{12} is a measure of cluster structure between dataset *1* and *2* for gene i.

MDI will be used to model gene expression data from the RNAseq experiments for **Os-3** and **Ir-10** with protein data from RPPA experiments for **Os-3** and **Ir-10**. Only those datasets generated after exposure to GI_{50} concentrations will be included, and only those genes which have associated protein measurements will be included. The table below lists the genes/proteins who's expression profiles included in the analysis.

Table 6.1: Table showing the genes/proteins used in the MDI analysis, together with their functional ontology. MDI will use the gene expressions and protein levels of these items after 4, 24, 48 and 72 h exposure to **Os-3** and **Ir-10**.

Ontology	Protein	Ontology	Protein
Apoptosis	BADP112	DDR	ATM
	BADP136		BRCA1
	BAK1		p21
	BAX		CHK2P
	BCL2		p53
	BIM		p53P
	BID	Cytokine	STAT1P727
	Survivin		STAT1P701
	CASP3		STAT5P
	PARP1	Signalling	AKT
	PARP1-cleaved		p38
Cell cycle	CycD		MTOR
	CycDP		MAP2K1
	CDC25A		PLCG1
	CDC25CP		PTEN
	CDK1P		PTENP
	CDK2		SRC
	RB1		MET
	RBP1		JAK1
	RBP2		JAK1P
	TUBB		IKK
Cell motility	E-cadherin	Transcription	p70
	B-catenin		MYC
	B-actin	Respiration	PDK1
	LKB1		
	RAP1A		
	FAK		

Every tenth sample was recorded, with a total of 3,00000 samples collected for a single MDI run. The analysis was run five times, and the convergence of the MCMC chains was assessed for each run. The aim of this analysis was to identify where genes and proteins were similarly co-regulated in response to treatment by both compounds. It also identified where genes and proteins are co-regulated differently in each compound.

6.2 Results

MDI estimates the pairwise similarity in clustering across each of the four dataset, with a mean $\hat{\phi}$ parameter, where $\phi_{1,2}$ measures the similarity between dataset 1 and 2 for a single gene and $\hat{\phi}_{1,2}$ measures the overall similarity between datasets 1 and 2.[1] Figure 6.2 plots this measure for each of the four datasets as a similarity matrix.

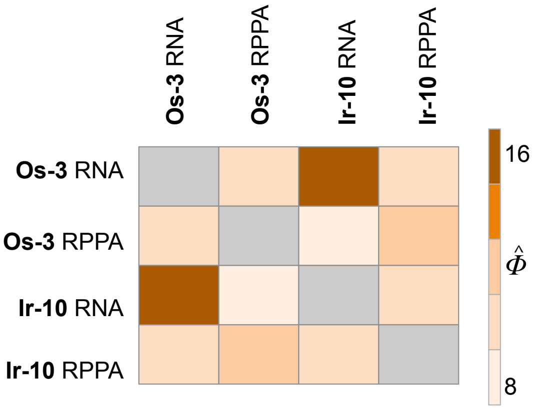

Figure 6.2: **Similarity matrix plotting pairwise $\hat{\phi}$ values.** $\hat{\phi}$ values are a measure of the pairwise similarity between each of the four datasets: **Os-3** RNAseq, **Ir-10** RNAseq, **Os-3** RPPA and **Ir-10** RPPA. The higher the value the more similar the pattern of clustering across pairs of datasets. The highest level of clustering similarity is between the gene expression profiles in response to both compounds.

Figure 6.2 shows that the highest similarity in clustering is between the RNAseq datasets for **Os-3** and **Ir-10** ($\hat{\phi}$= 16.2), with the biggest difference between the RPPA data for **Os-3** and the RNAseq data for **Ir-10** ($\hat{\phi}$= 8.9). This suggests that the genes used for MDI analysis had similar expression profiles in response to both compounds, however, the protein levels were different.

6.2.1 Clustering

The aim of using MDI is to identify items, in this case genes and proteins, which behave similarly and cluster together across different types of data i.e. transcriptomics and proteomics. A posterior similarity matrix (PSM) was plotted to visualise both the independent clustering in each of the four datasets, together with a consensus clustering structure.[7] This plot describes the posterior probabilities that two observations are in the same cluster.[8]

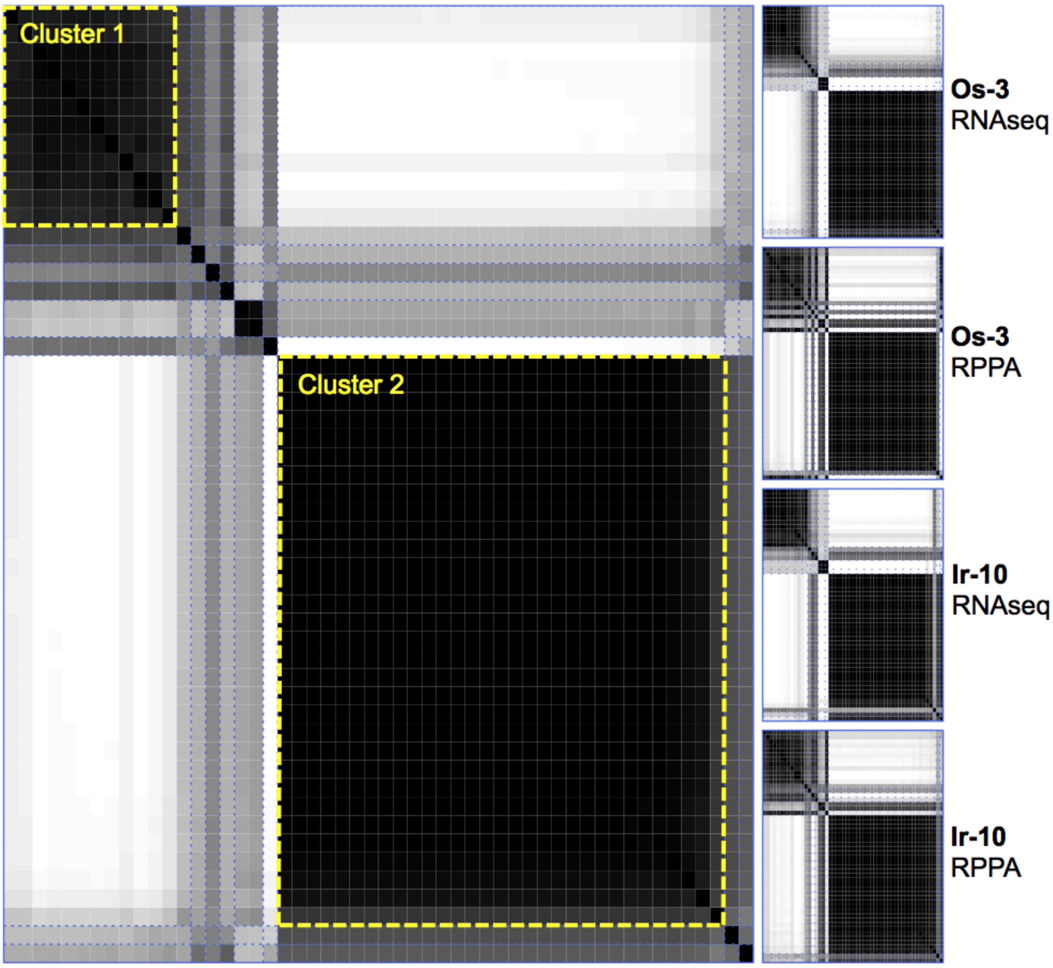

Figure 6.3: **Consensus posterior similarity matrix (PSM) showing the similarity in clustering structure across the Os-3 RNAseq, Os-3 RPPA, Ir-10 RNAseq and Ir-10 RPPA datasets.** Panels on the right present the independent clustering structure in each dataset, with the central plot showing an overlay of clustering in all four datasets. Darker spots indicate a higher probability that the given item (gene/protein) is clustered correctly. The two main clusters are highlighted in yellow.

Darker spots in the independent clustering patterns (right) indicate a high probability of a given pair of items belonging to the same cluster, the consensus plot shows the average probability over all four datasets, therefore darker spots indicate overlap in cluster assignments between datasets.[7] There are two main clusters of genes/proteins which show similar expression profiles across all four datasets.

The two main clusters in the consensus PSM are highlighted in yellow. The items (genes/proteins) associated with each cluster are described in Table 6.2 and 6.3.

Table 6.2: Table listing the genes/proteins associated with Cluster 1, sharing similarity in time series profiles across all four datasets.

Gene/protein	**Process**	**Function**
BID	Apoptosis	Pro-apoptotic
BAK1		Pro-apoptotic
BAX		Pro-apoptotic
p53	Cell cycle	Cell cycle arrest
p53P		Cell cycle arrest
p21		DNA repair
CDK1P		G2/M phase
PDK1	Metabolism	Respiratory enzyme
STAT1P701		Cytokine signalling
STAT1P727		Cytokine signalling
SRC	Signalling	Kinase activity

Table 6.3: Table listing the genes/proteins associated with Cluster 2, sharing similarity in time series profiles across all four datasets.

Gene/protein	**Process**	**Function**
ATM	Cell cycle	DNA repair/cell cycle arrest
CHK2P		DNA repair/cell cycle arrest
BRCA1		DNA repair/cell cycle arrest
CDC25A		G1/S phase
CDK2		G1/S phase
CYCD		G1/S phase
CYCDP		G1/S phase
RB1		G1/S phase
RBP1		G1/S phase
RBP2		G1/S phase
CDC25CP		G2/M phase
TUBB		M phase
CASP3	Apoptosis	Pro-apoptotic
BADP		Pro-apoptotic
BCL2		Pro-survival
PARP		Pro-survival
PTEN	Signalling	Kinase activity
PTENP		Kinase activity
AKT		Kinase activity
MAP2K1		Kinase activity
p38		Kinase activity
MTOR		Kinase activity
PLCG1		Various signalling
E-cadherin	Cell motility	Cell adhesion
LKB1		Cell polarity
RAP1A		Migration/adhesion
FAK		Migration
B-actin		Cell motility/structure
B-catenine		Cell-cell interactions
p70	Cell maintenance	Protein synthesis

All of the genes/proteins in Tables 6.2 and 6.3 had similar time series profiles in all four datasets i.e. the genes and proteins in these tables behaved the same in response to both **Os-3** and **Ir-10** at their GI_{50} concentrations. These include apoptotic markers like BID and BAX which were discussed in Chapters 4 and 5, where both compounds showed initiation of apoptosis with expression of *BID* and *BAX*. Both compounds also induced

DNA damage repair with the measurement of proteins like ATM and CHK2, both found in Cluster 2 showing that DNA damage repair was registered at the gene and protein level in response to **Os-3** and **Ir-10**.

The remaining items, not allocated to cluster 1 or 2, did not show a strong consensus clustering across the four datasets (Table 6.4).

Table 6.4: Table showing items which did not show similar time series profiles across all four datasets.

Gene/protein	**Process**	**Function**
BIM	Apoptosis	Pro-survival
Survivin	Apoptosis	Pro-survival
PARP-cleaved		Pro-apoptosis
PKCα	Signalling	Kinase
JAK1		Interferon γ
JAK1P		Interferon γ
IKK		Inflammatory
STAT5P		Cytokine

From Chapter 5, the survivin protein was measured in higher levels in response to **Os-3** than to **Ir-10** and from Chapter 4, the survivin gene (*BIRC5*) also showed higher levels of expression in response to **Os-3** compared to **Ir-10**. Thus resulting in non-consensus clustering across all four datasets.

6.3 Discussion

This chapter has assessed cellular response at the transcriptional and translational levels, in cells responding to **Os-3** and **Ir-10** over a time series. In previous chapters, this information was analysed independently. Here, MDI software has been used to analyse the data in a more integrative manner. Four datasets were analysed, **Os-3**-RNAseq, **Os-3**-RPPA, **Ir-10**-RNAseq and **Ir-10**-RPPA, each with three time points and 51 genes/proteins worth of data.

The aim of MDI is primarily to identify where cluster patterns overlap between different datasets. A consensus posterior similarity (PSM) matrix was constructed, which displayed this overlap in clustering structure, together with plots showing the independent clustering patterns (Figure 6.3).[7] Similar clustering was shown across all four datasets, splitting most of the items into two main clusters. The strongest similarity in clustering pattern was shown between the two RNAseq datasets, suggesting a high level of similarity in transcriptional response between the two compounds, for the genes/proteins included in the analysis.

All of the items included in Cluster 1 were similarly elevated in response to both **Os-3** and **Ir-10**. For example, *BID* and *BAX* were both up-regulated to initiate apoptosis between 12 and 24 h exposure to both compounds. And at the protein level, p53 was elevated in response to both compounds to activate DNA damage repair (DDR), primarily at 4 and 48 h. Of the STAT proteins, STAT1P was the most significantly up-regulated in response to both compounds, particularly after 72 h exposure. This was all demonstrated in heat maps in Chapters 4 and 5, where apoptotic initiation was shown for both compounds at the gene and protein level, yet late phase apoptosis markers, like CASP3 were not up-regulated. MDI has clustered these components together, quantifying the similarity in response for **Os-3** and **Ir-10** at the apoptotic, and DNA damage levels for specific components.

The items found in Cluster 2 were similarly elevated in response to both compounds. Tubulin (TUBB), BRCA1, CycD, p21, ATM, CHK2, CDC25CP and CDC25A were all elevated at 24 h at the protein level. In comparison, the proteins assigned to Cluster 1 were primarily elevated at different stages of the time series (4 and 48 h). Therefore MDI has separated these protein profiles by time series behaviour, as expected. The fact that p53, which is also a key component of DDR, was not clustered together with it's upstream activators suggests that p53 may also be modulated by different processes, and not just controlled by DDR.

The similar behaviours of these components in Cluster 1 and Cluster 2 across all four datasets, suggests that there is some underlying similarity in the cellular responses to both **Os-3** and **Ir-10**. Certainly, the work in Chapter 4 showed that both compounds induced oxidative stress, but that the compounds different favourability for their oxidative stress response pathways. Both compounds showed initiation of apoptosis, but no suggestions for activation of cell death through caspase cascades. And finally, both showed activation of DDR pathways, although this resulted in differential cell cycle arrest profiles by flow cytometry: **Os-3** arresting cells immediately in G1 phase and **Ir-10** showed slowing of the cell cycle, and some S phase arrest.

The remaining items, not allocated to Clusters 1 or 2, showed lower probabilities for being clustered similarly across all four datasets. This was supported in Chapter 5 for cleaved PARP protein, which was found in high levels after 48 h in response to **Os-3**, but not elevated in response to **Ir-10** until 72 h. This protein is a measure of apoptosis, as it is cleaved by CASP3. The expression and translation of survivin was also different across the two compounds, with **Os-3** generally inducing a higher level. This suggests that although the initiation of apoptosis was similar across both compounds, the down-stream components like caspase and caspase inhibitors are different in their response profiles.

6.4 Summary and Conclusions

Most of the biological interpretation of the RNAseq and RPPA data was done in previous chapters, however, MDI has quantified some of those findings. Highlighting the similarity in the initiation of apoptosis between both compounds, as well as the induction of DNA damage repair pathways in response to both.

To fully test MDI, there would need to be more components involved in the analysis, and there needs to be components involved which we know may behave differently to **Os-3** and **Ir-10**. This analysis could be achieved in the future by increasing the number of proteins measured by RPPA, and including this with the existing gene expression data collected by RNAseq. It could also be interesting to re-measure the protein levels used in this chapter in a different cell line, and compare findings between different compounds and different biological systems. However, for such an experiment it could be useful to perform experiments with synchronised cells, which could increase the performance of MDI by reducing the biological complexity of the data.

The larger the number of items used in this analysis, the more useful clustering analysis can become, negating the use for manual plotting and interpretation using heat maps and basic statistics.

References

[1] Kirk P, Griffin JE, Savage RS, Ghahramani Z, Wild DL (2012) Bayesian correlated clustering to integrate multiple datasets. *Bioinformatics* 28:3290–3297.

[2] Savage R, Ghahramani Z, Griffin JE, de la Cruz BJ, Wild DL (2010) Discovering transcriptional modules by Bayesian data integration. *Bioinformatics* 26:158–167.

[3] Verbanck M, Lê S, Pagès J (2013) A new unsupervised gene clustering algorithm based on the integration of biological knowledge into expression data. *BMC Bioinformatics* 14:42.

[4] Liu Y, Gu Q, Hou JP, Han J, Ma J (2014) A network-assisted co-clustering algorithm to discover cancer subtypes based on gene expression. *BMC Bioinformatics* 15:37.

[5] Polanski K, et al. (2014) Wigwams: Identifying gene modules co-regulated across multiple biological conditions. *Bioinformatics* 30:962–970.

[6] Ishwaran H, Zarepour M (2002) Dirichlet prior sieves in finite normal mixtures. *Statistica Sinica* 12:941–963.

[7] Savage RS, Ghahramani Z, Griffin JE, Kirk P, Wild DL (2013) Identifying cancer subtypes in glioblastoma by combining genomic, transcriptomic and epigenomic data. *International Conference on Machine Learning*.

[8] Fritsch A, Ickstadt K (2009) Improved criteria for clustering based on the posterior similarity matrix. *Bayesian Analysis* 4:367–392.

Chapter 7. Imaging

7.1 Introduction

This chapter focusses on investigating the mechanisms of action (MOA) of compounds **Os-1** (Os(η^6-bip)(NMe$_2$-azpy)I]PF$_6$), **Os-3** ([Os(η^6-p-cym)(NMe$_2$-azpy)I]PF$_6$), **Os-4** ([Os(η^6-bip)(F-azpy)I]PF$_6$), **Ir-9** (Ir(η^5-Cp^{xbiph})(ppy)Cl]) and **Ir-10** (Ir(η^5-Cp^{xph})(NMe$_2$-azpy)Cl]PF$_6$) by high content screening (HCS) and of **Ir-6** by transmission electron microscopy (TEM). **Os-3** and **Ir-10** were selected as they were the focus of the transcriptomics and proteomics analysis. **Os-4** and **Ir-9** were chosen for their novel patterns of selectivity in the cancer cell screens of Chapter 3. **Ir-6** was chosen for it's mid-level potency so that cells may not be too destroyed or degraded for visualisation by TEM.

7.1.1 High content screening

High content screening (HCS) has a prominent place in drug discovery and is simply the acquisition of images on a high-throughput scale, commonly capturing fluorescent microscopy readings.[1, 2] HCS systems operate on a similar principle to flow cytometry, measuring fluorescent readings on a single cell scale, except HCS captures images and not just fluorescent readings. Image analysis software, which is provided by the HCS system manufacturers allows accurate segregation of cells (Figure 7.1).

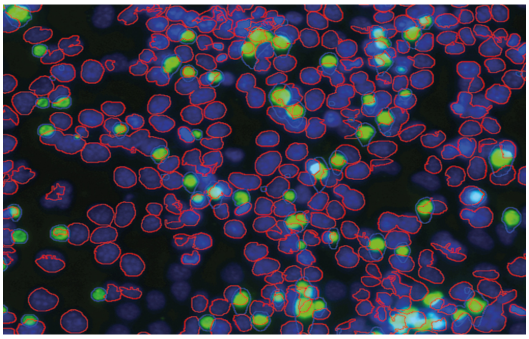

Figure 7.1: **High-content screening of rhesus monkey cells.** Cell nuclei appear blue and the infective 'elementary bodies' of chlamydia, which form blisters, fluoresce green. The red outlines are those after image analysis and show separation of fluoresence into individual cell structures. *Image provided by Dr S. Hess of the Max Planck Institute for Infection Biology, Berlin, Germany.*

In Figure 7.1, nuclear staining (blue) and chlamydia staining (green) are shown, with red outlining the cells as calculated by the image analysis software. Like flow cytometry, the HCS system will count the number of cells with a given fluorophore detected.

The fluorescent images are captured when light incident on a sample excites a fluorophore, which absorbs the light and emits light of a longer wavelength.[3] This occurs as the molecules in a sample absorb a photon of light, increasing their energy and causing an electron to enter an excited energy state. As the electron returns to a ground state, it loses energy in the form of light.

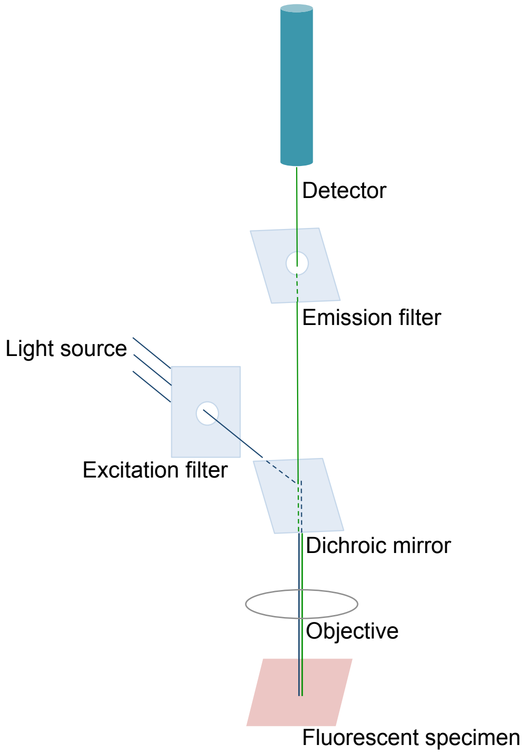

Figure 7.2: **Fluorescent confocal microscopy set-up.** A fluorescent or fluorescently-tagged sample is shown at the bottom of the image. A light source is used to excite the sample, using an excitation filter to all passage of light at specific wavelengths (e.g. blue) and using a dichroic mirror to focus the light onto the sample. The sample then emits light of a longer wavelength (e.g. green) which is focussed to the detector using the dichroic mirror and an emission filter. *Image adapted from Semwogerere (2008) Encyclopedia of Biomaterials and Biomedical Engineering. 705-714*

In Figure 7.2 a fluorescent marker in the sample is excited with a laser, passed initially through an excitation filter and dichroic mirror to allow passing of light in the blue region onto the sample.[3] After excitation, green light is emitted from the marker, and directed towards the detector by the dichroic mirror, through an emission filter which allows rejection of out-of-focus light. Fluorescence microscopy is a widely used tool in cancer research, applied to study both cellular drug effects and drug transport. A recent study by Guduru *et al* used confocal microscopy to study drug delivery of fluorescently-labelled paclitaxel into ovarian cancer cells when co-delivered with magneto-electric nanoparticles.[4]

High content fluorescent microscopy has been used in a plethora of biological studies, including those on cellular processes via individual protein tracking, as well as adapting the technology for use with other high-throughput techniques, like siRNA cell arrays.[5–7]

High content fluorescent screening was performed by Dr Neil Carragher at the Edinburgh Cancer Research Centre to make high throughput fluorescent measurements of A2780 ovarian cancer cells exposed to **Os-1**, **Os-3**, **Os-4**, **Ir-9** and **Ir-10**. After 48 h exposure, cells were extracted, dual-dyed and imaged. DAPI stain was used for nuclei measurements, to allow total cell counts to be obtained. DAPI is excited at 350 nm and emits at 455 nm as blue fluorescence. To measure the activation of apoptosis in compound-exposed cells, a NucView 488 Caspase-3 substrate was used. NucView was developed by Biotum, and follows caspase-3 activity inside cells. The substrate consists of a caspase-3 substrate peptide (DEVD) attached to a DNA binding fluorophore, and is excited at 485 nm, and emits at 515 nm. In the cytoplasm, caspase-3 cleaves the peptide, releasing the DNA binding probe which co-stains the nucleus (green) together with DAPI (blue).

Results from previous chapters showed little or no detection of caspase-3 in compound-exposed cells, therefore the concentrations were increased to a maximum of 2.5 μM to see if the extent of apoptosis could be increased.

The instrument used was The Olympus ScanR Screening Station, which allows image acquisition and analysis of cell samples in 96-well plates. Both green and blue fluorescence were taken for each sample and the total number of stained cells were counted.

7.1.2 Electron microscopy

Electron microscopy operates on the same principle as light microscopy, except an electron beam is used instead of light, allowing for greater resolution imaging. The approximate resolving power of a transmission electron microscope can be as low as 0.1 nm, compared to a standard light microscope with a resolving power of only 200 nm. Figure 7.3 shows the basic set up of a TEM instrument.

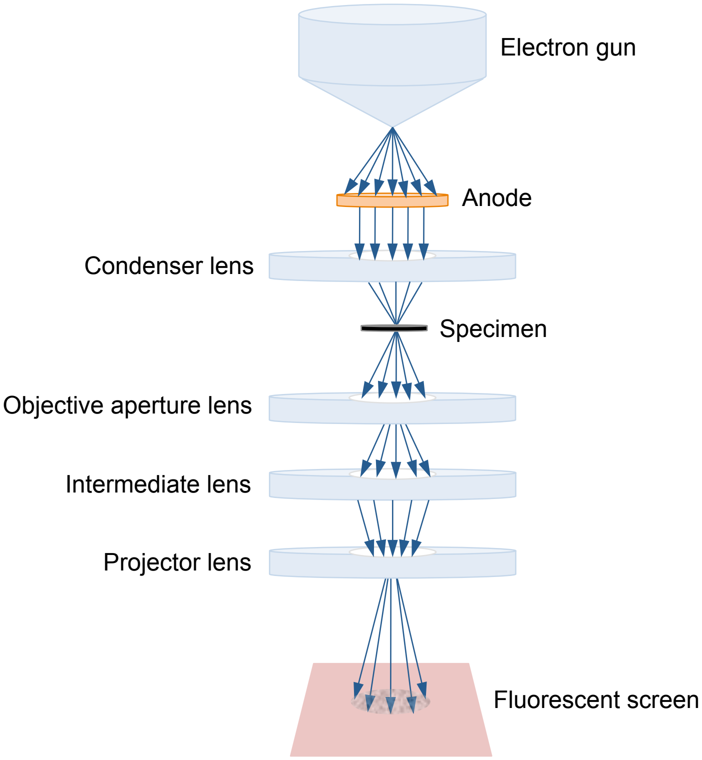

Figure 7.3: **Basic set up of a transmission electron microscope.** Electrons are fired from the electron gun and are focussed, through an anode and condenser lens, onto the sample. These electrons interact with the sample, some scattering and some transmitting. The transmitted electrons are passed through a series of lenses to project an image of the sample. The contrast seen in TEM imaging is a result of detracted electrons unable to pass through the specimen. The lighter regions in TEM images are created from transmitted electrons. *Image adapted from Joy (2008) Encyclopedia Britannica*

The electron gun produces a source of electrons with energies in the range 100,000 - 400,000 eV by heating a tungsten filament.[8] Negatively charged electrons are passed through a series of electromagnetic lens, where the image magnification is controlled by the strength of the lenses. The electron beam must pass through a vacuum to prevent absorption or deflection by particles in the air. Once the electron beam reaches the sample, it will either be transmitted through the sample or diffracted by it, the later creating contrast. When using this technique to image cells, the cells are first embedded in a polymer resin, before being thinly sliced on a diamond microtome, to a thickness of ca. 100 nm. Often, heavy metal dyes like OsO_4 are used as cell stains, where electrons from the electron beam are absorbed by the metal deposits lining the cellular compartments. The image formed by the interaction of the electron beam with the specimen is projected onto a fluorescent screen, which can be photographed.

For its resolving power, TEM is a valuable tool for cellular imaging and has been used successfully to explore drug effects on cellular morphology.[9] For example, a study by Morse *et al* studied cell death mechanisms in breast cell lines after exposure to docetaxel, showing non-apoptotic cell death through mitotic catastrophe.[10]

Whole-cell TEM images were taken of A2780 cells exposed to **Ir-6** at a high and low-dose, for 24 h. The machine used to capture the images was a JEOL 1200EXII TEM with a Gatan 1 k X 1 k CCD camera, situated in the University of Warwick Imaging Suite (School of Life Sciences). The resolving power of this instrument was leq 0.34 nm, providing high-resolution cell imaging.

7.2 Results

7.2.1 High content screening

Human ovarian cell lines A2780 and OVCAR-3 were exposed to compounds **Os-1** ($[Os(\eta^6\text{-bip})(NMe_2\text{-azpy})I]^+$), **Os-3** ($[Os(\eta^6\text{-}p\text{-cym})(NMe_2\text{-azpy})I]^+$), **Os-4** ($[Os(\eta^6\text{-bip})(F\text{-azpy})I]^+$), **Ir-9** ($[Ir(\eta^5\text{-}Cp^{xbiph})(ppy)Cl]$) and **Ir-10** ($[Ir(\eta^5\text{-}Cp^{xph})(NMe_2\text{-azpy})Cl]^+$) at an initial concentration of 2.5 μM, as well as a DMSO control, for 48 h. After this period, adherent cells were stained with DAPI, a blue stain to highlight cell nuclei, and Nucview, a green stain to highlight apoptotic caspase-3 expressing cells. Fluorescent images were taken in triplicate for each sample type, and the number of blue and green stained cells were counted. Figures 7.4 and 7.5 show a representative example of the fluorescent images taken in A2780 (Figure 7.4) and OVCAR-3 (Figure 7.5).

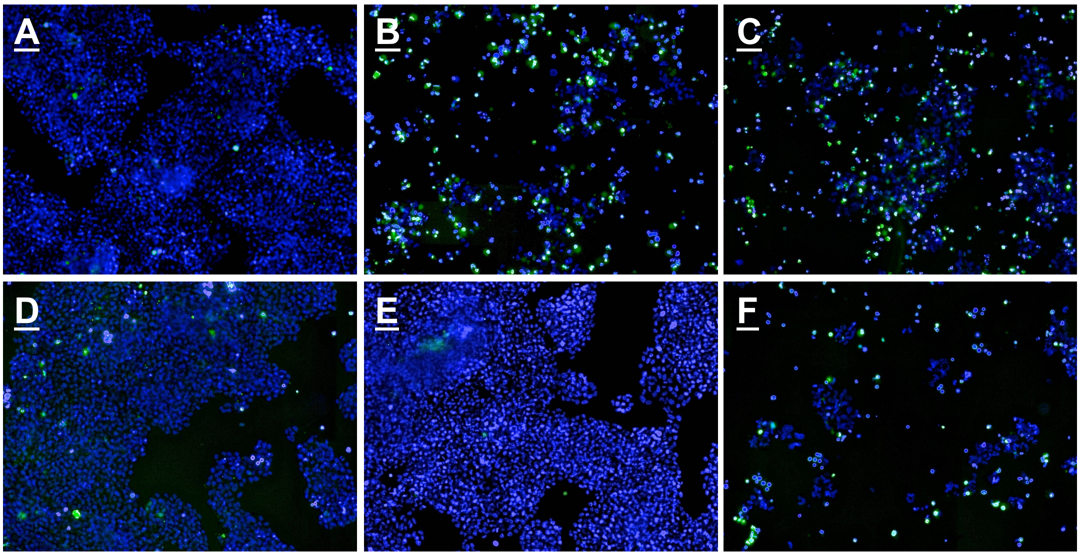

Figure 7.4: **Fluorescence images showing apoptotic A2780 human ovarian cancer cells after exposure for 48 h to (A) Control; (B) 2.5 μM Os-1; (C) 2.5 μM Os-3; (D) 2.5 μM Os-4; (E) 2.5 μM Ir-9; (F) 2.5 μM Ir-10.** DAPI is used to stain the nuclei of cells (blue), with the NucView reagent staining apoptotic cells (green). NucView is activated inside cells by caspase-3 and caspase-7 which are apoptotic effector proteins, therefore fluorescence of this probe is an indirect measure of apoptosis. Panels (B) **Os-2**, (C) **Os-3** and (F) **Ir-10** all show significant levels of apoptosis, together with a reduction in stained nuclei compared to the control (A). Panel (E) shows little nuclei reduction and no apoptosis, suggesting **Ir-9** is not cytotoxic at 2.5 μM. Panel (D) shows no apoptosis, but a reduction in the number of nuclei, suggesting that **Os-4** may be cytotoxic, but may not be activating cell death through apoptosis.

Figure 7.4 shows that each of the compounds behave differently in A2780 cells, with regards to apoptosis. This is interesting, given that anti proliferative activity is very similar (Table 1.1). Compounds **Os-1** and **Os-3** both cause significant apoptosis after 48 h exposure of the cells to 2.5 μM. For **Os-1** this is 18X the GI$_{50}$ value, and for **Os-3** this is 16X the GI$_{50}$ value. Compound **Ir-10** also activates apoptosis, at a concentration 6X its GI$_{50}$. **Os-4** and **Ir-9** do not activate a significant level of apoptosis (both at 4X GI$_{50}$ concentration), supported also by the large population of viable cells (blue fluorescence) remaining after exposure. The reduction in viability shown after exposure to **Os-1**, **Os-3** and **Ir-10** shows cytotoxic activity, with cell death occurring through apoptosis for **Os-1** and **Os-3** and partially through apoptosis for **Ir-10**. This supported findings by flow cytometry and RPPA, which showed a higher level of apoptosis activated by **Os-3** compared to **Ir-10**.

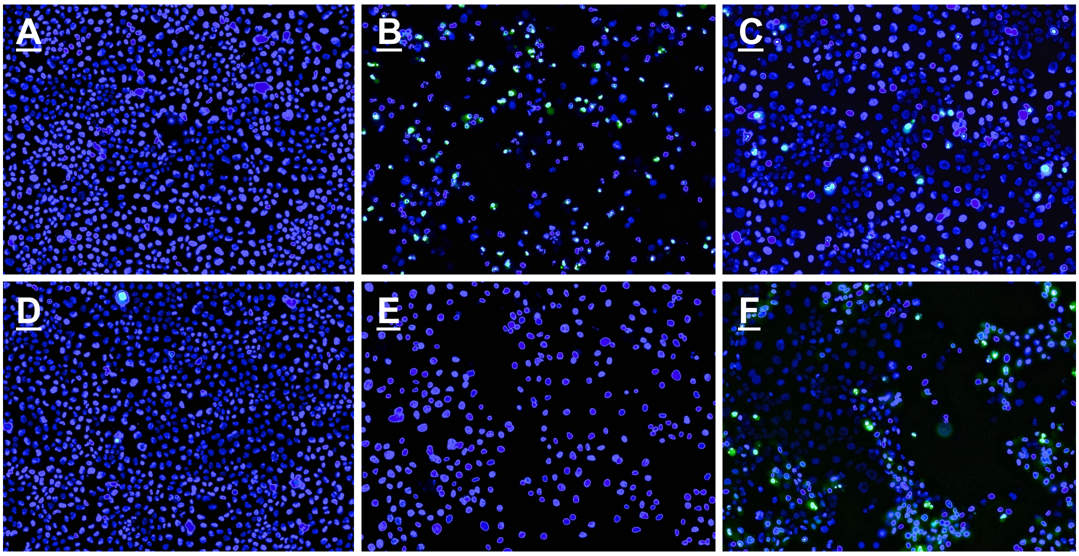

Figure 7.5: **Fluorescence images showing apoptotic OVCAR-3 human ovarian cancer cells after exposure for 48 h to (A) Control; (B) 2.5 μM Os-1; (C) 2.5 μM Os-3; (D) 2.5 μM Os-4; (E) 2.5 μM Ir-9; (F) 2.5 μM Ir-10.** DAPI is used to stain the nuclei of cells (blue), with the NucView reagent staining apoptotic cells (green). NucView is activated inside cells by caspase-3 and caspase-7 which are apoptotic effector proteins, therefore fluorescence of this probe is an indirect measure of apoptosis. Panels (B) **Os-2** and (F) **Ir-10** show small signs of apoptosis in OVCAR-3, much less than in A2780 cells. However, the number of stained nuclei is still decreased. Panels (C) **Os-3**, (D) **Os-4** and (E) **Ir-9** show no apoptosis, with (D) and (E) showing no reduction in nuclei count.

Figure 7.5 shows a similar trend in behaviour as that seen in A2780 cells with **Os-1** showing the most activation of apoptosis, this time at $23X$ times the GI_{50} value. **Os-3** and **Ir-10** show low levels of apoptosis in OVCAR-3 at $9X$ and $11X$ their GI_{50}, respectively. The reduction in cell count is notable for **Os-1**, **Ir-10** and to a lesser extent **Os-3**. Compounds **Os-4** (GI_{50}) and **Ir-9** ($4X$ times GI_{50}) showed no measurable apoptosis, although **Ir-9** showed stronger antiproliferative activity compared to **Os-4**.

The viable A2780 cell counts (blue), and A2780 apoptotic cell counts (green) were obtained after exposure to 2.5 μM of each of the compound, and were compared to cisplatin (CDDP) and to a DMSO control used against each compound (Table 7.1).

Table 7.1: Percentage of cells in apoptosis after exposure to compounds **Os-1**, **Os-3**, **Os-4**, **Ir-9**, **Ir-10** and CDDP at 2.5 μM for 48 h, ± SD. % of cells in apoptosis was calculated by dividing the number of cells with NucView fluorescence by the total number of cells (with DAPI fluorescence). This calculation was performed for compound-exposed samples and for control-exposed samples. The Ratio describes the number of apoptotic cells in compound-exposed samples compared to control-samples. In response to **Os-1** and **Ir-10** there is significant activation of apoptosis at 2.5 μM. In comparison, **Os-4** and CDDP do not activate apoptosis in A2780 cells.

Complex	**% Cells in apoptosis (compound-exposed)***	**% Cells in apoptosis (control-exposed)***	**Ratio****
Os-1	45.15 ± 481.5	0.78 ± 3.7	57.9
Os-3	25.46 ± 93.7	1.22 ± 4.6	20.9
Os-4	0.99 ± 5.9	0.49 ± 2.4	2.0
Ir-9	0.61 ± 5.5	1.07 ± 2.9	0.6
Ir-10	13.86 ± 64.5	0.27 ± 1.6	51.9
CDDP	1.45 ± 8.8	0.96 ± 3.5	1.5

*calculated as $[\frac{apoptotic\ cell\ count}{viable\ cell\ count}]$ **calculated as $[\frac{\%\ apoptosis\ compound-exposed}{\%\ apoptosis\ control}]$

Table 7.1 reflects the observations shown in Figure 7.4, where **Os-1** and **Ir-10** showed the highest level of apoptosis measured in viable cells, followed closely by **Os-3**. Compounds **Os-4**, **Ir-9** and CDDP all showed minimal apoptosis, due mainly to the large cell count remaining after exposure. This highlights them as primarily cytostatic agents, with **Os-1**, **Os-3** and **Ir-10** showing measurable cytotoxic behaviour in A2780.

The level of apoptosis was also measured at concentrations more relevant to the GI_{50} values of each compound in A2780 cells (Table 7.2).

Table 7.2: Percentage of cells in apoptosis after exposure to compounds **Os-1**, **Os-3**, **Os-4**, **Ir-9**, **Ir-10** and CDDP at ca. GI_{50} μM for 48 h, ± SD. % of cells in apoptosis was calculated by dividing the number of cells with NucView fluorescence by the total number of cells (with DAPI fluorescence). This calculation was performed for compound-exposed samples and for control-exposed samples. The Ratio describes the number of apoptotic cells in compound-exposed samples compared to control-samples. When A2780 cells are exposed to **Os-1**, **Os-3** and **Ir-10**, at its GI_{50} concentration there is poor activation of apoptosis compared to exposure at 2.5 μM, suggesting that these compounds have concentration-dependent mechanisms of action. In comparison, exposure to **Os-4**, **Ir-9** and CDDP at GI_{50} concentrations showed little difference in apoptosis activation compared to exposure at higher doses. This suggests that apoptosis is not concentration-dependent for these compound.

Complex	**Conc. μM**	**% Cells in apoptosis (compound)***	**% Cells in apoptosis (control)***	**Ratio****
Os-1	0.16	1.48 ± 6.7	0.78 ± 3.7	1.9
Os-3	0.32	2.93 ± 19.3	1.22 ± 4.6	2.4
Os-4	0.63	0.80 ± 2.5	0.49 ± 2.4	1.6
Ir-9	0.63	0.73 ± 4.7	0.77 ± 2.9	1.0
Ir-10	0.32	0.60 ± 2.6	0.27 ± 1.6	2.2
CDDP	1	1.58 ± 12.2	0.96 ± 3.5	1.7

*calculated as $[\frac{apoptotic\ cell\ count}{viable\ cell\ count}]$ **calculated as $[\frac{\%\ apoptosis\ compound-exposed}{\%\ apoptosis\ control}]$

After testing at approximately the GI_{50} concentrations for each compound, Table 7.2 shows a low level of apoptosis after exposure to all compounds, although **Os-1**, **Os-3** and **Ir-10** still show the highest levels.

7.2.2 Transmission electron microscopy for compound Ir-6

Bright field TEM was used to study the morphological changes associated with exposure of A2780 cells to **Ir-6** ($[Ir(\eta^5\text{-}Cp^{xbiph})(phen)Cl]^+$) at 1 μM (approx GI_{50}) and 5 μM (6.9 times GI_{50}) for 24 h. Cells were fixed, and stained with uranyl acetate and lead citrate before embedding, sectioning and imaging. A total of 48 control images were taken, with those presented in Figure 7.6 as representative subsets. Figure 7.6 shows TEM images of the negative control samples.

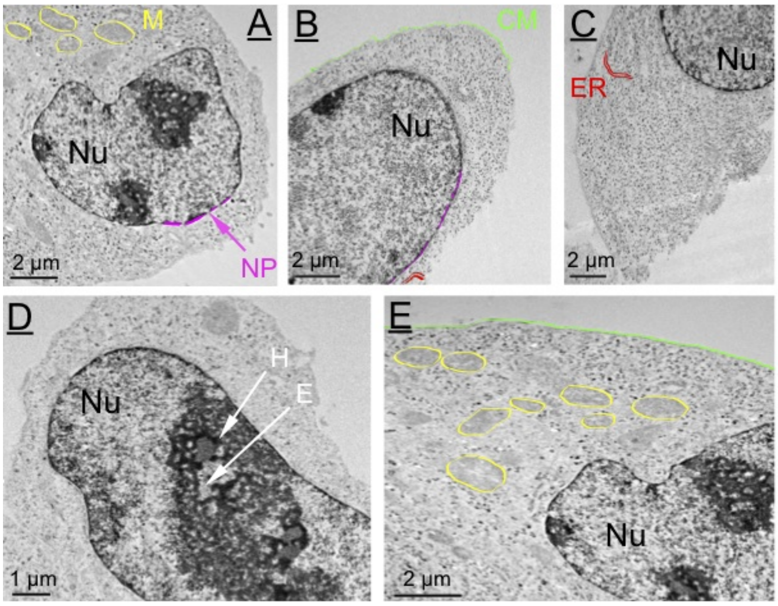

Figure 7.6: **A2780 control TEM images**. Images show typical heterochromatin (H) and euchromatin (E) distributions in panel D, mitochondria (M, yellow) in panels A and E, nuclear pores (NP, purple) in panel A, cell membrane (CM, green) in panel B and rough endoplasmic reticulum (ER, red) in panel C.

Figure 7.6 highlights the nucleus (Nu), abundant mitochondria (yellow, M) granular endoplasmic reticulum (red, ER), nuclear membrane with nuclear pores (purple, NP) and the cell membrane (green, CM). Also shown, is the heterochromatin (H) and euchromatin (E) of the nucleolus. Figure 7.7 shows TEM images of samples exposed to 1 μM **Ir-6**. A total of twenty-three images were taken, where images in Figure 7.7 are a representative subset.

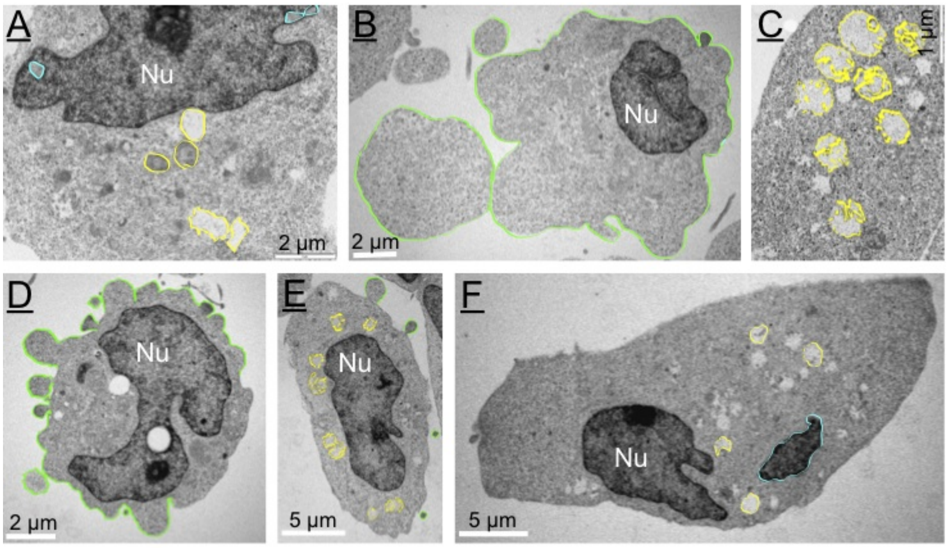

Figure 7.7: **TEM images of A2780 cells after exposure to 1 μM Ir-6 for 24 h.** Images show the nucleus (Nu), damaged mitochondria (yellow) in panels A, C and E and cell membrane blebbing (green) in panels B, D and E. Panel A also shows small nuclear vacuoles (blue). These structural changes are indicative of mitochondria damage and cell death.

Figure 7.7 highlights several changes associated with exposure to **Ir-6**. Highlighted in green is the cell membrane, which is shown to bleb and break apart into possible apoptotic bodies (7.7B and D). However, the cells appear to swell in comparison to those shown in the control, where apoptosis is associated with cell shrinkage. Instead this could be a sign of oncosis/necrosis, with the merging of apoptotic bodies as the cell swells.

Also shown, in yellow, are deformed mitochondria which no longer maintain their characteristic structure shown in Figure 7.6 (7.7A, C and E). Instead the mitochondria appear as vacuoles in the cytoplasm, although their double-layer membrane can still be identified.

Figure 7.8 shows TEM images of samples exposed to 5 μM **Ir-6**. A total of fifty-one images were taken, where the images in Figure 7.8 are a representative subset.

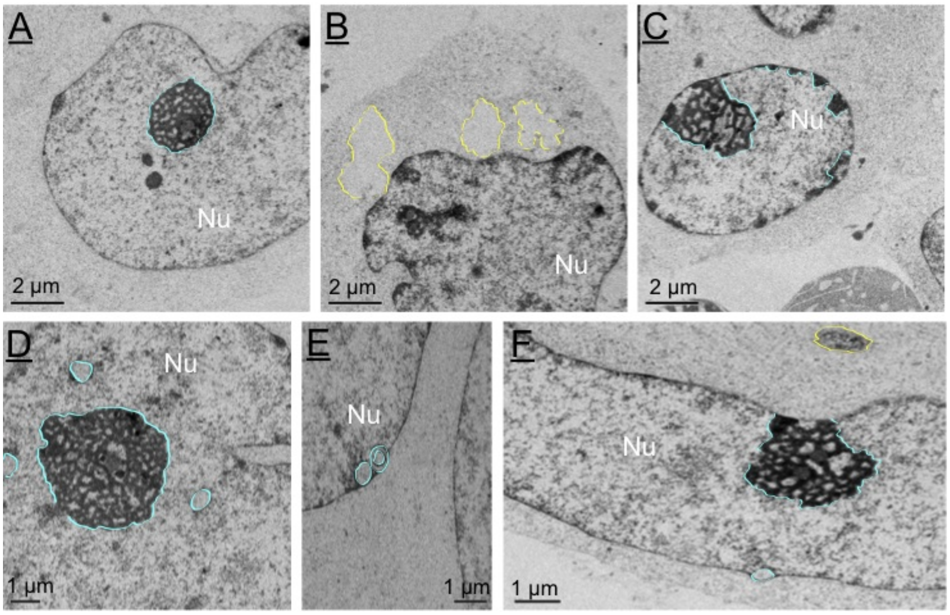

Figure 7.8: **TEM images of A2780 cells after exposure to 5 μM Ir-6 for 24 h.** Images show abnormal chromatin distributions (blue) and further mitochondria damage (yellow). These structural changes show that breakdown of the mitochondria is more significant at higher compound concentrations, and that higher doses of **Ir-6** also induce small vacuole formation around the nuclear membrane.

Figure 7.8 shows some signs of apoptosis with fragmentation of DNA in the nucleolus, however, there also appears to be a loss in membrane integrity, particularly in Figure 7.8B which could be indicative of late necrosis.

Importantly, Figure 7.8 also highlights abnormal mitochondria (Figure 7.8B), although after exposure to a higher dose of **Ir-6**, the double membrane is no longer identifiable, instead the mitochondria are completely devoid of inner structure. Shown in blue are bubble-like structures both surrounding the nucleolus and localised to the nuclear membrane. The structure of the nucleolus has also changed, becoming condensed, delineated masses localised on the nuclear membrane.

Figure 7.9 shows zoomed images of the mitochondria in samples exposed to 1 μM **Ir-6**. The cristae of the mitochondria are visibly detached (yellow circle), leading to complete mitochondrial breakdown.

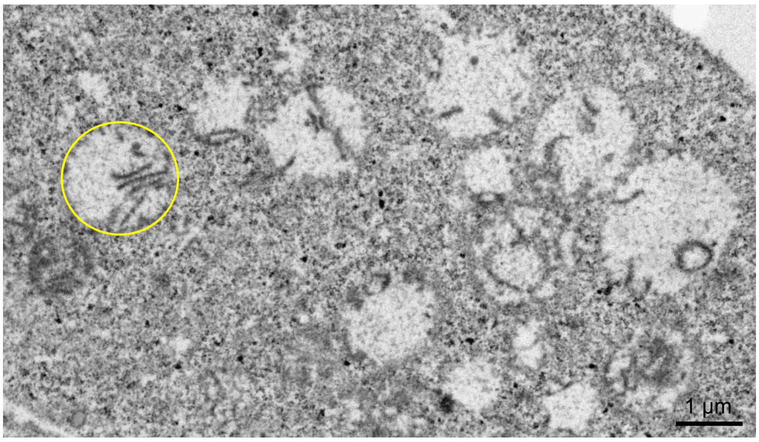

Figure 7.9: **TEM images of A2780 mitochondria after exposure to 1 μM Ir-6 for 24 h.** Circled area highlights a mitochondrion where the cristae are still partially structured. The remaining mitochondria are significantly damage by the mechanisms of **Ir-6**, losing both inner and outer membrane integrity.

To further investigate the effects of **Ir-6** on the mitochondria, the polarisation of the mitochondrial membrane was measured using flow cytometry. Here the fluorescence on a cationic and lipophillic dye, JC-10 is measured. Ordinarily the JC-10 protein will aggregate inside the mitochondria and emits red fluorescence. Upon mitochondrial membrane polarisation, this aggregation is reduced, together with the red light emission. The fluorescence of JC-10 was measured after 4 and 24 h exposure to **Ir-6** at 1 and 0.24 (1/3 GI_{50}) μM, against a positive control, carbonyl cyanide m-chlorophenylhydrazone (5 μM).

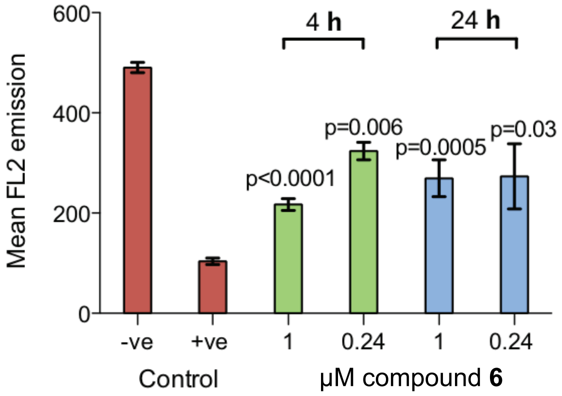

Figure 7.10: **Bar graph showing mitochondrial membrane polarisation after cells were exposed to Ir-6 at 0.24 μM ($\frac{1}{3}$GI$_{50}$) and 1 μM (ca. GI$_{50}$), for 4 and 24 h.** This assay uses a positively charged fluorescent probe (JC-10), which aggregates in the mitochondria and fluoresces red. Upon mitochondrial membrane polarisation, the aggregation of the probe decreases, and the red fluorescence drops. Therefore polarisation is determined by a reduction in red (FL2) fluorescence. *p* values were calculated after a Welch t-test against the negative control. Results show that mitochondrial membrane polarisation is activated after just 4 h exposure, at either concentration of **Ir-6**.

Figure 7.10 shows that the mitochondria of A2780 cells are polarised by **Ir-6** after just 4 h, even with a lower dose (p = 0.006, Welch paired t-test), compared to the negative control. After 24 h, there was a slight increase in membrane polarisation after 0.24 μM exposure (p = 0.03). This result further confirms the effects of **Ir-6** on the mitochondria, whether directly or indirectly.

7.3 Discussion

7.3.1 Cell death mechanisms

Apoptosis is the most common type of chemotherapy-induced cancer cell death, and can be determined using a range of techniques.[11, 12] The later phases of apoptosis are morphologically identifiable by microscopy.[13]

Using high-content screening (HCS) to detect levels of caspase-3, Chapter 7 explored the effector-phase of apoptosis. The morphological aspects of apoptosis were also studied, in cells exposed to **Ir-6**, using transmission electron microscopy (TEM). Previous chapters suggested little or no apoptosis was activated by these compounds at low doses, with NCI-60 screening results showing a primarily cytostatic behaviour, therefore imaging assays were performed at higher doses to see if cell death was concentration-dependent.

High-content screening proved to be a poor method for accurately quantifying apoptosis, with non-reproducible triplicate results. However, it was possible to extract compound-based trends and make predictions about the level of apoptosis at higher concentrations, where there was a significant increase in apoptotic cells at higher concentrations. For **Os-3**, this has been shown in a previous study in A549 lung cancer cells.[14]

The onset of apoptosis is often characterised by condensation of nuclear chromatin, into delineated masses that localise on the nuclear membrane.[11, 15] This behaviour was shown in cells exposed to **Ir-6** at both doses, although more evident at the higher dose. Such nuclear destabilisation is a result of enzymes called caspase-activated DNase (CAD) enzymes, which cleave DNA.[16] Also shown after exposure to **Ir-6** were small nuclear vacuoles, sometimes localised to the nuclear membrane. These could be an artefact of abnormal chromatic packaging as a result of CAD activity.[16]

The membrane of cells exposed to **Ir-6** also showed signs that cells were undergoing apoptosis, forming extensions termed ‘budding’, which would ultimately form ‘apoptotic bodies'.[11, 15] However, the cells appeared to grow in size, and the apoptotic bodies were quite large in some of the images. This could point towards a more necrotic form of cell death. In addition, organelles inside the cell would remain intact until apoptotic bodies were phagocytosed or degraded by secondary necrosis; however, TEM showed that the mitochondria were not staying intact.[17] It is possible that mitochondrial damage occurred, which prevented the maintenance of this organelle.

TEM images show signs of apoptosis after exposure to **Ir-6**, however, this was not supported by flow cytometry. There are alternative routes to cell death, namely oncosis, pyropotosis and autophagy. In fact oncosis can be characterised by vacuolisation of the cytoplasm; it is possible that at higher concentrations of **Ir-6**, the large vacuoles assumed to be mitochondria, were in fact signs of oncosis. Both these routes to cell death are linked to the release of cytokines from the cell, something not demonstrated for **Ir-6**, but proposed for both **Os-3** and **Ir-10**.

The TEM images therefore suggest a mix of cell death mechanisms for **Ir-6**, with some pictures highlighting apoptotic cell death and some highlighting oncotic cell death. Similarly, at lower concentrations, there were only a small number of cells in the effector-phase of apoptosis, yet there had been a drastic decrease in cell count for **Os-1**, **Os-3** and **Ir-10**, suggesting cells had died via different mechanisms. Assuming a link between **Ir-6**, **Os-3** and **Ir-10** this could explain why a low level of apoptosis was measured by flow cytometry, yet necrotic cells were counted. Collectively these compounds could be inducing apoptosis and necrotic-type cell death. As suggested in Chapter 5, performing these experiments more frequently between 4 and 48 h could help answer these questions, as could performing TEM analysis on cells exposed to **Os-3** and **Ir-10**.

7.3.2 Mitochondrial targeting by Ir-6

Swelling of the mitochondria, which could distort the visualisation of organelle structure by TEM, is associated with calcium imbalance inside cells, caused by drug-induced oxidative stress.[18–20] A prominent consequence of exposure to **Ir-6** was swelling of, and damage to, the mitochondria, evident by both TEM and flow cytometry. Assuming similarity between **Ir-6** and **Os-3**, which was demonstrated in the NCI-60 screen, transcriptomics of cells exposed to **Os-3** also showed a significant effect relating to the mitochondria. The mitochondrial membrane becomes polarised during apoptosis; however, given the low detection of apoptosis, it is likely that the significant membrane polarisation shown for **Ir-6** and for **Os-3** is due to mitochondrial targeting.[14]

As discussed in Chapter 4, there is significant interest in mitochondrial-targetting of anticancer agents which are able to exploit the differences in metabolism between normal and cancerous cells. In addition, A2780 human ovarian cancer cells are inherently mutated cancer cells, making them significantly more susceptible to attack and to damage by ROS production. A recent study by Maillet *et al* provided evidence for an osmium-based anticancer agent able to trigger the production of ROS through mitochondrial targeting.[21] This was a detailed comprehensive study, however the osmium compound used had a GI_{50} value between 50 and 75 μM. **Os-3** appears to achieve a similar MOA with a submicromolar GI_{50} value.

7.4 Summary and Conclusions

Imaging has proven a useful tool to visualise those findings proposed by the other methods used in previous chapters. Future work will collect TEM data for cells exposed to both **Os-3** and **Ir-10**. Cell death appears to increase with increasing concentration of compounds, however, the number of apoptotic cells identified with green fluorescence did not correlate with the reduction in total cell count. This suggests that apoptosis may account for some cell death, but it is possible that another mechanism of cell death is responsible for the remaining cell count reduction. This was demonstrated here for compound **Ir-6**. Modes like oncosis and pyroptosis are associated with cytokine release and immune response activation, so it is possible that these also play a role in compound response. The best way to investigate this would be to do an extensive TEM imaging study, backed up my flow cytometry/RPPA, across multiple time points between 4 and 48 h exposure.

A previous study has shown that cells can activate apoptosis, but switch to necrotic-type cell death if caspase-inhibitors are unregulated.[22] RNAseq and RPPA showed the initiation of apoptosis with components like BCL-2 and BAD, but showed inhibitor of apoptosis (IAP) proteins were highly up-regulated thus preventing caspase cascade activation. The study by Vercammen *et al* showed that when apoptosis was blocked, cells entered into a necrotic-type cell death involving ROS production. The activation of an immune response shown to **Os-3** and **Ir-10** supports a necrotic-type cell death, which activates the production of cytokines. The ROS production has also been heavily supported for **Os-3**, with flow cytometry experiments and RNAseq pathway analysis, and has been proposed for **Ir-10**.

This is a novel mode of activity for an anticancer compound, and would make for an exciting treatment program for cancers with inherently resistant apoptotic components, with ROS production causing irreversible damage to the cell.

References

[1] Rausch O (2006) High content cellular screening. *Current Opinion in Chemical Biology* 10:316–320.

[2] Zanella F, Lorens JB, Link W (2010) High content screening: Seeing is believing. *Trends in Biotechnology* 28:237–245.

[3] Semwogerere D, Weeks ER (2008) in *Encyclopedia of Biomaterials and Biomedical Engineering* Second edition, pp 705–714.

[4] Guduru R, et al. (2013) Magneto-electric Nanoparticles to Enable Field-controlled High-Specificity Drug Delivery to Eradicate Ovarian Cancer Cells. *Scientific Reports* 3:2953.

[5] Su X, Bernal JA, Venkitaraman AR (2008) Cell-cycle coordination between DNA replication and recombination revealed by a vertebrate N-end rule degron-Rad51. *Nature Structural & Molecular Biology* 15:1049–1058.

[6] Conrad C, Gerlich DW (2010) Automated microscopy for high-content RNAi screening. *The Journal of Cell Biology* 188:453–461.

[7] Erfle H, Simpson JC, Bastiaens PIH, Pepperkok R (2004) siRNA cell arrays for high-content screening microscopy. *BioTechniques* 37:454–458.

[8] Williams DB, Carter BC (1996) in *Transmission Electron Microscopy* pp 3–17.

[9] van Rijt SH, Mukherjee A, Pizarro AM, Sadler PJ (2010) Cytotoxicity, hydrophobicity, uptake, and distribution of osmium(II) anticancer complexes in ovarian cancer cells. *Journal of Medicinal Chemistry* 53:840–849.

[10] Morse DL, Gray H, Payne CM, Gillies RJ (2005) Docetaxel induces cell death through mitotic catastrophe in human breast cancer cells. *Molecular Cancer Therapeutics* 4:1495–1504.

[11] Kroemer G, et al. (2009) Classification of cell death: recommendations of the Nomenclature Committee on Cell Death 2009. *Cell Death and Differentiation* 16:3–11.

[12] Lazebnik YA, Cole S, Cooke CA, Nelson WG, Earnshaw WC (1993) Nuclear events of apoptosis in vitro in cell-free mitotic extracts: a model system for analysis of the active phase of apoptosis. *Journal of Cell Biology* 123:7–22.

[13] Degterev A, Boyce M, Yuan J (2003) A decade of caspases. *Oncogene* 22:8543–8567.

[14] van Rijt SH, Romero-Canelón I, Fu Y, Shnyder SD, Sadler PJ (2014) Potent organometallic osmium compounds induce mitochondria-mediated apoptosis and S-phase cell cycle arrest in A549 non-small cell lung cancer cells. *Metallomics* 6:1014–1022.

[15] Saraste A, Pulkki K (2000) Morphologic and biochemical hallmarks of apoptosis. *Cardiovascular Research* 45:528–537.

[16] Nagata S, Nagase H, Kawane K, Mukae N, Fukuyama H (2003) Degradation of chromosomal DNA during apoptosis. *Cell Death and Differentiation* 10:108–116.

[17] Kerr JF, Winterford CM, Harmon BV (1994) Apoptosis. Its significance in cancer and cancer therapy. *Cancer* 73:2013–2026.

[18] Zhou DF, et al. (2011) Anticancer activity, attenuation on the absorption of calcium in mitochondria, and catalase activity for manganese complexes of N-substituted di(picolyl)amine. *Inorganic Chemistry* 50:6929–6937.

[19] Perchellet EM, et al. (2007) Antitumor Triptycene Analogs Directly Interact with Isolated Mitochondria to Rapidly Trigger Markers of Permeability Transition. *Anticancer Research* 27:3259–3272.

[20] McKeage MJ, Maharaj L, Berners-Price SJ (2002) Mechanisms of cytotoxicity and antitumor activity of gold(I) phosphine complexes: the possible role of mitochondria. *Coordination Chemistry Reviews* 232:127–135.

[21] Maillet a, Yadav S, Loo YL, Sachaphibulkij K, Pervaiz S (2013) A novel Osmium-based compound targets the mitochondria and triggers ROS-dependent apoptosis in colon carcinoma. *Cell Death and Disease* 4:e653.

[22] Vercammen D, et al. (1998) Dual signaling of the Fas receptor: initiation of both apoptotic and necrotic cell death pathways. *The Journal of Experimental Medicine* 188:919–930.

Chapter 8. Concluding Remarks

The aim of this thesis has been to gain insights into the anticancer activity of organometallic compounds developed at The University of Warwick . Previous reports highlighted the promising characteristics of these compounds in trying to tackle the limitations with current metal-based anticancer agents used in the clinic. Namely, drug resistance and toxicity. Two important areas were explored in this thesis, firstly using cancer cell screens to identify whether there was a particular cancer subtype to which these compounds were most potent. The second, was to explore the mechanisms of activity of lead compounds.

8.1 Summary of results

The screening results presented a good level of selectivity, highlighting a selection of cell lines to which these compounds were particularly potent. Although these *in vitro* screens are far from conclusive with regards to patient selection, they have highlighted areas of importance going forward for *in vitro* work.

The mechanistic insights were gained by combining results from multiple techniques, aiming to study the cellular response of ovarian cancer cells to lead compounds **Os-3** ($[\mathrm{Os}(\eta^6\text{-}p\text{-cym})(\mathrm{NMe_2\text{-}azpy})\mathrm{I}]^+$] and **Ir-10** ($[\mathrm{Ir}(\eta^5\text{-}\mathrm{Cp}^{xph})(\mathrm{NMe_2\text{-}azpy})\mathrm{Cl}]^+$). Figure 8.1 summarises some of the proposed mechanisms of anticancer activity based on these results.

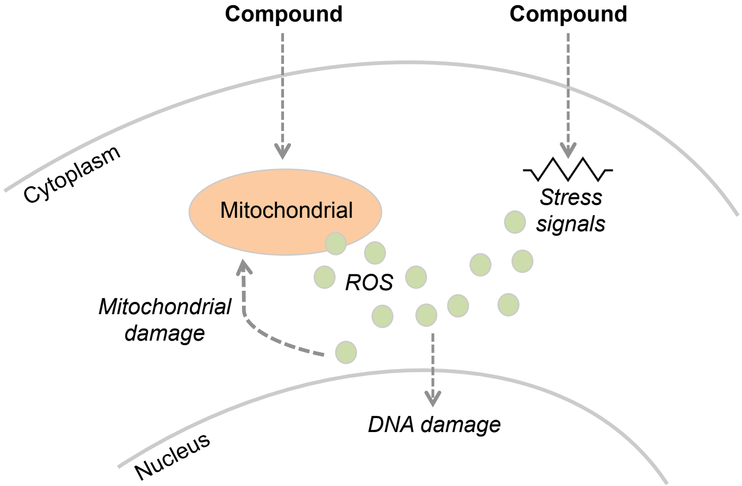

Figure 8.1: **Schematic summarising the proposed mechanisms of action of compounds studied in this work.** DNA image was adapted from psdgraphics.com.

Previous work has confirmed the presence of excessive ROS in response to **Os-3**, and although this is yet to be confirmed for **Ir-10**, a previous report has highlighted ROS production in cells responding to **Ir-9** ([Ir(η^5-Cp^{xbiph})(ppy)Cl]). The mechanism for inducing oxidative stress is yet to be determined, and has been suggested to occur through mitochondrial targeting and/or through stress response pathways.

If ROS production is mediated by the mitochondria then the proposed mechanism of action could provide a highly selective anticancer agent, exerting less of an effect in normal cells with functional mitochondria. This has been demonstrated previously for **Os-3**, which is much more potent in normal fast dividing fibroblasts. However, as more conclusive measure of toxicity this assay also needs to be repeated in normal cells that are not undergoing fast division.

The immune response activation may also contribute to mitochondrial ROS production, however, the dangers of activating this cellular mechanism needs to be established.[1] This can be strongly linked to increased tumorigenesis, and metastasis, which is one of the biggest clinical problems with chemotherapy treatment. Therefore future work should assess the metastatic behaviour of cells exposed to **Os-3** and **Ir-10** and conclude whether co-administration with an immune inhibitor is required.

The production of ROS can be highly damaging to cells, here, DNA damage in particular has been proposed, however proteins are also a viable target. At low concentrations, the oxidative stress and DNA damage caused by these compounds results in cell cycle arrest, but does not lead to cell death. Interestingly, increasing the concentration of these compounds may increase their cytotoxic activity. This was particularly evident in response to **Ir-6** ($[Ir(\eta^5$-$Cp^{xbiph})(phen)Cl]^+$), showing signs of apoptosis and necrosis. Therefore, these compounds could make viable cytostatic agents, particularly in cases of platinum resistance, to aid in tumour size control and management. At higher concentrations these agents could then provide more of a cytotoxic activity, arresting cell growth and destroying tumour cells. This could have applications both pre- and post-surgery.

8.2 Significance

8.2.1 Methods

Cancer cell screening can provide a wealth of information for cancer researchers, both on selectivity and mechanisms of action. However, there are several pitfalls which should be considered, and database screening should always be experimentally validated. One of the biggest problems, particularly in combining information from multiple screens, is the different methodology used by different institutes. For example the NCI and the Sanger Institute use different exposure period, and use different methods to measure antiprofilerative activity. Therefore, insights gained in using these screens should always be followed with in-house assays using uniform experimental conditions. Here, screening is used to select out two lead compounds and to make generalised selectivity predictions. Database correlations for the selected leads were then explored experimentally.

Methods like RNA sequencing are rarely used in drug development to study a new mechanism of action, instead sequencing is used together with prior knowledge i.e. to study a specific pathway or process of interest. Care was taken when sequencing ovarian cancer cells, to account for any copy number variations, which could swamp sequence reads. This thesis used RNA sequencing with little prior knowledge of what could be found and was therefore performed with sufficiently high-coverage, with paired-end reads, in efforts to capture as much information as possible. By using sequencing in place of microarrays, alternative splicing could be investigated in future work, using the existing sequencing files.

Using systems biology methodology, and combining sequencing with other state-of-the-art techniques has allowed detailed insights to be obtained. Zeptosens protein microarrays are the gold standard in this field, and offer unparalleled sensitivity. This has been particularly useful here, by detecting small changes in protein levels. RPPA, like sequencing, is an expensive method and using both techniques in this thesis has not created a sustainable workflow. However, studying the gene expression has provided useful information, therefore methods like DNA microarrays may make better alternatives for future work.

Modelling both the sequencing and proteomics data provided quantitative insights at both the transcriptional and translational response levels. To optimise the use of the MDI modelling software, the number of proteins included in the analysis needs to be increased to allow a better assessment of functional ontology in clusters. However, this study highlighted the potential of this software, identifying extensive co-regulation of proteins involved in DNA damage and cell cycle arrest. As biological methods seek to collect more and more data, software like MDI will be invaluable for informative data analysis, and has already shown promising clinical applications.[2]

Of the imaging techniques, the transmission electron microscopy results were highly fruitful. This is a relatively inexpensive method, and provided great detail highlighting mitochondrial damage and cell death. This should therefore remain a prominent part of future work with these organometallic compounds. Additions to this technique, perhaps using dark field electron microscopy, may also provide interesting results about metal distribution. As could the imaging mass spectrometry (IMS) technique nanoSIMS. Although for both these techniques, the level of osmium/iridium would have to be greatly increased to allow detection of metal accumulation.

Collectively, this thesis has demonstrated the merits of measuring gene expression, protein abundance and cell structure in investigating the mechanisms of action of anticancer agents. Identifying up- and down-stream drug effects and creating a timeline of activity. The information generated in this work can be used for more detailed *in vitro* mechanistic work, focussing on specific areas of the cell.

8.2.2 Results

The aim of this work was not to identify a biological target, but instead to assess cellular response. This captures not only mechanistic insights, but also toxicity and selectivity-focussed results. Simultaneously looking at all of these factors should better predict *in vivo* behaviour. The work presented here is of great interest to the metallo-chemistry community, showing that complex biological techniques have use in early drug development, and can help shape synthesis early on. The work published on NCI-screening demonstrated how useful this resource can be in drug development, and how much much more information can be gained, outside of selectivity. Measuring gene and protein profiles is not a new concept in cancer research, however, it is rarely used so early in drug development, and like screening data, can be used in future to help inform chemical synthesis.

Clinically, the significance of these findings are hard to predict. Certainly the most important aspect of cancer treatment is patient selection, identifying treatments to exploit cancer cell characteristics. This can be achieved without knowing the biological target. For example, from the results presented here, it is possible to postulate that patients with cancers lacking NRF-2 , or ROS-scavenger machinery, may be well selected for these organometallic compounds. Although not conclusive, this trait was demonstrated *in vitro* in MDA-MB-468, which has GSH deficiencies and was the most sensitive cell line in the NCI-60 screen. Given the detected DNA damage, patients with DNA damage repair deficiencies may also be well suited for this treatment. These insights could also help select drug cocktails. For example co-administering the organometallic compounds with L-BSO, which depletes cellular levels of the ROS-scavenger GSH, greatly increases the effect on cancer cells. Future work may explore other combination treatments linked to oxidative damage and DNA damage mechanisms.

References

[1] Yang D, et al. (2007) Pro-inflammatory cytokines increase reactive oxygen species through mitochondria and NADPH oxidase in cultured RPE cells. *Experimental Eye Research* 85:462–472.

[2] Savage RS, Ghahramani Z, Griffin JE, Kirk P, Wild DL (2013) Identifying cancer subtypes in glioblastoma by combining genomic, transcriptomic and epigenomic data. *International Conference on Machine Learning*.

Appendices

9.1 Supporting information for Chapter 3

Table 9.1: Table showing the genes contained within amplified regions *R184* and *R198*

R184	***R198***
CHMP4C	*ADCY8*
FABP4, FABP5, FABP9, FABP12	*ASAP1*
HEY1	*FAM498*
IL7	*GSDMC*
IMPA1	
MRPS28	
PAG1	
PKIA	
PMP2	
SLC10A5	
SNX16	
STMN2	
TPD52	
ZBTB10	
ZC2HC1A	
ZFAND1	
ZNF104	

9.2 Supporting information for Chapter 4

9.2.1 Experiment I sample quality checks

Table 9.2: Summary statistics for each sample. Showing total reads, mapping and quality scores

Sample number	**Sample name**	**A260/230**	**A260/280**	**RIN**
1	0 h control	2.28	1.95	10
2	0 h control	2.01	1.96	10
3	0 h control	2.25	1.94	10
4	0 h control	1.62	2.00	10
5	0 h control	2.22	1.94	10
6	0 h control	1.88	2.00	10
7	4 h control	2.22	1.93	10
8	4 h control	2.27	1.91	10
9	4 h control	2.30	1.92	10
10	4 h **3**	2.29	1.94	10
11	4 h **3**	2.24	1.94	10
12	4 h **3**	2.29	1.93	10
13	12 h control	2.24	1.94	10
14	12 h control	2.20	1.93	10
15	12 h control	2.28	2.00	10
16	12 h **3**	2.17	1.92	10
17	12 h **3**	2.13	1.94	10
18	12 h **3**	2.09	1.95	10
19	24 h control	2.22	2.02	10
20	24 h control	2.25	2.01	10
21	24 h control	2.21	2.01	10
22	24 h **3**	1.97	2.00	10
23	24 h **3**	1.96	2.00	10
24	24 h **3**	2.08	1.99	10
25	48 h control	2.19	1.95	10
26	48 h control	2.20	1.96	10
27	48 h control	2.19	1.95	10
28	48 h **3**	2.18	1.95	10
29	48 h **3**	2.25	1.96	10
30	48 h **3**	2.03	1.99	10

9.2.2 Experiment II

9.2.2.1 Sequence summary stats

Table 9.3: Summary statistics for each lane. Showing yields, mapping and quality scores

Lane[*]	**Yield (Mb Q20)**	**% Mapped reads**	**Mean quality score**
1	20,999	98.1	34.4
2	18,291	97.9	35.6
3	19,081	98.5	35.3
4	16,367	98.3	36.5
5	16,860	98.3	36.4

[*] 6 samples per lane

9.2.2.2 Sample quality checks

Table 9.4: Summary statistics for each sample. Showing total reads, mapping and quality scores

Sample number	**Sample name**	**A260/230**	**A260/280**	**RIN**
1	0 h control	2.28	1.95	10
2	0 h control	2.01	1.96	10
3	0 h control	2.25	1.94	10
4	0 h control	1.62	2.00	10
5	0 h control	2.22	1.94	10
6	0 h control	1.88	2.00	10
7	4 h control	2.22	1.93	10
8	4 h control	2.27	1.91	10
9	4 h control	2.30	1.92	10
10	4 h **3**	2.29	1.94	10
11	4 h **3**	2.24	1.94	10
12	4 h **3**	2.29	1.93	10
13	12 h control	2.24	1.94	10
14	12 h control	2.20	1.93	10
15	12 h control	2.28	2.00	10
16	12 h **3**	2.17	1.92	10
17	12 h **3**	2.13	1.94	10
18	12 h **3**	2.09	1.95	10
19	24 h control	2.22	2.02	10
20	24 h control	2.25	2.01	10
21	24 h control	2.21	2.01	10
22	24 h **3**	1.97	2.00	10
23	24 h **3**	1.96	2.00	10
24	24 h **3**	2.08	1.99	10

9.2.2.3 Summary stats

Table 9.5: Summary statistics for each sample. Showing total reads, mapping and quality scores

Sample number	Sample name	Total reads	% Mapped reads	Mean quality score
1	0 h control	58,453,334	98.53	36.5
2	0 h control	52,958,428	98.32	36.4
3	0 h control	52,411,032	98.11	36.5
4	0 h control	57,489,392	98.72	36.5
5	0 h control	53,112,138	97.75	36.5
6	0 h control	54,962,488	98.12	36.4
7	4 h control	82,071,522	98.19	34.4
8	4 h control	84,555,686	98.11	34.4
9	4 h control	73,333,434	97.93	34.4
10	4 h **3**	69,130,568	97.87	34.4
11	4 h **3**	59,742,704	97.99	34.5
12	4 h **3**	72,018,526	98.38	34.4
13	12 h control	50,690,134	97.87	36.4
14	12 h control	55,041,730	99.25	36.4
15	12 h control	60,723,390	97.88	36.4
16	12 h **3**	58,813,794	98.12	36.4
17	12 h **3**	57,945,078	98.82	36.4
18	12 h **3**	56,092,354	97.97	36.4
19	24 h control	60,331,926	98.14	35.6
20	24 h control	67,939,036	98.93	35.0
21	24 h control	59,240,982	98.09	35.6
22	24 h **3**	64,300,818	95.65	35.5
23	24 h **3**	61,522,272	98.48	35.6
24	24 h **3**	61,343,334	98.18	35.5

Table 9.6: Summary statistics for each sample. Showing total reads, mapping and quality scores

Time point (h)	**Sample name**	**Total reads**	**% Mapped reads**	**Mean quality score**
1	0 h control	58,453,334	98.53	36.5
2	0 h control	52,958,428	98.32	36.4
3	0 h control	52,411,032	98.11	36.5
4	0 h control	57,489,392	98.72	36.5
5	0 h control	53,112,138	97.75	36.5

9.3 Supporting information for Chapter 5

Table 9.7: RPPA protein details

Protein label	**Protein**	**Gene**
AKT	AKT	AKT1
ATM	ATM	ATM
ATM*	ATM/ATR Substrate P Ser/Thr	ATM
Aur***	Aurora A/B/C P Thr288/Thr232/Thr198	AURK
b-actin	beta-actin	ACTB
b-catenin	beta-catenin	CTNNB1
B-Tub	beta-tubulin	TUBB
BAD*	Bad P Ser112	BAD
BAD(*)	Bad P Ser136	BAD
BAK	BAK	BAK1
BAX	BAX	BAX
BCL-2	BCL-2	BCL2
BCL-2*	BCL-2 P Ser 70	BCL2
BCL-X	BCL-X	BCL2L1
BID	BID	BID
BIM	BIM	BCL2L11
BRCA1	BRCA1	BRCA1
CASP3	Caspase 3	CASP3
CASP3*	Caspase 3 cleaved	CASP3
CDC25A	CDC25A	CDC25A
CDC25C*	CDC25C P Ser216	CDC25C
CDK1	CDC2	CDK1
CDK1*	CDK1(p34cdc2) P Tyr15	CDK1
CDK2	CDK2	CDK2
CHK2*	CHK2 P Thr68	CHEK2
Cyc D1	CycD	CCND1
Cyc D1*	Cyc D	CCND1
E-cadherin	E-cadherin	CDH1
FLT3*	FLT3 P Tyr591 P Tyr591	FLT3
IKK*	IKK alpha P Ser32	IKK
JAK1	JAK1	JAK1
JAK1*	JAK1 P Tyr1022, Thr1023	JAK1
MEK1/2	MEK1/2	MAP2K1

Table 9.8: RPPA protein details

Protein label	**Protein**	**Gene**
MET	MET	MET
MTOR	MTOR	MTOR
MYC	C-MYC	MYC
p21	p21 CIP/WAF1	CDKN1A
p21*	CIP/WAF1 p Thr145	CDKN1A
p53	p53	TP53
p53*	p53 P Ser15	TP53
PARP	PARP	PARP1
PARP*	PARP cleaved	PARP1
PDK1	PDK1	PDK1
PLC-gamma1	PLC-gamma1	PLCG1
PKC-alpha	PKC-alpha	PRKCA
PTEN	PTEN	PTEN
PTEN*	PTEN P Ser380, Thr382, Thr383	PTEN
FAK1	FAK1	PTK2
PUMA	PUMA	PUMA
RAP1	RAP1	RAP1A
RB	RB	RB
RB*	RB P Ser780	RB
RB**	RB P Ser807, Ser811	RB
p70 *	p70 S6 kinase	RPS6KB1
SRC	SRC	SRC
STAT1	STAT1	STAT1
STAT1*	STAT1 P Tyr701	STAT1
STAT1(*)	STAT1 P Ser727	STAT1
STAT3	STAT3	STAT3
STAT3*	STAT3 P Tyr705	STAT3
STAT5	STAT5	STAT5
STAT5*	STAT5 P Tyr694	STAT5
STAT6	STAT6	STAT6
STAT6*	STAT6 P Tyr641	STAT6
LKB1	LKB1	STK11
Survivin	Survivin	BIRC5
TYK2*	TYK2 P Tyr1054, Tyr1055	TYK2
XIAP	XIAP	XIAP

List of Figures

Publications

J. M. Hearn, A. F. Munrow, I. Romero-Canelon, F. Ying, N. O. Carragher and P J. Sadler (2014) Potent organo-osmium complex targets metabolism in epithelial ovarian cancer cells. Submitted.

Z. Liu, I. Romero-Canelon, B. Qamar, **J. M. Hearn**, A. Habtemariam, N. P. E. Barry, A. M. Pizarro and P. J. Sadler (2013) Redox paradox: potent organoiridium anticancer agents use cellular antioxidants to generate reactive oxygen species (ROS). *Angew. Chem. Int. Ed. (VIP)*. 53(15): 3941-3946

Y. Fu, R. Soni, M. J. Romero, A. M. Pizarro, L. Salassa, G. J. Clarkson, **J. M. Hearn**, A. Habtemariam, M. Wills, and P. J. Sadler (2013) Mirror-image Organometallic Osmium Arene Iminopyridine Halido Complexes Exhibit Similar Potent Anticancer Activity. *Chem. Eur. J.* 19(45): 15199-15209

J. M. Hearn, I. Romero-Canelon, B. Qamar, Z. Liu, I. Hands-Portman and P. J. Sadler (2013) Organometallic iridium(III) anticancer complexes with new mechanisms of action: NCI-60 screening, mitochondrial targeting and apoptosis. *ACS Chem. Biol.* 8 (6): 1335-1343

Conferences and Meetings

Dalton meeting (**April 2014**, Warwick)*

AACR annual meeting (**April 2014**, San Diego)*

Sun Yat-Sen delegation (**March 2014**, Warwick)**

WSB annual conference (**March 2014**, Stratford)**,***

Mitochondria, energy metabolism and cancer (**February 2014**, UCL London)

ELRIG: drug discovery (**September 2013**, Manchester)*

1st International symposium on functional metal complexes that bind to biomolecules: COST action meeting (**September 2013**, Barcelona)*

Ovarian cancer, Leah Lederman lecture and annual general meeting (**September 2013**, RSM London)

WSB annual conference (**June 2013**, Stratford)*,***

ELRIG: research and innovation (**March 2013**, Telford)

Development of cancer medicines: preclinical in vivo models to interrogate cancer biology, biomarkers and therapeutic response (**November 2012**, RSM London)

2nd Protein array workshop (**November 2012**, Edinburgh)

24th EORTC-NCI-AACR symposium on molecular targets and cancer therapeutics (**November 2012**, Dublin)

WSB annual conference (**June 2012**, York)*,***

* Poster presented ** Talk given *** Prize awarded